Measuring relay exchange kinematics in short-track speed skating using a multi-camera network

HEXT, Andrew <http://orcid.org/0000-0003-2070-6601>

Measuring relay exchange kinematics in short-track speed skating using a multi-camera network

Andrew Hext

April 2019

Collaborating organisation: Great Britain Short-Track Speed Skating

A thesis submitted in partial fulfilment of the requirements of Sheffield Hallam University for the degree of Doctor of Philosophy

Candidate declaration

I hereby declare that:

1. I have not been enrolled for another award of the University, or other academic or professional organisation, whilst undertaking my research degree.
2. None of the material contained in the thesis has been used in any other submission for an academic award.
3. I am aware of and understand the University's policy on plagiarism and certify that this thesis is my own work. The use of all published or other sources of material consulted have been properly and fully acknowledged.
4. The work undertaken towards the thesis has been conducted in accordance with the SHU Principles of Integrity in Research and the SHU Research Ethics Policy.
5. The word count of the thesis is 63,192.

Name	Andrew Hext
Date	April 2019
Award	PhD
Faculty	Health and Wellbeing
Director of Studies	Simon Goodwill

Abstract

To support their targeted improvement of the relay exchange, Great Britain Speed Skating required a tool that could be used to advance knowledge on '*how to execute the relay exchange effectively*'. A tool that measures relay exchange kinematics in representative race scenarios, over its entirety, and with an acceptable level of measurement error (± 0.19 $m \cdot s^{-1}$). A review of existing measurement solutions found that the Olympic Oval (CAN) multi-camera network was the only tool that came close to meeting this criterion. However, while this multi-camera network satisfied the metrics, scenarios, and scope of relay exchange measurement, its ± 1.53 $m \cdot s^{-1}$ error exceeded the target measurement error. For these reasons, this thesis developed a multi-camera network to measure accurate, two-dimensional, relay exchange kinematics.

The literature review identified that the accuracy of the National Ice Centre (GBR) multi-camera network was dependent on five sources of measurement error. Accordingly, a series of investigations quantified how these errors propagated, independently, to errors in relay exchange kinematics. In the case where these errors exceeded the target measurement error, additional studies investigated minimising each error. Using this empirically informed measurement workflow, Monte Carlo simulations showed that the multi-camera network's *total error* was ± 0.17 $m \cdot s^{-1}$. This error was within the target measurement error and significantly less than the benchmark Olympic Oval (CAN) multi-camera network. Investigations into the execution of the relay exchange demonstrated how this reduction in error allowed Great

Britain Short-Track Speed Skating to advance knowledge on *'how to execute the relay exchange effectively'*. In turn, supporting the team's targeted improvement of the relay exchange, and ultimately, their aim of delivering medal-winning performances at the Winter Olympic Games.

Acknowledgments

I would like to thank Simon Goodwill, Ben Heller, and John Kelley for their supervision, Terry Senior for helping calibrate the multi-camera network, and Ciarán McInerney and David Higham for their contribution to countless technical discussions. I am also grateful to the Engineering and Physical Sciences Research Council and the English Institute of Sport for funding this doctorate, and Great Britain Short-Track Speed Skating for their collaboration and my secondment as their performance analyst. Finally, and most importantly, I would like to thank my friends and family for the reminder that there is life outside of a PhD. I'm looking forward to enjoying it.

Personal bibliography

Hext, A., Heller, B., Kelley, J. W., & Goodwill, S. R. (2017). Relay exchanges in elite short-track speed skating. *European Journal of Sport Science*, *17*(5), 503–510.

Hext, A., Heller, B., Kelley, J. W., & Goodwill, S. R. (2016). Measuring straight time in elite short-track speed skating relays. *Procedia Engineering*, *147*, 622–626.

Hext, A., Heller, B., Kelley, J. W., & Goodwill, S. R. (2014). Tactical positioning in the short-track speed skating relay. *Sheffield Hallam University Health & Wellbeing Faculty Research Conference*, Sheffield, UK.

Table of contents

Part I - Multi-camera network contextualisation

Part II - Multi-camera network development

Part III - Multi-camera network demonstration

Part IV - Summary and conclusion

Chapter 1

Introduction

Short-track speed skating has been part of the Olympic programme since its debut at the 1992 Winter Olympic Games in Albertville, France (Bullock, Martin, & Zhang, 2008). In its current format, individual (500 m, 1,000 m and 1,500 m) and relay (3,000 m and 5,000 m) events provide a country with the opportunity to win eight gold medals (ISU, 2016). The principal aim of Great Britain Short-Track Speed Skating – the project's collaborating organisation – is to deliver medal-winning performances at the Winter Olympic Games.

To earn a medal in short-track speed skating, a skater or team must advance through several qualification races to reach the medal contest, e.g. heats, quarter-finals, semi-finals. In all events, races – performed anticlockwise on a 111.12 m oval – involve four to six skaters racing head-to-head at speeds exceeding 12.5 $m \cdot s^{-1}$ (Landry, Gagnon, & Laurendeau, 2013). Advancement through these qualification races, and medal colour, is dependent on the finishing position in that race only, i.e. finishing time, with respect to other races, is irrelevant (ISU, 2016). For this reason, strategic aspects such as *'how long to draft for'* and *'when and where to overtake'*, are essential for success in short-track speed skating (Konings, Noorbergen, Parry, & Hettinga, 2016; Maw, Proctor, Vredenburg, & Ehlers, 2006; Muehlbauer & Schindler, 2011; Noorbergen, Konings, Micklewright, Elferink-Gemser, & Hettinga, 2016)

Raced over 3,000m (27 laps) for women and 5,000m (45 laps) for men, the relay event provides an additional strategic component to short-track speed skating races: the relay

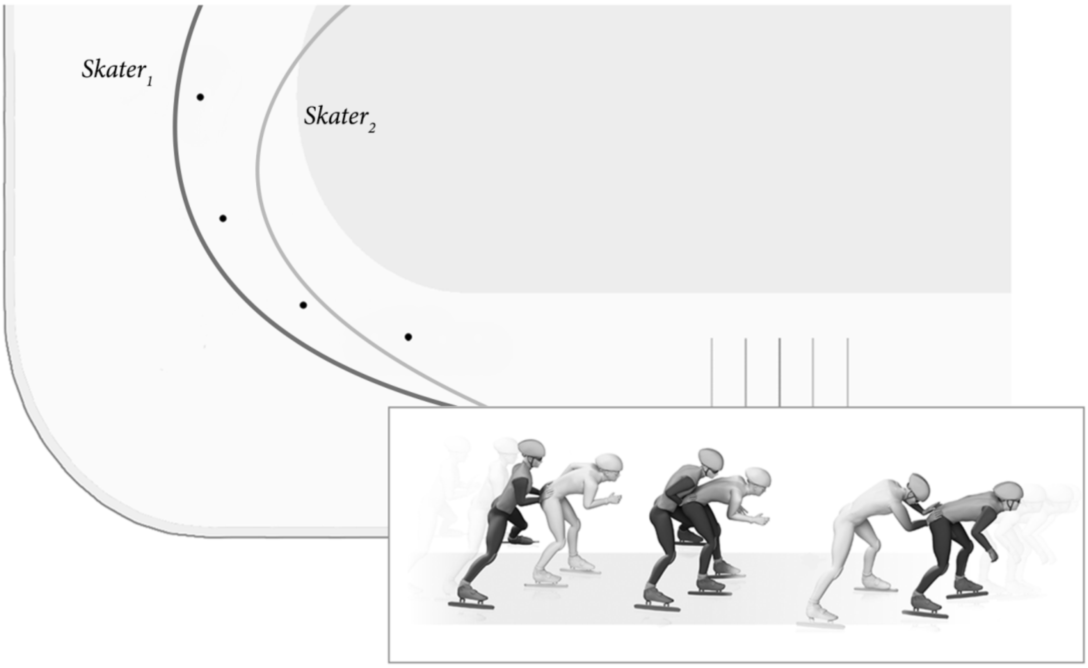

Figure 1-1. The short-track speed skating relay exchange. In preparation for the exchange, *Skater₂* builds up speed on the inside of the track to arrive at the start of the straight with a similar speed to *Skater₁*. Post relay exchange, *Skater₁* recovers inside of the track for future involvement in the race. Figure adapted from Hext et al. (2017).

exchange. Excluding the final two laps of the race, the relay exchange allows a team, consisting of four skaters, to change the skater involved in the pack race at any time (ISU, 2016). With change in race responsibility initiated by touch, the relay exchange – illustrated in Figure 1-1 – is typically executed by the skater involved in the pack race, *Skater₁*, pushing the new skater, *Skater₂*, at the start of the straight.

In a typical race, teams will execute the relay exchange every 1½ laps, resulting in 17 relay exchanges over 3,000 m and 29 relay exchanges over 5,000 m. Skaters and coaches believe that during this period of the race, time can be gained or lost depending on how well a team executes the relay exchange (Osborough & Henderson, 2009; Riewald, Broker, Smith, & Otter, 1997). For this reason, Great Britain Short-Track Speed Skating have targeted improving the execution of the relay exchange to support their aim of delivering medal-winning performances at the Winter Olympic Games.

Despite the purported effect of the relay exchange, scholars and practitioners –

including Great Britain Short-Track Speed Skating's coaches and sport science team – know very little about *'how to execute the relay exchange effectively'*, due to the difficulties in measuring the relay exchange in (1) representative race scenarios, i.e. for up to four team simultaneously, (2) over its entirety, i.e. the straight and proceeding corner, and (3) with an acceptable level of measurement error, i.e. the ability to measure skating velocity to within ± 0.19 $m{\cdot}s^{-1}$. Consequently, the factors currently reported critical for effective relay exchange execution are limited to the scenario where a team is isolated from the pack race, with the mechanisms that underlie each factor, unknown.

Accordingly, to support their targeted improvement of the relay exchange, Great Britain Short-Track Speed Skating require a tool that can be used to advance knowledge on *'how to execute the relay exchange effectively'*. A tool that measures relay exchange kinematics in representative race scenarios, over its entirety, and with an acceptable level of measurement error.

1.1 Thesis aim

This thesis investigates developing a tool to measure accurate, two-dimensional, relay exchange kinematics in short-track speed skating. More specifically, based on a review of existing short-track speed skating measurement solutions in Chapter 3, this thesis aims to develop a multi-camera network to measure accurate, two-dimensional, relay exchange kinematics. The overarching aim of this thesis, therefore, is to answer the research question *'Can multi-camera networks be used to measure accurate, two-dimensional, relay exchange kinematics in short-track speed* skating'.

1.2 Thesis structure

The remainder of this thesis is structured into four parts as follows,

Part I Multi-camera network contextualisation

The first part of the thesis contextualises the need for developing a multi-camera network to measure accurate, two-dimensional, relay exchange kinematics. First, Chapter 2 evidences the strategic opportunity of the relay exchange and provides a rationale for how future work should advance knowledge on *'how to execute the relay exchange effectively'*. Second, based on this rationale, Chapter 3 formulates a relay exchange measurement needs analysis and reviews existing short-track speed skating measurement solutions using the needs analysis as an evaluation criterion.

Part II Multi-camera network development

The second part of the thesis investigates developing the National Ice Centre multi-camera network to measure accurate, two-dimensional, relay exchange kinematics. First, Chapter 4 provides an overview of the multi-camera network installed at the home of Great Britain Short-Track Speed Skating's World Class Performance Programme. Second, Chapter 5 identifies its sources of measurement error and the most suitable method for quantifying its accuracy. Third, Chapters 6 to 13 quantify how these sources of measurement error propagate, independently, to errors in relay exchange kinematics. Finally, Chapter 14 determines whether the multi-camera network can measure accurate, two-dimensional, relay exchange kinematics.

Part III Multi-camera network demonstration

The third part of the thesis demonstrates how the developed multi-camera network allows Great Britain Short-Track Speed Skating to advance knowledge on *'how to execute the relay exchange effectively'*. Chapter 15 presents two investigations that, until now, were not possible due to the aforementioned difficulties in measuring the relay exchange.

Part IV Summary and conclusion

The fourth part of the thesis (Chapter 16) summarises the findings reported in this thesis, discusses their practical implications for Great Britain Short-Track Speed Skating, and presents an overall thesis conclusion.

Part I Multi-camera network contextualisation

Chapter 2

Relay exchange efficacy in elite short-track speed skating

2.1 Introduction

This thesis investigates developing a multi-camera network to measure accurate, two-dimensional, relay exchange kinematics. In this chapter, I begin to contextualise the need for this work by examining the efficacy of the relay exchange in elite short-track speed skating. The results are used to evidence the strategic opportunity of the relay exchange – ergo supporting its targeted improvement by Great Britain Short-Track Speed Skating – and provide a rationale for how future work should advance knowledge on *'how to execute the relay exchange effectively'*.

To examine the efficacy of the relay exchange in elite short-track speed skating, I quantify the relay exchange's effect on race time and race position during the 5,000 m short-track relay. First, to understand the relay exchange's effect on race time, I compare the time taken to complete the straight for the scenarios with and without the relay exchange at different corner skating speeds. Second, to understand the relay exchange's effect on race position, I compare both skating scenarios' overtaking effectiveness, i.e. their ability to achieve a gain-in-race position.

2.2 Method

The Faculty of Health & Wellbeing Research Ethics Committee, Sheffield Hallam University, UK, approved this investigation.

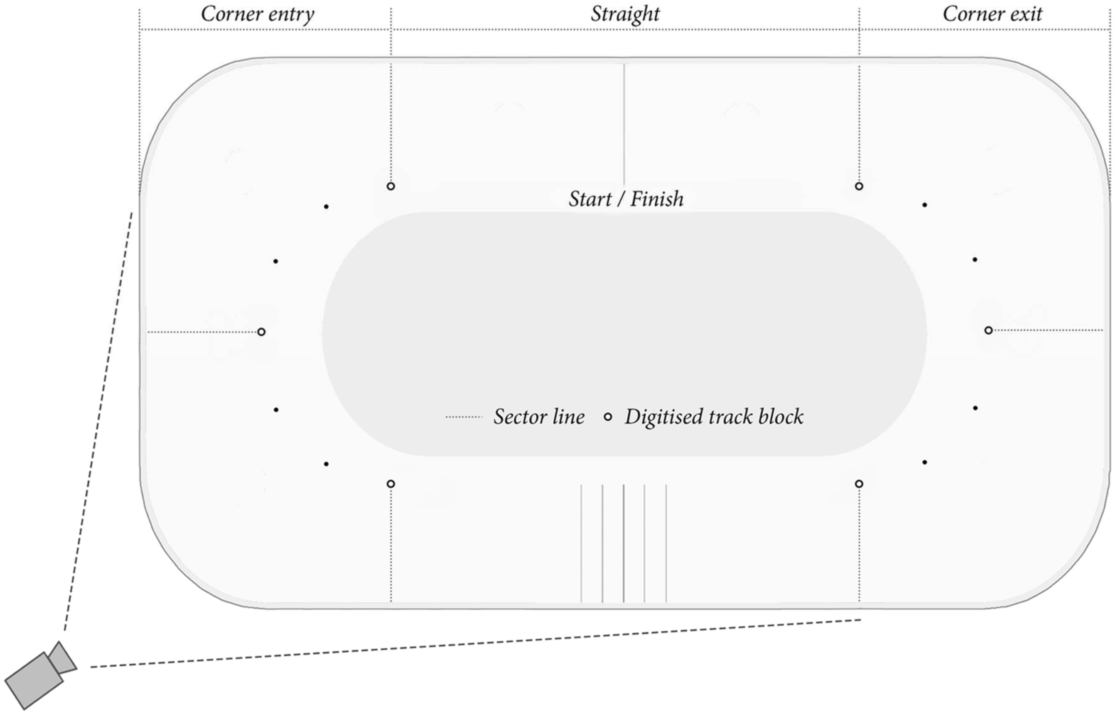

Figure 2-1. The experimental setup, highlighting (1) the camera location in relation to the rink, (2) the six digitised track marking blocks used in the calibration procedure, and (3) the sector lines that split the track into three main sections.

2.2.1 Performance data

This investigation used data collected from three International Skating Union (ISU) Short Track World Cups during the 2012–2013 season. The dataset consisted of 20 men's 5,000 m relay races: 12 heats, 6 semi-finals and 2 A-finals. Each race was captured using a single Sony HDR PJ260VE camcorder operating at 50 Hz (progressive scan). As illustrated in Figure 2-1, the camera was mounted on a tripod in the spectator gallery opposite the relay start line and fixed approximately 45° to the rink's longitudinal axis. The camera's field of view was adjusted to capture the full rink surface.

2.2.2 Calibration procedure

For each race, the investigation calibrated the rink surface using a two-dimensional direct linear transformation (DLT) (Walton, 1981). First, the procedure manually digitised six track marking blocks of known position to calculate the eight DLT coefficients necessary to reconstruct a 2D position of a point on a plane (Figure 2-1). A frame approximately two seconds into the captured footage was used to ensure that (1) the camera had settled in its fixed position after the operator pressed record, and (2) the track marking blocks had not yet been displaced from their correct location. Second, the procedure overlaid six sector lines onto the race footage by extending lines through the digitised track marking blocks. As illustrated in Figure 2-1, and in accordance with Bullock, Martin, and Zhang (2008), the six sector lines split the short-track into three main sections: the straight, the corner entry, and the corner exit. The typical mean reconstruction error of the calibration procedure was 0.05 m ± 0.05 m on the 60 × 30 m rink surface. For a detailed description of the method used to evaluate the calibration procedure, see part two of Dunn, Wheat, Miller, Haake, & Goodwill (2012).

2.2.3 Race analysis procedure

For each race, the procedure defined the start of the race as the first frame where the start gun was seen to fire. Accordingly, the analysis calculated all subsequent temporal race measurements using the camera frame rate at a resolution of 0.02 seconds. For each team, the procedure manually digitised the absolute time and rink position where the lead blade of the racing skater first passed through a sector line for the race's entirety (270 unique spatiotemporal events per team). For the corner exit and corner entry sector line events, the analysis also recorded the team's position in the pack race. If a skater fell, the procedure collected no further measurements for that team. All manual digitisation was performed by a single operator to negate inter-operator digitisation error.

2.2.4 Data analysis

For each instance of a relay exchange, i.e. the scenario where a relay exchange occurred during the straight, the analysis calculated five metrics – depicted in Figure 2-2a– using the absolute time, rink position, and race position data: (1) *corner exit time* (t_1): the time taken from the apex sector line to the exit sector line, (2) *straight time* (t_2): the time taken from the exit sector line to the entry sector line, (3) *apex block distance* (x_1): the

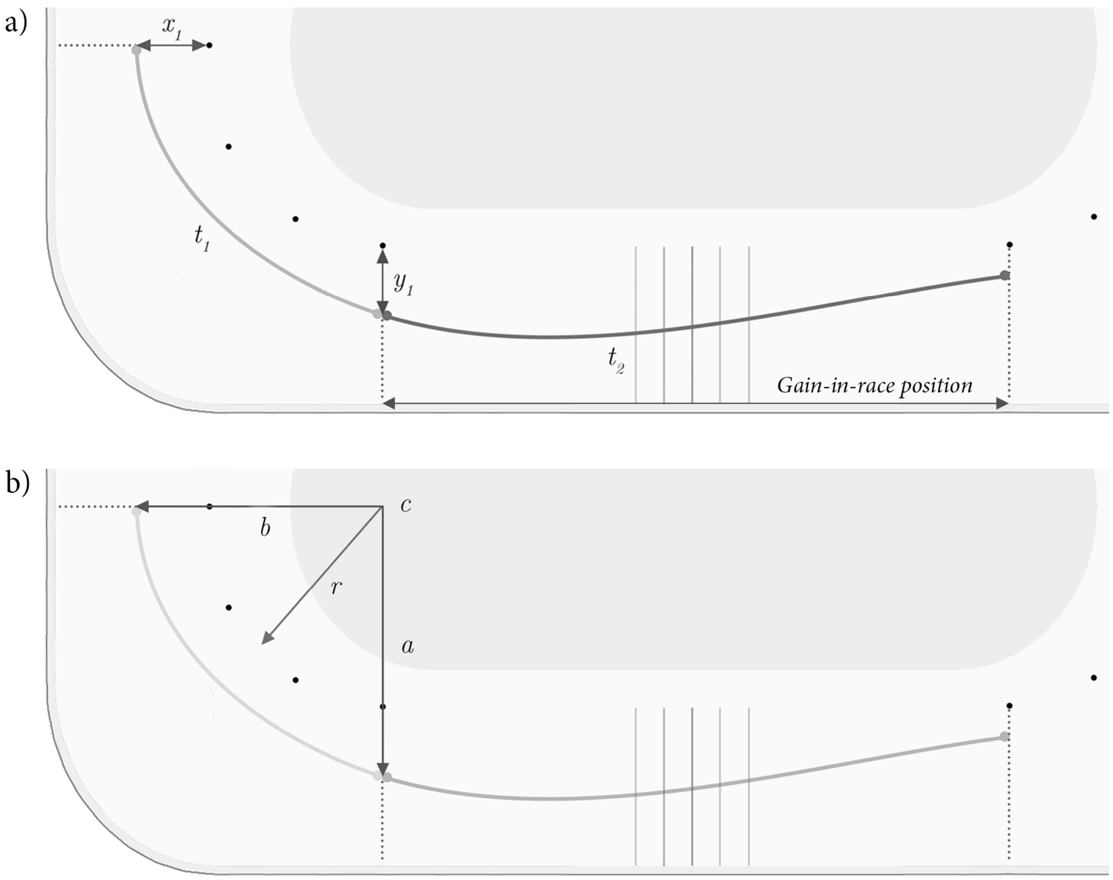

Figure 2-2. (a) The five metrics calculated for instance of a relay exchange or free skating scenario: corner exit time (t_1), straight time (t_2), apex block distance (x_1), exit block distance (y_1), and *gain-in-race position* count. (b) The centre of rotation (c), corner radius (r), and two metrics used to calculate the corner exit distance: the minor (b) and major (a) radii.

distance along the apex sector line from the track marking block to the skater's lead blade, (4) *exit block distance* (y_1): the distance along the exit sector line from the track marking block to the skater's lead blade, and (5) the *gain-in-race position* count: the number of positive changes in race position from the exit sector line to the following entry sector line, e.g. if a team moved from 3rd to 1st position in the race, this would count as two gain-in-race positions. The analysis also calculated the five metrics for the scenario where no relay exchange occurred during the straight, termed free skating.

The analysis computed corner exit speed by dividing the distance travelled by the skater during the sector, termed corner exit distance, by the corner exit time. As illustrated in Figure 2-2b, and in agreement with Yule & Payton (2000), the analysis assumed that skaters turn around a centre of rotation located at the corner centre, c. This allows the corner exit distance, d, to be calculated as an arc length of an ellipse

$$d \approx 0.25 \left\{ \pi(a+b) \left[1 + \frac{3\left(\frac{a-b}{a+b}\right)^2}{10 + \sqrt{\left(\frac{(a-b)}{(a+b)}\right)^2}} \right] \right\} \qquad (Eq.\, 2.1)$$

where a is the ellipse major radius, the sum of the exit block distance (x_1) and corner radius (r), and b is the ellipse minor radius, the sum of the apex block distance (y_1) and corner radius (r).

For each race, the analysis calculated the overtaking effectiveness of skating scenario i as a percentage of the total scenario i instances. For example, if a race had four *gain-in-race position*'s during the relay exchange scenario's 29 instances, the relay exchange would receive an overtaking effectiveness of 13.8%. After removing the race's first free skating instance – due to the initial jostling for position from the race start – a typical 5,000 m relay had 29 relay exchange instances and 60 free skating instances.

2.2.5 Reliability and validity

The level of human error in the race analysis procedure was assessed by digitising all 270 spatiotemporal events for a single team, from a randomly selected relay race, on two occasions separated by a day. The root mean square error (RMSE) was 0.02 m to 0.03 m and 0.002 to 0.003 seconds for the spatial and temporal metrics, respectively. The validity of the temporal metrics was assessed during a Great Britain Short-Track Speed Skating simulated relay race at the National Ice Centre (Nottingham, UK). As described by Hext, Heller, Kelley, & Goodwill (2016), I compared sector times, measured as per the race analysis procedure, to synchronised cameras located perpendicular to each sector line. The root mean square error was 0.011 seconds for both corner exit and straight times. Collectively, the reliability and validity for both spatial and temporal metrics are within the mean 0.05 m reconstruction error and the 0.02-second camera resolution.

2.2.6 Statistical analysis

SPSS 24 (IBM, 2016) was used to analyse both race time and race position data. For race time data, i.e. corner exit speed and straight time, the analysis discretised data into 0.5 $m{\cdot}s^{-1}$ groups; with a minimum of 10 instances of both relay exchange and free skating scenarios required for further analysis. For each group, the analysis compared differences in straight time between the relay exchange and free skating scenarios using an independent t-test (for normally distributed datasets) or a Mann–Whitney U-test (for non-normally distributed datasets). The analysis used Shapiro–Wilk tests to test for normality (Shapiro & Wilk, 1965).

For race position data, i.e. overtaking effectiveness, the analysis first calculated the relay exchange and free skating scenarios' $percent\ advantage$ (Graham & Mayberry, 2014). The $percent\ advantage$ represents the conditional percentage of relays in which skating scenario i had a greater overtaking effectiveness than skating scenario j. For example, if the relay exchange scenario had a greater overtaking effectiveness than the free skating scenario in three out of five relays, and the same overtaking effectiveness in one out of five relays, the relay exchange's overtaking effectiveness would receive a $percent\ advantage$ of 75%. To identify whether the scenarios percent advantages significantly differed from chance, i.e. 50%, the analysis performed conditional Binomial tests. In addition to the $percent\ advantage$, the analysis compared differences between the relay exchange and free skating scenarios' overtaking effectiveness using a Wilcoxon signed-rank test. This analysis used a non-parametric equivalent of the dependent t-test as the dataset violated the assumptions of normality, D (20) = 0.21, $p < 0.5$.

In all statistical tests, the significance level, α, was set at $p < 0.05$, with effect sizes calculated using Pearson's correlation coefficient, r, as described by Field (2009). Effect size magnitudes were interpreted using Cohen's thresholds; where < 0.1, is trivial; 0.1–0.3, small; > 0.3–0.5, moderate, and > 0.5, large (Cohen, 1988).

2.3 Results

2.3.1 Race time

Of the 1968 relay exchanges and 1971 free skating instances analysed, the analysis discretised 97.8% of the data into seven 0.5 $m \cdot s^{-1}$ groups ranging from 11.51 $m \cdot s^{-1}$ to 15 $m \cdot s^{-1}$. The distribution of each group's relay exchange and free skating instances are reported in Table 2-1. Note the shift towards slower corner exit speeds for the relay exchange scenario compared to the free skating scenario. All groups greater than 12.5 $m \cdot s^{-1}$ were analysed using a Mann–Whitney U-test, instead of an independent t-test, as the data violated the assumptions of normality.

Table 2-1 presents the descriptive statistics, significance test results, and effect sizes for each corner exit speed. At corner exit speeds lower than 13.5 $m \cdot s^{-1}$, straight times were significantly faster during the relay exchange scenario ($p < 0.01$). The exception being the 11.51 $m \cdot s^{-1}$ to 12 $m \cdot s^{-1}$ group, where no significant difference was observed ($p = 0.056$). This group did, however, exhibit the largest effect size ($r = 0.32$); the magnitude of the effect decreasing from moderate to small as the corner exit speed increased. For corner exit speeds of 13.51 $m \cdot s^{-1}$ to 14 $m \cdot s^{-1}$, the analysis found no significant difference between the relay exchange and free skating scenarios ($p = 0.093$), with the magnitude of the effect trivial ($r = -0.05$). In contrast, at corner exit speeds greater than 14 $m \cdot s^{-1}$, straight times were significantly slower during the relay exchange scenario ($p < 0.001$). Here, the magnitude of the effect increasing negatively, from small to moderate, as the corner exit speed increased.

2.3.2 Race position

Of the 169 gain-in-race positions observed, 79 gain-in-race positions occurred during the relay exchange scenario and 90 gain-in-race positions occurred during the free skating scenario. Table 2-2 presents the descriptive statistics and $percent\ advantage$ for each scenario's overtaking effectiveness. The relay exchange scenario's overtaking effectiveness ($\tilde{x} = 13.8\%$) was significantly larger than the free skating scenario ($\tilde{x} =$

6.7%), z = -2.8, p < 0.01, r = -0.44 (a moderate effect), and had a $percent\ advantage$ (80%) that significantly differed from chance, p < 0.05.

Table 2-1. Descriptive statistics (mean ± standard deviation), significance test results, and effect sizes for relay exchange and free skating straight times.

Corner exit speed	n (Re, Fs)	Relay exchange	Free skating	Test statistic	p	r
11.51 – 12.0 $m{\cdot}s^{-1}$	36 (25, 11)	2.55 ± 0.11 s	2.62 ± 0.12 s	-1.98[a]	0.056	0.32
12.01 – 12.5 $m{\cdot}s^{-1}$	135 (91, 44)	2.48 ± 0.07 s	2.52 ± 0.08 s	-3.24[a]	0.002	0.27
12.51 – 13.0 $m{\cdot}s^{-1}$	449 (307, 142)	2.40 ± 0.07 s	2.44 ± 0.07 s	15,045[b]	0.000	0.24
13.01 – 13.5 $m{\cdot}s^{-1}$	960 (616, 344)	2.34 ± 0.07 s	2.35 ± 0.07 s	88,043[b]	0.000	0.14
13.51 – 14.0 $m{\cdot}s^{-1}$	1158 (600, 558)	2.28 ± 0.07 s	2.27 ± 0.07 s	157,899[b]	0.093	-0.05
14.01 – 14.5 $m{\cdot}s^{-1}$	839 (272, 567)	2.23 ± 0.06 s	2.20 ± 0.06 s	54,366.5[b]	0.000	-0.24
14.51 – 15.0 $m{\cdot}s^{-1}$	277 (42, 235)	2.19 ± 0.05 s	2.15 ± 0.05 s	2,452.5[b]	0.000	-0.31

Notes: Re = relay exchange, Fs = free skating. Statistical test performed: [a] Independent t-test, [b] Mann-Whitney U-test.

Table 2-2. Overtaking effectiveness descriptive statistics and percent advantage.

Skating scenario	n (% of total dataset)	Median (Q_1, Q_3)	% advantage
Relay exchange	79 (46.7%)	13.8 (6.9, 17.2)	80%*
Free skating	90 (53.3%)	6.7 (5.0, 10.0)	20%*

Notes: Q_1 = lower quartile, Q_3 = lower quartile. * $p < 0.05$.

2.4 Discussion

To begin to contextualise the need for developing a multi-camera network to measure accurate, two-dimensional, relay exchange kinematics, this investigation examined the efficacy of the relay exchange in elite short-track speed skating. In this section, I discuss the effect of the relay exchange on race time and race position, i.e. the two metrics used to quantify the relay exchange's efficacy, the strategic opportunity of the relay exchange, the limitations of the investigation, and how future work should advance knowledge on *'how to execute the relay exchange effectively'*.

2.4.1 Race time

To understand the effect of the relay exchange on race time, I compared the time taken to complete the straight for the scenarios with and without the relay exchange at different corner skating speeds prior to the straight. Overall, the results show that the relay exchange's effect on race time is dependent on the corner exit speed; having a positive effect at slower speeds and a negative effect at faster speeds.

At slower corner exit speeds, the positive effect of the relay exchange, that is, faster straight times for the relay exchange scenario, was consistent with other elite sports relays. In swimming, the occurrence of the relay exchange accounted for significantly faster mean individual split times compared to individual events (Skorski, Etxebarria, & Thompson, 2016). While in athletics, the relay exchange had a significant positive effect on progression through the 4 × 100 m relay, due to the baton being passed forward by up to 2 m for no loss in time (Ward-Smith & Radford, 2002). This mechanism is analogous to the short-track relay exchange where instead of the baton, the skater active in the race moves forward for no loss in time, i.e. from $Skater_1$ to $Skater_2$. Despite this, however, as the corner exit speed increased the positive effect of the relay exchange transitioned to having no, and then a negative effect, highlighted by the Pearson correlation coefficient values in Table 2-1. The transition suggests that in addition to moving forward a body length for no loss in time, other factors determine the effect of the relay exchange on race time.

One explanation for the relay exchange's 'positive to negative transition' is that the relay exchange requires $Skater_2$ (the incoming skater) to arrive at the start of the straight with a similar speed to that of $Skater_1$ (the outgoing skater involved in the pack race). As $Skater_2$ generates this speed on the inside of the short-track over a tighter corner radius, $Skater_2$ expends more energy to overcome the higher cornering forces for comparable speeds (Rundell, 1996). Accordingly, as the race speed increases, $Skater_2$ may struggle to match the speed of $Skater_1$. To explore the consequence of differences in speed between $Skater_1$ and $Skater_2$ at first-contact, I modelled the relay exchange as a one-dimensional collision using the mean energy exchange efficiency reported by Riewald, Broker, Smith, & Otter (1997). Figure 2-3a shows that when the relative speed at first-contact increases, i.e. a larger difference in $Skater_1$ and $Skater_2$'s speed, $Skater_2$'s final-contact speed relative to $Skater_1$'s first-contact speed – i.e. the current speed of the race – decreases.

Another explanation for the relay exchange's 'positive to negative transition' is that when $Skater_1$ pushes $Skater_2$ during the relay exchange, they apply a force over the duration of the contact, i.e. an impulse. By assuming that both components of this impulse remain constant for all relay exchanges, we can explore the effect of the impulse on the relay exchange using the impulse-momentum theorem. Figure 2-3b and Figure 2-3c show that as the race speed increases (1) $Skater_2$'s final-contact speed relative to their first-contact speed decreases, i.e. the impulse has a lessened effect on the relay exchange, and (2) $Skater_2$ has less distance to accelerate after the relay exchange; potentially explaining why Osborough & Henderson (2009) found relay exchanges initiated greater than 4.5 m from the straight's start had slower mean skating speeds than relay exchanges initiated 4 to 4.5 m from the start.

An additional finding from this part of the investigation was the observed differences in distributions for the relay exchange and free skating instances over the seven-corner exit speed groups. Specifically, the greater number of relay exchange instances at slower

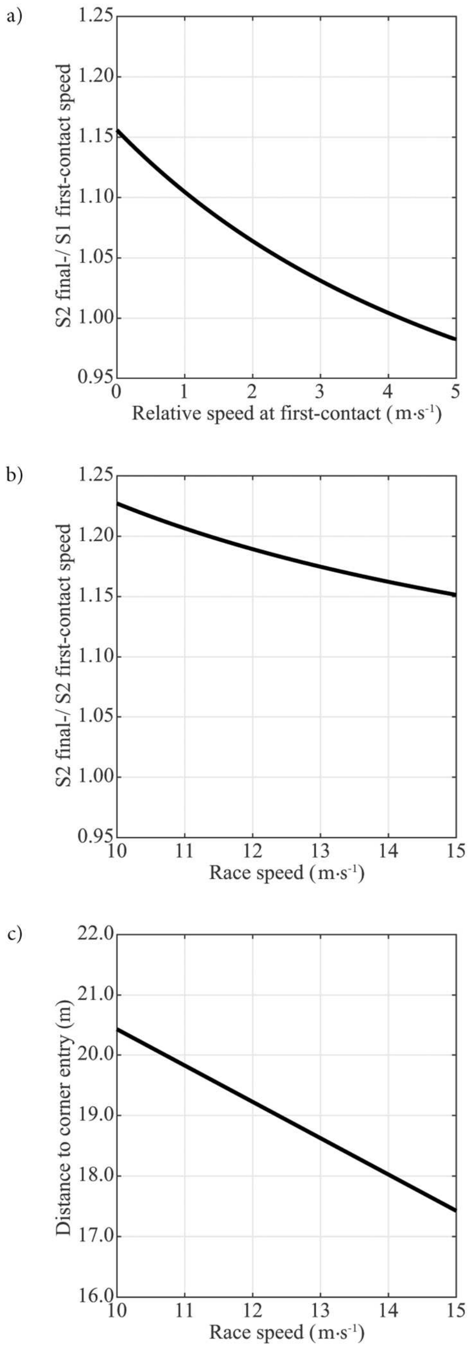

Figure 2-3. (a) The effect of relative speed at first-contact on the relative speed of *Skater*$_2$ at final-contact and the speed of *Skater*$_1$ at first-contact. (b) The effect of increasing race speed on the relative speed of *Skater*$_2$ at final-contact and the speed of *Skater*$_2$ at first-contact. (c) The effect of increasing race speed on *Skater*$_2$'s distance to corner entry at final-contact, assuming a constant first-contact position of 4 m.

corner exit speeds compared to the greater number of free skating instances at faster corner exit speeds. This difference in distributions suggests that either (1) the additional constraints of the relay exchange, such as *Skater*$_1$ ensuring that they are well positioned to push $Skater_2$ at the start of the straight, results in a lower upper limit of corner exit speed, or (2) that $Skater_1$ is slower during the relay exchange's corner exit due to fatigue; the sector representing the final period of the skater's current involvement in the pack race. The latter agrees with Riewald et al. (1997), who reported losses in speed for $Skater_1$ prior to the relay exchange contact.

2.4.2 Race position

To understand the effect of the relay exchange on race position, I compared the relay exchange and free skating scenarios' overtaking effectiveness, i.e. each scenario's ability to achieve a gain-in-race position. Overall, the results show that the relay exchange scenario presents a superior opportunity for a team to overtake in elite short-track speed skating. To the author's knowledge, this finding is the first empirical data presented on the overtaking effectiveness of the relay exchange in head-to-head sports.

To provide a theoretical reasoning to why the relay exchange presents a superior opportunity for a team to overtake, I consider the relay event as a complex dynamical system that consists of many degrees of freedom in constant flux, e.g. athlete, teammates, and opponents. In dynamical systems, perturbations can create temporary periods of instability before the system returns to the same or a previous/ new stable state (McGarry, Anderson, Wallace, Hughes, & Franks, 2002). In sporting competition, these stability disrupting perturbations occur when the typical rhythm of play – or in our case, the race – is disturbed by a high or low skill (McGarry, Khan, & Franks, 1999; Reed & Hughes, 2006). By viewing the relay exchange as a high-skill perturbation in the short-track relay, I would expect the relay exchange's overtaking effectiveness to be superior to free skating, as it represents a period in the race where the current stable race state, i.e. the current race positions, reorganise themselves into the same or previous/ new stable race states.

As the relay exchange offers a superior opportunity for a team to overtake, it is essential that a team knows how to execute the relay exchange effectively. More specifically, *'how* *to execute the relay exchange to achieve a gain-in-race position'*. Current opinion suggests that two factors appear critical (1) the time for $Skater_1$ to contact $Skater_2$ after exiting the corner, and (2) the efficiency of the energy exchange during skater contact (Riewald et al., 1997). With initiating the relay exchange between 3.5 m and 4 m from the start of the straight also being reported as producing the fastest skating speed during the straight (Osborough & Henderson, 2009). Both these investigations, however, only analysed one team on the short-track, i.e. the scenario where a team is isolated from the pack race, over the duration of the straight. Accordingly, we do not know if these factors are discriminative of achieving a gain-in-race position, and irrespective of this, the mechanisms that underlie each factor, e.g. how does the actions of $Skater_1$ and $Skater_2$ in the corner affect the time for $Skater_1$ to contact $Skater_2$ after exiting the corner?

2.4.3 Practical implications

To the author's knowledge, the study presented in this chapter is the first to investigate the efficacy of the relay exchange in elite short-track speed skating. Accordingly, Great Britain Short-Track Speed Skating can use the findings to improve their tactical preparation and decision-making before and during relay races. First, when considering the relay exchange as a strategic component of the 5,000 m relay, it is important to note that races typically exhibit a negative pacing strategy, i.e. the race starts slow and finishes fast. Therefore, Section 2.3.1's race time results suggest that varying the frequency of relay exchange execution could improve performance compared to the current norm of every 1½ laps (note that in this study, the 1½ lap frequency accounted for 96% of the relay exchanges analysed). For example, at slow race speeds, increasing the frequency of the relay exchange so that they are executed while other teams are free skating could allow time to be gained relative to these teams. In contrast, at fast race speeds typical of the race end, decreasing the frequency of the relay exchange could likewise allow time to be gained relative to other teams in the race.

Second, a team's ability to use the relay exchange to gain both race time and race position could facilitate the implementation of other race strategies. For example, in short-track speed skating drafting, i.e. one skater, skating closely behind another, has been shown to reduce heart rate and blood lactate (Hoshikawa et al., 2005; Rundell, 1996). In turn, allowing a skater or team to conserve energy for the later stages of the race where improved performance has been shown to result in better final race position (Konings et al., 2016). Despite this, however, Hoffman, Listemann, McManaman, & Rundell (1998) reported that many skaters and coaches are reluctant to utilise drafting as a race strategy due to the difficulties in overtaking. This investigation's results show that this difficulty could be alleviated by (1) increasing or decreasing the frequency of relay exchange execution; the fastest skating scenario equating to differences of up to 0.84 m at the end of the straight, or (2) targeting the relay exchange as the period of the race to overtake; assuming that a team knows '*how to execute the relay exchange to achieve a gain-in-race position*'.

2.4.4 Limitations

Note that while the above findings demonstrate the efficacy of the relay exchange in elite short-track speed skating, the observations are only applicable for the men's 5,000 m relay and not the women's 3,000 m relay. Although other strategic aspects of short-track speed skating races, such as the relationship between start and finishing position, have shown to exhibit similar relationships when comparing sex (Maw et al., 2006; Muehlbauer & Schindler, 2011), these analyses compared events with the same race distances. Consequently, it is currently unclear whether an analysis of the 3,000 m relay event would lead to the same findings as reported in this chapter. Still, this approach is sufficient for this thesis, as Great Britain Short-Track Speed Skating's targeted relay exchange improvement is primarily focussed on the 5,000 m relay event, as this was the distance funded for the Winter Olympic Games.

2.4.5 Future work

In addition to providing evidence to support Great Britain Short-Track Speed Skating's targeted improvement of the relay exchange execution, the chapter's results provide a rationale for how Great Britain Short-Track Speed Skating should start to advance knowledge on *'how to execute the relay exchange effectively'*. In turn, supporting their aim of delivering medal winning performances at the Winter Olympic Games. First, future work should validate the mechanisms proposed in Section 2.4.1 regarding why the relay exchange's effect on race time is dependent on the speed of the race. For example, if the relative velocity at impact increases with race speed, Great Britain Short-Track Speed Skating can explore the optimum methods for $Skater_2$ to match the speed of $Skater_1$, i.e. different skating trajectories/ trajectory timings. Second, due to the superior overtaking effectiveness of the relay exchange, future work should investigate *'how to execute the relay exchange to achieve a gain-in-race position'*. This aspect of future work should begin by investigating whether the current factors reported critical for effective relay exchange execution – based on the scenario where a team is isolated from the pack race – are discriminative of achieving a gain-in-race position, and if so, the mechanisms that underlie each factor.

2.5 Chapter summary

This chapter began to contextualise the need for developing a multi-camera network to measure accurate, two-dimensional, relay exchange kinematics. First, by examining the relay exchange's effect on race time and race position, the results evidenced the strategic opportunity of the relay exchange; ergo providing empirical data to support its targeted improvement by Great Britain Short-Track Speed Skating. For the former, the results showed that the relay exchange's effect on race time is dependent on race speed; having a positive effect at slower speeds and a negative effect at faster speeds. This finding suggests that the current norm of executing the relay exchange every 1½ laps may not be optimal. Instead, varying the frequency of the relay exchange execution could allow time to be gained relative to other teams in the race. For the latter, the results showed that the relay exchange offers a superior opportunity for a team to overtake. Accordingly, if a team knows *'how to execute the relay exchange to achieve a gain-in-race position'*, the relay exchange could facilitate race strategies which are underutilised due to the difficulties in overtaking, e.g. drafting. Second, the results provided a rationale for how future work should advance knowledge on *'how to execute the relay exchange effectively'*. This work focuses on validating the proposed theoretical mechanisms for why the relay exchange's effect on race time is dependent on race speed and understanding *'how to execute the relay exchange to achieve a gain-in-race position'*.

Chapter 3

Relay exchange measurement needs analysis

3.1 Introduction

In Chapter 2, I began to contextualise the need for developing a multi-camera network to measure accurate, two-dimensional, relay exchange kinematics. By examining the relay exchange's efficacy in elite short-track speed skating, I (1) evidenced the strategic opportunity of the relay exchange; ergo supporting its targeted improvement by Great Britain Short-Track Speed Skating, and (2) used this evidence to provide a rationale for how Great Britain Short-Track Speed Skating should advance current knowledge on *'how to execute the relay exchange effectively'*.

In this chapter, I continue to contextualise the need for this programme of work. First, I use Chapter 2's rationale to formulate a relay exchange measurement needs analysis. The needs analysis includes the required metrics, scenarios, and scope of relay exchange measurement and its acceptable level of measurement error. Second, I review existing, vision-based, short-track speed skating measurement solutions using the needs analysis as an evaluation criterion. Finally, I summarise the findings and practical implications of Part I of the thesis.

3.2 Needs analysis I – Metrics, scenarios, and scope

To conduct the work described in Section 2.4.5, and consequently advance knowledge on *'how to execute the relay exchange effectively'*, Great Britain Short-Track Speed Skating need to measure short-track speed skating kinematics during the relay exchange, i.e. the position and velocity of a skater. This data, coupled with the point in time of *Skater*$_1$ and *Skater*$_2$'s first- (t_{fir}) and final- (t_{fin}) contact, will enable Great Britain Short-Track Speed Skating to compute the required kinematic metrics-of-interest. These metrics, described in Section 3.2.1, include those necessary to validate the theoretical mechanisms proposed in Section 2.4.1 for why the relay exchange's effect on race time is dependent on race speed, and the two factors reported critical for effective relay exchange execution in Section 2.4.2.

3.2.1 Metrics

Section 2.4.1 described four metrics when proposing theoretical mechanisms for why the relay exchange's effect on race time is dependent on race speed (1) *Skater*$_1$'s corner exit speed, v_{1exit}, (2) the relative velocity between *Skater*$_1$ and *Skater*$_2$ at first-contact, $v_{2fir|1fir}$, (3) the relative velocity between *Skater*$_2$'s velocity at final-contact and *Skater*$_1$'s velocity at first-contact, $v_{2fin|1fir}$, and (4) *Skater*$_2$'s distance to the end of the straight at final-contact, d_{fin}.

The first metric, v_{1exit}, is computed as

$$v_{1exit} = \frac{d_{1exit}}{t_{1exit}} \qquad (Eq. 3.1)$$

where d_{1exit} is *Skater*$_1$'s corner exit distance and t_{1exit} is *Skater*$_1$'s corner exit time. As detailed in Section 2.2.4, d_{1exit} is computed as an arc length of an ellipse and t_{1exit} is computed as the period of time between *Skater*$_1$ first passing through the corner apex and corner exit sector lines.

The second metric, $v_{2fir|1fir}$, is computed as

$$v_{2fir|1fir} = v_{2fir} - v_{1fir} \qquad (Eq. 3.2)$$

where v_{2fir} is *Skater*$_2$'s velocity at first-contact and v_{1fir} is *Skater*$_1$'s velocity at first-contact.

The third metric, $v_{2fin|1fir}$, is computed as

$$v_{2fin|1fir} = v_{2fin} - v_{1fir} \qquad (Eq. 3.3)$$

where v_{2fin} is *Skater$_2$*'s velocity at final-contact and v_{1fir} is *Skater$_1$*'s velocity at first-contact.

Finally, the fourth metric, d_{fin}, is computed as

$$d_{fin} = \mid x_{2fin} - x_{ln.entry} \mid \qquad (Eq. 3.4)$$

where x_{2fin} is *Skater$_2$*'s x-coordinate at final-contact – where x represents the rink's longitudinal axis – and $x_{ln.entry}$ is the x-coordinate of the corner entry sector line at the end of the straight (described in Section 2.2.2).

Section 2.4.2 reported that two metrics appear critical for effective relay exchange execution (1) the time for *Skater$_1$* to contact *Skater$_2$* after exiting the corner, t_{cont}, and (2) the efficiency of the energy exchange during skater contact, η_e.

The first metric, t_{cont}, is computed as

$$t_{cont} = t_{fir} - t_{1ln.exit} \qquad (Eq. 3.5)$$

where t_{fir} is the point in time of *Skater$_1$* and *Skater$_2$*'s first-contact and $t_{1ln.exit}$ is the point in time when *Skater$_1$* first passes through the corner exit sector line at the start of the straight (described in Section 2.2.2).

The second metric, termed 'contact energy exchange efficiency', η_e, is computed as

$$\eta_e = \frac{E_{k2fin}}{E_{k1fir} + E_{k2fir}} \qquad (Eq. 3.6)$$

where E_{k2fin} is *Skater$_2$*'s kinetic energy at final-contact, E_{k1fir} is *Skater$_1$*'s kinetic energy at first-contact, and E_{k2fir} is *Skater$_2$*'s kinetic energy at first-contact. In this equation, each skater's kinetic energy, E_k, is calculated as

$$E_k = 0.5mv^2 \qquad (Eq.\,3.7)$$

where m is the skater's mass and v is the skater's velocity at that point in time.

3.2.2 Scenarios

Importantly, to advance knowledge on *'how to execute the relay exchange effectively'*, Great Britain Short-Track Speed Skating need to measure these metrics in representative race scenarios, i.e. for up to four teams simultaneously. For example, as the relay exchange offers a superior opportunity for a team to overtake, Great Britain Short-Track Speed Skating need to know *'how to execute the relay exchange to achieve a gain-in-race position'*. This work necessitates the measurement of more than one team on the short-track to determine the factors of the relay exchange that are discriminative of successful overtakes. Similarly, the factors currently reported critical for effective relay exchange execution are limited to the scenario where a team is isolated from the pack race. Riewald, Broker, Smith, & Otter (1997) only examined one team on the short-track to avoid measurement occlusion, i.e. one skater skating in front of the skater-of-interest. As we would expect situational conditions such as race position in the pack to influence *'how to execute the relay exchange effectively'*, future work necessitates the measurement of the relay exchange in more competitive race scenarios.

3.2.3 Scope

In addition to measuring the relay exchange in representative race scenarios, to advance knowledge on *'how to execute the relay exchange effectively'*, Great Britain Short-Track Speed Skating need to measure the relay exchange over its entirety, i.e. the straight and proceeding corner. At present, current research into the relay exchange's execution has only measured the relay exchange during the straight due to the short-track's large measurement area, ~1,800 m^2. As a result, this research did not investigate the mechanisms that underlie the factors critical for effective relay exchange when a team is isolated from the pack race. For example, how do the actions of $Skater_1$ and $Skater_2$ during the corner influence the time for $Skater_1$ to contact $Skater_2$ after exiting the corner? As Great Britain Short-Track Speed Skating need to understand these mechanisms to achieve their targeted improvement of the relay exchange execution, future work needs to measure the entirety of the relay exchange.

3.2.4 Summary

To advance knowledge on *'how to execute the relay exchange effectively'*, Great Britain Short-Track Speed Skating need to measure short-track speed skating kinematics during the relay exchange. This data, coupled with the point in time of $Skater_1$ and $Skater_2$'s first- and final-contact, will enable the necessitated kinematic metrics-of-interest to be computed. Importantly, Great Britain Short-Track Speed Skating need to measure these metrics in (1) representative race scenarios, i.e. for up to four teams simultaneously, and (2) overs its entirety, i.e. the straight and proceeding corner.

3.3 Needs analysis II – Measurement error

When measuring the relay exchange metrics reported in Section 3.2, we would expect some amount of measurement error, i.e. a difference between a measured and reference value (JCGM, 2012). In sports performance research, the 'absence of measurement error', also referred to as a measurement's reliability, is critical (Atkinson & Nevill, 1998; Currell & Jeukendrup, 2008). For example, Great Britain Short-Track Speed Skating need to know whether an observed improvement in the execution of the relay exchange is real or merely due to measurement error. For this reason, Great Britain Short-Track Speed Skating requires a tool where the measurement error in the relay exchange is acceptable for practical use, i.e. advancing knowledge on *'how to execute the relay exchange effectively'*.

To determine whether a tool's measurement error is acceptable for practical use, Atkinson & Nevill (1998) suggest that the user should relate measurement error to an analytical goal. In elite sports research, a well-established analytical goal is the ability of a measurement tool to detect the smallest worthwhile enhancement in performance (Bernards, Sato, Haff, & Bazyler, 2017; Currell & Jeukendrup, 2008). This concept refers to the smallest change in an athlete's performance that has a substantial effect on their chances of winning (Hopkins, Hawley, & Burke, 1999; Malcata & Hopkins, 2014). If this value can be detected, the analytical goal is attained, and the tool's measurement error is deemed acceptable for practical use.

Scholars typically estimate the smallest worthwhile enhancement in performance as an improvement equal to 0.3 of the coefficient of variation in an athlete's race-to-race performance, i.e. the within-athlete race-to-race variability (Hopkins et al., 1999; Konings & Hettinga, 2018; Malcata & Hopkins, 2014). This approach, however, is limited in short-track speed skating due to the race format prioritising race position not race time. Konings & Hettinga (2018) showed that large variability in race time, predominantly caused by tactical decisions at the beginning of the race, resulted in large coefficients of variation compared to other elite sports. For example, the 1,500 m event had a smallest worthwhile enhancement in race time of 1.8 seconds.

Accordingly, Konings & Hettinga (2018) suggested estimating the smallest worthwhile enhancement in performance using the lap with the lowest within-athlete race-to-race variability instead of the total race time, i.e. the lap where athletes tend to follow their own strategy and are not influenced too much by opponents' actions. In comparison to the typical approach, this method led to a smallest worthwhile enhancement in performance of 0.09 seconds in lap 11 of the 1,500 m event. Still, while this value represents a more realistic estimate of the smallest worthwhile enhancement in performance, it is not suitable for determining whether the measurement error in the relay exchange is acceptable for practical use as its resolution is over the entirety of a lap. As reported by Hext, Heller, Kelley, & Goodwill (2016), in short-track speed skating the relay exchange accounts for less than 30% of the total lap time.

For these reasons, Section 3.3.1 presents an alternative method for estimating the smallest worthwhile enhancement in performance in short-track speed skating. Importantly, unlike the approaches described above, the method is based on measuring the smallest worthwhile enhancement in performance during the relay exchange. This value is used in Section 3.3.2 to determine the acceptable level of measurement error in the relay exchange for advancing knowledge on *'how to execute the relay exchange effectively'*.

3.3.1 Smallest worthwhile enhancement in relay exchange performance

Chapter 2 showed that the relay exchange scenario presents a superior opportunity for a team to achieve a gain-in-race position. This is important in the relay event as it facilitates the implementation of other race strategies, such as drafting, which are underutilised due to the difficulties in overtaking (Hoffman et al., 1998). Accordingly, Section 2.4.5 suggested that to advance knowledge on *'how to execute the relay exchange effectively'*, future work should investigate *'how to execute the relay exchange to achieve a gain-in-race position'*. For this reason, this method defines the smallest worthwhile enhancement in relay exchange performance as the smallest enhancement in skating velocity required to achieve a gain-in-race position.

To estimate the smallest enhancement in skating velocity required to achieve a gain-in-race position, I simulate overtake scenarios for the range of corner exit velocities reported in Chapter 2 (11.5 $m \cdot s^{-1}$ to 15 $m \cdot s^{-1}$). As illustrated in Figure 3-1, the simulation spans the exit of one corner to the entrance of the next, i.e. the period of short-track races where overtakes typically occur (Haug, Drinkwater, Mitchell, & Chapman, 2015). The simulation assumes that (1) $Skater_2$ (the trailing skater) is level with $Skater_1$ (the leading skater) at the start of the straight, i.e. the best-case scenario/ most conservative simulation of an overtake manoeuvre, and (2) to ensure a clean overtake, $Skater_2$ needs to be 1 m in front of $Skater_1$ by the time $Skater_1$ arrives at the end of the straight. This value represents the most conservative estimate of existing values used to determine

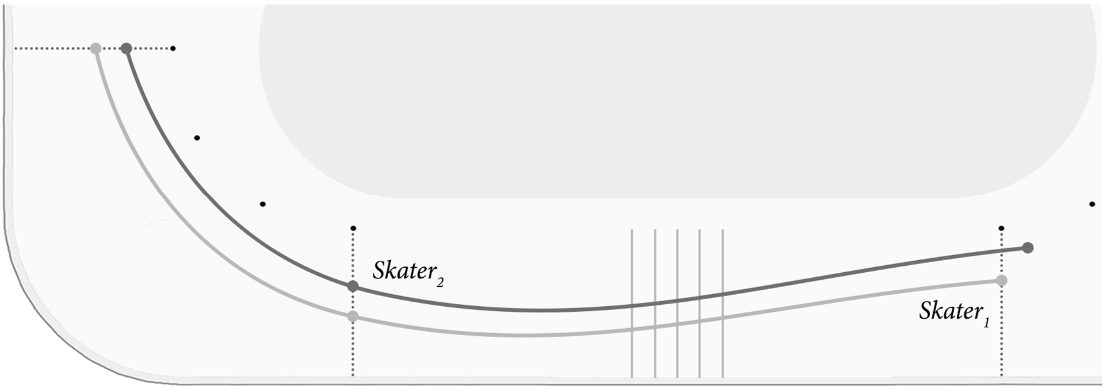

Figure 3-1. The overtake simulation. *Skater$_2$* is level with *Skater$_1$* at the start of the straight. However, by the time *Skater$_1$* has reached the entry of the proceeding corner, *Skater$_2$* is now 1 m ahead.

whether a skater is drafting, i.e. skating closely behind another skater, mimicking their stride (Hoffman et al., 1998; Rundell, 1996).

The results of the simulation show that – over the range of simulated *Skater$_1$* velocities – *Skater$_2$* needs to increase their skating velocity by a minimum of 0.38 $m \cdot s^{-1}$ to 0.49 $m \cdot s^{-1}$ to ensure a clean overtake. Importantly, for each simulated velocity, this represents a relative enhancement in skating velocity of 3.3%. For this reason, this method estimates the smallest enhancement in relay exchange performance as a 3.3% increase in skating velocity.

3.3.2 Acceptable level of measurement error

In this section, I use the estimate of the smallest worthwhile enhancement in relay exchange performance (i.e. a 3.3% increase in skating velocity) to determine the acceptable level of measurement error in the relay exchange for advancing knowledge on *'how to execute the relay exchange effectively'*. Figure 3-2 illustrates this procedure. $m_1$and m_2 represent two measurements: m_1 is a baseline performance and m_2 the baseline performance with the addition of the smallest worthwhile enhancement in performance. As illustrated by the shaded areas, each of these measurements has an associated uncertainty, i.e. the potential deviation of the measure from its true value (Challis, 2018). If there is a gap between each measures bounds of uncertainty, the

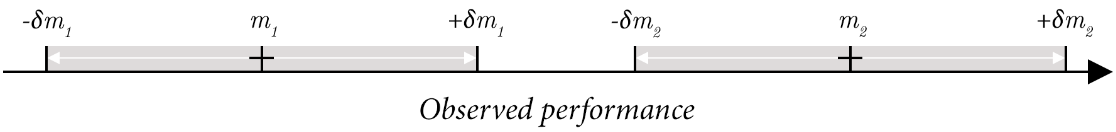

Figure 3-2. Determining the acceptable level of measurement error in the relay exchange. m_1 is a baseline performance and m_2 is the baseline plus the smallest worthwhile enhancement in relay performance. If there is a gap between each measures' bounds of uncertainty ($\pm\delta$), a measurement tool can detect the smallest worthwhile enhancement in relay exchange performance.

measurement tool can detect the smallest worthwhile enhancement in performance. If not, users cannot be certain whether the observed difference in performance is real or due to measurement error (Hudson, 2015).

A measurement's bounds of uncertainty are related to the accuracy of the measurement tool. As illustrated in Figure 3-3, as the accuracy of a measurement increases, the uncertainty decreases. The *International Vocabulary of Metrology* defines accuracy as 'the closeness of agreement between a measured and true value'. It does not have a numerical value, but instead is a descriptive and comparative term that reflects both the trueness and precision of the measurement (JCGM, 2012). The former is defined as 'the closeness of agreement between the average of an infinite number of measured values and a reference value' (JCGM, 2012). Typically expressed in terms of bias, trueness represents the systematic measurement error, i.e. the general trend for measurements to be different in a particular direction (Figure 3-3) (Atkinson & Nevill, 1998; ISO, 1994). The latter is defined as 'the closeness of agreement between results obtained by replicate measurements on the same or similar object under specified conditions' (JCGM, 2012). In other words, precision represents the random measurement error inherent in every measurement procedure (Figure 3-3) (ISO, 1994). Importantly, both errors should be considered when defining the acceptable level of measurement error in the relay exchange.

Using the aforementioned bounds of uncertainty method, and the smallest worthwhile enhancement in relay exchange performance, the acceptable level of measurement error

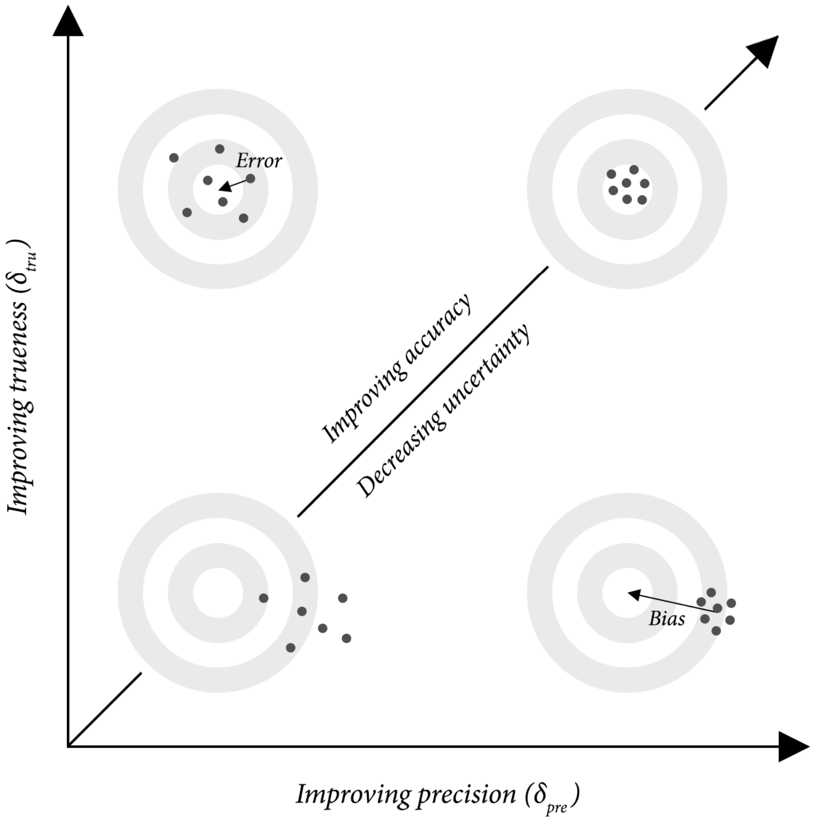

Figure 3-3. The meaning and inter-relationship of the terms error, uncertainty, accuracy, trueness, bias, and precision are depicted using the analogy of a dart board to illustrate the centre of a target and the spread of values.

in the relay exchange can be defined as the ability to measure skating velocity to within ± 1.65%. Note, however, that this relative measurement error only reflects the precision of the measurement (i.e. the random error). For example, irrespective of whether the measurement has a systematic error of 0.1 $m \cdot s^{-1}$ or 10 $m \cdot s^{-1}$, Great Britain Short-Track Speed Skating can detect the smallest worthwhile enhancement in relay exchange performance if the precision of the measurement is within ± 1.65% of this value. As a result, while this definition suffices for identifying the smallest worthwhile enhancement in relay exchange performance – and therefore investigating *'how to execute the relay exchange to achieve a gain-in-race position'* – it does not facilitate other aspects of future work proposed for advancing knowledge on *'how to execute the relay exchange effectively'*.

Chapter 2 showed that the relay exchange's effect on race time is dependent on the race speed; having a positive effect at slower speeds and a negative effect at faster race speeds. Accordingly, Section 2.4.5 suggested that future work should validate the theoretical mechanisms proposed for this phenomenon. For example, as the race speed increases from 11.5 m·s^{-1} to 15 m·s^{-1}, the relay exchange's effect on race time transitions from positive to negative due to the relative velocity at first-contact increasing. For this reason, the definition of the acceptable level of measurement error also needs to reflect the trueness of the measurement (i.e. the systematic error). Section 3.3.1 reported that over this range of speeds, *Skater$_2$* needs to increase their skating velocity by a minimum of 0.38 m·s^{-1} to 0.49 m·s^{-1} to ensure a clean overtake. Based on the aforementioned bounds of uncertainty method, these values lead to acceptable levels of measurement error ranging from ± 0.19 m·s^{-1} to ± 0.25 m·s^{-1}. Therefore, to ensure that Great Britain Short-Track Speed Skating can (1) detect the smallest worthwhile enhancement in relay exchange performance for all expected race speeds, and (2) validate the theoretical mechanisms proposed for why the relay exchange's effect on race time is dependent on race speed, the acceptable level of measurement error is defined as the ability to measure skating velocity to within ± 0.19 m·s^{-1}.

3.3.3 Summary

All measured values contain error. Accordingly, Great Britain Short-Track Speed Skating requires a tool where the measurement error in the relay exchange is acceptable for advancing knowledge on *'how to execute the relay exchange effectively'*. In elite sports research, the acceptable level of measurement error is typically defined as the tool's ability to detect the smallest worthwhile enhancement in performance. As the relay exchange scenario presents a superior opportunity for a team to overtake, Section 3.3.1 estimated this value as the smallest enhancement in skating velocity required to achieve a gain-in-race position. Over the range of race speeds reported in Chapter 2 (11.5 m·s^{-1} to 15 m·s^{-1}), this equated to an increase in skating velocity of 0.38 m·s^{-1} to 0.49 m·s^{-1}, i.e. a relative increase of 3.3%. Based on a bounds of uncertainty method, this led to the acceptable level of measurement error in the relay exchange ranging from ± 0.19 m·s^{-1} to

± 0.25 $m \cdot s^{-1}$, i.e. a relative error of ± 1.65%. Of these values, Section 3.3.2 defined the acceptable level of measurement error in the relay exchange as the ability to measure skating velocity to within ± 0.19 $m \cdot s^{-1}$. This absolute error, which reflects both the trueness (i.e. the systematic error) and precision (i.e. the random error) of the measurement, ensures that Great Britain Short-Track Speed Skating can (1) detect the smallest enhancement in skating velocity required to achieve a gain-in-race position for all race speeds, and (2) validate the theoretical mechanisms proposed for why the relay exchange's effect on race time transitions from positive to negative as the race speed increases.

3.4 Existing vision-based measurement solutions

In this section, I use the needs analysis to review existing, vision-based, measurement solutions for measuring short-track speed skating kinematics. Radio frequency identification methods such as local position measurement (Stelzer, Pourvoyeur, & Fischer, 2004) are excluded, as Great Britain Short-Track Speed Skating require a tool that simultaneously provides video-feedback. The review groups these existing vision-based measurement solutions into three broad categories (1) existing relay exchange measurement methods, (2) single-panning cameras, and (3) multi-camera networks. First, I evaluate each categories' solutions on their ability to measure the metrics, scenarios, and scope of the relay exchange (Section 3.2). Second, if these solutions meet these measurement requirements, I evaluate the solutions' accuracy using the definition of an acceptable level of measurement error (Section 3.3).

3.4.1 Existing relay exchange measurement methods

The investigations of Riewald et al. (1997) and Osborough & Henderson (2009) used two different methods to measure kinematics during the relay exchange. Riewald et al. (1997) used a two-camera pan-tilt system, and Osborough & Henderson (2009) used three static cameras positioned perpendicular to the straight. Position, velocity, and kinetic energy were computed as a three- and two-dimensional point estimate by manually digitising a single mid-pelvic point on each skater.

When considering the metrics, scenarios, and scope of relay exchange measurement, these methods have two limitations. Firstly, both methods only allow the measurement of the relay exchange with one team on the short-track due to the potential for measurement occlusion, i.e. another skater occluding the mid-pelvic point on the skater-of-interest. Secondly, due to the mid-pelvic point being susceptible to occlusion in the two-camera pan-tilt system and the field-of-view being constrained to the straight in the three-camera system, these methods only allow the relay exchange to be measured during the straight. Accordingly, both methods cannot measure the relay exchange in (1) representative race scenarios, i.e. for up to four teams simultaneously, and (2) over its entirety, i.e. the straight and proceeding corner. As discussed in Section 3.2, both are critical for advancing knowledge on *'how to execute the relay exchange effectively'*.

3.4.2 Single-panning cameras

In short-track speed skating, much work has focused on the measurement of kinematics using single panning camera footage recorded from a position in the spectator gallery close to the start/ finish line (Liu, 2014; Liu & Tang, 2009; Liu, Tang, Cheng, Huang, & Liu, 2009; Liu, Tang, Huang, Liu, & Sun, 2007; Wang, 2012; Wang, Cheng, & Shan, 2014; Wang, Liu, Liu, Tang, & Liu, 2009). These methods compute position and velocity as a two-dimensional point estimate by (1) automatically computing the transformation matrices that map each frame to a global rink model, and (2) tracking skater's motion automatically by inputting observation models, based on colour extraction from the head and body, into a Kalman filter.

When considering the metrics, scenarios, and scope of relay exchange measurement, single panning-cameras do enable the relay exchange to be measured over its entirety, i.e. the straight and proceeding corner. However, as the performance of these methods is affected by continuous sections of partial or full skater occlusion (Liu et al., 2009), this solution does not enable the measurement of the relay exchange in representative race scenarios as the likelihood of skater occlusion would increase due to up to 16 skaters being on the short-track. As discussed in Section 3.2.2, this is critical for advancing knowledge on *'how to execute the relay exchange effectively'*.

3.4.3 Multi-camera network

Landry, Gagnon, & Laurendeau (2013) described using a multi-camera network to measure kinematics during short-track speed skating. The multi-camera network – installed at the Olympic Oval in Calgary (CAN) – consisted of four cameras fixed 22.5 m above the rink surface. Collectively, the four cameras' field-of-view covered the entirety of the short-track. The multi-camera network computed position and velocity as a two-dimensional point estimate by (1) establishing a common rink plane between the four camera views, and (2) tracking skaters' motion automatically by inputting observation models – based on a 16-bin grey level histogram – into a particle filter.

When considering the metrics, scenarios, and scope of relay exchange measurement, the multi-camera network satisfies all criteria. The method facilitates the measurement of the relay exchange in (1) representative race scenarios, i.e. for up to four teams simultaneously, and (2) over its entirety, i.e. the straight and proceeding corner, as the overhead view negates measurement occlusion and covers the whole short-track. However, as Landry et al. (2013) reported overall errors in velocity measurements of ± 1.53 $m \cdot s^{-1}$, the multi-camera network does not meet the level of measurement error required for advancing knowledge on *'how to execute the relay exchange effectively'*; the magnitude of error considerably larger than the ± 0.19 $m \cdot s^{-1}$ deemed acceptable in Section 3.3.

3.4.4 Summary

A variety of vision-based measurement solutions have been used in short-track speed skating to measure a two-dimensional point estimate of a skater's position and velocity. In general, these solutions are inappropriate for advancing knowledge on *'how to* *execute the relay exchange effectively'*, as they are unable to measure the relay exchange in (1) representative race scenarios, i.e. for up to four teams simultaneously, and (2) over its entirety, i.e. the straight and proceeding corner. At present, the only solution that meets these criteria is a multi-camera network. However, while the multi-camera network satisfies the metrics, scenarios, and scope of relay exchange measurement, the measurement error is unsuitable for detecting the smallest enhancement in performance during the relay exchange. Accordingly, this measurement error needs to be minimised if a multi-camera network is to be used to advance knowledge on *'how to execute the relay exchange effectively'*.

3.5 Part I summary

Part I of the thesis contextualised the need for developing a multi-camera network to measure accurate, two-dimensional, relay exchange kinematics. First, by examining the relay exchange's effect on race time and race position, Chapter 2 evidenced the strategic opportunity of the relay exchange and thus provided empirical data that supported its targeted improvement by Great Britain Short-Track Speed Skating (Chapter 1). For the former, the results showed that the relay exchange's effect on race time is dependent on race speed; having a positive effect at slower speeds and a negative effect at faster speeds. This finding suggests that the current norm of executing the relay exchange every 1½ laps may not be optimal. Instead, varying the frequency of the relay exchange execution could allow time to be gained relative to other teams in the race. For the latter, the results showed that the relay exchange offers a superior opportunity for a team to achieve a gain-in-race position. Accordingly, the relay exchange could facilitate race strategies which are currently underutilised due to the difficulties in overtaking. The chapter concluded by using these results to provide a rationale for how Great Britain Short-Track Speed Skating should advance knowledge on *'how to execute the relay exchange effectively'*. This work focuses on (1) validating the theoretical mechanisms proposed for why the relay exchange's effect on race time is dependent on race speed, and (2) understanding *'how to execute the relay exchange to achieve a gain-in-race* *position'*.

Second, Chapter 3 used this rationale to formulate a relay exchange measurement needs analysis. The needs analysis showed that to advance knowledge on *'how to execute the relay exchange* effectively', Great Britain Short-Track Speed Skating need to be able to measure relay exchange kinematics in (1) representative race scenarios, i.e. for up to four teams simultaneously, (2) over its entirety, i.e. the straight and proceeding corner, and (3) with an acceptable level of measurement error; operationally defined as the ability to measure skating velocity to within ± 0.19 $m{\cdot}s^{-1}$. This absolute error reflected both the trueness (i.e. the systematic error) and precision (i.e. the random error) of the measurement to ensure that Great Britain Short-Track Speed Skating could (1) detect the smallest enhancement in skating velocity required to achieve a gain-in-race position, and (2) validate the proposed theoretical mechanisms for why the relay exchange's effect on race time is dependent on race speed.

The chapter concluded by using the needs analysis as a criterion to review existing, vision-based, short-track speed skating measurement solutions. The review showed that although a variety of different measurement solutions have been used in short-track speed skating, only one method facilitated the measurement of the relay exchange in (1) representative race scenarios, and (2) over its entirety: the multi-camera network installed at the Olympic Oval in Calgary (CAN). However, while this multi-camera network satisfied the metrics, scenarios, and scope of relay exchange measurement, its ± 1.53 $m{\cdot}s^{-1}$ error in skating velocity did not meet the ± 0.19 $m{\cdot}s^{-1}$ target measurement error. For these reasons, this thesis investigates developing a multi-camera network to measure accurate, two-dimensional, relay exchange kinematics.

Part II Multi-camera network development

Chapter 4

The National Ice Centre multi-camera network

4.1 Introduction

The first part of this thesis contextualised the need for developing a multi-camera network to measure accurate, two-dimensional, relay exchange kinematics. First, Chapter 2 evidenced the strategic opportunity of the relay exchange and provided a rationale for how future work should advance knowledge on *'how to execute the relay exchange effectively'*. Second, Chapter 3 formulated a relay exchange measurement needs analysis and reviewed existing short-track speed skating measurement solutions. The review showed that while the Olympic Oval (CAN) multi-camera network was the only measurement solution that satisfied the metrics, scenarios, and scope of relay exchange measurement, its ± 1.53 $m \cdot s^{-1}$ error did not meet the ± 0.19 $m \cdot s^{-1}$ target measurement error. Therefore, the second part of this thesis investigates developing a multi-camera network to measure accurate, two-dimensional, relay exchange kinematics. Before Chapter 5 reviews the literature with regards to such an investigation, this chapter provides an overview of the multi-camera network developed in the thesis and outlines several image characteristics that will influence the multi-camera network's ability to measure accurate, two-dimensional, relay exchange kinematics.

4.2 The multi-camera network

The multi-camera network developed in this thesis is installed at the National Ice Centre in Nottingham; the home of Great Britain Short-Track Speed Skating's World Class Performance Programme. The National Ice Centre (GBR) multi-camera network

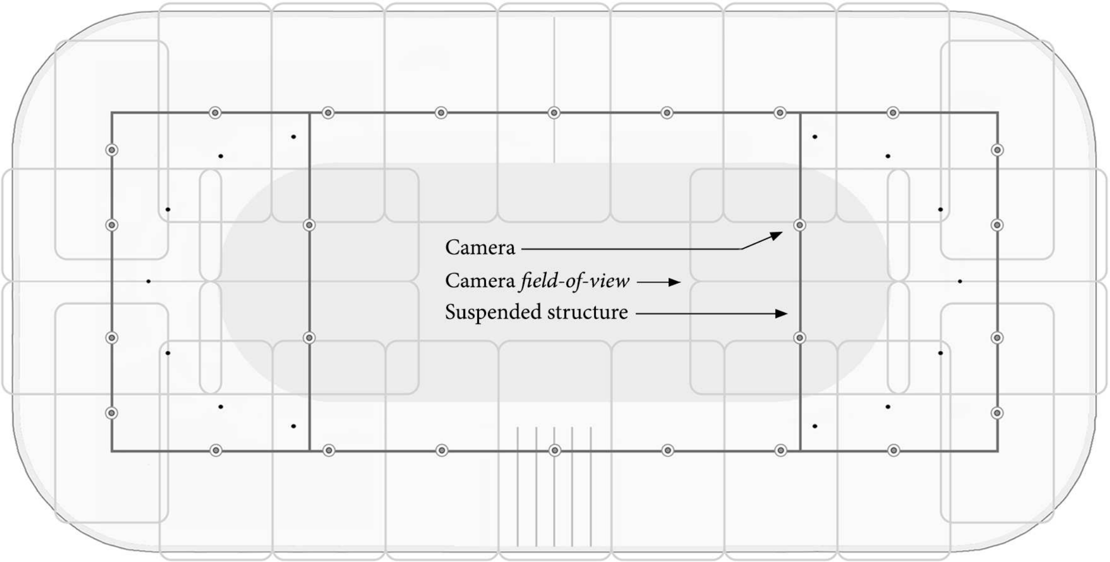

Figure 4-1. A schematic of the National Ice Centre (GBR) multi-camera network.

consists of 26 Axis M3204 network cameras (Axis Communications, Lund, Sweden). All cameras are fixed on a suspended structure – nine metres above the short-track – and positioned so that the network's collective field-of-view covers 90% of the 1800 m^2 capture area (60 x 30 m short-track). Figure 4-1 illustrates the position of each camera on the suspended structure and the camera's approximate field-of-view. Each camera delivers 25 MJPEG images per second (progressive scan), at a resolution of 1280 x 800 pixels, and exposure time of 0.004 seconds. As the Axis M3204 cameras do not support generator locking, i.e. using a reference signal to synchronise two or more cameras, each camera's shutter can be out-of-phase by up-to ± 0.02 seconds with all other cameras.

Table 4-1 compares the National Ice Centre (GBR) multi-camera network to the Olympic Oval (CAN) multi-camera network described in Section 3.4.3. While the sampling frequencies of the cameras are identical, the National Ice Centre (GBR) multi-camera network uses an additional 22 cameras to cover the short-track and captures images at a higher resolution. The former is due to the building restricting the camera height above the short-track, i.e. four cameras' field-of-view would not cover the short-track at the National Ice Centre, the latter due to differences in the camera make/ model.

Table 4-1. The multi-camera network configuration at the National Ice Centre and Olympic Oval.

Multi-camera network	National Ice Centre (GBR)	Olympic Oval (CAN)
Camera model	Axis M3204	Prosilica GC 650
Number of cameras	26	4
Camera height	9 m	22.5 m
Image resolution	1280 x 800 pixels	659 x 493 pixels
Sampling frequency	25 Hz	25 Hz

4.3 Image characteristics

The National Ice Centre (GBR) multi-camera network's images each comprise of 1,024,000 (1280 x 800) pixels. These pixels – each consisting of three numerical RGB components ranging from 0 to 255 – determine the overall appearance of an image. Importantly for this thesis, the image's appearance and skater's appearance within that image varies for several reasons. These characteristics, outlined below, will influence the multi-camera network's ability to measure accurate, two-dimensional, relay exchange kinematics and are considered throughout the remainder of this thesis.

4.3.1 Image appearance

The multi-camera network's images have two distinct artefacts: horizontal banding and lens distortion. In addition to these artefacts, the overall appearance of an image is dependent on the ambient lighting and the network setup.

Horizontal banding & lens distortion

Figure 4-2 shows four pairs of high- and low-intensity horizontal bands in two images from a single camera. These bands, common to all images in the multi-camera network, are the result of the light sources' alternating current (AC) power supply and the image sensor's electronic rolling shutter. Figure 4-3 illustrates how the waveform of an AC power supply corresponds to a change in brightness of the corresponding light source (Yoo, Im, & Paik, 2014). The multi-camera network captures this change in brightness

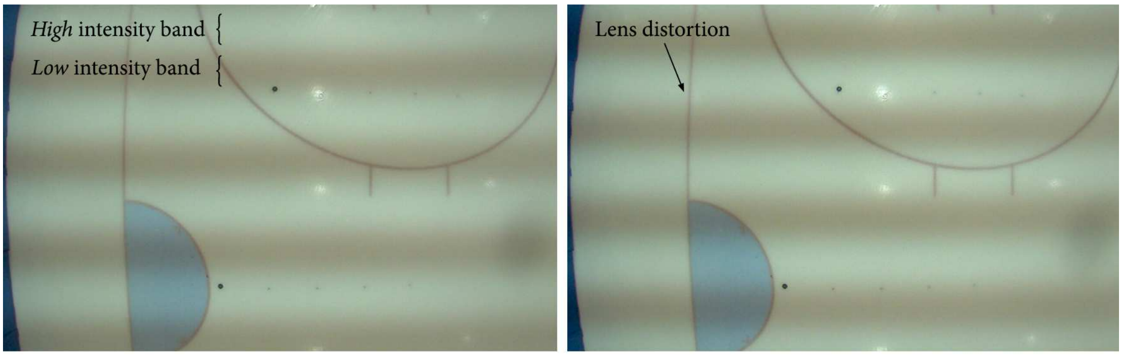

Figure 4-2. Two images from a single camera in the National Ice Centre (GBR) multi-camera network. The images demonstrate the two artefacts of all multi-camera network images (1) horizontal banding, i.e. four pairs of high- and low-intensity horizontal bands, and (2) lens distortion, i.e. straight lines appearing curved.

in each image as the electronic rolling shutter exposes and readouts each scanline (row of pixels) sequentially from top to bottom over the duration of the sampling interval. As a result, the bottom scanline is exposed 0.04 seconds (1/sampling frequency) later than the top scanline (Bradley, Atcheson, Ihrke, & Heidrich, 2009; Wilburn, Joshi, Vaish, Levoy, & Horowitz, 2004). Moreover, as the electronic rolling shutter and AC power supply are not in-phase, the position of the banding changes over time (Figure 4-2).

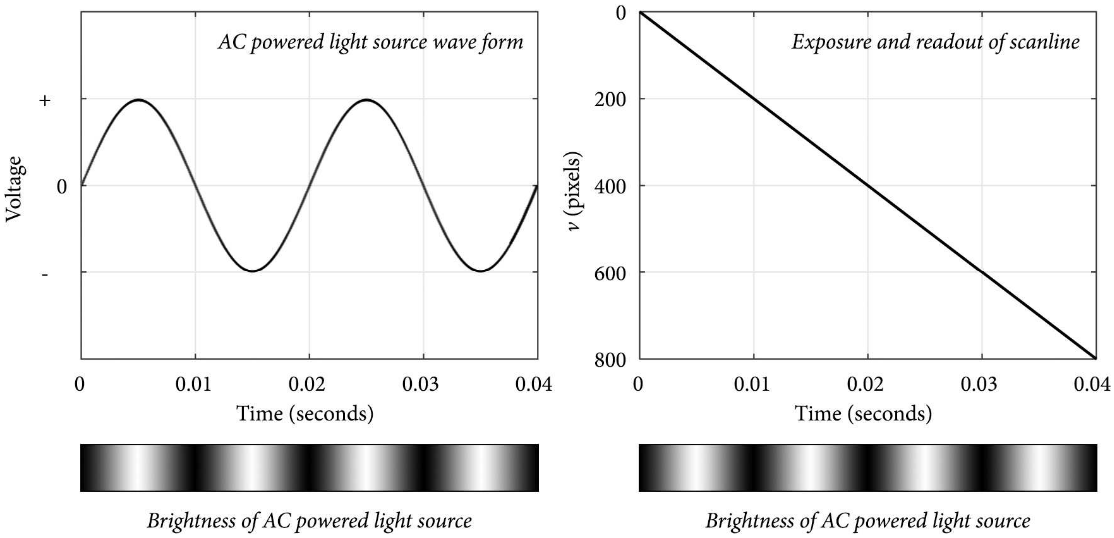

Figure 4-3. The effect of an AC power supply on the brightness of a corresponding light source (left). The National Ice Centre (GBR) multi-camera network captures this change in brightness in each image as the image sensor's electronic rolling shutter exposes and readouts each scanline (row of pixels) sequentially from top to bottom over the duration of the 0.04-second sampling interval (right).

In addition to horizontal banding, each camera in the multi-camera network is subject to radial and tangential lens distortion. The spherical shape of the lens causes radial distortion and manufacturing defects, i.e. the non-alignment of the camera lens and imaging plane, causes tangential distortion (Bradski & Kaehler, 2008). Figure 4-2 illustrates how this lens distortion results in straight lines appearing curved in an image.

Ambient lighting & network setup

The National Ice Centre's ambient lighting, i.e. the available light in the rink environment, varies for two reasons (1) daylight, as one side of the rink has windows, and (2) the lighting's colour temperature. Great Britain Short-Track Speed Skating selects the highest setting of colour temperature to improve skating visibility. This change, however, is not instantaneous. Figure 4-4 shows how changes in weather (e.g. sunny and overcast) and lighting (e.g. 0 minutes to 20 minutes after the change in colour temperature) alters the appearance of a camera's images within a training session.

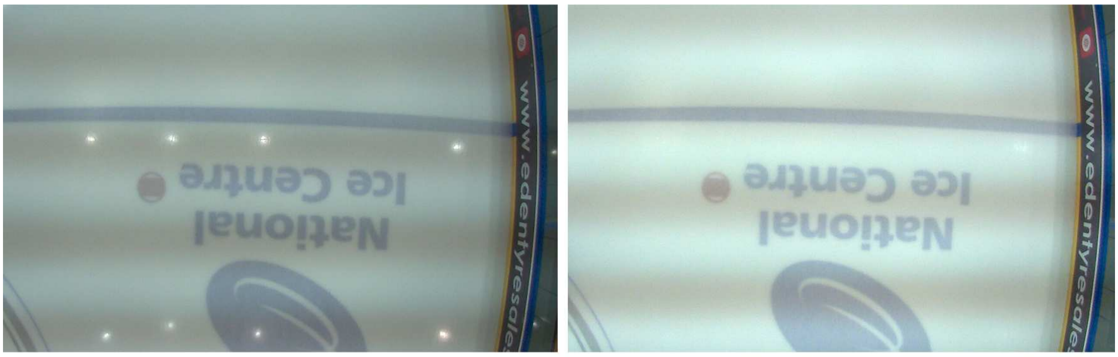

Figure 4-4. Images from a single camera in the National Ice Centre (GBR) multi-camera network during a Great Britain Short-Track Speed Skating training session. The appearance of the camera's images differs due to changes in daylight and colour temperature.

As outlined in Section 4.2, the positions of the 26 cameras allow the National Ice Centre multi-camera network to capture 90 % of the short-track. As a result, each camera's proximity to the available light sources in the rink environment differs. As shown in Figure 4-5, this varying proximity results in an image from one camera appearing lighter or darker than images from another camera captured at the same time.

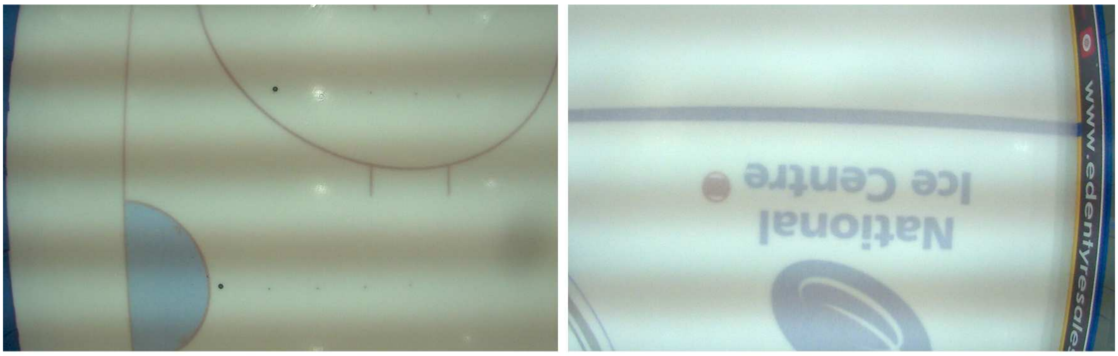

Figure 4-5. Images from two cameras in the National Ice Centre (GBR) multi-camera network during a Great Britain Short-Track Speed Skating training session. The appearance of the cameras' images differs due to varying proximities to the available light sources.

4.3.2 Skater appearance

In addition to the characteristics outlined in Section 4.3.1, the appearance of a skater in an image is dependent on the skating condition, track position, and skating velocity.

Skating condition

A single lap of a short-track contains two different skating conditions, the corner and straight, both of which are repeated twice per lap. The skating technique in each of these condition differs. The straight skating condition typically contains one glide on each blade (Hesford, Laing, Cardinale, & Cooper, 2012; Hettinga, Konings, & Cooper, 2016). The skater adopts a crouched skating position, i.e. the trunk is kept close to horizontal, to minimise the skater's frontal area and thus reduce frictional losses from air friction (van Ingen Schenau, 1982). In addition to maintaining a crouched skating position, the corner skating condition contains three-sub phases: the entry, hang and exit (Hesford et al., 2012; Hettinga et al., 2016). Here, the skater leans towards the centre of rotation to maintain the balance of forces between the skate and ice (Chun, 2001; Yule & Payton, 2000). Figure 4-6 illustrates the differences in a skater's appearance between the straight and corner skating conditions in the multi-camera network.

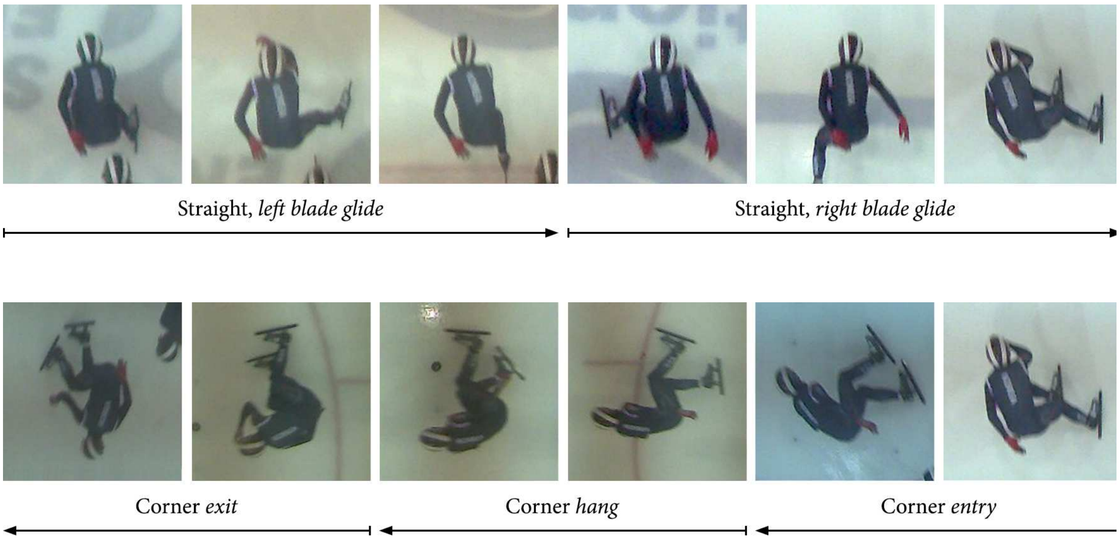

Figure 4-6. The appearance of a skater in the National Ice Centre (GBR) multi-camera network during the straight (top) and corner (bottom) skating conditions.

Track position

The short-track, a 111.12 m oval, is defined by 14 moveable track marking blocks positioned on the ice (ISU, 2016). As illustrated in Figure 4-7, from the central track position these track marking blocks are moved by one or two metres in either direction to define five different short-tracks. Great Britain Short-Track Speed Skating uses all

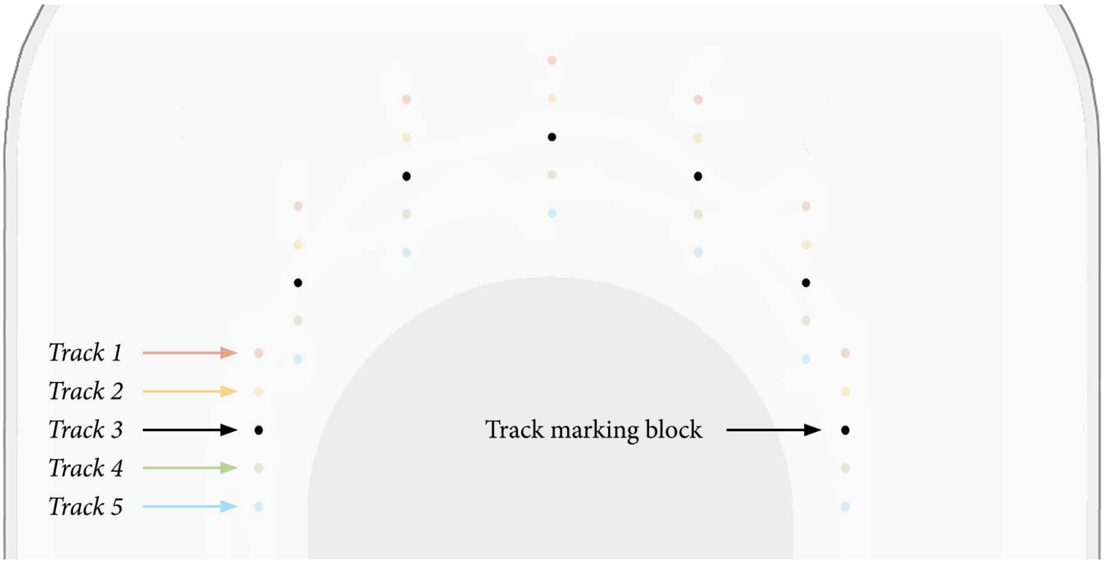

Figure 4-7. From the central track position (Track 3), each corner's seven-track marking blocks can be moved by one or two metres in either direction to define five different short-tracks.

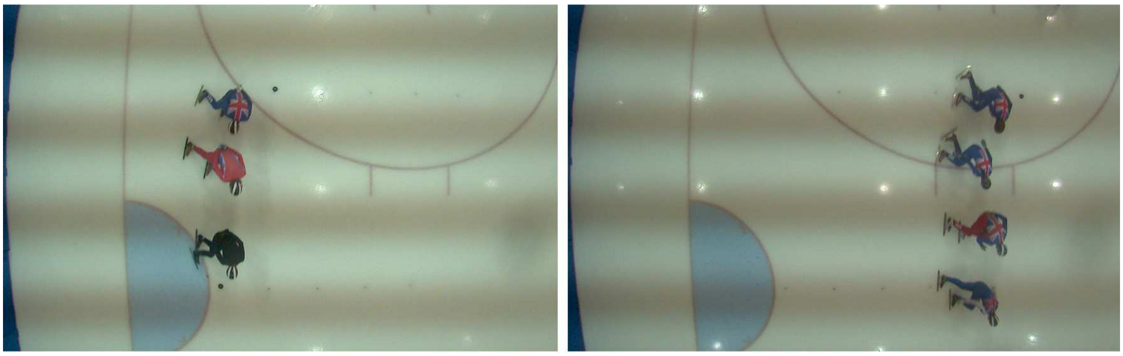

Figure 4-8. The effect of track position on a skater's appearance in the National Ice Centre (GBR) multi-camera network during the corner skating condition. Track 1 (left) and Track 5 (right).

these track positions throughout training sessions to preserve good ice conditions. Figure 4-8 shows how a skater's appearance in an image varies between different short-tracks in the corner skating condition.

Skating velocity

As shown in Chapter 2, skating velocity changes throughout the short-track relay. These different skating velocities affect a skater's appearance in an image in two ways. Firstly, at faster skating velocities, a skater travels further in a camera's 0.004 second exposure time. As illustrated in Figure 4-9, this leads to the skater appearing more blurred in an image. Secondly, as the skating velocity increases during the corner skating condition, a skater leans further towards the centre of rotation to maintain the balance of forces

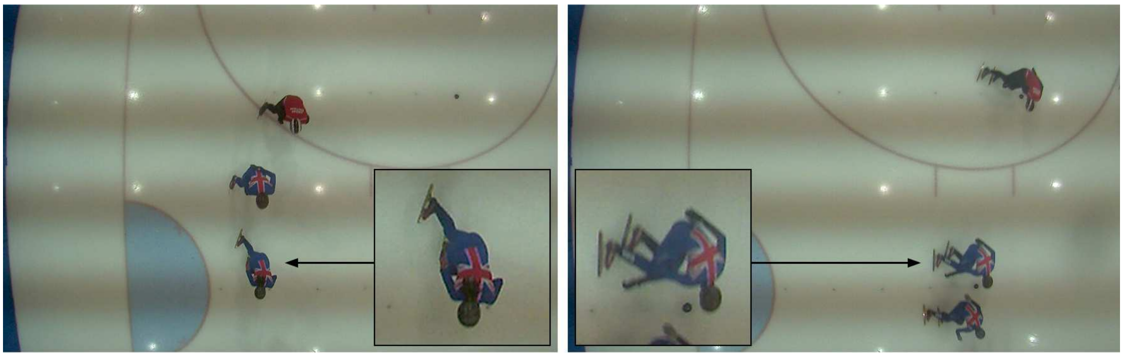

Figure 4-9. The effect of velocity on a skater's appearance in the National Ice Centre (GBR) multi-camera network. At faster velocities (right) a skater (1) appears more blurred in an image due to travelling less distance in a single exposure (0.004 seconds), and (2) has a more pronounced lean in a corner skating condition image due to having to balance the larger centripetal force.

between the skate and ice. As shown in Figure 4-9, the lean angle changes the appearance of a skater in an image.

4.4 Chapter summary

This chapter provided an overview of the multi-camera network developed in this thesis. The National Ice Centre (GBR) multi-camera network uses 26 cameras – fixed on a suspended structure nine metres above the rink surface – to capture the 60 x 30 m short-track. Compared to the Olympic Oval (CAN) multi-camera network, which does not meet the ± 0.19 $m \cdot s^{-1}$ target measurement error for advancing knowledge on *'how to execute the relay exchange effectively'*, the National Ice Centre (GBR) multi-camera network uses an additional 22 cameras to capture the short-track and records images at a higher resolution. The chapter concluded by demonstrating how the appearance of images in the multi-camera network is dependent on four characteristics (horizontal banding, lens distortion, ambient lighting, and the network setup), with the appearance of skaters within each image dependent on an additional three characteristics (skating condition, track position, and skating velocity). These characteristics are considered throughout the remainder of this thesis, as they will influence the multi-camera network's ability to measure accurate, two-dimensional, relay exchange kinematics.

Chapter 5

Literature review

5.1 Introduction

The second part of this thesis investigates developing the National Ice Centre (GBR) multi-camera network to measure accurate, two-dimensional, relay exchange kinematics. In this chapter, I review the literature with regards to such an investigation. The review is formed of two parts. First, the review examines the four stages of the multi-camera network's measurement workflow (1) measuring skater position in an image, (2) measuring skater position on the short-track, (3) measuring skater position over time, and (4) computing skater velocity. Second, the review evaluates different approaches for determining whether the multi-camera network can measure accurate, two-dimensional, relay exchange kinematics. The chapter concludes by using the outcomes of the review to formulate the thesis's objectives.

5.2 Part I. Measuring skater position in an image

The first step in measuring two-dimensional relay exchange kinematics using the National Ice Centre (GBR) multi-camera network is to digitise the position of a skater in the image's pixel coordinate system. The pixel coordinate system has a u- and v-axis, with the origin located at the top left corner. Users can digitise the position of a skater in the pixel coordinate system in two ways (1) manually, by visually identifying and selecting the skater in the image (Payton, 2008), or (2) automatically, using digital image processing techniques (Barris & Button, 2008). While both methods introduce error into the measurement process, manual digitisation is also a time-consuming procedure

(Ceccon et al., 2013; Payton, 2008). For example, in the National Ice Centre (GBR) multi-camera network, it takes approximately one hour to digitise a single skater over a ten-second lap. For this reason, the multi-camera network must automatically digitise the position of a skater in the pixel coordinate system. In this section, I provide an overview of automated digitisation principles (Section 5.2.1), before reviewing existing methods used in short-track speed skating (Section 5.2.2) and human motion analysis (Section 5.2.3).

5.2.1 Principles of automated digitisation

Automated digitisation consists of two processes: segmentation and representation (Moeslund & Granum, 2001). Segmentation separates objects of interest, referred to as the foreground (e.g. skaters), from the rest of the image, referred to as the background (e.g. the rink surface) (Moeslund, Hilton, & Krüger, 2006). Figure 5-1 illustrates the typical output of the segmentation process; a binary image where the background is black and the foreground is white (Hudson, 2015).

Segmentation methods are based on either temporal or spatial information and are routinely used in combination to separate the foreground from the background (Hudson, 2015; Moeslund & Granum, 2001). Temporal-based segmentation assumes that the background of an image is static. Subsequently, the difference between images originates from the movement of the object of interest. For example, image subtraction subtracts the current image from a reference image that contains only the background. This reference image can either be a single static image or an image that is continually updated (Moeslund & Granum, 2001; Sobral & Vacavant, 2014). Spatial segmentation assumes that the appearance of the object of interest, i.e. the pixel intensities, are different from the rest of the image. A straightforward spatial segmentation approach is histogram thresholding. Here, each pixel in an image is classified as either background or foreground if its intensity is either less or greater than a set threshold. This threshold is selected either manually or automatically (Russ & Brent, 2011).

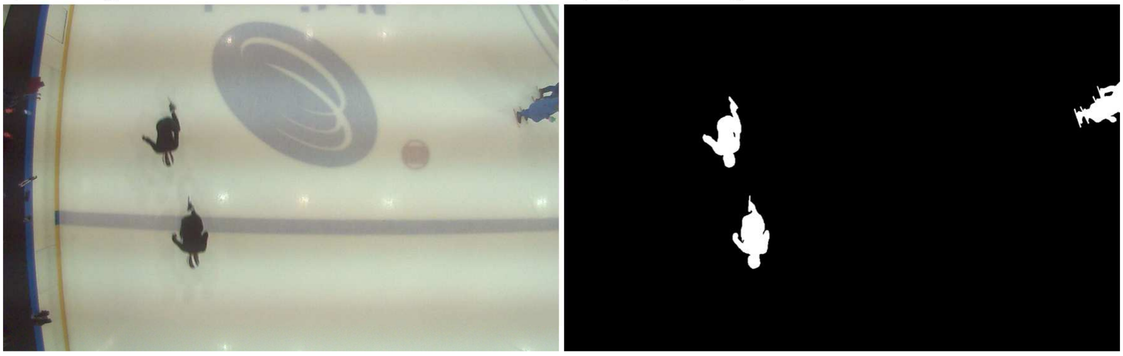

i) Raw *image*

ii) Segmented *image*

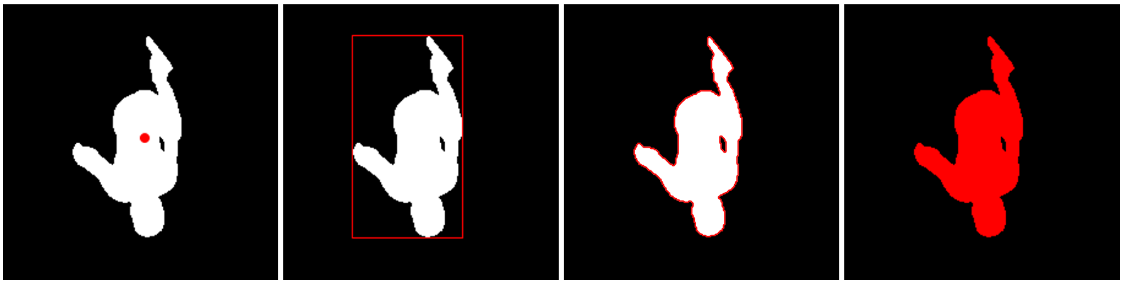

iii) Single point

iv) Bounding box

v) Edge

vi) Blob

Figure 5-1. The two processes of automated digitisation: segmentation (top) and representation (bottom). Segmentation separates objects of interest, referred to as the foreground (e.g. skaters), from the rest of the image, referred to as the background (e.g. the rink surface). Representation then describes these foreground objects in some convenient manner. Examples include single points, bounding boxes, edges, and blobs.

Representation then describes foreground objects in the binary image using some convenient manner (Moeslund & Granum, 2001). As illustrated in Figure 5-1, examples include single points, bounding boxes, edges, and blobs.

5.2.2 Automated digitisation in short-track speed skating

The Olympic Oval (CAN) multi-camera network described in Section 3.4.3 is the most relevant example of automated digitisation in this review. This multi-camera network uses a combination of subtraction and thresholding to automatically digitise a skater's position in the pixel coordinate system.

Segmentation method

First, Landry et al. (2013) subtracted the current image from a reference image; the average of several images where no skaters were on the rink. Second, Landry et al.

Item removed for copyright reasons

Figure 5-2. The Olympic Oval (CAN) multi-camera network automated digitisation procedure. From left to right, the associated image from (1) the background subtraction, (2) the global threshold, and (3) the local threshold. Figure adapted from Landry et al. (2013).

(2013) applied a threshold to this subtracted image globally, and then locally to the identified foreground objects. This two-stage process – illustrated in Figure 5-2 – ensured that the final foreground objects were more robust to cast shadows.

Landry et al. (2013) used Otsu's (1979) method to select the two threshold values automatically. This method assumes that the histogram of the subtracted image is bimodal; one mode represents the background's pixel intensities (i.e. the rink surface), and the other mode represents the foreground's pixel intensities (i.e. the skaters). The method selects the intensity that minimises the intra-class variance as the threshold value.

Representation method

Landry et al. (2013) represented each identified foreground object as a pair of single coordinates. In each foreground object, each pixel was assumed to have an equal mass and the geometric centroid calculated,

$$Centroid_u = \frac{\sum_{i=1}^{n} u_i}{n} \qquad Centroid_v = \frac{\sum_{i=1}^{n} v_i}{n} \qquad (Eq. 5.1)$$

where n is the total number of foreground object pixels, u_i is the u-coordinate of the ith pixel, and v_i is the v-coordinate of the ith pixel.

National Ice Centre (GBR) multi-camera network feasibility

The Olympic Oval (CAN) multi-camera network's automated digitisation algorithm has two limitations that warrant consideration. First, using the average of several images to create the subtraction reference image is not feasible in the National Ice Centre (GBR) multi-camera network as horizontal banding and ambient lighting changes throughout a training session (Section 4.3.1). Instead, a continuously updated reference image – known as a background model – would be required (Sobral & Vacavant, 2014). Second, when comparing the algorithm to manually digitised data, the uncertainty in the automated digitisation of a skater (2.61 pixels) propagated to errors in velocity (± 1.04 $m \cdot s^{-1}$) that exceeded the ± 0.19 $m \cdot s^{-1}$ target measurement error (Section 3.3). Landry et al. (2013) reported that the magnitude of this uncertainty was due to ambiguity in the digitised point. Human operators digitised a skater's two-dimensional centre-of-mass point estimate – a point between the coccyx and belly button (equivalent to the 1st lumbar vertebra) – using cues such as the relative position of the limbs and head. In contrast, the algorithm used the foreground object's geometric centroid. Accordingly, a simple way to reduce this error would be to use a marker to define a skater's centre-of-mass point estimate. This approach is frequently used in human motion analysis to identify landmarks of interest (Payton, 2008).

5.2.3 Automated digitisation in human motion analysis

In human motion analysis, optical motion capture is considered the gold standard measurement technique as it offers high spatial accuracy (less than a millimetre) and high temporal resolution (upwards of several hundred frames per second) (Song & Godøy, 2016). The process utilises data captured from image sensors to triangulate the three-dimensional position of anatomical landmarks between two or more calibrated cameras with overlapping projections. These landmarks, such as joint centres or segment endpoints (Payton, 2008), are typically identified using either retroreflective (passive) or light-emitting (active) fiducial markers. The former being advantageous due to the absence of wires, batteries and pulsing circuitry on the participant under analysis (Chiari, Croce, Leardini, & Cappozzo, 2005).

When filmed using infrared lights, the light reflected from retroreflective passive markers is easy to locate in an otherwise dark image (Peikon, Fitzsimmons, Lebedev, & Nicolelis, 2009; Pintaric & Kaufmann, 2007). When these markers are not retroreflective, the properties of the background and marker are manipulated to create high contrast images. For example, scholars have ensured a dark image background by covering both the capture volume and participant in dark materials (Ceccon et al., 2013; Sampe, Vijai, Latifah, & Aprintono, 2009; Yeasin & Chaudhuri, 2000) and selected the colour of the marker to maximise the image contrast (Sampe et al., 2009; Theobalt, Albrecht, Haber, Magnor, & Seidel, 2004).

In addition to the fiducial marker’s colour, scholars also manipulate the marker's shape and size; with both influencing the overall measurement accuracy. For example, passive fiducial markers are typically either sphere- or disc-shaped (Magalhães et al., 2013). While spherical markers assist in the accurate calculation of the marker centroid – as they always appear as a circle in a two-dimensional image – they also protrude from the athlete's body. In swimming, Kjendlie and Bjørn (2012) reported that the protruding nature of 24 spherical markers (19 mm in diameter) increased passive drag by up to 10%. As a result, Ceccon et al. (2013) used disk-shaped markers in a kinematic analysis of the front crawl. However, as the appearance of a disk-shaped marker is dependent on the marker's position relative to the camera, the calculation of a marker’s centroid may have been less accurate due to a smaller count of foreground pixels. Likewise, the selected size of a marker is a trade-off between accuracy and digitisation error; while a larger marker theoretically increases the automated digitisation accuracy, it may also interfere with other markers and the athlete’s movement (Chiari et al., 2005; Payton, 2008).

Segmentation methods

By creating high contrast images, fiducial markers can be segmented using thresholding

Item removed for copyright reasons

Figure 5-3. Morphological erosion (left) and dilation (right) operations. The 3 x 3-pixel structuring element removes or adds pixels to the foreground object's boundary (centre) based on the minimum or maximum value in the structuring element's pixel neighbourhood. Figure adapted from Dunn (2014).

techniques. However, even with the most elaborate segmentation methods, the result of this segmentation is rarely perfect, i.e. the segmentation method misclassifies pixels as either foreground and background (Russ & Brent, 2011). For this reason, before representing foreground objects as single points, binary images are processed.

One approach to processing binary images is to apply morphological operations such as dilation and erosion. As shown in Figure 5-3, the two operations add (dilation) and remove (erosion) pixels from the foreground object's boundary. The number of pixels added or removed is dependent on the size and shape of a structuring element (Comer & Delp, 1999). For example, during dilation, the value of the processed image's ith pixel is the maximum value of all pixels in the binary image's ith pixel neighbourhood (defined by the structuring element). In contrast, during erosion, the value of the processed image's ith pixel is the minimum value of all pixels in the binary image's ith pixel neighbourhood.

An alternative approach to processing binary images in optical motion capture is to apply constraints to foreground objects based on *a posteriori* knowledge of the object's image appearance. For example, Flam, de Souza Ramos, de Queiroz, de Albuquerque Araújo and Gomide (2009) used a minimum and maximum foreground object area constraint, while Shafiq, Tümer and Güler (2001) defined the minimum and maximum foreground object width and height. In both examples, if the foreground object did not meet the predefined criteria, the associated pixels were reclassified as background.

Representation methods

Optical motion capture represents each fiducial marker foreground object using a single pair of coordinates that define the marker's centre. While the centre of a marker can be estimated using various methods, Chiari et al. (2005) reported that optical motion capture commonly uses the geometric centroid and circle-fitting methods.

As reported in Section 5.2.2, when Landry et al. (2013) calculated the geometric centroid of a skater's foreground object, the calculation ($Eq. 5.1$) assumed that each pixel had an equal mass. In optical motion capture, an alternative brightness-weighted approach is also used (Peikon et al., 2009). This method assumes that the mass of each pixel is equivalent to the pixel's intensity,

$$Centroid_u = \frac{\sum_{i=1}^{n} u_i Br_i}{\sum_{i=1}^{n} Br_i} \qquad Centroid_v = \frac{\sum_{i=1}^{n} vBr_i}{\sum_{i=1}^{n} Br_i} \qquad (Eq. 5.2)$$

where n is the total number of foreground object pixels, u_i is the u-coordinate of the ith pixel, v_i is the v-coordinate of the ith pixel, and Br_i is the intensity of the ith pixel.

Circle-fitting procedures estimate the marker's centroid as the centre of a circle fitted to the edge of a foreground object using a least-squares method (Chiari et al., 2005). The method minimises the mean square distance from the circle to the data points. The objective function, F, is defined by,

$$F = \sum_{i=1}^{n} d_i^2 \qquad (Eq. 5.3)$$

where d_i is the Euclidean distance from the point to the circle.

Based on the equation of a circle,

$$(x-a)^2 + (y-b)^2 = R^2 \qquad (Eq. 5.4)$$

where (a, b) is its centre and R is its radius, d_i is given by,

$$d_i = \sqrt{(x_i - a)^2 + (y_i - b)^2} - R \qquad (Eq. 5.5)$$

This method can be extended to ellipses to account for sphere-shaped markers that do not appear as circles in a two-dimensional image (Fitzgibbon, Pilu, & Fisher, 1999). However, this procedure is more computationally expensive due to the additional parameters required to define an ellipse.

National Ice Centre (GBR) multi-camera network feasibility

The use of retroreflective markers in the National Ice Centre (GBR) multi-camera network is not feasible as the installation does not include infrared lights. In contrast, the use of non-retroreflective markers is feasible, as both the properties of the background (e.g. skin-suit) and marker (e.g. colour, shape and size) can be manipulated. Considering that most of each camera's field-of-view is ice, a dark skin suit with a contrasting coloured fiducial marker seems most suitable. The marker should also be disk-shaped – as air friction accounts for approximately 75% of the frictional forces that a skater has to overcome (de Koning, de Groot, & van Ingen Schenau, 1992; van Ingen Schenau, 1982) – and the size of the marker maximised to minimise the error in the automated digitisation algorithm. Finally, due to the appearance a disk-shaped marker being dependent on its position relative to the camera, the geometric centroid should be used to calculate the centre of the fiducial marker.

5.2.4 Section summary

The first step in measuring two-dimensional relay exchange kinematics using the National Ice Centre (GBR) multi-camera network is to digitise the skater's position in the pixel coordinate system. The multi-camera network should automate this procedure due to the associated time cost of manual digitisation. The most relevant example of automated digitisation in short-track speed skating is not suitable for the National Ice Centre (GBR) multi-camera network as ambiguity in the digitised point propagated to errors that exceed the ± 0.19 $m \cdot s^{-1}$ target measurement error. The simplest way to reduce this ambiguity is to place a fiducial marker at the skater's two-dimensional centre-of-mass point estimate. To automatically digitise this fiducial marker requires high contrast between the marker and background. When specialist equipment cannot be used (e.g. infrared cameras with retroreflective markers), manipulating the background and marker properties can create the necessary contrast. In the multi-camera network, a dark skin suit with a coloured marker seems the best solution. The marker should be disk-shaped to minimise air friction and the geometric centroid used to calculate the marker's centre.

5.3 Part I. Measuring skater position on the short-track

The second step in measuring two-dimensional relay exchange kinematics using the National Ice Centre (GBR) multi-camera network is to transform the position of a skater from the pixel coordinate system to the global coordinate system. The global coordinate system represents three-dimensional points in the real world and has an x-, y-, and z-axis. The transformation from pixel to global coordinate systems is called reconstruction, and the reverse is called projection.

To reconstruct (pixel) and project (global) coordinates, a calibration model is required. The calibration model – calculated using a calibration procedure – defines the relationship between the pixel and global coordinate systems and the equations for reconstruction and projection. In a recent review of calibration procedures, Hudson (2015) deemed that a nonlinear calibration procedure – which implemented the methods of Heikkilä and Silvén (1997) and Zhang (1999) – was most suitable for correcting the lens distortion detailed in Section 4.3.1. However, the Olympic Oval (CAN) multi-camera network used an image rectification calibration procedure. In the following sections, I review both approaches for use at the National Ice Centre.

5.3.1 Image rectification calibration procedure

Image rectification is a transformation process used to project images onto a common

Item removed for copyright reasons

Figure 5-4. The result of a 3rd order image rectification in the Olympic Oval (CAN) multi-camera network (left) and the pixel reprojection error for a 2nd, 3rd and 4th order polynomial rectification (right). Figure adapted from Landry et al. (2013).

image plane. This procedure requires several positions – termed control points – where both pixel and global coordinates are known. In the Olympic Oval (CAN) multi-camera network, Landry et al. (2013) used features of the short-track such as track marking blocks to define these points. As illustrated in Figure 5-4, image rectification warps the source image to the global coordinate system by applying a high-order polynomial transformation,

$$x' = \sum_{i}^{I} \sum\nolimits_{j}^{J} a_{i,j}\, x^i y^j \qquad y' = \sum_{i}^{I} \sum\nolimits_{j}^{J} b_{i,j}\, x^i y^j \qquad (Eq. 5.6)$$

For all control points, Landry et al. (2013) used singular value decomposition factorisation to find the coefficient $a_{i,j}$ and $b_{i,j}$ linking all points to their projection (x', y'). The appearance of the other pixels was then determined using bilinear or bicubic interpolation. Figure 5-4 demonstrates the results of a 2nd, 3rd and 4th order polynomial rectification in the Olympic Oval (CAN) multi-camera network.

National Ice Centre (GBR) multi-camera network feasibility

The Olympic Oval (CAN) multi-camera network's calibration procedure has two limitations that warrant consideration. First, the mean root mean square reprojection error for the selected 4th order polynomial rectification (0.2235 pixels) propagated to errors in velocity (± 0.48 $m \cdot s^{-1}$) that exceed the ± 0.19 $m \cdot s^{-1}$ target measurement error.

Second, Landry et al. (2013) reported that the calibration's reprojection error grew rapidly outside the areas covered by the control points, e.g. inside the short-track. In order for Great Britain Short-Track Speed Skating to advance knowledge on *'how to execute the relay exchange effectively'*, accurate measurement in this area is essential as oncoming skaters build up speed on the inside of the short-track in preparation for the relay exchange. This limitation is more of a concern than the former, as the reported reprojection error would likely propagate to smaller velocity errors in the multi-camera network due to the system having a higher spatial resolution, i.e. a greater number of pixels per metre (Section 4.2).

5.3.2 Nonlinear calibration procedure

A nonlinear calibration procedure uses an intrinsic and extrinsic calibration model to calculate the relationship between the pixel and global coordinates systems. The intrinsic calibration accounts for the effects that the camera lens and camera construction has on an image, i.e. radial and tangential lens distortion, and the extrinsic calibration estimates the camera's pose, i.e. the position and orientation of the camera in the global coordinate system. Bouguet's (2015) *Camera Calibration Toolbox for MATLAB* – a popular implementation of the nonlinear calibration procedure – uses seven steps to construct the two calibration models.

1. Set and lock the camera and lens settings (e.g. image resolution and focus).
2. Record images of a calibration object, e.g. a planar checkerboard pattern, in a range of positions and orientations that cover the camera's field-of-view.
3. Select a subset of calibration object images that cover the camera's field-of-view evenly in a range of orientations.
4. Use the geometry of the checkerboard pattern to calculate the global coordinates of the calibration object's intersections (i.e. the checkerboard's corners).
5. Use digital image processing techniques to extract the pixel coordinates of the checkerboard intersections.

6. Calculate the intrinsic parameters (focal length, principal point and pixel skew) and the camera's distortion coefficients (radial and tangential). An optimisation routine is used to minimise the reprojection error, i.e. the sum of the distances between the extracted and projected checkerboard intersections.
7. Calculate the extrinsic parameters (rotation and translation matrix). This procedure requires the intrinsic parameters and four control points. If a user provides more than four control points, the toolbox performs an error minimisation process.

The nonlinear calibration procedure uses the camera's intrinsic and extrinsic parameters to project global coordinates into the pixel coordinate system and reconstruct pixel coordinates into the global coordinate system.

Projection

Four steps are required to project a three-dimensional point in the global coordinate system to a two-dimensional point in the pixel coordinate system. The first step transforms the three-dimensional point from the global coordinate system (x_g, y_g, z_g) to the camera coordinate system (x_c, y_c, z_c). This transformation consists of a rotation (R) followed by a translation (T) to collocate the coordinate systems,

$$\begin{bmatrix} x_c \\ y_c \\ z_c \end{bmatrix} = R \begin{bmatrix} x_g \\ y_g \\ z_g \end{bmatrix} + T \qquad (Eq. 5.7)$$

The second transformation is from the camera coordinate system (x_c, y_c, z_c) to the undistorted normalised image coordinate system (u_{ud}, v_{ud}). This procedure consists of projecting the three-dimensional point on the calibrated plane to the image plane. Here, a pinhole camera model is assumed,

$$\begin{bmatrix} u_{ud} \\ v_{ud} \end{bmatrix} = \begin{bmatrix} x_c/z_c \\ y_c/z_c \end{bmatrix} \qquad (Eq. 5.8)$$

The third transformation is from the undistorted normalised image coordinate system (u_{ud}, v_{ud}) to the distorted normalised image coordinate system (u_d, v_d). This transformation applies radial $(Eq.\,5.10)$ and tangential $(Eq.\,5.11)$ lens distortion to the point,

$$\begin{bmatrix} u_d \\ v_d \end{bmatrix} = \left(\delta_r \begin{bmatrix} u_{ud} \\ v_{ud} \end{bmatrix} \right) + \begin{bmatrix} \delta_u \\ \delta_v \end{bmatrix} \qquad (Eq.\,5.9)$$

$$\delta_r = 1 + \; k_1 r^2 + \; k_2 r^4 + \; k_3 r^6 \qquad (Eq.\,5.10)$$

$$\begin{bmatrix} \delta_u \\ \delta_v \end{bmatrix} = \begin{bmatrix} 2k_4 u v_{ud} + \; k_5 (r^2 + \; 2{u_{ud}}^2) \\ 2k_5 u v_{ud} + \; k_4 (r^2 + \; 2{v_{ud}}^2) \end{bmatrix} \qquad (Eq.\,5.11)$$

where r is the magnitude of (u_{ud}, v_{ud}), k_{1-3} are radial distortion coefficients, and k_{4-5} are the tangential distortion coefficients.

The fourth transformation is from the distorted normalised image coordinate system (u_d, v_d) to the pixel coordinate system (u, v),

$$\begin{bmatrix} u \\ v \end{bmatrix} = \begin{bmatrix} u_d f_x + v_d \, \varsigma + c_x \\ v_d \, f_y + c_y \end{bmatrix} \qquad (Eq.\,5.12)$$

where c_x and c_y are the coordinates of the principal point (in pixels), f_x and f_y are the focal length (in pixels), and ς is the pixel skew.

Reconstruction

Four steps are required to reconstruct a two-dimensional point in the pixel coordinate system to a three-dimensional point in the global coordinate system. The first transformation is from the pixel coordinate system (u, v) to distorted normalised image coordinate system (u_d, v_d). Here, $Eq.\,5.12$ is rearranged to give,

$$\begin{bmatrix} u_d \\ v_d \end{bmatrix} = \begin{bmatrix} (u - v_d \varsigma - \; c_x)/f_x \\ (v - \; c_y)/f_y \end{bmatrix} \qquad (Eq.\,5.13)$$

The second transformation is from the distorted normalised image coordinate system (u_d, v_d) to the undistorted normalised image coordinate system (u_{ud}, v_{ud}). This removes both radial and tangential distortion,

$$\begin{bmatrix} u_{ud} \\ v_{ud} \end{bmatrix} = \frac{1}{\delta_r} \left(\begin{bmatrix} u_d \\ v_d \end{bmatrix} - \begin{bmatrix} \delta_u \\ \delta_v \end{bmatrix} \right) \qquad (Eq. 5.14)$$

where δ_r, δ_u and δ_v are defined as in $Eq. 5.10$ and $Eq. 5.11$.

The third transformation is from the undistorted normalised image coordinate system (u_{ud}, v_{ud}) to the camera coordinate system (x_c, y_c, z_c). This is achieved using line-plane interception geometry,

$$\begin{bmatrix} x_c \\ y_c \\ z_c \end{bmatrix} = d \begin{bmatrix} u_{ud} \\ v_{ud} \\ 1 \end{bmatrix} \qquad (Eq. 5.15)$$

where d is the distance between the optical centre and point in the camera coordinate system (Dunn et al., 2012).

The fourth transformation is from the camera coordinate system (x_c, y_c, z_c) to the global coordinate system (x_g, y_g, z_g). This is the reverse of the transformation in $Eq. 5.7$,

$$\begin{bmatrix} x_g \\ y_g \\ z_g \end{bmatrix} = R^{-1} \left(\begin{bmatrix} x_c \\ y_c \\ z_c \end{bmatrix} - T \right) \qquad (Eq. 5.16)$$

National Ice Centre (GBR) multi-camera network feasibility

While the accuracy of the nonlinear calibration procedure is unknown in the National Ice Centre (GBR) multi-camera network, the procedure appears better suited to transforming the position of a skater from the pixel coordinate system to the global coordinate system. In tennis, Dunn et al. (2012) showed that compared to other calibration models, a nonlinear calibration model reduced reconstruction errors outside

Item removed for copyright reasons

Figure 5-5. Vertical out-of-plane error relative to the camera's central axis, where p_c is the calculated position, p_a is the actual position, and e is the out-of-plane error. The measurement or estimation of the camera-to-calibrated plane distance, b, and out-of-plane distance, d, allows the calculation of p_a and e from p_c. Figure adapted from Sih et al. (2001).

the court's control points as the calibration model was more efficient at correcting lens distortion. Accordingly, this procedure enables the multi-camera network to measure skaters on the inside of the short-track as they prepare for the relay exchange. Of note, Landry et al. (2013) trialled and disregarded the nonlinear calibration procedure at the Olympic Oval due to the checkerboard intersections not covering the image sensor sufficiently in a variety of poses. Landry et al. (2013) positioning a 11 x 9 square checkerboard pattern (each 0.5 m x 0.5 m) on the rink surface. The implementation of this procedure at the National Ice Centre would need to resolve this issue.

5.3.3 Out-of-plane error

In the calibration procedures described in Section 5.3.1 and Section 5.3.2, the relationship between the pixel and global coordinate systems is only valid for the calibrated plane. As illustrated in Figure 5-5, reconstructed points of interest (e.g. a fiducial marker) not on this calibrated plane (e.g. the rink surface) are subject to out-of-plane error (Sih, Hubbard, & Williams, 2001). Despite this, Landry et al. (2013) did not consider this source of error in the Olympic Oval (CAN) multi-camera network.

In both vertical and horizontal axes, the magnitude of out-of-plane error, e, is equivalent to,

$$e = \left(\frac{d}{b}\right) p_c \qquad (Eq. 5.17)$$

where d is the out-of-plane distance, b is the camera-to-calibrated plane distance, and p_c is the reconstructed position. As a result, the easiest way to minimise the magnitude of out-of-plane error is to increase the camera-to-calibrated plane distance (Payton, 2008). This approach, however, is not feasible in the National Ice Centre (GBR) multi-camera network as all 26 cameras are fixed on a suspended structure 9 m above the rink surface (Section 4.2). This approach also demonstrates that the magnitude of out-of-plane error will be more substantial in the National Ice Centre (GBR) multi-camera network, as the Olympic Oval (CAN) multi-camera network's cameras are fixed 22.5 m above the short-track (Table 4-1).

The alternative approach to minimise out-of-plane error is to use an elevated calibration plane to reduce out-of-plane distances. In tennis, Dunn (2014) showed that compared to the court surface, a calibrated plane elevated to the height of the tennis net, i.e. the expected height of the players centre-of-mass, reduced root mean square reconstruction errors by up to 0.24 m. Dunn (2014) used two different methods to construct this elevated calibration plane, both of which used elevated control points. The first method defined the elevated control points by positioning a rigid object – set to the height of the tennis net – at known locations in the global coordinate system (e.g. court line intersections). As illustrated in Figure 5-6, the digitisation of these points defined the location of the control points in the pixel coordinate system. In contrast, the second method used a camera-court plane calibration model – constructed using the nonlinear calibration procedure described in Section 5.3.2 – to project the elevated plane control points into the pixel coordinate system.

Item removed for copyright reasons

Figure 5-6. The digitised court plane (red circle) and elevated plane (yellow circle) control points used to construct camera-court plane and camera-court elevated plane calibration models. Figure adapted from Dunn (2014).

5.3.4 Section summary

The second step in measuring two-dimensional relay exchange kinematics using the National Ice Centre (GBR) multi-camera network is to use a calibration model to transform the position of a skater from the pixel coordinate system to the global coordinate system. The most relevant example – an image rectification calibration procedure implemented at the Olympic Oval (CAN) multi-camera network – is not suitable for the multi-camera network as the calibration's reprojection error increases rapidly outside the areas covered by the control points, e.g. inside the short-track. For Great Britain Short-Track Speed Skating to advance knowledge on *'how to execute the relay exchange effectively'*, accurate measurement in this area is essential as oncoming skaters build up speed on the inside of the short-track in preparation for the relay exchange. Instead, a nonlinear calibration procedure seems more suitable as the method is better equipped to correct for lens distortion outside the areas covered by the control points. However, this technique requires the projected checkerboard intersections used in the intrinsic calibration to sufficiently cover the image sensor. Finally, the nonlinear calibration model is only valid for the calibrated plane. As a result, any measured point (e.g. the fiducial marker) not on this plane (e.g. the rink surface) is subject to out-of-plane error. The magnitude of this error, unknown in short-track speed skating multi-camera networks, can be reduced using elevated calibration planes if required.

5.4 Part I. Measuring skater position over time

The third step in measuring two-dimensional relay exchange kinematics using the National Ice Centre (GBR) multi-camera network is to track the skater's position over time, i.e. in consecutive images. In a multi-camera network, this tracking procedure consists of two parts (1) tracking the skater within a camera's field-of-view, termed intra-camera tracking, and (2) tracking the skater between different cameras field-of-view, termed inter-camera tracking. Importantly, both are performed in the global coordinate system to facilitate inter-camera tracking (Wang, 2013).

5.4.1 Fiducial marker tracking in human motion analysis

In optical motion capture, a passive fiducial marker is tracked from the current image, f_i, to the next image, f_{i+1}, by looking at the displacement of the marker over a four-frame window (Malik, Dracos, & Papantoniou, 1993). The displacement of the marker from f_{i-1} into f_i predicts the position of the marker in the next image, f_{i+1}. Then the actual position of the fiducial marker in f_{i+1}, and a further prediction of the marker into the next image, f_{i+2}, confirms the previously made hypothesis by eliminating any ambiguities in the prediction. This 'predict and confirm' strategy – illustrated in Figure 5-7 – is described below in detail.

In Figure 5-7, the fiducial marker being tracked, m_1, in the current image, f_i, has an established tracking link from the previous image, f_{i-1}. The displacement between these two positions is applied to the fiducial marker position in f_i to predict a search neighbourhood in the next image, f_{i+1}. This search neighbourhood, centred on the predicted position, is the region where the fiducial marker is expected to be located. If

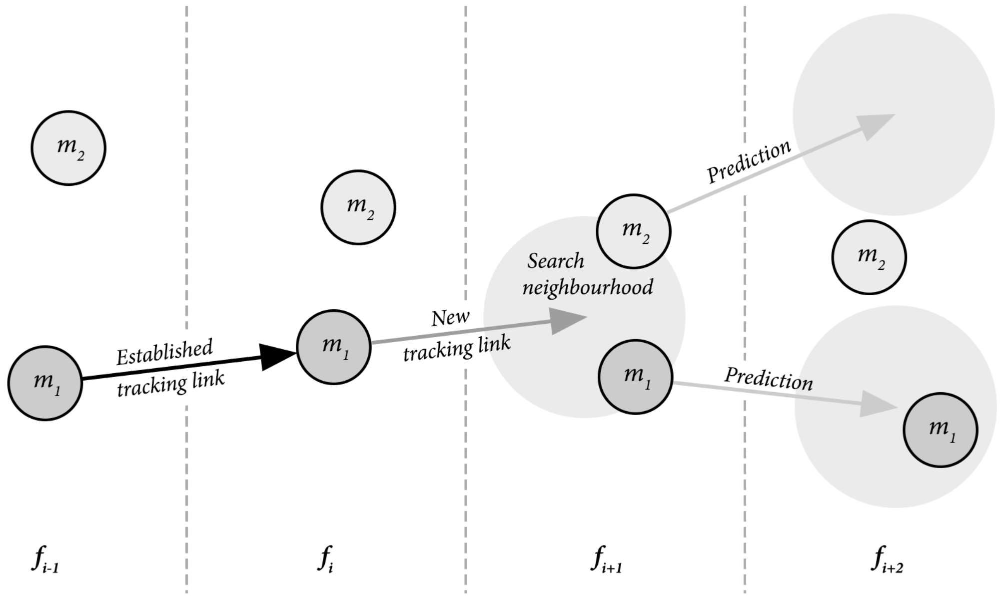

Figure 5-7. Illustration of the four-frame tracking procedure. The displacement between the tracked fiducial marker, m_1, in f_{i-1} and f_i is used to predict a search neighbourhood in f_{i+1}. As this search neighbourhood contains two candidate markers, the prediction is prolonged into f_{i+2}, and a new search neighbourhood generated for each candidate marker. As these search neighbourhoods only contain one marker, m_1, this marker is confirmed as the correct marker in f_{i+1} and a new tracking link is established between f_i and f_{i+1}.

the search neighbourhood only contains one marker, a tracking link is established from f_i to f_{i+1}. However, this is not the case in Figure 5-7 as two candidate markers, m_1 and m_2, are detected in the search neighbourhood. In this scenario, the movement is prolonged into the next image, f_{i+2}, and a new search neighbourhood generated for each candidate marker. As the search neighbourhoods in f_{i+2} only contain one marker, m_1, this marker is confirmed as the correct marker in f_{i+1}, and a tracking link established between f_i and f_{i+1}. If the search neighbourhoods in f_{i+2} contain two candidate markers, e.g. m_1 and m_2, another criterion is required to determine the correct tracking link from f_i to f_{i+1}. Example criteria include (1) selecting the marker in f_{i+2} that has the smallest Euclidian distance from the predicted positions, (2) selecting the trajectory with the smoothest acceleration over the four-frame period (Herda, Fua, Plänkers, Boulic, & Thalmann, 2001), and (3) selecting the trajectory with the most consistent fiducial marker size (Peikon et al., 2009).

Importantly, for this four-frame tracking procedure to work well a minimum displacement condition is required (Song & Godøy, 2016). In other words, the time interval between two successive images should be short enough to avoid rapid changes in a fiducial marker's trajectory. Although the National Ice Centre (GBR) multi-camera network sampling interval is relatively low (25 Hz, Table 4-1), as trajectories in short-track speed skating are highly constrained to the short-track, rapid changes in a marker trajectory are unlikely. Still, if a trajectory violates the minimum displacement condition, a more sophisticated prediction method is required.

5.4.2 Tracking prediction methods

Peikon et al. (2009) used two marker states to predict the position of the search neighbourhood (1) the marker's current position, x_s, and (2) the marker's current velocity, v_s. By assuming a constant velocity over the time interval, Δt, Peikon et al. (2009) projected the position state forward to predict its value in the next image, f_{i+1},

$$x_{s+1} = x_s + (\Delta t \cdot v_s) \qquad (Eq. 5.18)$$

Based on the measured position, x_m, in f_{i+1}, both state variables were then updated ($Eq.$ 5.19 and $Eq.$ 5.20) and reused in $Eq.$ 5.18 to predict the search neighbourhood in the proceeding image, f_{i+2}.

$$x_{s+1} = x_m \qquad (Eq. 5.19)$$

$$v_{s+1} = \frac{(x_m - x_s)}{\Delta t} \qquad (Eq. 5.20)$$

This approach, like the four-frame tracking procedure described in Section 5.4.1, assumes that the state variables contain no error. However, in real applications, the actual position x_m of the marker is almost never the predicted position (Flam et al., 2009). This difference, r, is known as the residual error,

$$r = x_m - x_{s+1} \qquad (Eq.\,5.21)$$

To include this residual error in the update of the both state variables, Flam et al. (2009) used an alpha-beta tracking filter (Yoo & Kim, 2003). The alpha-beta tracking uses the residual error, together with the alpha α and beta β constants, to update the position and velocity state variables,

$$x_{s+1} = x_{s+1} + \alpha r \qquad (Eq.\,5.22)$$

$$v_{s+1} = v_s + \left(\frac{\beta}{\Delta t}\right) r \qquad (Eq.\,5.23)$$

where α and β are smoothing parameters ranging from 0 to 1 (alpha) and 0 to 2 (beta). Large parameters produce a fast-tracking response to changes in the trajectory while small values reduce the level of noise in the state variables.

In more difficult tracking scenarios, such as skater's undergoing long periods of occlusion in panning camera systems, scholars use more complex tracking procedures. For example, in short-track speed skating the Kalman filter (Liu & Tang, 2009), unscented Kalman filter (Liu, Tang, Cheng, Huang, & Liu, 2009; Liu, Tang, Huang, Liu, & Sun, 2007), and particle filter (Wang, Liu, Liu, Tang, & Liu, 2009) have been used to track skaters in successive images. In these methods, rather than only using the previous position, velocity, and residual error to predict the current state variables, a probability density function – constructed of all previous measurements – is used. While Kalman filters assume that the distribution of the previous states is Gaussian, particle filters do not restrict the shape of the distribution (de Queiroz, Gomide, & de Albuquerque Araújo, 2012).

5.4.3 Tracking search neighbourhoods

In addition to enabling tracking links to be established between fiducial markers in consecutive images, search neighbourhoods – also called prediction radii (Song & Godøy, 2016) or tracking windows (Gilbert, Giles, Flachs, Rogers, & Hsun U, 1980) –

can be used to increase the accuracy and efficiency of the automated digitisation procedures discussed in Section 5.2. By cropping the original image to the search neighbourhood, the algorithms only need apply the image processing operations to the region of interest (Gilbert et al., 1980; Kelley, 2011). Accordingly, the smaller number of processed pixels reduces the chance of false positive fiducial marker detection and the required computation.

5.4.4 Tracking initialisation

In the four-frame tracking example presented in Figure 5-7, the tracking procedure had already identified the fiducial marker's position in the previous, f_{i-1}, and current, f_i, image. As a result, the fiducial marker's state (e.g. the position and velocity) was already known, and the tracking procedure could predict the marker's position in the next image, f_{i+1}. However, when the tracking procedure first starts, this *a posteriori* knowledge is unknown. For this reason, an initialisation procedure is required to ensure that the tracking procedure commences operation with the correct interpretation of the scene, i.e. the fiducial marker's current state (Moeslund & Granum, 2001). While this initialisation procedure can be automated, typically the procedure involves the manual detection of the marker in the first (Magalhães et al., 2013) or first two (Yeasin & Chaudhuri, 2000) images of the analysis. While both methods measure the marker’s current position, in the single image procedure a default marker displacement or velocity is also required. Finally, in addition to defining the fiducial marker's state, the initialisation procedure can also be used to associate semantics with the fiducial marker. For example, Flam et al. (2009) used the procedure to define the name of each marker's appropriate anatomical landmark. In the National Ice Centre (GBR) multi-camera network, this could be used to associate the marker with the relevant athlete's identity or the athlete's relay team.

5.4.5 Section summary

The third step in measuring two-dimensional relay exchange kinematics using the

National Ice Centre (GBR) multi-camera network is to track the skater’s position over time in the global coordinate system. This tracking procedure – performed within and between-cameras’ field-of-view – uses a ‘predict and confirm’ strategy over a four-image period to establish a fiducial marker’s tracking link from the current image, f_i, to the next image, f_{i+1}. The complexity of this prediction is dependent on the skater’s displacement in consecutive images, with a search neighbourhood used to (1) minimise the number of candidate tracking links, and (2) increase the accuracy and efficiency of the automated digitisation algorithm. This prediction also requires an initialisation procedure to ensure that the tracking procedure commences operation with the correct interpretation of the scene, e.g. the marker's current position and velocity. This process – achieved by digitising and labelling the first one or two images in the analysis manually – can also be used to associate an athlete’s identity, or the athlete's relay team, to the fiducial marker.

5.5 Part I. Computing skater velocity

The fourth step in measuring two-dimensional relay exchange kinematics using the National Ice Centre (GBR) multi-camera network is to use the skater’s tracked position to compute the resultant velocity. Great Britain Short-Track Speed Skating is interested in the resultant velocity, as skaters generate propulsive forces by pushing-off at right angles relative to the gliding motion of the skate (de Koning & van Ingen Schenau, 2000). As illustrated in Figure 5-8, the sideward (v_2) and gliding (v_1) velocity determine the new magnitude and direction of the skater’s centre-of-mass velocity (v_3); calculated as,

$$v_3 = \sqrt{{v_1}^2 + {v_2}^2} \qquad (Eq.\,5.24)$$

Velocity can be computed using either analytical, graphical, or numerical techniques (Gordon & Caldwell, 2014). Of these three methods, human motion analysis generally uses numerical differentiation due to the data's format, i.e. position coordinates equally

Item removed for copyright reasons

Figure 5-8. A skater generates propulsive forces by pushing-off at right angles relative to the gliding motion of the skate. This push-off results in a sideward velocity (v_2) of the body's centre-of-mass with respect to the skate. Together with the velocity of the gliding skate (v_1), this determines the new magnitude and direction of the body's centre-of-mass velocity (v_3). Figure adapted from de Koning and van Ingen Schenau (2000).

spaced in time, being in the precise format for applying numerical techniques. While there are various numerical deviation formulas, the equations presented below are examples of finite difference techniques.

For a sample of n points, the velocity v_i at the ith point,

when i = 1, is computed using the forward difference method,

$$v_i = \frac{s_{i+1} - s_i}{\mathit{\Delta} t} \qquad (Eq. 5.25)$$

when i = 2 to n – 1, is computed using the central difference method,

$$v_i = \frac{s_{i+1} - s_{i-1}}{2\Delta t} \qquad (Eq. 5.26)$$

and when i = n, is computed using the backward difference method,

$$v_i = \frac{s_i - s_{i-1}}{\Delta t} \qquad (Eq. 5.27)$$

where s is the position of the skater (measured in the global coordinate system) and Δt is the sampling interval of the data (calculated as one over the camera's sampling frequency).

5.5.1 Sampling interval error and uncertainty

When computing velocity, the finite difference techniques presented in $Eq. 5.25$ to $Eq. 5.27$ assume that the sampling interval of the data is constant. As described below, in the National Ice Centre (GBR) multi-camera network this is not the case both within- and between-cameras' field-of-view.

Within-camera sampling interval error

As illustrated in Figure 5-9, data collected from a camera with a global shutter meets the constant sampling interval assumption as the shutter starts and stops light integration for every pixel in the sensor at the same time. As readout time is sequential by scanlines, i.e. each row of pixels, each pixel requires a sample and hold circuit to preserve the value from when the time integration ends until it can be read out (Wilburn et al., 2004).

In contrast, data collected from cameras with an electronic rolling shutter – for example, the National Ice Centre (GBR) multi-camera network (Section 4.3.1) – do not meet the constant sampling interval assumption. As shown in Figure 5-9, an electronic rolling shutter exposes each scanline just before it is read out. As readout time is sequential by scanline, a row of pixels lower in the image starts and stops light integration nearly an image later than a row of pixels at the top of the image (Wilburn et al., 2004). This slice

Item removed for copyright reasons

Figure 5-9. Effect of camera shutter type in the spatiotemporal volume. Global shutters capture the entire image at the same time, so each image is vertical in the volume. In contrast, electronic rolling shutters capture lower rows in the image later in time, so each image lies on a slanted plane in the volume. Figure adapted from Wilburn et al. (2004).

in the spatiotemporal volume, known as temporal shear (Bradley et al., 2009), means that the sampling interval is only constant in consecutive images between scanlines. The effect of this sampling interval error in the computation of skating velocity within-cameras' field-of-view is unknown in the National Ice Centre (GBR) multi-camera network.

To account for temporal shear, Bradley et al. (2009) modelled the camera's electronic rolling shutter readout time. The model, illustrated in Figure 5-10, calculates the readout time $r_y^{(i)}$, for scanline y, in image i, as,

$$r_y^{(i)} = t^{(i)} + \left(\frac{y}{S}\right) \cdot \Delta t \qquad (Eq.\,5.28)$$

where Δt is the frame duration (one over the sampling frequency), S is the total number of scanlines in the image, and $t^{(i)}$ is the first scanline's readout time in image i. Bradley et al. (2009) noted that the total number of scanlines might be larger than the number of visible scanlines, i.e. the number of rows in an image, as invisible scanlines can exist for synchronisation signals. For example in high definition video, there are 1125 scanlines but only 1080 visible scanlines (ITU, 2011).

Item removed for copyright reasons

Figure 5-10. The electronic rolling shutter readout time model. Just-in-time exposure (Δe) and sequential scanline readout, create a shear of exposure time intervals in the time domain. The slope of this temporal shear is the function of (1) the camera's sampling interval (Δt), and (2) the total number of scanlines (S); where N is the number of visible scanlines. Figure adapted from Bradley et al. (2009).

The model's readout times can be used to estimate the true sampling interval, $\Delta t'$, between consecutive frames as follows,

$$\Delta t' = \left(r_y^{(i)} + \Delta t\right) - r_y^{(i-1)} \qquad (Eq. 5.29)$$

Between-camera sampling interval uncertainty

As reported in Section 4.2, the cameras in the National Ice Centre (GBR) multi-camera network can be out-of-phase by up-to ± 0.02 seconds, as the Axis M3204 cameras do not support generator locking. Like the within-camera sampling interval error reported previously, the effect of this sampling interval uncertainty in the computation of skating velocity between-cameras' field-of-view is unknown in the multi-camera network.

5.5.2 Removing high-frequency noise

Before the computation of velocity, position data needs to be processed to attenuate high-frequency noise in the automated digitisation procedure (Bartlett, 2014; Derrick &

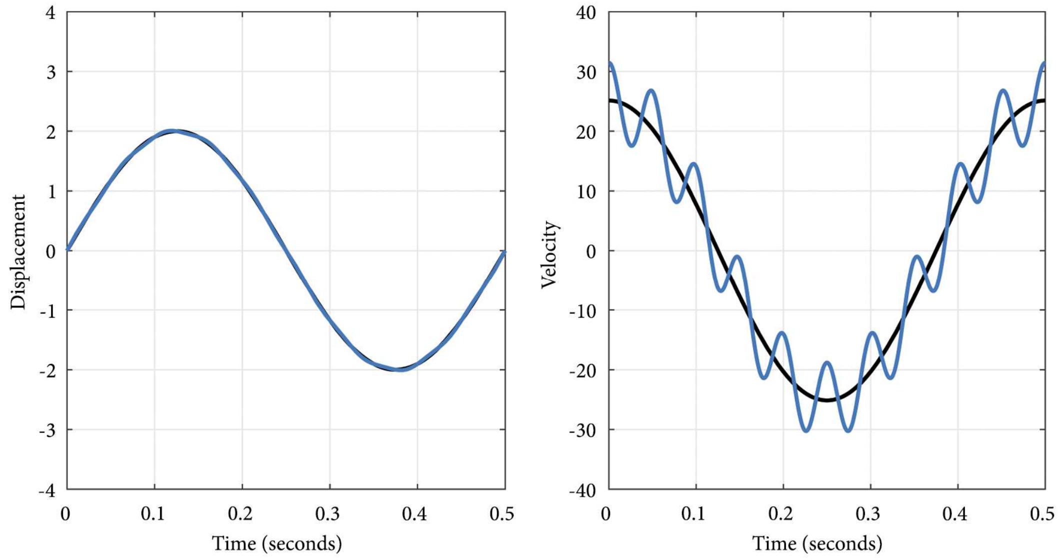

Figure 5-11. The effect of high-frequency noise propagation in displacement (left) and velocity (right) data. Noise-free and noisy measurements are denoted by the black and blue line, respectively.

Gordon, 2014). Bartlett (2014) highlighted the importance of removing high-frequency noise using a simplified representation of a recorded sports movement. Consider coordinate r expressed by the equation,

$$r = 2sin4\pi t + 0.02sin40\pi t \qquad (Eq. 5.30)$$

the first term, $2sin4\pi t$, represents the observed motion, known here as the signal. The signal's amplitude is 2, and its frequency is 2 Hz (indicated by $sin4\pi t$). The second term, $0.02sin40\pi t$, represents the noise. The noise's amplitude is equivalent to 1% of the motion, and its frequency is 20 Hz (indicated by $sin40\pi t$). Figure 5-11 shows that there is little difference between the noise-free and noisy displacement trajectories. However, when $Eq. 5.30$ is differentiated with respect to time in $Eq. 5.31$, the noise's amplitude increases to 10% of the noise-free velocity signal (Figure 5-11).

$$v = 8\pi cos4\pi t + 0.8\pi cos40\pi t \qquad (Eq. 5.31)$$

One approach to removing this high-frequency noise is to use a digital filter to attenuate different elements of the frequency spectrum (Sinclair, Taylor, & Hobbs, 2013). For example, when using a low-pass filter, the cut-off frequency is selected so that the lower frequencies remain (e.g. skater motion) and the high frequencies reduce (e.g. digitisation error). In biomechanics, the fourth order zero-lag Butterworth filter is typically used (Yu, Gabriel, Noble, & An, 1999). As the Butterworth filter's cut-off frequency increases, the influence of the filter on the data reduces, i.e. the data will become more like the raw signal. In short-track speed skating, previous studies have selected frequencies of 6- and 10-Hz (Chun, 2001; Kim, Jun, Yoo, & Park, 2013).

Another approach to removing high-frequency noise is to use a smoothing spline. A smoothing spline is a series of polynomial curves joined together at points called knots. Performed in the time domain, smoothing splines can be considered as the numerical equivalent to drawing a smooth curve through the complete set of data points (Bartlett, 2014). A smoothing parameter, λ, ranging from 0 to 1, controls the extent of this smooth curve. For example, when $\lambda = 0$ a least-squares straight line is fit to the data. In contrast, when $\lambda = 1$ a cubic spline interpolant is fit to the data. When compared to the Butterworth filter, the smoothing spline has the advantage that it does not require a constant sampling frequency (Derrick & Gordon, 2014). As discussed in Section 5.5.1, this is the case in the National Ice Centre (GBR) multi-camera network, as the sampling interval is only constant between scanlines in consecutive images due to the cameras' electronic rolling shutter.

Finally, human motion analysis applies both Butterworth filters and smoothing splines to the raw coordinate data in the global coordinate system. Scholars typically remove the noise at this point as, in three-dimensional studies, each camera's pixel coordinate system raw coordinate data does not contain the full information about the recorded movement (Bartlett, 2014).

5.5.3 Section summary

The fourth step in measuring two-dimensional relay exchange kinematics using the National Ice Centre (GBR) multi-camera network is to use the skater's tracked position to compute the resultant velocity. This step first attenuates high-frequency noise, associated with the automated digitisation of a skater, before using finite differencing techniques to compute velocity. In the multi-camera network, this computation is subject to within-camera sampling errors and between-camera sampling interval uncertainties. The former is due to each camera's electronic rolling shutter causing temporal shear within each image, the latter due to each camera's shutter being out-of-phase by up-to ± 0.02 seconds. The effect of both is currently unknown.

5.6 Part I. Summary

The first part of the literature review examined the four stages of the multi-camera network's measurement workflow. These stages included (1) measuring skater position in an image, (2) measuring skater position on the short-track, (3) measuring skater position over time, and (4) computing skater velocity. Based on the review, the multi-camera network's ability to measure accurate, two-dimensional, relay exchange kinematics is dependent on five sources of measurement error. These errors, defined below, combine to form the multi-camera network's *total error*.

- Section 5.2 concluded that the multi-camera network should use a fiducial-marker based digitisation algorithm to automatically digitise a skater's position in the pixel coordinate system. *Skater point error* describes how uncertainty in this automated digitisation propagates to errors in position and velocity.

- Section 5.3 showed that the multi-camera network requires a calibration model to transform the position of a skater from the pixel coordinate system to the global coordinate system. *Calibration model error* describes how incorrect relationships between the pixel and global coordinate systems propagate to errors in position and velocity within- and between-cameras' field-of-view.

- Section 5.3 demonstrated that a calibration model's relationship between the pixel and global coordinate system is only valid for the calibrated plane. *Out-of-*

plane error describes how any measured point (i.e. a fiducial marker) not on this plane (i.e. the rink surface) propagates to errors in position and velocity.

- Section 5.5 showed that due to the image sensor's electronic rolling shutter, each camera in the multi-camera network is subject to temporal shear, i.e. the sampling interval is only constant between scanlines in successive images. *Rolling shutter error* describes how the resulting within-camera sampling interval error propagates to errors in velocity.

- Section 5.5 reported that due to the Axis M3204 cameras not supporting generator locking, all cameras in the multi-camera network are out-of-phase by up-to ± 0.02 seconds. *Out-of-phase error* describes how the subsequent between-camera sampling interval uncertainty propagates to errors in velocity.

Based on the Olympic Oval (CAN) multi-camera network, the magnitude of *skater point error* (± 1.04 $m{\cdot}s^{-1}$) and *calibration model error* (± 0.48 $m{\cdot}s^{-1}$) exceed the ± 0.19 $m{\cdot}s^{-1}$ target measurement error. In contrast, the magnitude of *out-of-plane error*, *rolling shutter error*, and *out-of-phase error* is unknown. Accordingly, I need to quantify all sources of measurement error in the National Ice Centre (GBR) multi-camera network. First, the quantification of these errors, independently, allows the multi-camera network's measurement workflow to be empirically informed by identifying the errors that exceed the ± 0.19 $m{\cdot}s^{-1}$ target measurement error and need to be minimised, e.g. *skater point error* and *calibration model error*. Second, the quantification of these errors, collectively, would determine whether the multi-camera network can measure accurate, two-dimensional, relay exchange kinematics.

5.7 Part II. Error quantification

The first part of the literature review identified five sources of measurement error that would determine the National Ice Centre (GBR) multi-camera network's ability to measure accurate, two-dimensional, relay exchange kinematics. Section 5.6 concluded that the quantification of these errors (1) independently, would allow the multi-camera network's measurement workflow to be empirically informed, and (2) collectively, would determine whether the multi-camera network can measure accurate, two-dimensional, relay exchange kinematics. In the second part of this literature review, I evaluate different approaches for quantifying the multi-camera network's measurement error. First, Section 5.7.1 outlines several metrics used to quantify the systematic and random components of measurement error. Second, Section 5.7.2 discusses the validity of the criterion values used in the calculation of these metrics, termed *ground truth data*. Third, Sections 5.7.3 to 5.7.5 review the relative advantages and disadvantages of creating ground truth datasets manually, automatically, and synthetically.

5.7.1 Error metrics

As detailed in Section 3.3.2, the accuracy of a measurement reflects both its trueness and precision (JCGM, 2012). Typically expressed in terms of bias, trueness represents the systematic measurement error, i.e. the general trend for measurements to be different in a particular direction. Accordingly, a measurement made with high trueness will have little error. $Eq.\,5.32$ to $Eq.\,5.34$ present three different approaches to quantifying this component of measurement error: the mean ($\bar{x}$), absolute mean ($|\bar{x}|$), and root mean square (RMS) error.

$$\bar{x} = \frac{1}{n}\sum_{i=1}^{n}\Delta x_i \qquad (Eq.\,5.32)$$

$$|\bar{x}| = \frac{1}{n}\sum_{i=1}^{n}|\Delta x_i| \qquad (Eq.\,5.33)$$

$$RMS = \sqrt{\frac{\sum_{i=1}^{n}(\Delta x_i)^2}{n}} \qquad (Eq.\,5.34)$$

where Δx_i is the difference between a measure and a criterion value – termed the ground truth – and n is the number of measurements. Of these three criteria, Challis

(2018) recommends the RMS error, as this is the most conservative metric. For example, in $Eq. 5.32$ positive and negative measurements would cancel one and other out leading to smaller error values.

In contrast, precision represented the random measurement error inherent in every measurement procedure. Accordingly, measurements made with high precision have a small deviation of errors. This deviation is typically quantified using the standard deviation, σ,

$$\sigma = \left(\frac{1}{n-1}\sum_{i=1}^{n}(x_i - \bar{x})^2\right)^{\frac{1}{2}} \qquad (Eq. 5.35)$$

where x_i is the difference between the observed and ground truth value, and $\bar{x}$ is the mean value of these observations.

5.7.2 Ground truth data

The quality of any error quantification is dependent on the accuracy and validity of the ground truth values used in $Eq. 5.32$ to $Eq. 5.35$. In this thesis, the term validity refers to whether the ground truth values, termed the ground truth dataset, are representative of the National Ice Centre (GBR) multi-camera network's intended use-cases (Krig, 2014), i.e. the different measurement scenarios where the system will be required to measure accurate, two-dimensional, relay exchange kinematics. The following subsections present examples of these intended use-cases for the sources of measurement error identified in part one.

Skater point error intended use-cases

Section 4.3 demonstrated that the appearance of images in the National Ice Centre (GBR) multi-camera network is dependent on four characteristics (horizontal banding, lens distortion, ambient lighting, and the network setup), with the appearance of skaters within each image dependent on an additional three characteristics (skating condition, track position, and skating velocity). As the multi-camera network's automated digitisation algorithm (Section 5.2) needs to work independently of these characteristics, the ground truth dataset used to quantify the multi-camera network's measurement error should include a range of these scenarios.

Calibration model error intended use-cases

Section 4.3.2 highlighted that in the National Ice Centre (GBR) multi-camera network, the position of a skater in an image is dependent on the position of the short-track (ranging from 1 to 5) and the skater's trajectory. As the performance of the multi-camera network's calibration model (Section 5.3) will not be constant over the whole image plane, the magnitude of *calibration model error* may be dependent on the position of a skater. For this reason, the ground truth dataset used to quantify the multi-camera network's measurement error should include different short-track positions and a range of skater trajectories.

Out-of-plane error intended use-cases

Section 4.3.2 described how the skating technique differs between the corner and straight in short-track speed skating. These differences in technique may lead to different magnitudes of *out-of-plane error*. For example, as skaters lean towards the centre of rotation during the corner, the *out-of-plane error* may be smaller. Similarly, the magnitude of *out-of-plane error* may be dependent on the skater's stature, as the knee and trunk angle characterise the crouched skating position (Konings et al., 2015). As a result, the ground truth dataset used to quantify the National Ice Centre (GBR) multi-camera network's measurement error should include skating from both the corner and straight for a range of different skater statures.

Sampling interval error intended use-cases

Chapter 2 showed that during the short-track speed skating relay, skating velocities vary from 11.5 $m \cdot s^{-1}$ to 15 $m \cdot s^{-1}$. This range of velocities may propagate to different magnitudes of *rolling shutter error* and *out-of-phase error* for a given sampling interval error or uncertainty. Therefore, the ground truth dataset used to quantify the multi-camera network's measurement accuracy should include various skating velocities.

5.7.3 Manual ground truth

In the Olympic Oval (CAN) multi-camera network, Landry et al. (2013) used a manually created ground truth dataset to quantify the network's measurement error. This dataset included 1163 points, each measured two times, from 15 independent skater trajectories. Landry et al. (2013) defined the system's measurement error as the difference between the manual and automated digitisation methods.

Manual ground truth advantages

A manually created ground truth dataset enables the ground truth dataset to include several of the multi-camera network's intended use-cases. For example, by sampling ground truth points from different cameras, trajectories, and training sessions, the ground truth dataset could include the different appearances of an image and skater reported in Section 4.3.

Manual ground truth disadvantages

A manually created ground truth dataset only allows three of the five sources of measurement error to be quantified: *skater point error*, *rolling shutter error*, and *out-of-phase error*. The other two sources of error, *calibration model error* and *out-of-plane error*, are both included in the manual and automated digitisations' reconstructed pixel coordinates. Furthermore, due to the high-frequency noise expected in the manual digitisation of the ground truth pixel coordinates, the quantification of the three sources of error could be attenuated or amplified.

5.7.4 Automated ground truth

van der Kruk, Schwab, van der Helm, and Veeger (2016) automatically created a ground truth dataset using an optical motion capture system. The dataset was used to quantify error in three inertial measurement unit filter designs that measured the orientation of a skate. Twenty infrared cameras were used to cover a 50 m long-track speed skating straight. The ground truth dataset comprised of the skate's lean angle for two elite long-track speed skaters, at a skating velocity of 10.3 $m \cdot s^{-1}$, for three complete straights.

Automated ground truth advantages

An automatically created ground truth dataset like van der Kruk, Schwab, van der Helm, and Veeger (2016) has a high degree of accuracy as optical motion capture can measure position in three-dimensions to less than a millimetre (Song & Godøy, 2016). Moreover, the ground truth dataset enables all five sources of measurement error to be quantified.

Automated ground truth disadvantages

To create a ground truth dataset that covers both the corner and straight skating conditions requires a high number of optical motion cameras. For example, Kim et al. (2013) used eight cameras alone to cover the period from the 4th to 6th track marking block. This complicated experimental setup does not facilitate the repeated measurements over multiple days to account for the different appearances of an image and skater reported in Section 4.3.

5.7.5 Synthetic ground truth

Hudson (2015) used a synthetic ground truth dataset to quantify errors in a video-based system that automatically measured swimming speed. The synthetic dataset was created by recording a swimming pool scale model – illustrated in Figure 5-12 – from a typical viewpoint of a performance analyst. The ground truth dataset consisted of the checkerboard intersection coordinates in both the pixel and global coordinate systems.

Hudson (2015) proceeded to use the ground truth dataset in a series of computer simulations to investigate different sources of measurement error. For example, he

Item removed for copyright reasons

Figure 5-12. Example view of the swimming pool scale model used by Hudson (2015) to define the ground truth datasets pixel and global coordinate system data. Figure adapted from Hudson (2015).

simulated the effect of automated digitisation uncertainty on a swimmer's reconstructed position by adding randomly sampled pixel uncertainties from a Gaussian distribution to all pixel coordinates in the ground truth dataset. In each iteration (n = 10, 000), the new pixel coordinates were reconstructed into the global coordinate system and compared to the associated ground truth coordinate. Of note for this thesis, Hudson (2015) created the Gaussian distribution by quantifying the digitisation precision in 96 different swimming points. All 96 points were sampled from a 400 m individual race that included four different swimming strokes and a variety of different colour swimming caps, i.e. the system's different intended use-cases.

Synthetic ground truth advantages

A synthetic ground truth dataset of three-dimensional trajectories projected into a camera's pixel coordinate system would allow all sources of error in the National Ice Centre (GBR) multi-camera network to be quantified. Furthermore, by using computer simulations to explore individual sources of measurement error, all intended use-cases could be investigated. For example, by sampling points from different cameras, trajectories, and training sessions, a modelled distribution of digitisation uncertainty could account for the different appearances of an image/ skater reported in Section 4.3.

Synthetic ground truth disadvantages

Like the automatic ground truth dataset, a synthetic ground truth dataset requires the measurement of three-dimensional trajectories using a gold-standard measurement technique. However, unlike the automated ground truth dataset, this data would only need to be collected on a single day as the effect of changes in image/ skater appearance could be simulated.

5.7.6 Section summary

The sources of measurement error in the National Ice Centre (GBR) multi-camera network need to be quantified (1) independently, to allow the multi-camera network's measurement workflow to be empirically informed, and (2) collectively, to determine whether the multi-camera network can measure accurate, two-dimensional, relay exchange kinematics. The quality of this error quantification is dependent on the ground truth dataset's accuracy and validity. Compared to other created ground truth datasets, a synthetic, three-dimensional, ground truth dataset seems most appropriate. The dataset allows the multi-camera network's five sources of measurement error to be quantified and the effect of its intended use-cases to be considered, e.g. the effect of skating condition on *out-of-plane error*.

5.8 Chapter summary & thesis objectives

The second part of this thesis investigates developing the National Ice Centre (GBR) multi-camera network to measure accurate, two-dimensional, relay exchange kinematics. In this chapter, I reviewed the literature with regards to such an investigation. First, by reviewing the four stages of the multi-camera network's measurement workflow, part one of the review identified five sources of measurement error that would determine the multi-camera network's accuracy. Second, by evaluating different approaches for quantifying the multi-camera network’s measurement error, part two of the review concluded that a synthetic, three-dimensional, ground truth dataset would facilitate a more detailed quantification of error by allowing all sources of measurement error, in addition to the multi-camera network's intended use-cases, to be considered. The quantification of these errors, and the creation of the ground truth dataset, form the first six objectives of the thesis.

1. To quantify *rolling shutter error* in the multi-camera network
2. To quantify *out-of-phase error* in the multi-camera network
3. To quantify *calibration model error* in the multi-camera network
4. To create a representative dataset of ground truth kinematics.
5. To quantify *out-of-plane error* in the multi-camera network
6. To quantify *skater point error* in the multi-camera network

Finally, using the measurement workflow empirically informed during objectives one through six, the seventh objective of the thesis is,

7. To quantify *total error* in the multi-camera network

Chapter 6

Rolling shutter error in the multi-camera network

6.1 Introduction

This chapter addresses the first objective of the programme of research: to quantify *rolling shutter error* in the multi-camera network. *Rolling shutter error* describes how errors in the sampling interval within a camera's field-of-view propagate to errors in velocity. As detailed in Section 5.5.1, and demonstrated in Figure 6-1, within-camera sampling interval errors are the result of the image sensor's electronic rolling shutter causing temporal shear.

In the following sections, I describe the investigation into the multi-camera network's *rolling shutter error*. To provide a more detailed insight, the investigation also considers the effect of skating velocity on *rolling shutter error*.

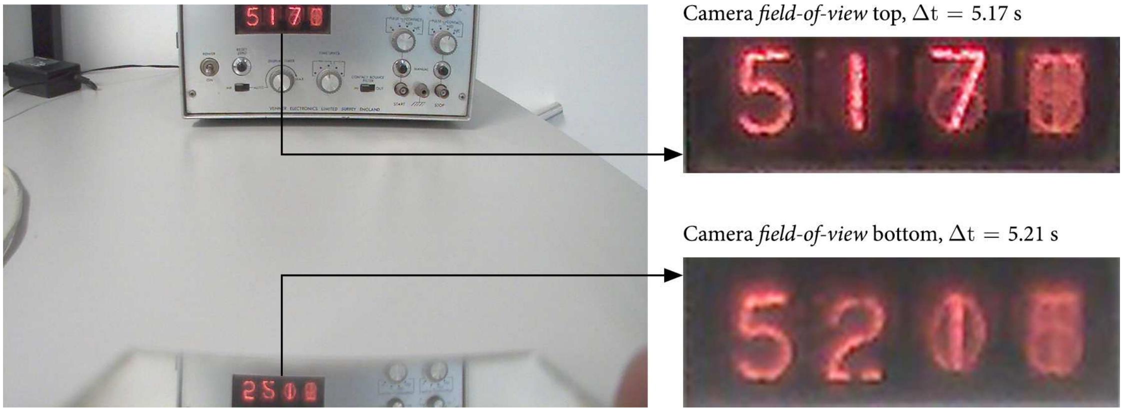

Figure 6-1. Temporal shear in an Axis M3204 camera, i.e. the National Ice Centre (GBR) multi-camera network's camera make and model (Table 4-1). By using a mirror to record an electronic clock at the top and bottom of the camera's field-of-view, the image shows that the difference in the clocks time is equivalent to the camera's sampling interval (0.04 seconds).

6.2 Method

Rolling shutter error was quantified using a computer simulation in MATLAB R2016a (MathWorks, 2016). The simulation fixed all other sources of measurement error in the multi-camera network at zero (Section 5.6).

6.2.1 Ground truth trajectories

Six ground truth trajectories – representing constant velocities from 10 m·s^{-1} to 15 m·s^{-1} (at 1 m·s^{-1} intervals) – were used to simulate the effect of *rolling shutter error* in the multi-camera network. These trajectories covered the range of velocities expected to be measured by the multi-camera network; Chapter 2 reporting velocities of 11.5 m·s^{-1} to 15 m·s^{-1} during elite short-track speed skating relays.

Each ground truth trajectory was projected onto a simulated image plane (1280 x 800 pixels) – in the dominant skating direction – over a five-image period (0.2 seconds). Figure 6-2 demonstrates these projections for the slowest and fastest trajectory. The projections assumed that (1) the ground truth trajectories were sampled at the sampling frequency of the multi-camera network (25 Hz, Table 4-1), and (2) each pixel on the image plane represented 0.01 m x 0.01 m in the global coordinate system. The latter value was determined by measuring, in pixels, an object of known length positioned on the rink surface at the centre of a camera's field-of-view. The simulated image plane's resolution was set at 1280 x 800 pixels, as this replicated the image resolution of the National Ice Centre cameras (Table 4-1).

6.2.2 Simulation

For each ground truth trajectory, I simulated two scenarios. The first scenario simulated an image sensor with a global shutter, i.e. a sensor with a constant sampling interval (Section 5.5.1). The second scenario simulated an image sensor with an electronic rolling shutter, i.e. a sensor where the sampling interval is only constant between scanlines in consecutive images (Section 5.5.1). In both scenarios, the simulation

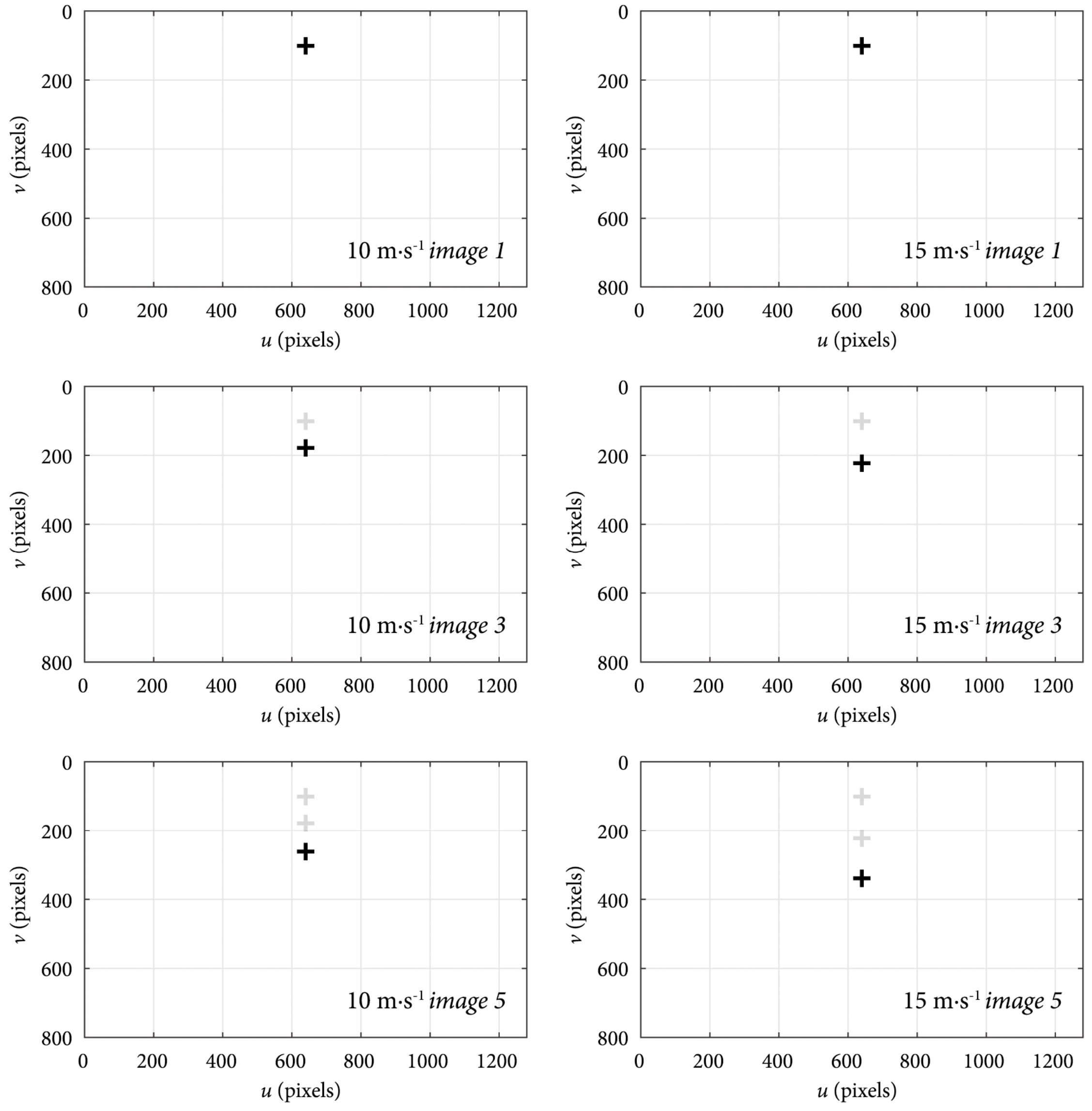

Figure 6-2. The simulation's slowest (10 m·s^{-1}, left) and fastest (15 m·s^{-1}, right) ground truth trajectories projected onto an image plane over a five-image period (0.2 seconds).

reconstructed the ground truth trajectories into the world coordinate system using a linear scaling coefficient. Resultant velocity was then calculated using $Eq.\ 5.24$, with finite difference techniques – detailed in $Eq.\ 5.25$ to $Eq.\ 5.27$ – used to compute velocity in the x- and y-axis.

In the global shutter scenario, the simulation used a sampling interval based on the sampling frequency of the camera to compute velocity. As all cameras at the National Ice Centre capture images at 25 Hz (Table 4-1), this equated to 0.04 seconds. To account for temporal shear (Section 5.5.1), the rolling shutter scenario used a sampling interval based on the position of the skater in successive images. First, $Eq. 5.28$ was used to calculate the readout time in each image, $r_y^{(i)}$, with the skater's v pixel coordinate defining the scanline of interest, y. Second, $Eq. 6.1$ was used to calculate the sampling interval,

$$\Delta t' = \left(r_y^{(i)} + \Delta t\right) - r_y^{(i-1)} \qquad (Eq. 6.1)$$

where i is the current image and Δt is the sampling interval based on camera's sampling frequency (0.04 seconds).

6.2.3 Data analysis

For each ground truth trajectory, the simulation calculated two metrics (1) the sampling interval error, defined as the difference between the global and rolling shutter scenarios' sampling interval, and (2) the *rolling shutter error*, defined as the difference between the global and rolling shutter scenarios' computed skating velocity. Both metrics assumed that the rolling shutter scenario's sampling interval and skating velocity were the true values.

6.3 Results

Figure 6-3 presents the sampling interval error and *rolling shutter error* for each ground truth trajectory. The magnitude of both metrics was dependent on the skating velocity.

6.4 Discussion

This investigation quantified *rolling shutter error* in the multi-camera network, i.e. how within-camera sampling interval error, caused by the image sensor's electronic rolling shutter, propagated to errors in velocity. Overall, the magnitude of *rolling shutter error* exceeded the ± 0.19 $m{\cdot}s^{-1}$ target measurement error. Furthermore, the magnitude of *rolling shutter error* was found to be dependent on the skating velocity; smaller at slower velocities and larger at faster velocities.

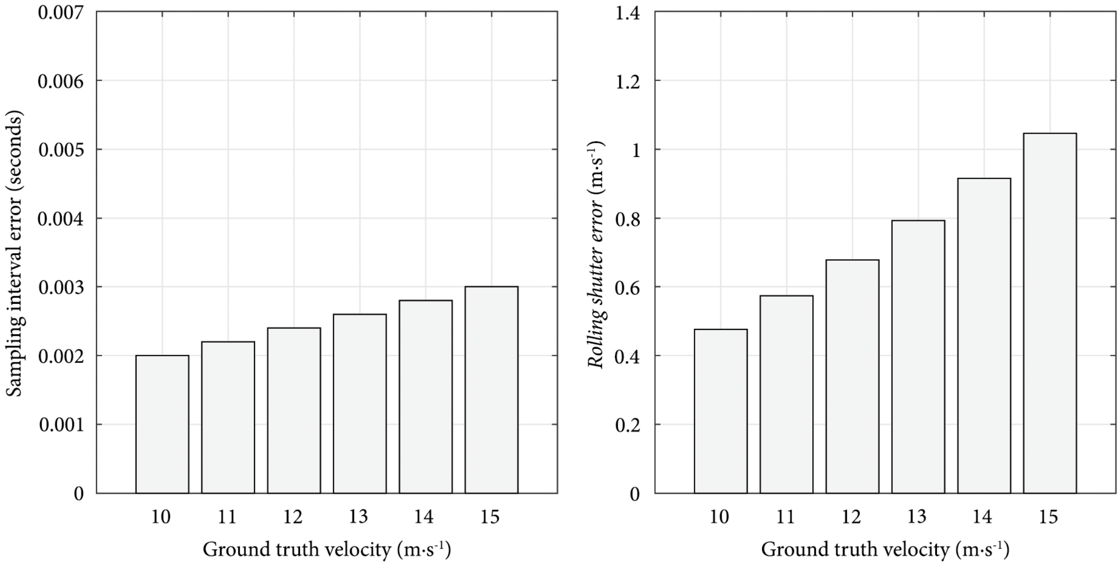

Figure 6-3. Sampling interval error (left) and rolling shutter error (right) in the National Ice Centre (GBR) multi-camera network.

The dependency of *rolling shutter error* on skating velocity is explained by how the multi-camera network's electronic rolling shutters operate. At faster velocities, skaters travel further in consecutive images. As illustrated in Figure 6-2, the outcome of this is a more substantial difference between the skater's v pixel coordinates. As these coordinates define the scanline of interest in $Eq.\,6.1$, when calculating the readout time in $Eq.\,5.28$, faster velocities lead to a greater sampling interval error. For example, in this simulation the sampling interval error increased from 0.002 seconds to 0.003 seconds over the range of ground truth trajectories.

It is important to note, however, that when considering the effect of skater velocity on *rolling shutter error*, the simulation projected the ground truth trajectories in the dominant skating direction, i.e. parallel to the progression of an image's scanline exposure and readout. As shown in Figure 6-4a, this scenario is where *rolling shutter error* is most severe, as the difference between the skater's v pixel coordinates is at its maximum. In contrast, Figure 6-4b shows that in the scenario where a skater moves perpendicular to the progression of an image's scanline exposure and readout, no *rolling shutter error* is present as there is no difference between the skater's v pixels coordinates.

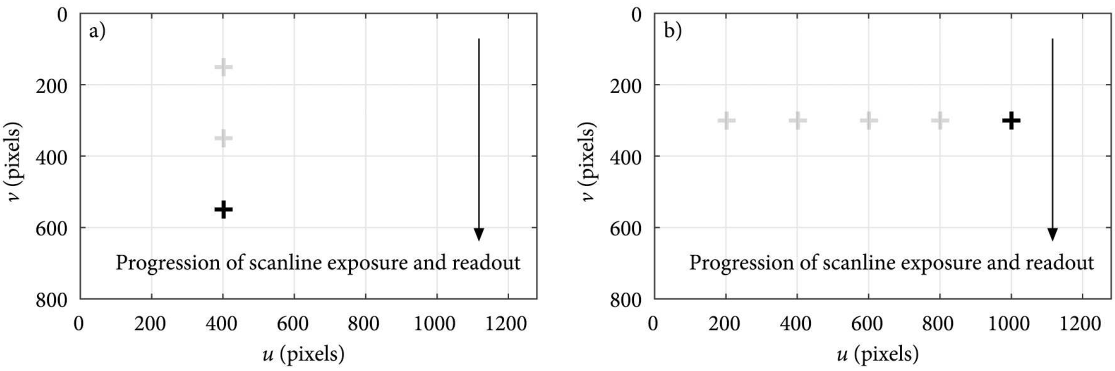

Figure 6-4. The effect of skating direction on *rolling shutter error*. When a skater moves parallel to the progression of the image's scanline exposure and readout (left), *rolling shutter error* is at its greatest as the difference between a skater's v pixel coordinates is at its maximum. In contrast, when a skater moves perpendicular to the progression of the image's scanline exposure and readout (right), *rolling shutter error* is zero as there is no difference between a skater's v pixel coordinates.

In the National Ice Centre (GBR) multi-camera network, the likelihood of the second scenario is small as the dominant direction of skater motion is typically parallel to the progression of an image's scanline exposure and readout. Still, the magnitude of *rolling shutter error* would be less than reported in Section 6.3 if a skater moved predominantly perpendicular to the progression of an image's scanline exposure and readout. As illustrated in Figure 6-5, this is the case for the four cameras that cover the hang phase of the corner skating condition (Section 4.3.2).

Nevertheless, with the predominant skating direction in 22 cameras parallel to the progression of an image's scanline exposure and readout, the multi-camera network's within-camera sampling interval error needs to be reduced. This reduction can be achieved in four ways (1) using cameras with a global shutter, (2) aligning the cameras so that the dominant skating direction is perpendicular to the scanline progression, (3) increasing the cameras sampling frequency, and (4) modelling the electronic rolling shutter's readout time. Solution one negates *rolling shutter error* as global shutters do not cause temporal shear within an image (Section 5.5.1). Solution two reduces *rolling shutter error* by minimising the difference between a skater's v pixels coordinates in consecutive images. Solution three reduces *rolling shutter error* by minimising the

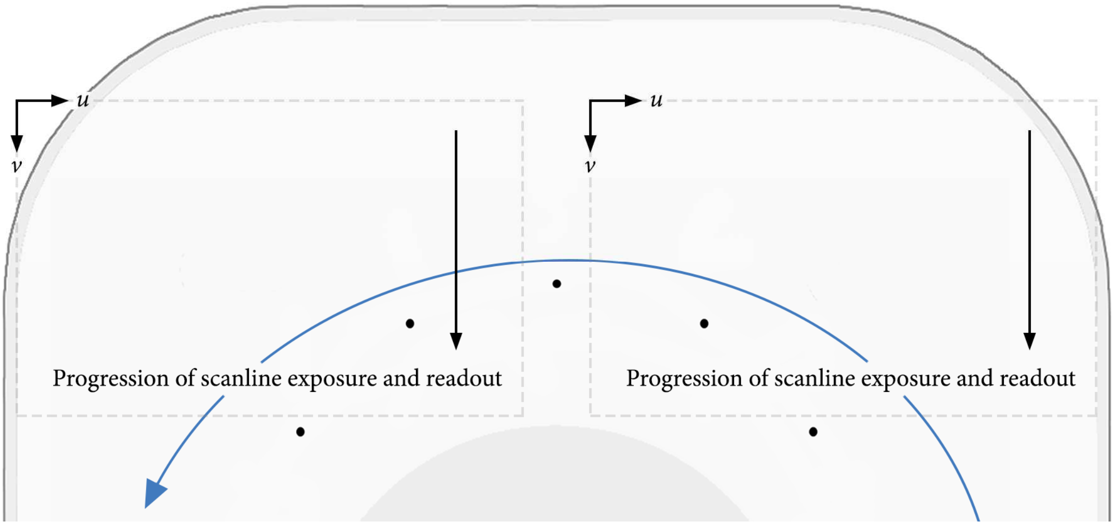

Figure 6-5. The two National Ice Centre (GBR) multi-camera network cameras (in each corner) where skaters (denoted in blue) move predominantly perpendicular to the progression of an image's scanline exposure and readout. As a result, the magnitude of *rolling shutter error* would be less in these cameras.

difference in readout times for a set difference in v pixel coordinates, and solution four corrects *rolling shutter error* by using the calculated readout times to correct the within-camera sampling interval error.

Critically for this thesis, solution one to three are not feasible. The first two are unpractical due to the scale and associated cost of either replacing or realigning the cameras at the National Ice Centre, while the third is unattainable due to the cameras' sampling frequency already being set to the maximum capacity. For this reason, to achieve the ± 0.19 $m \cdot s^{-1}$ target measurement error, an electronic rolling shutter model should be used to correct the *rolling shutter error*.

6.4.1 Limitations

The simulation used in this investigation assumed that each pixel represented 0.01 m x 0.01 m in the global coordinate system (Section 6.2.1). Therefore, as illustrated in Figure 6-6, the projection of a straight-line trajectory in the global coordinate system appeared as a straight-line trajectory in the pixel coordinate system. However, as reported in Section 4.3.1, this is not the case in the National Ice Centre (GBR) multi-camera

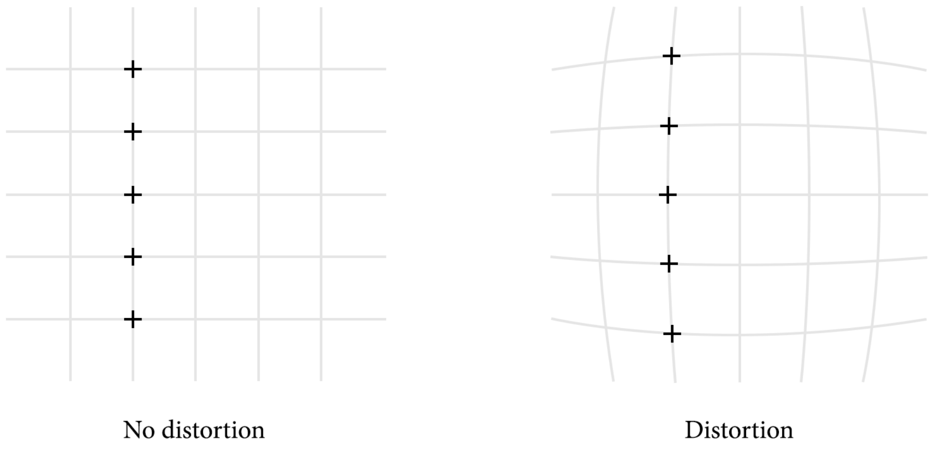

Figure 6-6. The appearance of a global coordinate system straight-line trajectory projected into a pixel coordinate system with no lens distortion (left) and lens distortion (right).

network. Instead, straight-line trajectories appear curved in the pixel coordinate system due to lens distortion (Figure 6-6). This distortion – caused by the image magnification decreasing as the distance from the optical axis increases – means that at the periphery of an image, more of the global coordinate system fits into a single pixel's area. Subsequently, this investigation may have overestimated the multi-camera network's *rolling shutter error* in the image periphery, as the difference between the projected skater's v pixel coordinates would have been smaller than simulated. Nevertheless, as the simulation's results would have been similar towards the centre of the image, i.e. where distortion is negligible, the findings still demonstrate the necessity for using an electronic rolling shutter model to correct the within-camera sampling interval error.

6.5 Chapter summary

This chapter used a computer simulation to address the first objective of the programme of research: to quantify *rolling shutter error* in the multi-camera network. More specifically, how within-camera sampling interval error – caused by temporal shear from the image sensor's electronic rolling shutter – propagated to errors in velocity. The simulation showed that the multi-camera network's *rolling shutter error* exceeded the ± 0.19 $m \cdot s^{-1}$ target measurement error. Moreover, the magnitude of this *rolling shutter* *error*, which ranged from 0.48 $m \cdot s^{-1}$ to 1.04 $m \cdot s^{-1}$, was dependent on the current skating velocity. For these reasons, the chapter concluded that the multi-camera network should minimise *rolling shutter error* by using an electronic rolling shutter model to correct within-camera sampling interval errors.

Chapter 7

Out-of-phase error in the multi-camera network

7.1 Introduction

Chapter 6 showed that the multi-camera network's *rolling shutter error* exceeded the ± 0.19 m·s^{-1} target measurement error. Within-camera sampling interval errors – dependent on the skating velocity – leading to *rolling shutter errors* ranging from 0.48 m·s^{-1} to 1.05 m·s^{-1}. For this reason, the chapter concluded that multi-camera network should minimise *rolling shutter error* by using an electronic rolling shutter model to correct within-camera sampling interval errors. In this chapter, I continue to explore sampling interval errors in the multi-camera network by addressing the second objective of the programme of research: to quantify *out-of-phase error* in the multi-camera network. *Out-of-phase error* describes how uncertainty in the sampling interval between two cameras' field-of-view propagates to errors in velocity. As detailed in Section 5.5.1, between-camera sampling interval uncertainties are caused by the multi-camera network's camera shutters being out-of-phase by up-to ± 0.02 seconds. In the following sections, I describe the investigation into the multi-camera network's *out-of-phase error*. To provide a more comprehensive insight, the investigation considers the effect of skating velocity on *out-of-phase error*.

7.2 Method

Out-of-phase error was quantified using a computer simulation in MATLAB R2016a (MathWorks, 2016). The simulation fixed all other sources of measurement error in the multi-camera network at zero (Section 5.6).

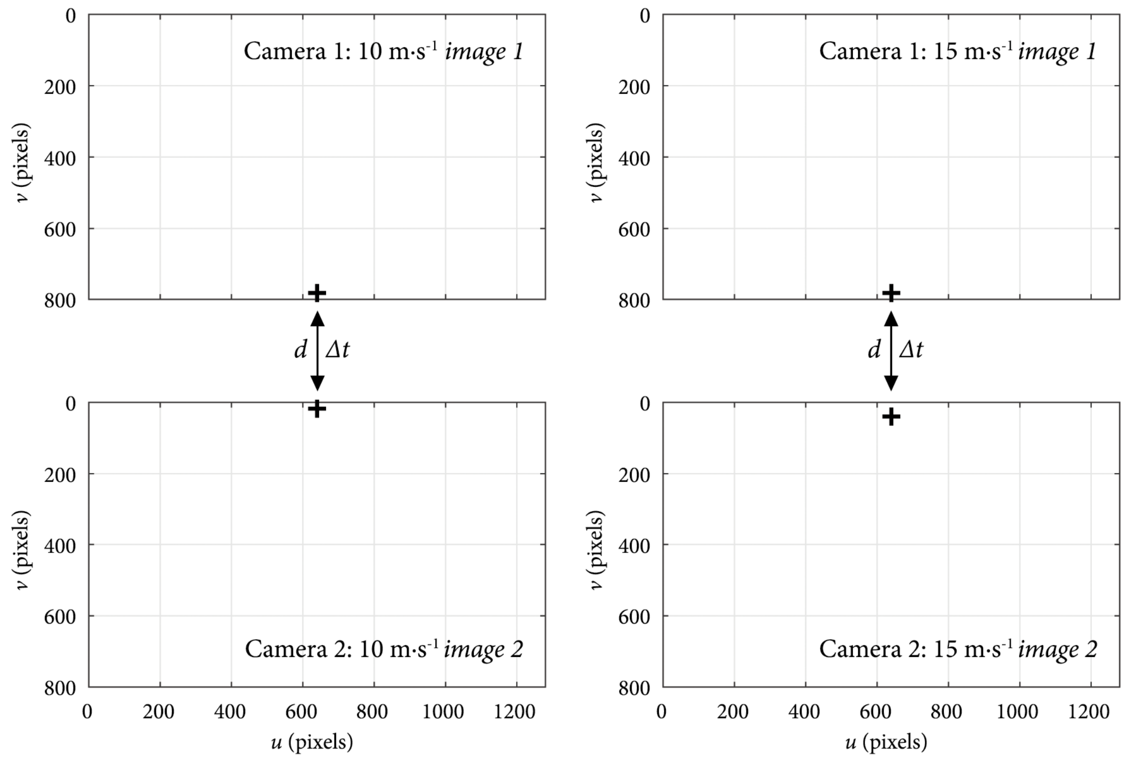

Figure 7-1. The slowest (10 m·s^{-1}, left) and fastest (15 m·s^{-1}, right) ground truth trajectories projected between two, non-overlapping, simulated image planes (Camera 1 top, Camera 2 bottom) over a two-image period. While the skater distance, *d,* is known, the sampling interval, Δt, between *image 1* (top) and *image 2* (bottom) is not, due to the camera shutters being out-of-phase by up-to ± 0.02 seconds.

7.2.1 Ground truth trajectories

Six ground truth trajectories – representing constant velocities from 10 m·s^{-1} to 15 m·s^{-1} – were used to simulate the effect of *out-of-phase error* in the multi-camera network. As described in Section 6.2.1, these trajectories represented the expected range of velocities during elite short-track speed skating relays. The simulation projected each ground truth trajectory between two, non-overlapping, simulated image planes (1280 x 800 pixels) – in the dominant skating direction – over a two-image period (0.08 seconds). Figure 7-1 illustrates these projections for the slowest (10 m·s^{-1}) and fastest (15 m·s^{-1}) trajectory. As in the *rolling shutter error* simulation (Section 6.2.1), the projections assumed that (1) the ground truth trajectories were sampled at 25 Hz, and (2) each pixel represented 0.01 m x 0.01 m in the global coordinate system. The simulated image planes' resolution was set at 1280 x 800 pixels, as this replicated the image resolution of the cameras at the National Ice Centre (Table 4-1).

7.2.2 Simulation

For each ground truth trajectory, I simulated two scenarios. The first scenario simulated two cameras' shutters being in-phase. The second scenario simulated two cameras' shutters being out-of-phase. In both scenarios, the simulation reconstructed the ground truth trajectory into the global coordinate system using a linear scaling coefficient. Resultant velocity was then calculated using $Eq. 5.24$, with the backward difference used to compute velocity in the x- and y-axis ($Eq. 5.27$).

In the in-phase scenario, the simulation used a sampling interval based on the sampling frequency of the camera to compute velocity. As all cameras at the National Ice Centre capture images at 25 Hz (Table 4-1), this equated to 0.04 seconds. In the out-of-phase scenario, the simulation used all possible between-camera sampling intervals (at 0.001-second intervals). Based on the in-phase sampling interval, and camera shutters being out-of-phase by up-to ± 0.02 seconds (Section 4.2), this equated to 0.02 seconds to 0.06 seconds.

7.2.3 Data analysis

For each ground truth trajectory, the simulation calculated two metrics for each simulated sampling interval (1) the sampling interval error, defined as the difference between the in- and out-of-phase scenarios' sampling interval, and (2) the *out-of-phase error*, defined as the difference between the in- and out-of-phase scenarios' computed velocity. Both metrics assumed that the out-of-phase scenario's sampling interval and velocity were the true values.

7.3 Results

Figure 7-2 shows each ground truth trajectory's sampling interval error and *out-of-phase*

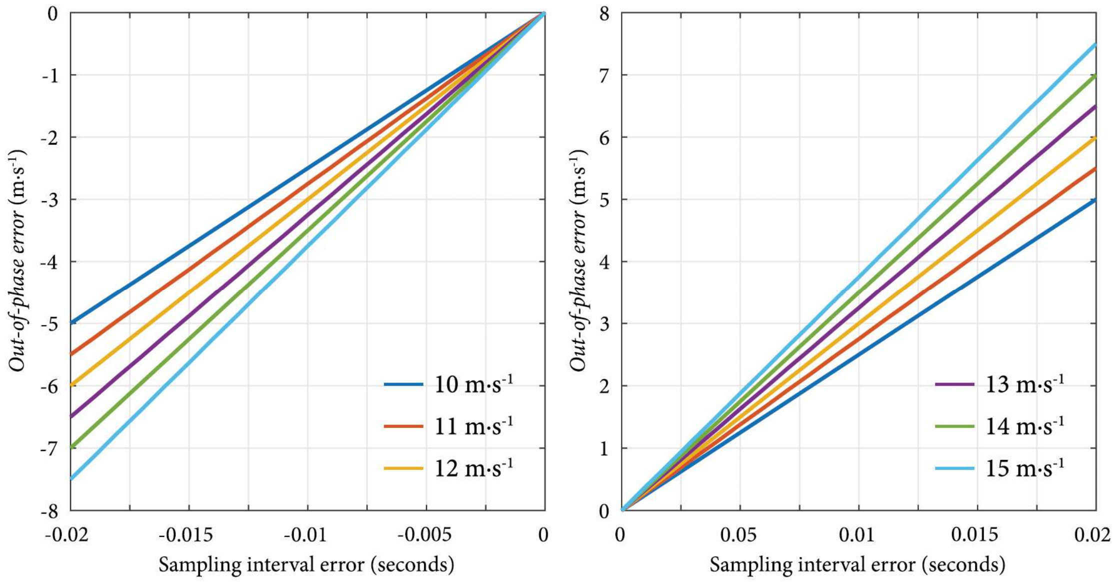

Figure 7-2. *Out-of-phase error* in the National Ice Centre (GBR) multi-camera network.

error for all out-of-phase scenarios. The absolute magnitude of o*ut-of-phase error* increased with the sampling interval error and the skating velocity.

7.4 Discussion

This investigation quantified *out-of-phase error* in the multi-camera network, i.e. how uncertainty in the sampling interval between two cameras’ field-of-view, caused by the multi-camera network’s camera shutters being out-of-phase by up-to ± 0.02 seconds, propagated to errors in velocity. Overall, the magnitude of *out-of-phase error* exceeded the ± 0.19 m·s^{-1} target measurement error. Moreover, the absolute magnitude of *out-of-phase error* was found to be dependent on two factors (1) the sampling interval uncertainty; smaller at lesser uncertainties and larger at greater uncertainties, and (2) the skating velocity; smaller at slower velocities and larger at faster velocities.

The computation of velocity – specifically the backward difference method used in this investigation – explains the dependency of *out-of-phase error* on both the sampling interval uncertainty and skating velocity. Sampling interval uncertainty manifests in $Eq. 5.27$’s denominator, as Δt represents the sampling interval, whereas skating velocity manifests in the equation's numerator, as faster velocities lead to larger differences between the current (s_i) and previous (s_{i-1}) skater position. Here, it is important to note that only the absolute magnitude of *out-of-phase error* is dependent on the skating velocity. Skating velocity does not affect the magnitude of *out-of-phase error* when expressed as a percentage of the ground truth velocity. For example, a sampling interval uncertainty of ± 0.02 seconds leads to relative *out-of-phase errors* of ± 50% for all six ground truth trajectories.

As all absolute *out-of-phase errors* exceed the ± 0.19 m·s^{-1} target measurement error, the multi-camera network needs to minimise between-camera sampling interval uncertainties. Payton (2008) describes two-ways to do this: generator locking and using an event marker such as a strobe light. The former uses a reference signal to ensure that all camera shutters are in-phase. The latter uses the event marker – which can be seen by all cameras – to determine the sampling interval uncertainty. Unfortunately, neither solution is feasible in the multi-camera network as the Axis M3204 cameras do not support generator locking and there isn't a position on the rink surface that all cameras can see. Furthermore, regardless of the event marker position, this method only allows cameras to be in-phase to the nearest half-an-image (i.e. 0.02 seconds). As reported in Section 7.3, a 0.02-second sampling interval error leads to relative *out-of-phase errors* of ± 50%. Therefore, to meet the ± 0.19 m·s^{-1} target measurement error, the results of this investigation suggest that the multi-camera network should only calculate two-dimensional relay exchange kinematics within a camera's field-of-view.

7.5 Chapter summary

This chapter used a computer simulation to address the second objective of the programme of research: to quantify *out-of-phase error* in the multi-camera network. More specifically, how between-camera sampling interval uncertainty – caused by two cameras shutters being out-of-phase by up-to ± 0.02 seconds – propagated to errors in velocity. The simulation showed that the multi-camera network's *out-of-phase error* exceeded the ± 0.19 $m \cdot s^{-1}$ target measurement error. Moreover, the absolute magnitude of *out-of-phase error*, which ranged from -7.5 $m \cdot s^{-1}$ to 7.5 $m \cdot s^{-1}$, was dependent on the sampling interval uncertainty and the current skating velocity. As the multi-camera network cannot minimise between-camera sampling interval uncertainties, the chapter concluded that *out-of-phase error* should be negated in the multi-camera network by only calculating two-dimensional relay exchange kinematics within each camera's field-of-view.

Chapter 8

Calibration model error in the multi-camera network

8.1 Introduction

This chapter addresses the third objective of the programme of research: to quantify *calibration model error* in the multi-camera network. *Calibration model error* describes how incorrect relationships between the pixel and global coordinate systems propagate to errors in position and velocity within (intra-) and between (inter-) cameras' field-of-view. However, as Chapter 7 concluded that the multi-camera network should only calculate relay exchange kinematics within each camera's field-of-view, to negate *out-of-phase error*, inter-camera *calibration model error* is only concerned with how reconstructed positions from different cameras align in the global coordinate system.

In the following sections, I describe the calibration of the multi-camera network and the investigation into its intra- and inter-camera *calibration model error*. To provide a more detailed insight, the investigation considers the effect of skating condition and skating velocity on intra- and inter-camera *calibration model error*.

8.2 Multi-camera network calibration

The National Ice Centre (GBR) multi-camera network was calibrated using the nonlinear calibration procedure described in Section 5.3.2. This method was deemed most suitable for correcting the lens distortion documented in Section 4.3.1, outside the areas covered by the calibration's control points. The following subsections describe the details of the calibration procedure specific to the multi-camera network.

8.2.1 Camera settings

As reported in Table 4-1, all cameras had a sampling frequency of 25 Hz, an image resolution of 1280 x 800 pixels, and an exposure time of 0.004 seconds. In addition to these settings, each camera's field-of-view was maximised and focused at 1 m above the rink surface. A height of 1 m was selected, as this represented the estimated height of a fiducial marker during the crouched skating position. Chun (2001), Park, Yun, Lee and Baik (1998), and van der Kruk, Veeger, van der Helm and Schwab (2017) showing that skaters' whole body centre-of-mass range from 0.4 m to 0.8 m above the rink surface. To focus each camera, a black and white checkerboard pattern – fixed on a tripod at 1 m above the rink surface – was placed in the camera's field-of-view. The camera was deemed to be in focus when the contrast between the checkerboard's black and white tiles was sharpest.

8.2.2 Calibration object

Images of a planar checkerboard pattern (8 x 8 squares, each 0.03 m x 0.03 m) were collected on an elevated work platform – located 2 m underneath each camera – as described in Section 5.3.2. Using an elevated work platform ensured that the projection of the checkerboard's intersection pixel coordinates on the image plane covered the image sensor sufficiently for accurate calibration (Wang, 2013). As reported in Section 5.3.2 this insufficient coverage of the image sensor was why Landry et al. (2013) disregarded the nonlinear calibration procedure in the Olympic Oval (CAN) multi-camera network. Figure 8-1 shows the calibration object as seen on the rink surface and the elevated work platform.

8.2.3 Intrinsic model parameters

Check2D (Centre for Sports Engineering Research, 2013) was used to calculate each camera's focal length, principal point, pixel scale factor and three-parameter radial distortion model. The intrinsic model's goodness of fit was evaluated using the RMS reprojection error. As outlined in Section 5.3.2, the reprojection error describes the sum

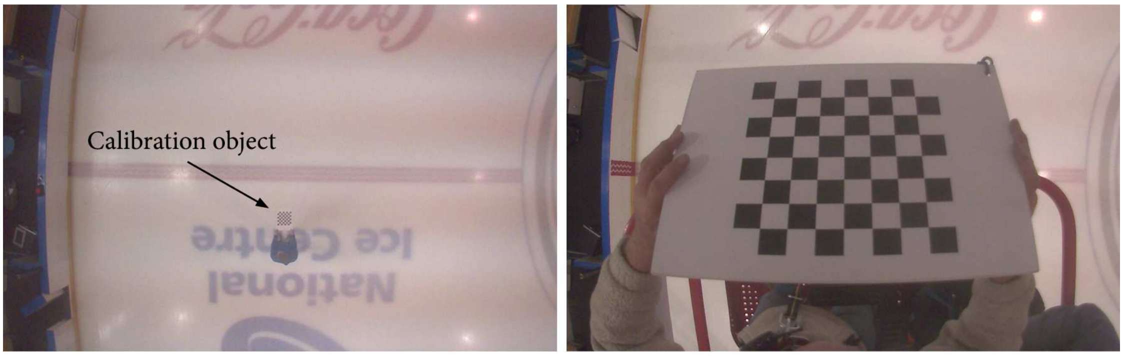

Figure 8-1. The calibration object as seen on the rink surface (left) and elevated work platform (right) at the National Ice Centre. Using the elevated work platform ensured that the projection of the checkerboard intersections on the image plane sufficiently covered the image sensor.

of the distances between the extracted and projected intersections of the image's checkerboard. Overall, the multi-camera network's mean camera RMS reprojection error was 0.26 ± 0.03 pixels. This error was less than the 0.33 ± 0.04 pixels reported by Zhang (1999) in his real-world example and similar to the 0.22 pixels in the Olympic Oval (CAN) multi-camera network (Landry et al., 2013).

8.2.4 Extrinsic model parameters

Bouguet's (2015) *Camera Calibration Toolbox for MATLAB* was used to calculate each camera's rotation and translation matrix. The toolbox required the intrinsic model parameters – determined in Section 8.2.3 – and four control points, i.e. positions where both pixel and global coordinates are known. Figure 8-2 shows the typical position of these control points in a camera's field-of-view.

Check2D (Centre for Sports Engineering Research, 2013) was used to manually digitise the centre of each control point on five occasions separated by a day. The mean of these five trials defined each control point's pixel coordinates and mitigated the random error expected in the digitisation process (Payton, 2008). A reference grid constructed on the rink surface was used to calculate each control point's position in the global coordinate system. The reference grid – illustrated, in part, in Figure 8-2 – consisted of two vertical

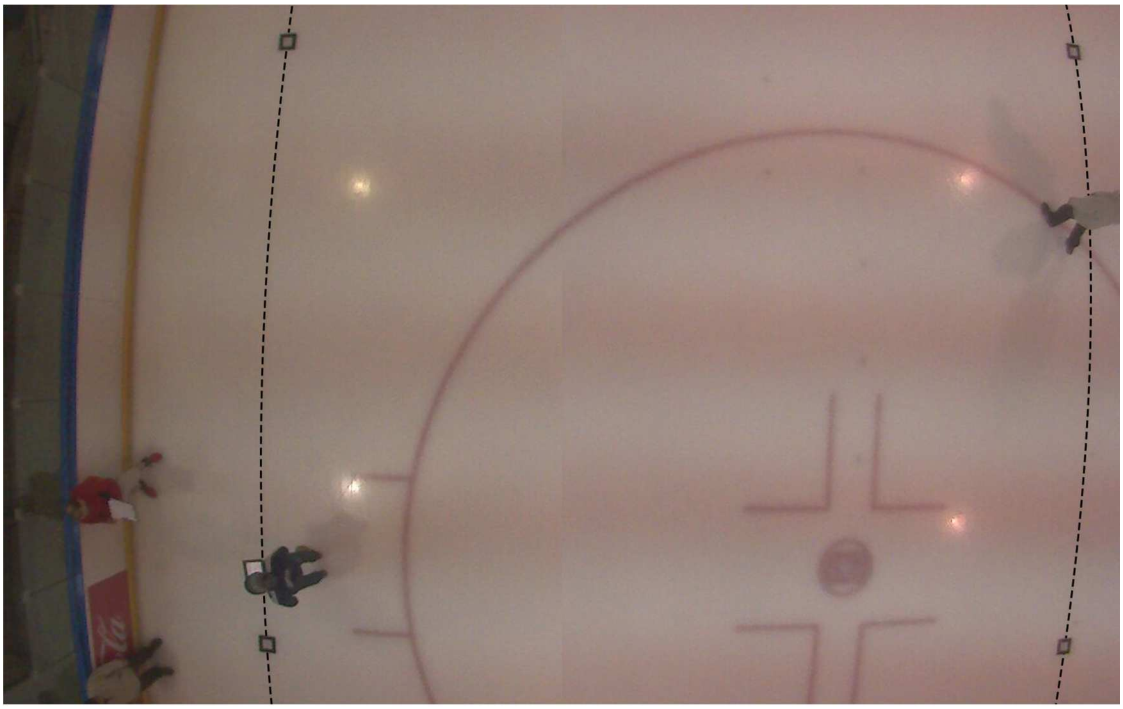

Figure 8-2. The typical position of a camera’s four control points in the National Ice Centre (GBR) multi-camera network. The dashed line denotes the reference grid used to define each control points position in the global coordinate system.

axis tape measures, aligned on the inside edge of the ice hockey rink’s goal lines, and twelve horizontal axis tape measures.

8.3 Method

The Faculty of Health & Wellbeing Research Ethics Committee (Sheffield Hallam University, UK) approved the *calibration model error* investigation.

8.3.1 Intra-camera calibration model error

The investigation quantified intra-camera *calibration model error* by filming a planar checkerboard pattern (4 x 4 squares, each 0.3 m x 0.3 m) sliding over the rink surface in a range of positions and orientations that covered each camera's field-of-view. An example of the planar checkerboard, as seen in the multi-camera network, is shown in Figure 8-3. By assuming that the checkerboard’s ground truth distances (0.0424 m and 0.6 m) were covered in consecutive images (Δt = 0.04 seconds), the board’s geometry

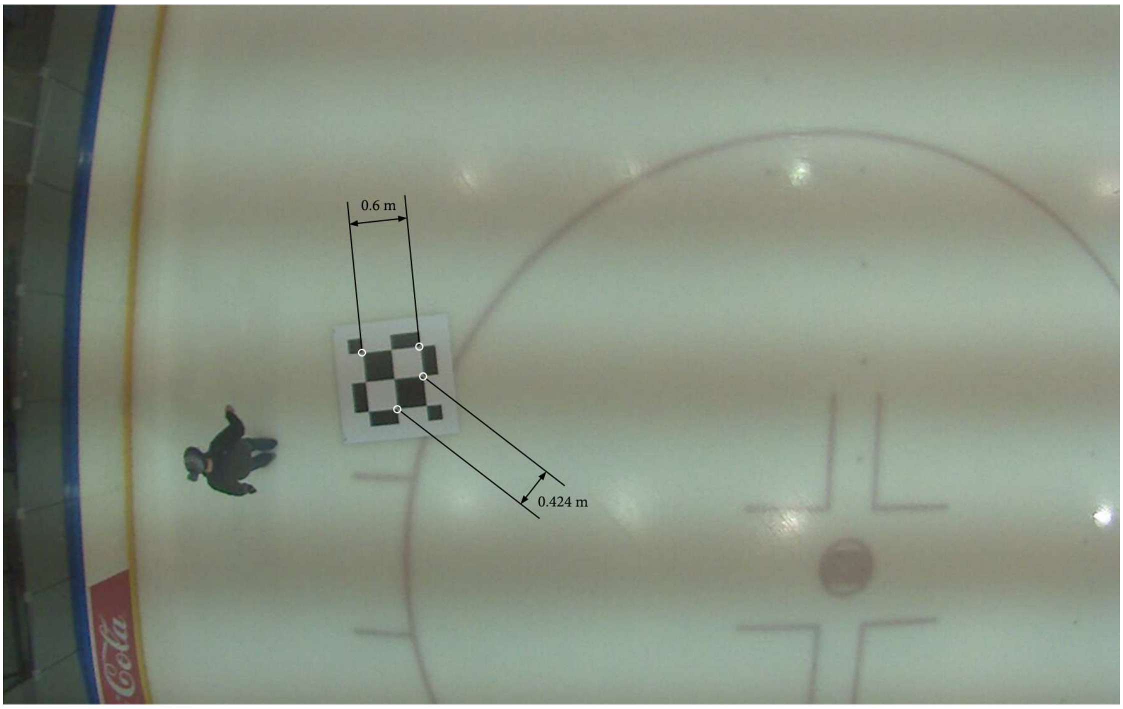

Figure 8-3. The intra-camera *calibration model error* planar checkerboard. By assuming that the checkerboard's ground truth distances (0.0424 m and 0.6 m) were covered in consecutive images (Δt = 0.04 seconds), the board's geometry defined two ground truth velocities (10.6 m·s^{-1} and 15 m·s^{-1}).

defined two ground truth velocities (10.6 m·s^{-1} and 15 m·s^{-1}). Collectively, these ground truth velocities covered the range of velocities expected during short-track speed skating relays; Chapter 2 observing skating velocities ranging from 11.51 m·s^{-1} to 15 m·s^{-1}.

Data analysis

For each camera in the multi-camera network, Emgu CV-3.0.0 (Emgu, 2015) was used to automatically extract the pixel coordinates of the checkerboard's intersections in each image of the checkerboard. The analysis removed false positive checkerboard intersection extractions – illustrated in Figure 8-4 –if the image's maximum reprojection error was higher than the camera's mean maximum reprojection error plus two standard deviations.

For each image in a camera's checkerboard image dataset, the extracted pixel coordinates were reconstructed into the global coordinate system – as described in Section 5.3.2 – using the relevant camera-rink plane calibration model constructed in

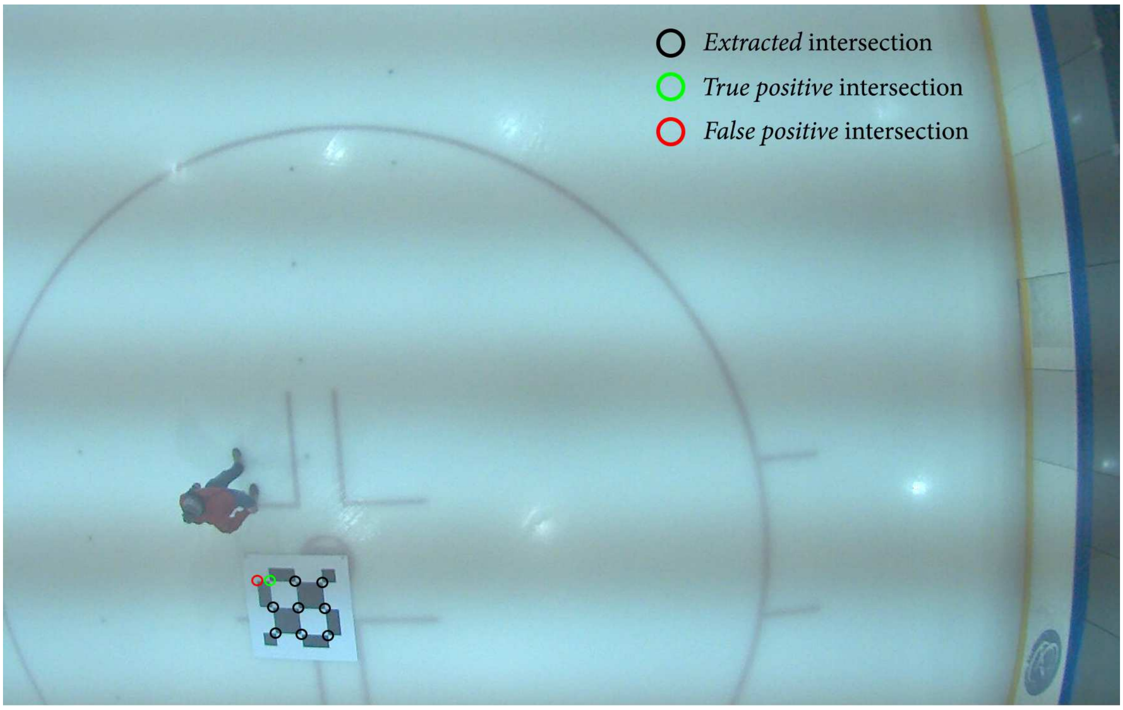

Figure 8-4. *False positive* intersection extraction in the National Ice Centre (GBR) multi-camera network. In this example, Emgu CV-3.0.0 should have extracted the *true positive* intersection.

Section 8.2. For each pair of global coordinates, resultant velocity was then calculated using $Eq. 5.24$, with the backward difference method used to compute velocity in both the x- and y-axis ($Eq. 5.25$). As the investigation mitigated *rolling shutter error* by sliding the checkerboard at less than 0.5 m·s^{-1}, $Eq. 5.25$ used a 0.04-second sampling interval. The analysis defined intra-camera *calibration model error* as the difference between the ground truth and computed velocity.

8.3.2 Inter-camera calibration model error

The investigation quantified inter-camera *calibration model error* by identifying positions on the rink surface seen in two-or-more cameras' field-of-view. These positions – termed static reference points – included control points used in the multi-camera network's extrinsic calibration (Section 8.2.4) and the short-track's track marking blocks (Section 4.3.2). The static nature of these positions negated *rolling shutter error* in the analysis.

Data analysis

Check2D (Centre for Sports Engineering Research, 2013) was used to manually digitise the point centre of each static reference point on five occasions separated by a day. The investigation used the mean of these five trials to define each reference point's pixel coordinates, as this minimised the random errors expected in the digitisation procedure (Payton, 2008). Each mean pixel coordinate was reconstructed into the global coordinate system – as described in Section 5.3.2 – using the relevant camera-rink plane calibration model constructed in Section 8.2. For each position seen in two cameras' field-of-view, the analysis defined inter-camera *calibration model error* as the difference between the reconstructed positions in the x- and y-axis.

8.3.3 Skating condition

The investigation calculated both intra- and inter-camera *calibration model error* for the two skating conditions described in Section 4.3.2. The analysis classified cameras as covering either the corner or straight based on their rink surface field-of-view. The field-of-view was calculated by reconstructing the image's perimeter pixel coordinates into the global coordinate system – as described in Section 5.3.2 – using the camera-rink plane calibration models constructed in Section 8.2. Figure 8-5 illustrates these rink surface field-of-views and the final classification of skating condition cameras. In total, the corner skating condition had 16 cameras and the straight skating condition had 10 cameras. In the inter-camera *calibration model error* analysis, in the scenario where the multi-camera network saw a static reference point in both corner and straight cameras' field-of-view, the investigation included the magnitude of inter-camera *calibration model* error in both skating conditions' statistics.

8.3.4 Statistical analysis

SPSS 24 (IBM, 2016) was used to calculate intra- and inter-camera *calibration model error* descriptive statistics (median, first quartile, third quartile, minimum, and

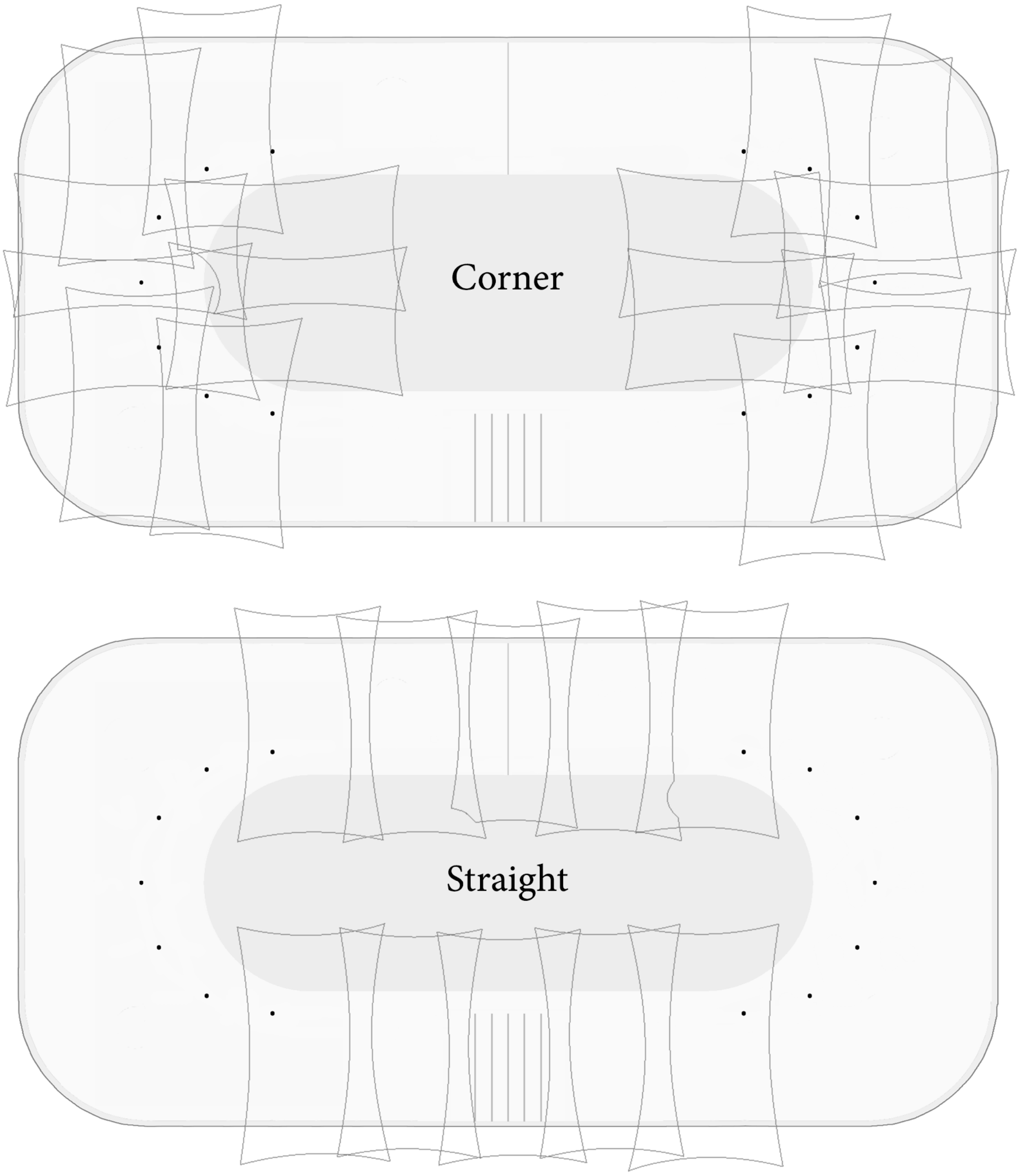

Figure 8-5. Skating condition camera classification in the multi-camera network.

maximum error) for each ground truth velocity in the corner and straight skating conditions. The analysis calculated the median and the first and third quartiles, instead of the arithmetic mean and standard deviation, as these statistics are more representative of systematic and random error in non-normally distributed datasets.

The effect of skating condition on intra- and inter-camera *calibration model error* was determined using a Mann Whitney *U*-test. Data were treated as non-parametric, as the underlying assumptions of parametric statistical tests, i.e. normality and homogeneity of variance, were violated. Similarly, for both skating conditions, a Mann Whitney U-test was used to determine the effect of skating velocity on intra-camera *calibration model error*. Effect sizes were also calculated using Pearson's correlation coefficient, r, in accordance with Field (2009),

$$r = \frac{z}{\sqrt{n}} \qquad (Eq. 8.1)$$

where z is the standardised test statistic. The magnitudes of the correlations were interpreted using Cohen's thresholds; where < 0.1, is trivial; 0.1–0.3, small; > 0.3–0.5, moderate; and > 0.5, large (Cohen, 1988).

8.4 Results

8.4.1 Intra-camera calibration model error

A total of 59,836 images of the checkerboard were captured using the National Ice Centre (GBR) multi-camera network. This image set reduced to 57,470 images after false positives were removed (Section 8.3.1). Table 8-1 reports the descriptive statistics for each skating condition and ground truth velocity, with an example checkerboard

Table 8-1. Intra-camera *calibration model error* descriptive statistics.

Condition	Statistic	Ground truth 10.6 m·s^{-1}	Ground truth 15 m·s^{-1}
Corner	Median	-0.014	-0.027
	Q_1, Q_3	-0.052, 0.023	-0.076, 0.019
	Minimum	-0.385	-0.364
	Maximum	0.358	0.423
Straight	Median	-0.014	-0.028
	Q_1, Q_3	-0.051, 0.022	-0.074, 0.016
	Minimum	-0.303	-0.369
	Maximum	0.296	0.244

Notes: Q_1 and Q_3 = first and third quartiles. Resultant velocity measured in m·s^{-1}.

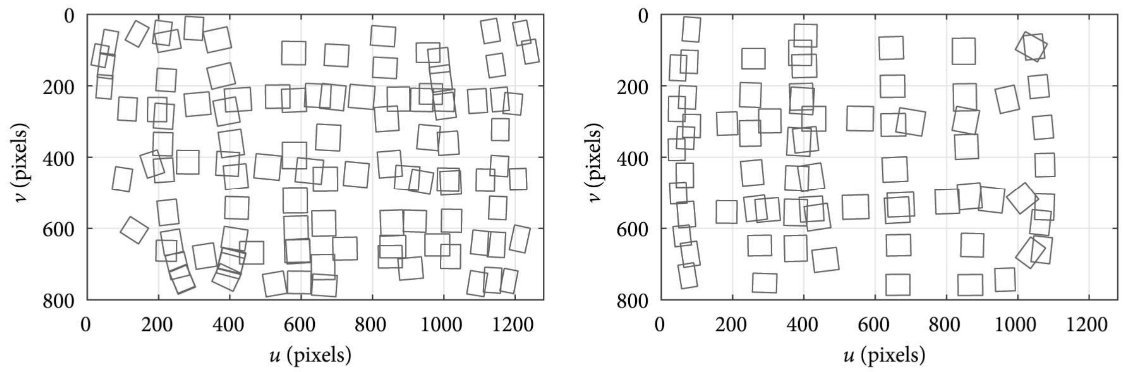

Figure 8-6. Example intra-camera *calibration model error* checkerboard coverage for a National Ice Centre (GBR) multi-camera network camera.

coverage for a corner and straight camera field-of-view presented in Figure 8-6. Overall, the multi-camera network had a RMS intra-camera calibration model error of 0.06 m·s^{-1}.

Skating condition

There was a significant difference in intra-camera *calibration model error* between the corner and straight skating conditions, U = 7.60 x 10^{10}, p = 0.000, r = 0.00 (a trivial effect). The median velocity error was smaller during the corner (-0.0189 m·s^{-1}) than the straight (-0.0194 m·s^{-1}).

Skating velocity

There was a significant difference in intra-camera *calibration model error* between the two skating velocities in both corner (U = 2.67 x 10^{10}, p = 0.000, r = -0.11, i.e. a small effect) and straight (U = 9.99 x 10^{9}, p = 0.000, r = -0.11, i.e. a small effect) skating conditions.

8.4.2 Inter-camera calibration model error

A total of 119 pairs of static reference points were identified in the multi-camera network's field-of-view. The points consisted of 75 track marking blocks and 41 control points. Table 8-2 reports the descriptive statistics for each skating condition, with both corner and straight skating conditions' static reference points shown in Figure 8-7.

Overall, the multi-camera network had a RMS inter-camera *calibration model error* of 0.01 m and 0.02 m in the x- and y-axis, respectively.

Table 8-2. Inter-camera *calibration model error* descriptive statistics.

Statistic	X position error		Y position error	
	Corner	Straight	Corner	Straight
Median	0.01	0.01	0.01	0.02
Q_1, Q_3	0.00, 0.02	0.00, 0.01	0.01, 0.03	0.01, 0.02
Minimum	0.00	0.00	0.00	0.01
Maximum	0.03	0.02	0.07	0.02

Notes: Q_1 and Q_3 = first and third quartiles. Resultant velocity measured in m·s^{-1}.

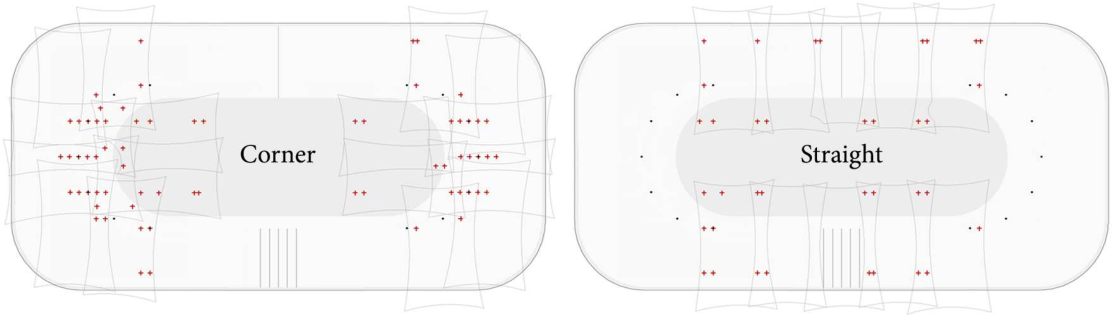

Figure 8-7. The inter-camera *calibration model error* static reference points in the National Ice Centre (GBR) multi-camera network.

Skating condition

There was no significant difference in inter-camera *calibration model error* between the corner and straight skating conditions in the x- (U = 1.31 x 10^3, p = 0.088, r = -0.15, i.e. a small effect) and y- (U = 1.64 x 10^3, p = 0.996, r = 0.00, i.e. a trivial effect) axis.

8.5 Discussion

This investigation quantified the multi-camera network's *calibration model error*. More specifically, how incorrect relationships between the pixel and global coordinate systems propagated to (1) errors in position and velocity within (intra-) cameras' field-of-view, and (2) errors in position between (inter-) cameras' field-of-view. To provide a more detailed insight, the investigation considered the effect of skating condition and skating velocity.

8.5.1 Intra-camera calibration model error

Overall, the multi-camera network's intra-camera *calibration model error* was within the ± 0.19 $m \cdot s^{-1}$ target measurement error and significantly less than the Olympic Oval (CAN) multi-camera network's ± 0.48 $m \cdot s^{-1}$ intra-camera *calibration model error*. As both multi-camera networks had similar reprojection errors (Section 8.2.3), this sizeable reduction in intra-camera *calibration model error* was attributed to the National Ice Centre (GBR) multi-camera network having a superior spatial resolution, i.e. greater number of pixels per metre. As documented in Section 4.2, the Olympic Oval (CAN) multi-camera network uses four cameras to capture the short-track (each at a resolution of 659 x 493 pixels). In contrast, the National Ice Centre multi-camera network uses 26 cameras to capture the short-track (each at a resolution of 1280 x 800 pixels). Consequently, for a given pixel error, error in the reconstructed distance – and thus velocity – is larger in the Olympic Oval (CAN) multi-camera network.

Effect of skating condition on intra-camera calibration model error

Intra-camera *calibration model error* was effectively invariant to the skating condition. Although the velocity error was significantly larger in the straight skating condition, the size of the effect was trivial; the difference between the median intra-camera *calibration model errors* (0.0005 $m \cdot s^{-1}$) equivalent to ± 0.3 % of the ± 0.19 $m \cdot s^{-1}$ target measurement error. This finding is unsurprising considering that the nonlinear calibration procedure described in Section 8.2 was the same for all cameras in the multi-camera network. The observed significant difference was likely due to the large sample size (n = 804,540) increasing the statistical power of the Mann-Whitney test, i.e. the ability of the test to detect an effect between the two skating conditions. Hopkins, Marshall, Batterham, &

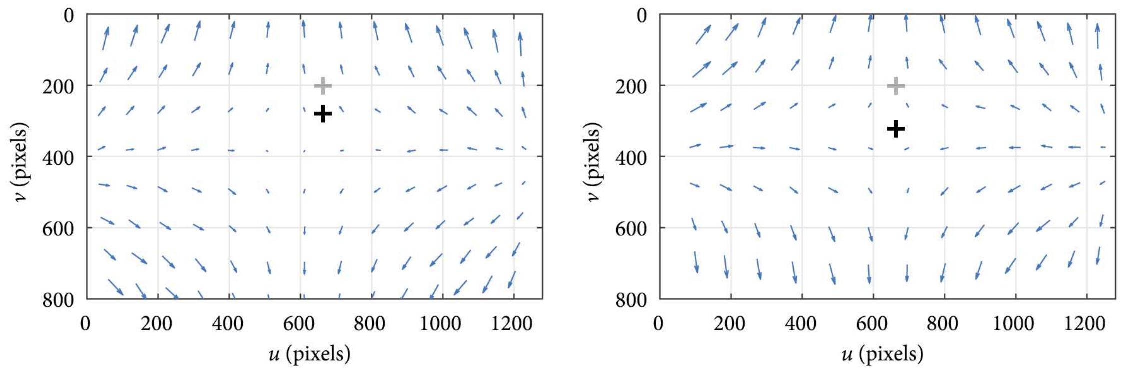

Figure 8-8. Intrinsic *calibration model error* for a corner (left) and straight (right) camera in the National Ice Centre (GBR) multi-camera network. The blue vectors – amplified for visualisation purposes – demonstrate the non-uniformity of the reprojection error. Consequently, skating velocity has a significant effect on intra-camera *calibration model error*, as the difference between two positions' intrinsic model error is less severe at slow velocities (left) compared to fast velocities (right).

Hanin (2009) state that with a large enough sample size, all effects would be statistically significant.

Effect of skating velocity on intra-camera calibration model error

In both corner and straight skating conditions, the intra-camera *calibration model error* was significantly greater for the faster-skating velocity. This was due to velocity dependent errors in the sampling interval and velocity dependent uncertainties in the checkerboard's reconstructed intersection positions. Error in the sampling interval was caused by filming the planar checkboard pattern sliding over the rink surface at 0.5 m·s^{-1}. As a result, the investigation only mitigated *rolling shutter error* in the analysis. Chapter 6 showed that when a skater moves predominantly parallel to the progression of scanline exposure and readout, the magnitude of sampling interval error – and consequently *rolling shutter error* – is greater at faster skating velocities due to a more substantial distance between the v-pixel coordinates in consecutive images. Uncertainty in the checkerboard's reconstructed intersection positions was due to errors in each camera's intrinsic model. Figure 8-8 illustrates these errors – over the 1280 x 800 pixel image plane – for a corner and straight skating condition camera. In both examples, the magnitude of intrinsic error is non-uniform, i.e. the magnitude and direction of the model's reprojection error changes over the image plane. As a result, the difference between two positions' intrinsic model error is more severe at faster velocities as the positions cover a larger distance on the image plane. This greater magnitude of intrinsic model error leads to significantly larger errors in velocity.

Critically, the effect of skating velocity on intra-camera *calibration model error* was small in both skating conditions. The difference between the skating velocities median error in the corner (0.013 $m \cdot s^{-1}$) and straight (0.015 $m \cdot s^{-1}$) equated to only 6.9 % and 8 % of the ± 0.19 $m \cdot s^{-1}$ target measurement error. Based on this target error, the results demonstrate that the multi-camera network's intra-camera *calibration model error* is effectively invariant to the skating velocity.

8.5.2 Inter-camera calibration model error

Chapter 7 showed that the multi-camera network should only calculate two-dimensional relay exchange kinematics within each camera's field-of-view to negate *out-of-phase error*. Therefore, in this chapter, inter-camera *calibration model error* was only concerned with how reconstructed positions – seen in two cameras' field-of-view – aligned in the global coordinate system. Overall, the multi-camera network's inter-camera *calibration model error* was undetectable from one camera to the next when visualising a trajectory over the 60 x 30 m rink surface; the RMS inter-camera *calibration model error* was of 0.01 m and 0.02 m in the x- and y-axis, respectively.

Effect of skating condition on inter-camera calibration model error

The magnitude of inter-camera *calibration model error* was invariant to the skating condition. In both the x- and y-axis, the analysis found no significant differences between the corner and straight skating condition. As described in Section 8.5.1, this is unsurprising as the nonlinear calibration procedure was the same for all cameras in the multi-camera network.

8.6 Chapter summary

This chapter addressed the third objective of the programme of research: to quantify *calibration model error* in the multi-camera network. More specifically, how incorrect relationships between the pixel and global coordinate systems propagated to (1) errors in position and velocity within (intra-) cameras' field-of-view, and (2) errors in position between (inter-) cameras' field-of-view. For the former, the chapter showed that the multi-camera network's intra-camera *calibration model error* was within the ± 0.19 $m \cdot s^{-1}$ target measurement error, significantly less than the Olympic Oval (CAN) multi-camera network ± 0.48 $m \cdot s^{-1}$ intra-camera *calibration model error*, and effectively invariant to the skating condition and skating velocity. The multi-camera network had an overall RMS intra-camera *calibration model error* of 0.06 $m \cdot s^{-1}$. As both multi-camera networks had similar reprojection errors, the chapter attributed this significant reduction in intra-camera *calibration model error* to the National Ice Centre (GBR) multi-camera network having a superior spatial resolution of the rink surface. For the latter, the chapter established that the multi-camera network's inter-camera *calibration model* error – in both skating conditions – was undetectable from one camera to the next when visualising a trajectory over the 60 x 30 m rink surface. The multi-camera network had an overall RMS inter-camera *calibration model error* of 0.01 m and 0.02 m in the x- and y-axis, respectively.

Chapter 9

A representative dataset of ground truth kinematics

9.1 Introduction

This chapter addresses the fourth objective of the programme of research: to create a representative dataset of ground truth short-track speed skating kinematics. Ground truth short-track speed skating kinematics represent the criterion values used in the quantification of the multi-camera network's measurement error. As detailed in Section 5.7.2, the quality of the multi-camera network's error quantification is dependent on the validity of this ground truth dataset. More specifically, the dataset's representativeness of the multi-camera network's intended use-cases, i.e. the different measurement scenarios where the system will be required to measure accurate, two-dimensional, relay exchange kinematics. Section 5.7.2 concluded that compared to other methods of creating ground truth datasets, a synthetic, three-dimensional, ground truth dataset seemed most appropriate. The dataset enables (1) the multi-camera network's five sources of measurement error to be quantified, and (2) the effect of the multi-camera network's intended-use cases to be considered.

In the following sections, I describe the two-stage process used to create this synthetic dataset. First, Section 9.2 details the collection of real-world, three-dimensional, fiducial marker kinematics during a Great Britain Short-Track Speed Skating training session. Second, Section 9.3 documents how these trajectories were used to create a representative synthetic dataset. Finally, Section 9.4 discusses the overall validity of the synthetic ground truth dataset.

9.2 Real-world fiducial marker kinematics

The Faculty of Health & Wellbeing Research Ethics Committee, Sheffield Hallam University, UK, approved this study.

9.2.1 Participants

Two male elite short-track speed skaters from the Great Britain Short-Track Speed Skating World Class Performance Programme (mean ± standard deviation age = 18.5 ± 0.7 years, stature = 178.5 ± 4.9 cm, mass = 69.3 ± 5.8 kg) participated in this study. Before testing, both skaters gave their written informed consent.

9.2.2 Experimental procedure

Testing took place during a Great Britain Short-Track Speed Skating training session at the National Ice Centre, Nottingham, GBR. Participants were asked to complete three trials equivalent to fast (9 seconds), medium (10.5 seconds) and slow (12 seconds) lap times. In each trial, participants skated a corner and proceeding straight with a flying start. The three-dimensional position of the fiducial marker was measured using high-speed video cameras and the multi-camera network. The former measured the fiducial marker height, the latter the fiducial marker rink position. The fiducial marker – a red foam hemisphere, 0.12 m in diameter – was positioned on a black vest 0.1 m above the participant's two-dimensional centre-of-mass point estimate, i.e. the 1st lumbar vertebra. As shown in Figure 9-1, this allowed the marker to be seen clearly in all cameras, even when participants placed their arms behind their back, and minimised the injury potential in the scenario where a participant fell.

9.2.3 One-dimensional fiducial marker kinematics

In each trial, I measured the position of the fiducial marker in the z-axis during the corner and the straight using four high-speed video cameras. As illustrated in Figure 9-2, the trial started and ended when the fiducial marker was in line with the corner's 2nd track marking block and the proceeding corner's 1st track marking block.

Figure 9-1. The fiducial marker as seen in the high-speed video cameras (top) and multi-camera network (bottom).

Experimental setup

Two gen-locked high-speed video cameras (Phantom V4.3, Vision Research, Wayne, USA) – operating at 100 Hz, a resolution of 800 x 160 pixels, and exposure time of 0.001 seconds – filmed the corner. I positioned each camera in the viewing gallery opposite the corner-of-interest to maximise the camera-to-calibrated plane distance and aligned the optical axes perpendicular to the dominant plane of motion. The first camera's field-of-view covered the 2nd to 4th track marking block (Camera 1 in Figure 9-2) and the second camera's field-of-view covered the 4th to 6th track marking block (Camera 2 in Figure 9-2). The study excluded the remainder of the corner from the analysis due to the increased potential for marker occlusion.

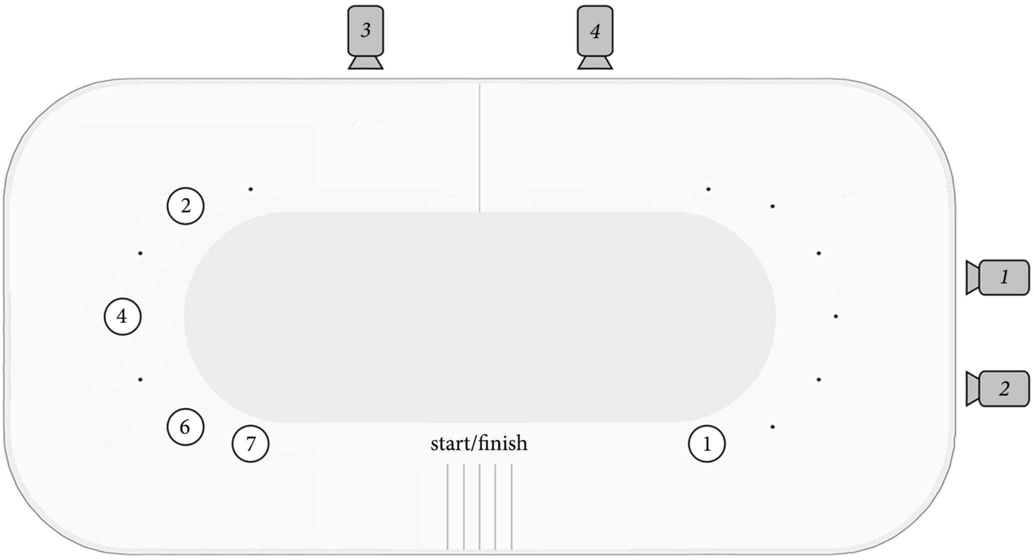

Figure 9-2. The high-speed video camera experimental setup. The cameras captured each trial from when the fiducial marker was in line with the corner's 2nd track marking block and the proceeding corner's 1st track marking block.

Two gen-locked high-speed video cameras (Phantom Miro 340, Vision Research, Wayne, USA) – operating at 100 HZ, a resolution of 1280 x 160 pixels, and exposure time of 0.001 seconds – filmed the straight. Similarly, I positioned each camera in the viewing gallery opposite the straight-of-interest and aligned their optical axes aligned perpendicular to the dominant plane of motion. The first camera's field-of-view covered the 7th track marking block to the start/finish line (Camera 3 in Figure 9-2) and the second camera's field-of-view covered the start/finish line to the 1st track marking block of the proceeding corner (Camera 4 in Figure 9-2).

Calibration procedure

Each high-speed video camera was calibrated using a linear scaling coefficient function

$$S = Function(u, v) \qquad (Eq. 9.1)$$

where S is the linear scaling coefficient used to reconstruct the fiducial marker's z position from the pixel coordinate system to the global coordinate system and (u, v) are the pixel coordinates that define the skater's current plane of motion. Using a scaling

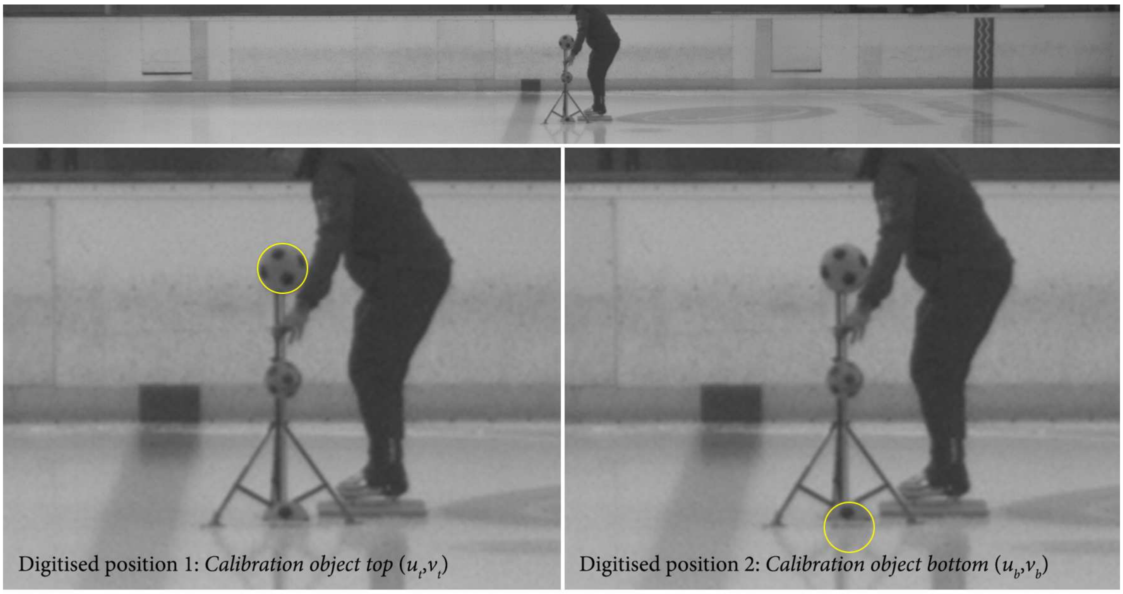

Figure 9-3. The high-speed video camera's calibration object digitised positions.

coefficient specific to the current plane of motion mitigated *out-of-plane error* in the analysis by reducing the out-of-plane distance (Section 5.3.3).

I constructed each camera's linear scaling coefficient function by collecting images of a calibration object, 1 m in height, over the entirety of the camera's capture volume (corner = 36 images, straight = 70 images). For each calibration object image, Check2D (Centre for Sports Engineering Research, 2013) was used to manually digitise the centre of the sphere at the top of the calibration object (u_t, v_t) and the centre of the sphere fitted to the hemisphere at the bottom of the calibration object (u_b, v_b). Figure 9-3 illustrates these digitised positions. The image was zoomed to enlarge the view of each sphere, with the cursor's diameter adjusted and aligned to match the sphere's outline. Each image's digitised pixel coordinates then defined a linear scaling coefficient at that location,

$$S(u_i, v_i) = \frac{H}{|v_t - v_b|} \qquad (Eq. 9.2)$$

where (u_i, v_i) are the pixel coordinates of the sphere centroid fitted to the hemisphere at the bottom of the calibration object, H is the height of the calibration object in the global coordinate system (1 m), and v_t and v_b are the vertical pixel coordinates of the calibration object's top and bottom sphere centroid. All location specific linear scaling coefficients were used to define the linear scaling coefficient function – a piecewise triangle surface over the image plane – by acting as the function's nodes. The function applied a bivariate linear interpolation within each triangle to return the location-specific linear scaling coefficient.

The validity of the calibration procedure, i.e. the degree to which the calibration functions succeed in reconstructing the actual height, was ± 0.005 m. I determined this value by using the linear scaling coefficient functions to reconstruct the pixel coordinates that defined the calibration object's known height in 40 additional calibration object images (10 images per high-speed video camera). The investigation defined the validity of the calibration procedure as the RMS error between the known and reconstructed calibration object height.

Digitisation & reconstruction procedure

For each high-speed video camera, Check2D (Centre for Sports Engineering Research, 2013) was used to manually digitise the fiducial marker, defined as the centre of a sphere fitted to the foam hemisphere (u_{ti}, v_{ti}), and the skate blade, defined as the point of contact between the rink surface and blade (u_{bi}, v_{bi}). Figure 9-4 illustrates theses two digitised positions. I then used $Eq. 9.3$ to reconstruct the position of the fiducial marker in the z-axis,

$$z_i = S_i(|v_{ti} - v_{bi}|) \qquad (Eq. 9.3)$$

where S_i is the linear scaling coefficient returned from the camera specific calibration function $(Eq. 9.1)$ and v_t and v_b are the vertical pixel coordinates of the digitised fiducial marker and skate blade in the ith image. $Eq. 9.1$ used the skate blade pixel coordinates (u_{bi}, v_{bi}) to define the current plane of motion.

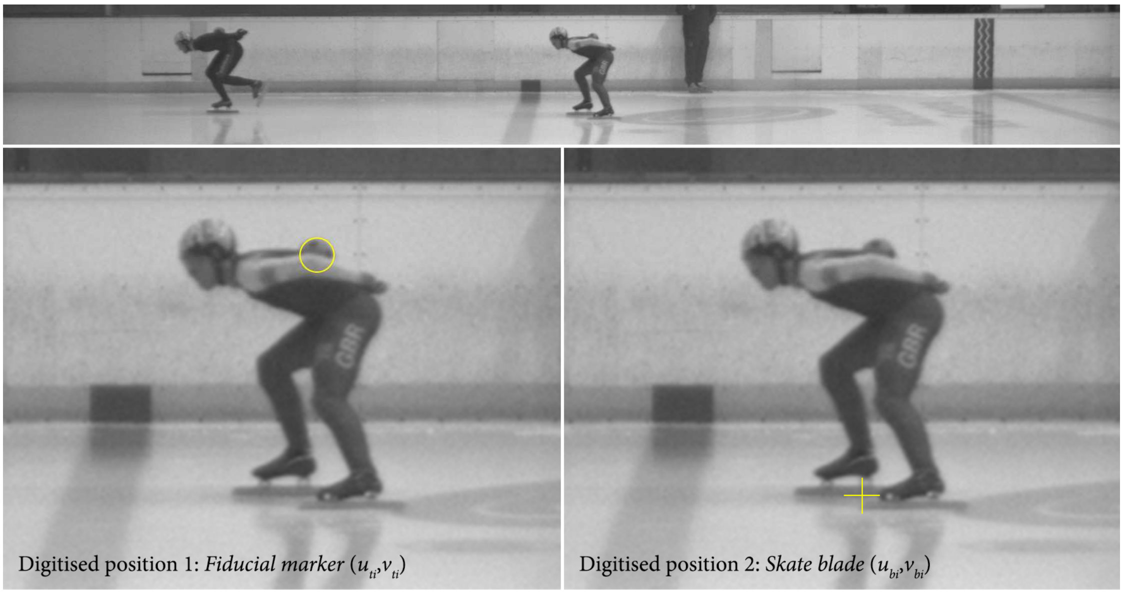

Figure 9-4. The high-speed video camera's fiducial marker and skate blade digitised positions.

All manual digitisation was performed by a single operator to negate inter-operator digitisation error. The level of intra-operator error in the high-speed video *digitisation and reconstruction procedure* was ± 0.003 m (± 0.32 pixels). I determined this value by digitising the fiducial marker in 40 images (10 per high-speed video camera) on two occasions separated by a week. The investigation defined intra-operator error as the mean absolute error between all pairs of reconstructed fiducial marker positions.

The *out-of-plane error* in the high-speed video *digitisation and reconstruction procedure* was ± 0.013 m. I determined this value using a computer simulation. The simulation – illustrated in Figure 9-5 – investigated how expected differences in the skate blade and fiducial marker plane of motion led to errors in the reconstructed fiducial marker position in the corner and straight high-speed video cameras.

Data processing

For each trial, MATLAB R2016a (MathWorks, 2016) was used to join the position of the fiducial marker in the corner and straight onto a single timestamp. This process consisted of four stages. The first stage used a zero-phase 4th order Butterworth filter to

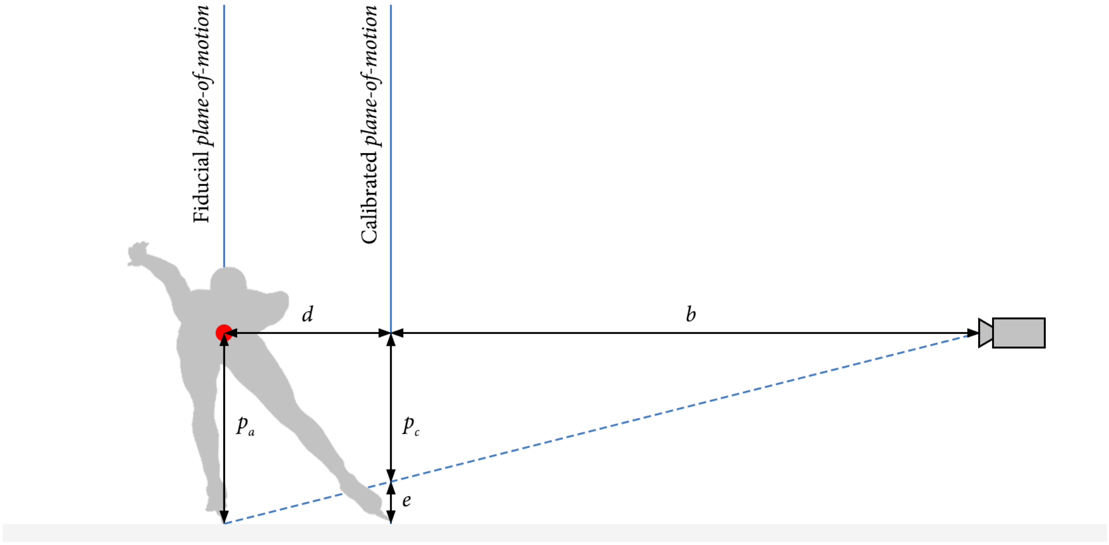

Figure 9-5. The high-speed video camera *out-of-plane error* simulation, where b is the camera-to-calibrated plane distance, d is the out-of-plane distance, p_a is the true height, p_c is the measured height, and e is the *out-of-plane error*.

attenuate high-frequency noise in the manual digitisation of the fiducial marker and skate blade (Bartlett, 2014). In accordance with Chun (2001), the filter used a cut-off frequency of 6 Hz. The second stage used the trial's start and end timestamps – measured in the multi-camera network – to determine the overall trial length. This length was used to create a 1-by-n matrix of the trial sampled at 100 Hz as follows,

$$F_z = [z_1 \quad z_2 \quad z_3 \quad \cdots \quad z_n] \qquad (Eq. 9.4)$$

The third stage mapped the position of the fiducial marker in the corner and straight onto F_z. The corner data beginning at z_1, and the straight data ending at z_n. Lastly, the fourth stage used a cubic spline to interpolate the position of the fiducial marker from the 6th to 7th track marking block, with the final data downsampled to 25 Hz to allow allignment with the multi-camera network's data.

9.2.4 Two-dimensional fiducial marker kinematics

In each trial, I measured the fiducial marker's x- and y-axis position during the corner and straight using the National Ice Centre (GBR) multi-camera network. As in Section

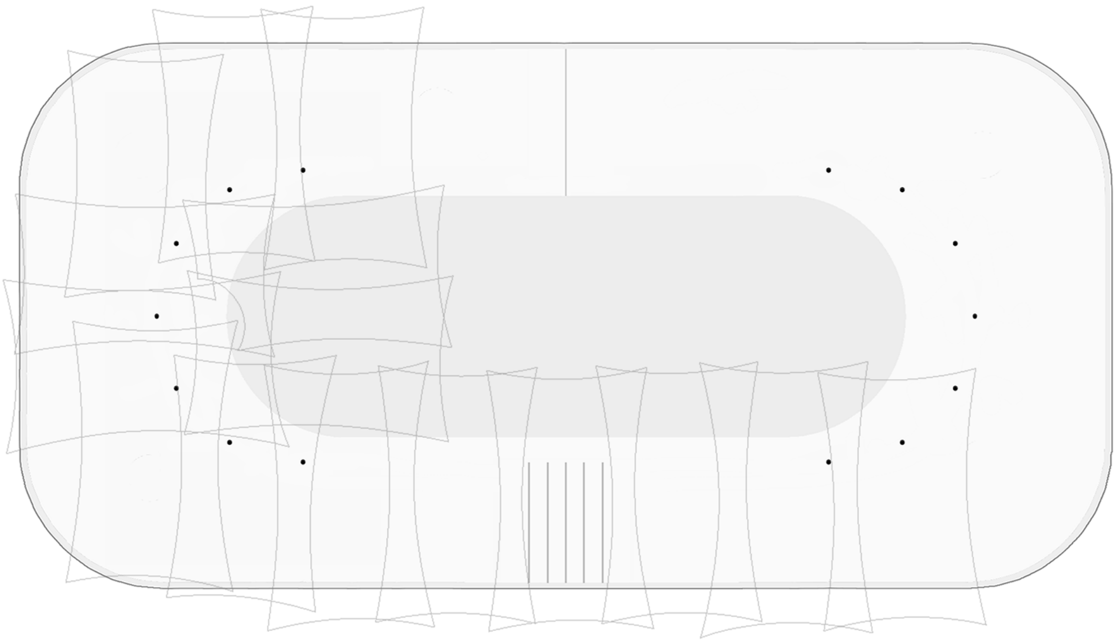

Figure 9-6. The fifteen-camera field-of-views used to collect two-dimensional fiducial marker kinematics.

9.2.3, the trial started and ended when the fiducial marker was in line with the corner's 2nd track marking block, and the proceeding corner's 1st track marking block.

Experimental setup

Fifteen of the multi-camera network's twenty-six cameras – operating at 25 Hz, a resolution of 1280 x 800 pixels, and exposure time of 0.004 seconds – filmed the corner and straight. Figure 9-6 illustrates these cameras' field-of-view.

Calibration procedure

As documented in Chapter 8, each camera was calibrated using the nonlinear calibration procedure described in Section 5.3.2. Based on the results from Chapter 8, in the worst-case scenario the validity of the calibration procedure, i.e. the degree to which the calibration models succeeded in reconstructing the actual distance, was ± 0.016 m. I determined this value by using the camera-rink plane calibration models to reconstruct pixel coordinates that defined two known distances in 59,836 images.

Figure 9-7. The multi-camera network's digitised position (denoted by the circular yellow cursor).

Digitisation & reconstruction procedure

For each trial, Check2D (Centre for Sports Engineering Research, 2013) was used to manually digitise the centre of the fiducial marker in each image. First, the image was zoomed to enlarge the view of the marker. Then, the cursor's diameter adjusted and aligned to match the fiducial marker's outline. Figure 9-7 illustrates this procedure. All digitisation was performed by a single operator to negate inter-operator digitisation error. The level of intra-operator error in the multi-camera network digitisation procedure was ± 0.005 m (± 0.52 pixels). I determined this value by digitising the fiducial marker in 40 images (10 per high-speed video camera) on two occasions separated by a week. The study defined intra-operator error as the mean absolute error between all pairs of reconstructed fiducial marker positions.

For each trial, I reconstructed the fiducial marker's pixel coordinates into the global coordinate system using camera-elevated plane calibration models specific to each digitised point. This process – consisting of three stages – negated *out-of-plane error* in the analysis (Section 5.3.3). The first stage used the timestamp of each digitised image to align the pixel coordinates onto the fiducial marker's z-position timestamp created in Section 9.2.3. Accordingly, each digitised image, i, had the format $[Timestamp_i, CameraID_i, u_i, v_i, z_i]$. Note that due to the multi-camera network's overlapping camera field-of-views, each timestamp could contain more than one $CameraID$ and associated u_i, v_i, z_i coordinates. The second stage constructed the camera-elevated plane calibration model for each digitised image – as described in Section 5.3.3 – using the relevant control point and camera-rink plane calibration model constructed in Chapter 8. For each image, the analysis projected the camera's control points to the height of z_i. The third stage then reconstructed each images pixel coordinates into the global coordinates system – as described in Section 5.3.2 – using the camera-elevated calibration model constructed in stage two.

Data processing

For each trial, a smoothing spline – implemented in MATLAB R2016a (MathWorks, 2016) – was used to combine each camera's reconstructed fiducial marker positions into a single trajectory (Section 5.5.2). The smoothing parameter, λ, was set empirically at 0.3. The smoothing spline was sampled at 25 Hz to create the trial's final fiducial marker positions.

9.2.5 Three-dimensional fiducial marker kinematics

For each trial, I joined the position of the fiducial marker in the z-axis (measured in Section 9.2.3) and the x- and y-axis (measured in Section 9.2.4), to create five real-world, three-dimensional, fiducial marker kinematics. Note that one of the six trials were omitted at this stage, due to an error in the multi-camera network's data collection. Figure 9-8 illustrates an example of the three-dimensional fiducial marker kinematics.

9.3 Synthetic fiducial marker kinematics

The real-world fiducial marker trajectories collected in Section 9.2 only (1) covered half-a-lap, (2) characterised five of the infinite number of skating trajectories, and (3) represented two skater statures from Great Britain Short-Track Speed Skating's World Class Performance Programme. For these reasons, I applied a suite of geometric transformations to each real-world trajectory to create a more representative dataset of ground truth short-track speed skating kinematics.

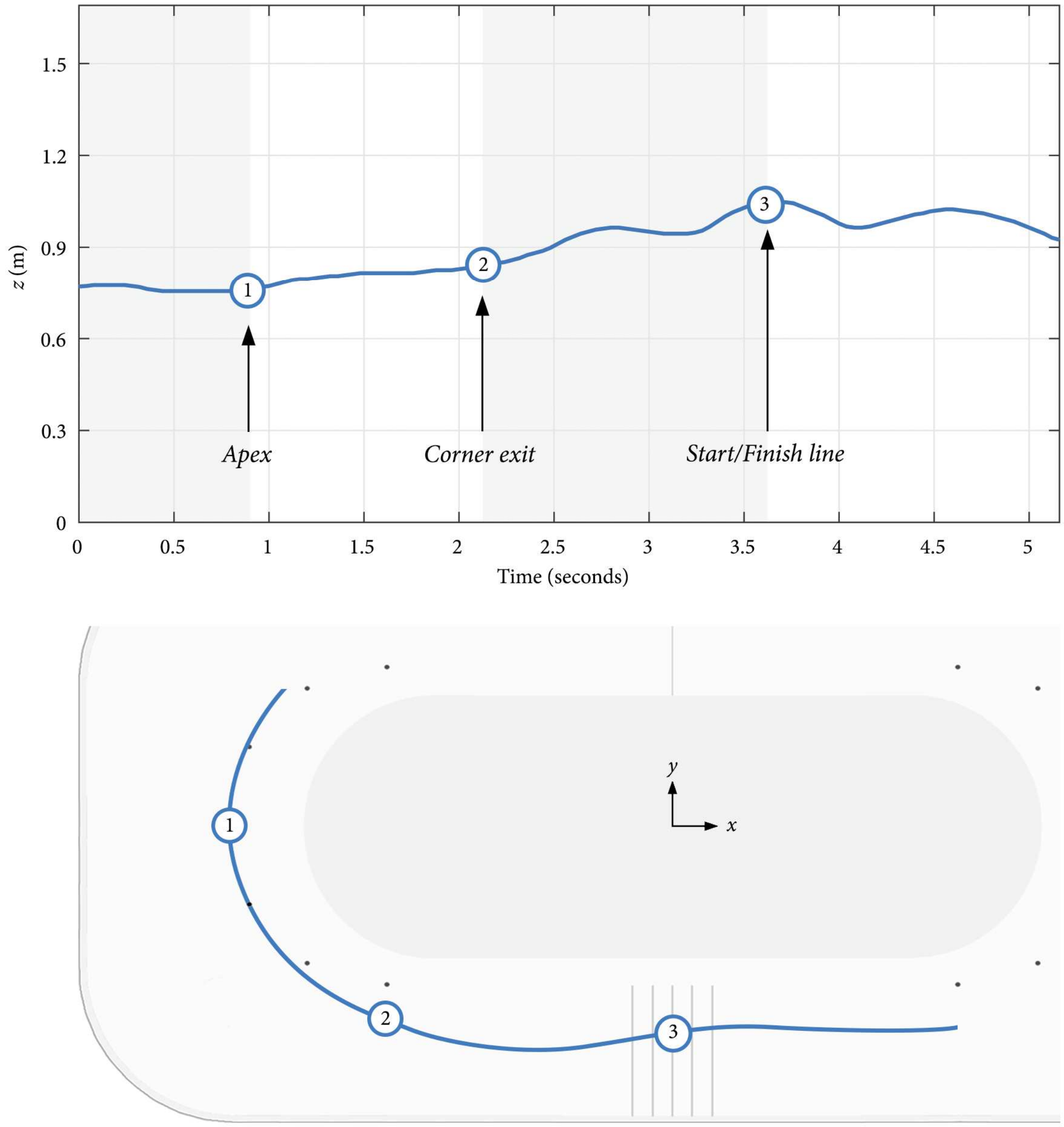

Figure 9-8. An example real-world, three-dimensional, fiducial marker trajectory.

MATLAB R2016a (MathWorks, 2016) was used to apply four geometric transformations to each real-world trajectory. These transformations – described below and illustrated in Figure 9-9 – created 63 synthetic trajectories for each real-world trajectory.

1. The first transformation reflected the real-world trajectory through the rink origin and ensured that the trajectory covered most of a full-lap (Figure 9-9a).

2. The second transformation translated the real-world trajectories x component over a period of 14 m, at 2 m intervals (Figure 9-9b). This transformation ensured that the real-world trajectory covered (1) the five-different short-track positions (Section 4.3.2), and (2) the inside of the short-track, i.e. where skaters build up speed prior to the relay exchange.

3. The third transformation translated the y component of the real-world trajectory by ± 2 m (Figure 9-9c). This transformation ensured that the trajectory covered a range of each cameras' field-of-view.

4. The fourth and final transformation multiplied the z component of the real-world trajectory – normalised to the skater's stature – by 1.52 m, 1.69 m and 1.86 m. This transformation ensured that the trajectory represented the minimum, mean, and maximum skater stature in Great Britain Short-Track Speed Skating's Word Class Performance Programme.

For each synthetic fiducial marker trajectory, the ground truth resultant velocity was calculated using $Eq.\ 5.24$, with finite difference techniques used to compute velocity in the x- and y-axis ($Eq.\ 5.25$ to $Eq.\ 5.27$). I used a sampling interval of 0.04 seconds to compute velocity as the ground truth trajectories had a sampling frequency of 25 Hz (Section 9.2.4).

9.4 Discussion

Sections 9.2 and 9.3 described the two-stage process used to create a dataset of ground truth short-track speed skating kinematics. The thesis requires this dataset to act as the criterion values used in the quantification of the multi-camera network's measurement error. As a result, the quality of the multi-camera network's error quantification is dependent on the ground truth dataset's validity. More specifically, the dataset's representativeness of the multi-camera network's intended use-cases, i.e. the different measurement scenarios where the system will be required to measure accurate, two-

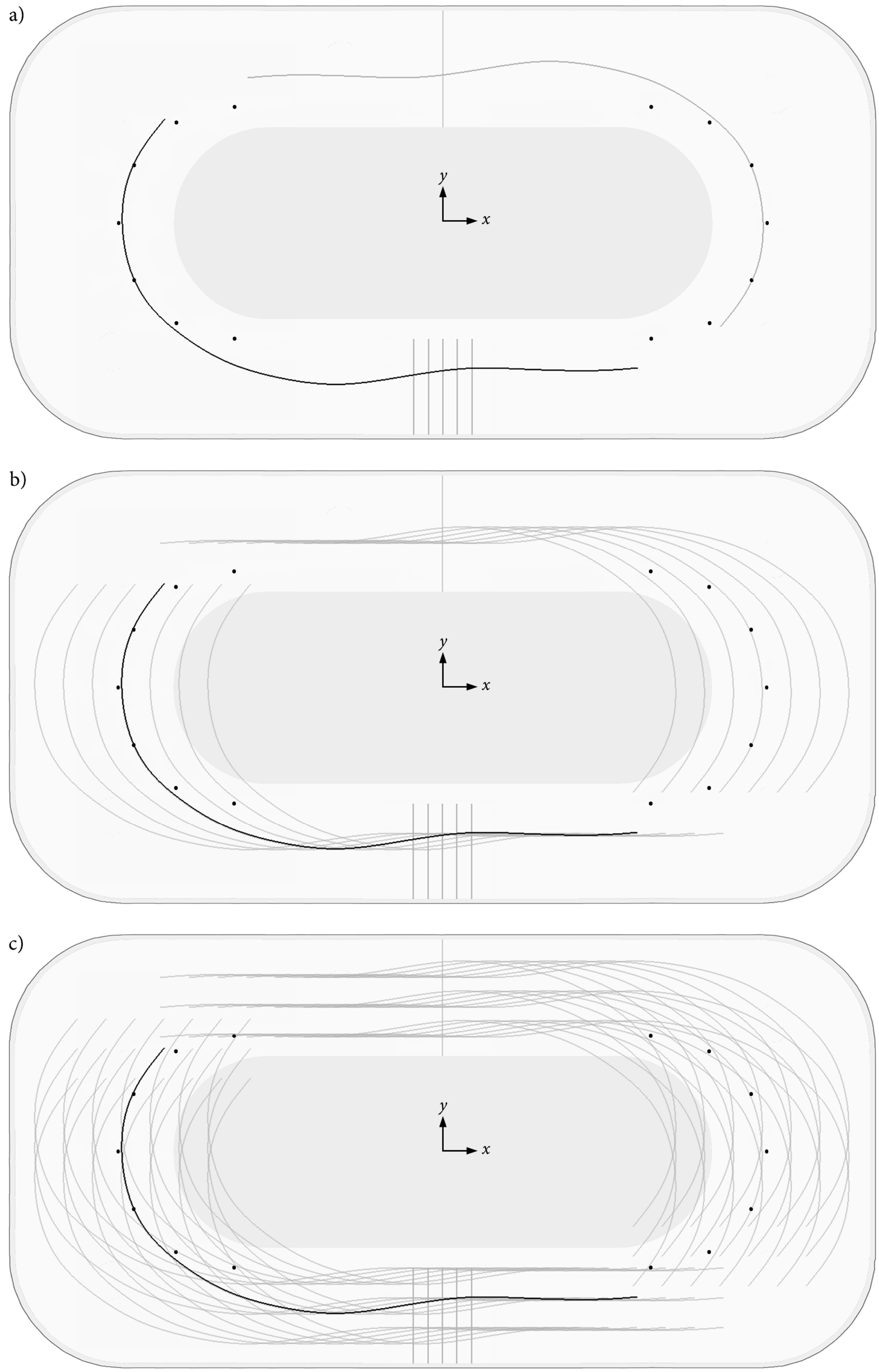

Figure 9-9. The first three geometric transformations applied to each real-world fiducial marker trajectory: (a) transformation 1 reflected the trajectory – denoted by the black line - through the rink origin, (b) transformation 2 translated the trajectories x component over a period of 14 m (at 2 m intervals), (c) transformation 3 translated the y component of the real-world trajectory by ± 2 m.

dimensional, relay exchange kinematics. Overall, the created dataset consists of 315 synthetic trajectories that cover a range of skating velocities, skater statures, and skating trajectories. The validity of each aspect, along with the measurement of the real-world fiducial marker trajectories, is discussed below.

Real-world fiducial marker trajectories

First and foremost, the validity of the ground truth dataset is dependent on the accuracy of the real-world fiducial marker trajectories, as these trajectories form the basis of the dataset. In an ideal scenario, these trajectories would have been captured using a gold-standard measurement technique, e.g. optical motion capture. Although considered, optical motion capture was not feasible due to the limited capture volume it afforded. For example, Kim et al. (2013) used eight cameras to cover the period from the 4th to 6th track marking block alone. In this thesis, it was essential that I captured fiducial marker kinematics during both the corner and straight skating conditions due to the differences in skating technique (Section 4.3.2). Unfortunately, the estimated 42 cameras needed to cover the volume of interest were not available. Instead, the two techniques used in this study measured the fiducial marker to within ± 0.02 m when considering (1) the validity of the calibration, (2) the intra-operator digitisation error, and (3) the out-of-plane error. Furthermore, any noise in the measurement was reduced by filtering (z-axis) and smoothing (x- and y-axis) the raw kinematic data. Although these signals are still likely to contain error when compared to optical motion capture, I believe that they are still valid representations of a fiducial marker in short-track speed skating.

Skating velocities in the ground truth dataset

The ground truth dataset includes five different skating velocities equivalent to 10.12 to 11.88 second lap times. Note that the skaters did not complete the fastest trial, i.e. a 9 second lap time, due to fatigue. First, it is important to have a representative range of velocities in the ground truth dataset as Chapter 2 showed that the skating velocity varies during the relay event. Second, as detailed in Section 5.7.2, the multi-camera network’s sources of error may be sensitive to velocity-dependent differences in fiducial marker kinematics. For example, during the corner, the magnitude of *out-of-plane error* may be smaller at faster velocities, as skaters will lean further towards the centre of rotation to maintain the balance of forces between the skate and ice (Chun, 2001; Yule & Payton, 2000). Consequently, the dataset can be used to quantify the effect of skating velocity on the multi-camera network's sources of measurement error for slow-to-medium skating velocities, but only infer the effect of skating velocity at the fastest skating velocities in short-track speed skating.

Skater statures in the ground truth dataset

The ground truth dataset encapsulates the full range of skater's statures in Great Britain Short-Track Speed Skating's World Class Performance Programme, i.e. the skaters who will be analysed using the National Ice Centre (GBR) multi-camera network. I achieved this by multiplying the skater statures by the normalised z component of the five real-world trajectories. This technique has been used previously in short-track speed skating to compare the kinematic characteristics of different skater statures during the corner skating condition. Importantly, Chun (2001) described how the vertical displacement of the whole-body centre-of-mass was similar for the normalised data. It is important to have a range of skater statures in the ground truth dataset as the multi-camera network’s sources of error may be dependent on stature-dependent differences in fiducial marker kinematics. For example, in short-track speed skating, skaters adopt a crouched skating position to minimise their frontal area and thus reduce frictional losses from air friction (Section 4.3.2). As detailed in Section 5.7.2, as the knee and trunk angle characterise this crouched skating position (Konings et al., 2015), for a given set of angles, the height of the fiducial marker – and thus the magnitude of *out-of-plane error* - is likely to be greater for a tall stature skater. The dataset created in this chapter can be used to investigate/ quantify this type of effect.

Skating trajectories in the ground truth dataset

The ground truth dataset includes 105 different full-lap skating trajectories. These trajectories cover the five-different short-track positions (Section 4.3.2) and the inside of the short-track, i.e. where skaters build up speed prior to the relay exchange. I achieved this trajectory coverage by applying three geometric transformations to each real-world fiducial marker trajectory. It is essential to have this variety of skating trajectories in the ground truth dataset as the multi-camera network's sources of error may be position-dependent. For example, Chapter 8 demonstrated that the intrinsic *calibration model error* was not constant over the whole image plane; Figure 8-8 illustrating the reprojection error's non-uniformity. By having a variety of skating trajectories in the ground truth dataset, the quantification of the multi-camera network's measurement error can include these position-dependent errors.

9.5 Chapter summary

This chapter described the two-stage process used to address the fourth objective of the programme of research: to create a representative dataset of ground truth short-track speed skating kinematics. Ground truth short-track speed skating kinematics represent the criterion values used in the quantification of the multi-camera network's measurement error. The first stage used four high-speed video cameras, and the multi-camera network, to measure five, real-world, three-dimensional trajectories of a fiducial marker positioned at a skater's two-dimensional centre-of-mass point estimate. These five trajectories – collected over a corner and proceeding straight – covered a range of skating velocities equivalent to 10.12 second and 11.88 second lap times. The second stage applied a suite of geometric transformations to each real-world trajectory to create 21 different full-lap skating trajectories for the minimum, mean, and maximum skater statures in Great Britain Short-Track Speed Skating's World Class Performance Programme. By including various skater statures and skating trajectories, the synthetic ground truth dataset (n = 315) was deemed suitable for assessing the multi-camera network's sources of measurement error over the range of skating velocities.

Chapter 10

Out-of-plane error in the multi-camera network

10.1 Introduction

This chapter addresses the fifth objective of the programme of research: to quantify *out-of-plane error* in the multi-camera network. *Out-of-plane error* describes how any measured point not on the calibrated plane propagates to errors in position and velocity. As detailed in Section 5.3.3, in the National Ice Centre (GBR) multi-camera network, *out-of-plane error* is caused by using fiducial markers to define skaters' rink position. These fiducial markers – positioned at a skater's two-dimensional centre-of-mass point estimate – are always located above the calibrated rink surface (Section 8.2).

In the following sections, I describe the investigation into the multi-camera network's *out-of-plane error*. To provide a more detailed insight, the investigation considers the effect of skating condition, skater stature, and skating velocity.

10.2 Method

The multi-camera network's *out-of-plane error* was quantified using a computer simulation in MATLAB R2016a (MathWorks, 2016).

10.2.1 Ground truth trajectories

All 315 synthetic ground truth trajectories created in Chapter 9 were used to simulate the effect of *out-of-plane error* in the multi-camera network. These trajectories included three representative skating velocities (equivalent to ~ 10 s, 11 s and 12 s lap times),

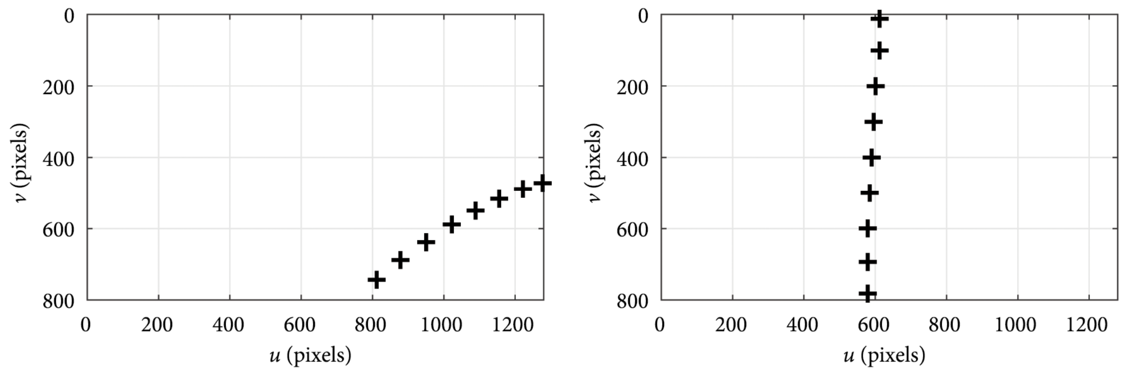

Figure 10-1. An example of a ground truth trajectory projected onto a corner (left) and straight (right) skating condition camera image plane.

three skater statures (1.52 m, 1.69 m and 1.86 m), and 105 independent full-lap trajectories.

The simulation projected each ground truth trajectory onto the multi-camera network's 26 image planes – as described in Section 5.3.2 – using the camera-rink plane calibration models constructed in Chapter 8. Figure 10-1 illustrates a projected ground truth trajectory for a corner and straight skating condition camera. Before the projection procedure, I partitioned each ground truth trajectory so that the simulation only projected the relevant ground truth coordinates into each camera's field-of-view.

Ground truth trajectory partitioning was performed using each camera's global coordinate system field-of-view (defined in Section 8.3.3). If the ground truth coordinates were inside a camera's field-of-view, the simulation assigned these coordinates to that camera. If the coordinates appeared in more than one camera's field-of-view, the simulation assigned these coordinates to both cameras.

10.2.2 Simulation

For each ground truth trajectory, the simulation reconstructed each camera's ground truth pixel coordinates into the global coordinate system – as described in Section 5.3.2 – using the camera-rink plane calibration models constructed in Chapter 8. Resultant velocity was then calculated using $Eq.$ 5.24, with finite difference techniques used to compute velocity in the x- and y-axis ($Eq.\ 5.25$ to $Eq.\ 5.25$). The simulation used a sampling interval of 0.04 seconds to compute velocity, as the ground truth trajectories had a sampling frequency of 25 Hz (Section 9.2).

10.2.3 Data analysis

For each ground truth trajectory, the simulation calculated two metrics for each camera (1) the out-of-plane distance, defined as the median z component of the camera's ground truth trajectory, and (2) the *out-of-plane error*, defined as the RMS error ($Eq.\ 5.34$) between the camera's ground truth and reconstructed position and velocity trajectories. This calculation assumed that the ground truth condition represented the actual values of position and velocity.

10.2.4 Statistical analysis

SPSS 24 (IBM, 2016) was used to calculate the out-of-plane distance and *out-of-plane error* descriptive statistics (median, first quartile, third quartile, minimum, maximum, and ± 95% confidence bounds) for the corner and straight skating conditions (defined in Section 8.3.3). The analysis calculated the median and first and third quartiles, instead of the arithmetic mean and standard deviation, as these statistics are more representative of systematic and random error in non-normally distributed datasets. As all *out-of-plane errors* were positive due to the calculation of the RMS error, the ± 95% confidence bounds represented the 95th percentile, i.e. the value below which 95% of the *out-of-plane errors* were found.

A Mann Whitney U-test was used to analyse differences in *out-of-plane error* between the corner and straight skating condition. Data were treated as non-parametric, as the underlying assumptions of parametric statistical tests, i.e. normality and homogeneity of variance, were violated. For each skating condition, one-way Kruskal-Wallis ANOVAs were used to examine differences in *out-of-plane error* between the three skater statures and investigate differences in *out-of-plane error* between the three skating velocities.

Where main effects occurred, post hoc pairwise comparisons (Mann Whitney U-test) were used to identify the observed differences. The analysis used the RMS velocity error as the sole metric of *out-of-plane error*, as the numerical computation of velocity amplifies any uncertainty in position (Section 5.5.2).

In all statistical tests, the significance level, α, was set at $p < 0.05$. For post hoc comparisons, the Bonferroni correction was used to correct each pairwise α so that the overall significance remained at $p < 0.05$ (Field, 2009). Effect sizes were also calculated using Pearson's correlation coefficient ($Eq.$ 8.1), with the magnitudes interpreted using Cohen's thresholds; where < 0.1, is trivial; 0.1–0.3, small; > 0.3–0.5, moderate; and > 0.5, large (Cohen, 1988).

10.3 Results

A total of 6,846 ground truth and reconstructed position and velocity trajectories were compared (corner = 3,713, straight = 3,133). The descriptive statistics are reported in Table 10-1, with an example *out-of-plane error* for both corner and straight skating conditions shown in Figure 10-2. Overall, the multi-camera network's ± 95% confidence bounds in *out-of-plane error* was ± 1.49 $\text{m}\cdot\text{s}^{-1}$.

Table 10-1. *Out-of-plane error* descriptive statistics for the corner and straight skating conditions in the National Ice Centre (GBR) multi-camera network.

Statistic	Out-of-plane distance		X position error		Y position error		Resultant velocity error	
	Corner	Straight	Corner	Straight	Corner	Straight	Corner	Straight
Median	0.77	0.98	0.23	0.24	0.22	0.19	0.93	1.23
Q_1, Q_3	0.71, 0.84	0.90, 1.05	0.17, 0.32	0.22, 0.26	0.18, 0.34	0.11, 0.32	0.84, 1.01	1.11, 1.36
Minimum	0.60	0.63	0.02	0.11	0.02	0.01	0.66	0.67
Maximum	1.10	1.20	0.66	0.43	0.68	0.64	1.59	1.85
± 95% CB	0.94	1.14	0.50	0.28	0.49	0.45	1.20	1.57

Notes: Q_1 and Q_3 = first and third quartiles. CB = Confidence bounds. Out-of-plane distance, X position error, and Y position error measured in metres. Resultant velocity measured in $m \cdot s^{-1}$.

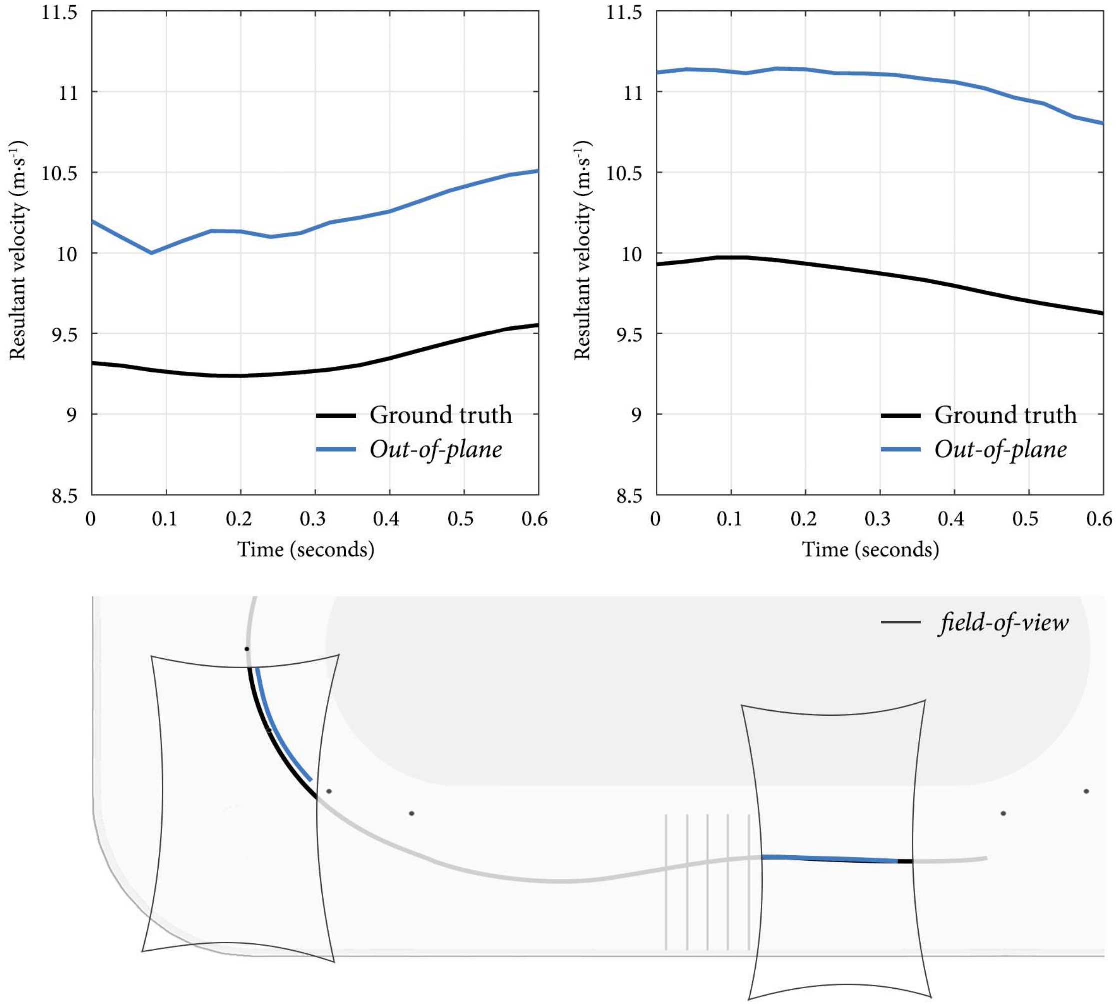

Figure 10-2. Example *out-of-plane errors* for a corner (left) and straight (right) skating condition camera in the National Ice Centre (GBR) multi-camera network.

10.3.1 Skating condition

There was a significant difference in *out-of-plane error* between the corner and straight skating conditions, U = 1.05 x 10^7, p = 0.000, r = 0.69 (a large effect). The RMS velocity error was smaller during the corner ($\widetilde{v_3}$ = 0.93 m·s^{-1}) than the straight ($\widetilde{v_3}$ = 1.23 m·s^{-1}).

10.3.2 Skater stature

There was a significant main effect for skater stature on *out-of-plane error* in both corner ($H(2)$ = 1.90 x 10^3, p = 0.000) and straight ($H(2)$ = 1.21 x 10^3, p = 0.000) skating conditions. The post hoc pairwise comparisons are summarised in Table 10-2. In both

Table 10-2. Effect of skater stature on *out-of-plane error*: post hoc pairwise comparisons.

Condition	Stature $_{(1-2)}$	$\tilde{z}$ Dist$_1$	$\tilde{z}$ Dist$_2$	$\widetilde{v_3}$ Error$_1$	$\widetilde{v_3}$ Error$_2$	U	p	r
Corner	Min - Mean	0.69	0.77	0.81	0.91	-2.70×10^2	0.000	-0.45
	Min - Max	0.69	0.85	0.81	1.02	-1.88×10^3	0.000	-0.88
	Max - Mean	0.85	0.77	1.02	0.91	-9.09×10^2	0.000	-0.42
Straight	Min - Mean	0.89	0.99	1.10	1.23	-7.18×10^2	0.000	-0.40
	Min - Max	0.89	1.09	1.10	1.37	-1.37×10^3	0.000	-0.76
	Max - Mean	1.09	0.99	1.37	1.23	-6.56×10^2	0.000	-0.36

Notes: Skater statures (min, mean and max) represent values of 1.52, 1.69 and 1.86 m, respectively. $\tilde{z}$ Dist = Median out-of-plane distance measured in metres. $\widetilde{v_3}$ Error = Median *out-of-plane error* measured in m·s^{-1}. U = Mann-Whitney U-Test. Significance values adjusted using the Bonferroni correction to control for family-wise error. Magnitude of effect, r, measured using Pearson's correlation coefficient.

skating conditions, the magnitude of *out-of-plane error* was significantly smaller for the minimum stature compared to the mean stature (r_c = -0.45, r_s = -0.4), the mean stature compared to the maximum stature (r_c = -0.42, r_s = -0.36), and the minimum stature compared to the maximum stature (r_c = -0.88, r_s = -0.76).

10.3.3 Skating velocity

There was a significant main effect for skating velocity on *out-of-plane error* in both corner ($H(2) = 2.28 \times 10^1$, p = 0.000) and straight ($H(2) = 4.52 \times 10^2$, p = 0.000) skating conditions. The post hoc pairwise comparisons are summarised in Table 10-3. In the corner, the magnitude of *out-of-plane error* was significantly smaller for the medium velocity compared to the fast velocity (r_c = -0.06), and the slow velocity compared to the fast velocity (r_c = -0.1). Note that the *out-of-plane error* was smaller for the slow velocity compared to the medium velocity, but not statistically significant (p = 0.08, r_c = -0.04). In the straight, the magnitude of *out-of-plane error* was significantly smaller for the slow velocity compared to the medium velocity (r_s = -0.3), the medium velocity compared to the fast velocity (r_s = -0.17), and the slow velocity compared to the fast velocity (r_s = -0.46).

Table 10-3. Effect of skating velocity on *out-of-plane error*: post hoc pairwise comparisons.

Condition	Velocity $_{(1-2)}$	$\tilde{z}$ Dist$_1$	$\tilde{z}$ Dist$_2$	$\widetilde{v_3}$ Error$_1$	$\widetilde{v_3}$ Error$_2$	U	p	r
Corner	Slow - Med	0.80	0.76	0.92	0.93	-8.71 x 10^1	0.081	-0.04
	Slow - Fast	0.80	0.75	0.92	0.94	-2.29 x 10^2	0.000	-0.10
	Fast - Med	0.75	0.76	0.94	0.93	-1.42 x 10^2	0.009	-0.06
Straight	Slow - Med	0.95	1.00	1.17	1.29	-5.49 x 10^2	0.000	-0.30
	Slow - Fast	0.95	0.98	1.17	1.35	-8.75 x 10^2	0.000	-0.46
	Fast - Med	0.98	1.00	1.35	1.29	-3.26 x 10^2	0.000	-0.17

Notes: Skating velocity (slow, med and fast) akin to approximately 12, 11, and 10 second lap times, respectively. $\tilde{z}$ Dist = Median out-of-plane distance measured in metres. $\widetilde{v_3}$ Error = Median *out-of-plane error* measured in m·s^{-1}. U = Mann-Whitney U-Test. Significance values adjusted using the Bonferroni correction to control for family-wise error. Magnitude of effect, r, measured using Pearson's correlation coefficient.

10.4 Discussion

This investigation aimed to quantify *out-of-plane error* in the multi-camera network. More specifically, how measured points (i.e. the fiducial marker) not on the calibrated plane (i.e. the rink surface) propagated to errors in position and velocity. To provide a more detailed insight, the investigation also considered the effect of skating condition, skater stature, and skating velocity on the magnitude of *out-of-plane error*. Overall, the results showed that the multi-camera network's *out-of-plane error* (± 1.49 m·s^{-1}) exceeded the ± 0.19 m·s^{-1} target measurement error. Fiducial marker out-of-plane distances, ranging from 0.6 m to 1.2 m, leading to substantial errors in position (0.01 m to 0.68 m) and velocity (0.66 m·s^{-1} to 1.85 m·s^{-1}). For this reason, *out-of-plane error* must be minimised in order to measure accurate, two-dimensional, relay exchange kinematics.

Effect of skating condition on out-of-plane error

The magnitude of *out-of-plane error* in the multi-camera network was dependent on the skating condition. The RMS velocity errors were significantly smaller in the corner than the straight due to differences in skating technique. As outlined in Section 4.3.2, in addition to maintaining a crouched skating position, skaters lean towards the centre of rotation during the corner to maintain the balance of forces between the skate and ice (Chun, 2001; Yule & Payton, 2000). As a result, the corner skating condition exhibits smaller out-of-plane distances (Table 10-1), and thus *out-of-plane error*, as the fiducial marker is closer to the calibrated rink surface.

Effect of skater stature on out-of-plane error

Irrespective of skating condition, the multi-camera network's *out-of-plane error* was dependent on the skater stature. RMS velocity errors significantly increased from the minimum, to mean, to maximum stature in Great Britain Short-Track Speed Skating's World Class Performance Programme due to larger out-of-plane distances. This result is unsurprising considering that the crouched skating position is characterised using the knee and trunk angle (Konings et al., 2015). Subsequently, for a given set of angles, I would expect that the height of the fiducial marker (located on the trunk), and thus the out-of-plane distance, to be greater for a taller stature skater.

Effect of skating velocity on out-of-plane error

In the corner skating condition, out-of-plane distances decreased as skating velocity increased, due to the skaters leaning further towards the centre of rotation. As reported in Section 4.3.2, as the centripetal force increases with skating velocity, skaters lean further towards the centre of rotation to maintain the balance of forces between the skate and ice. Despite this, the results showed that the RMS velocity error significantly increased with skating velocity, i.e. as the out-of-plane distance decreased. While this result contradicts the chapter's earlier findings, where smaller out-of-plane distances led to smaller RMS velocity errors, the result is consistent with the findings in Chapter 8.

In Chapter 8, intra-camera *calibration model error* significantly increased with skating velocity due to velocity dependent errors in the sampling interval and velocity dependent uncertainties in the checkerboard's reconstructed intersection positions. While the former is irrelevant in this study, as the ground truth trajectories created in

Chapter 9 had a constant 0.04-second sampling interval, the latter, caused by non-uniform errors in each camera's intrinsic model, is still relevant in this investigation. This result suggests that the effect of skating velocity in the corner skating condition is more sensitive to intra-camera *calibration model error* than *out-of-plane error*. Importantly for the multi-camera network, the size of this effect was small (Table 10-3). The difference between the slow and fast velocity condition's median RMS velocity error (0.02 m·s^{-1}) equated to only 11% of the ± 0.19 m·s^{-1} target measurement error. This value suggests that the multi-camera network's *out-of-plane error* is effectively invariant to skating velocity in the corner skating condition.

In the straight skating condition, no relationship existed between the out-of-plane distance and skating velocity, as skaters attempt to maintain an aerodynamically favourable trunk angle (van Ingen Schenau, 1982). Nevertheless, as witnessed in the corner skating condition, the RMS velocity error significantly increased with skating velocity due to intra-camera *calibration model error*. In contrast to the corner, however, the difference between the slow and fast velocity condition's median RMS velocity error (0.18 m·s^{-1}) was equivalent to 96% of the ± 0.19 m·s^{-1} target measurement error. Considering that the two skating conditions exhibited the same range of median out-of-plane distances (0.05 m), this suggests that other factors were present in the analysis.

One explanation for the large difference between the slow and fast velocity condition's median RMS velocity error is that the analysis of the straight skating condition included skating typical of the corner skating condition. This reasoning is highlighted in Figure 10-3, and evidenced in Table 10-1, as the straight skating condition exhibits a greater range of out-of-plane distances and a similar minimum out-of-plane distance. If the analysis had correctly classified the skating condition cameras for all trajectories in the ground truth dataset, I would expect the straight to have a smaller range of out-of-plane distances and a greater minimum out-of-plane distance, as the skaters do not have to lean towards the centre of rotation. Instead, as the cameras did not correctly classify the skating condition cameras for all ground truth trajectories, this artefact increased the

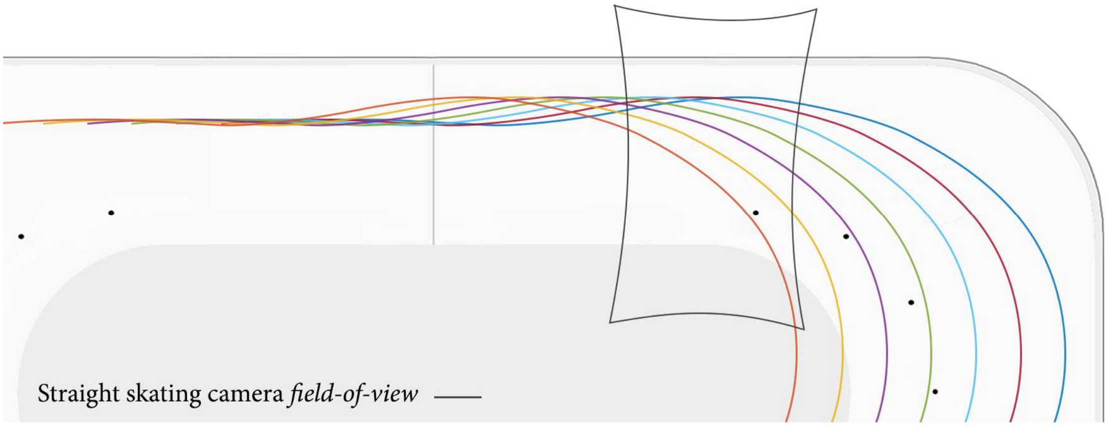

Figure 10-1. Examples of corner skating captured (and analysed) in a straight skating condition camera in the National Ice Centre (GBR) multi-camera network.

range of RMS velocity errors in each velocity condition and, as a result, increased the differences between each skating condition's RMS velocity error. For this reason, I believe that the multi-camera network's *out-of-plane error* is also effectively invariant to skating velocity in the straight skating condition.

10.5 Chapter summary

This chapter used a computer simulation to address the fifth objective of the programme of research: to quantify *out-of-plane error* in the multi-camera network. More specifically, how measured points (i.e. the fiducial marker) not on the calibrated plane (i.e. the rink surface) propagated to errors in position and velocity. The simulation showed that the multi-camera network's *out-of-plane error* (± 1.49 $m \cdot s^{-1}$) exceeded the ± 0.19 $m \cdot s^{-1}$ target measurement error. Fiducial marker out-of-plane distances, ranging from 0.6 m to 1.2 m, leading to substantial errors in position (0.01 m to 0.68 m) and velocity (0.66 $m \cdot s^{-1}$ to 1.85 $m \cdot s^{-1}$). Furthermore, the simulation demonstrated that the magnitude of this *out-of-plane error* was dependent on (1) the skating condition; significantly smaller in the corner than the straight, and (2) the skater stature; significantly increasing from the minimum, to mean, to maximum skater stature in Great Britain Short-Track Speed Skating's World Class Performance Programme. For these reasons, the multi-camera network's *out-of-plane error* must be minimised in order to measure accurate, two-dimensional, relay exchange kinematics.

Chapter 11

Minimising out-of-plane error

11.1 Introduction

Chapter 10 showed that the multi-camera network's *out-of-plane error* (± 1.49 m·s^{-1}) exceeded the ± 0.19 m·s^{-1} target measurement error. Out-of-plane distances, ranging from 0.6 m to 1.2 m, leading to substantial errors in position (0.01 m to 0.68 m) and velocity (0.66 m·s^{-1} to 1.85 m·s^{-1}). The chapter also demonstrated that the magnitude of *out-of-plane error* was dependent on (1) the skating condition; significantly smaller in the corner than the straight, and (2) the skater stature; significantly increasing from the minimum, to mean, to maximum skater stature in Great Britain Short-Track Speed Skating's World Class Performance Programme. For these reasons, Chapter 10 concluded that the multi-camera network's *out-of-plane error* must be minimised in order to measure accurate, two-dimensional, relay exchange kinematics.

In this chapter, I explore minimising this *out-of-plane error* by constructing camera-elevated plane calibration models. As reported in Section 5.3.3, camera-elevated plane calibration models minimise *out-of-plane error* by reducing the out-of-plane distance. In this case, elevating the calibration plane to the expected height of the fiducial marker. The following sections describe the investigation into the multi-camera network's *out-of-plane error* when using camera-elevated plane calibration models. The investigation also considers the effect of skating condition, skater stature, and skating velocity on *out-of-plane error*, to provide a more detailed understanding of the efficacy of camera-elevated plane calibration models in the multi-camera network.

11.2 Method

The multi-camera network's *out-of-plane error* was quantified using a revised version of the simulation described in Chapter 10. All revisions are detailed in Section 11.2.1.

11.2.1 Revisions

First, in Chapter 10 the simulation reconstructed each camera's ground truth trajectories into the global coordinate system using the camera-rink plane calibration models constructed in Chapter 8. In this investigation, the simulation reconstructs each camera's ground truth trajectories into the global coordinate system using the camera-elevated plane calibration models detailed in Section 10.2.2.

Second, in Chapter 10 the simulation defined the out-of-plane distance as the median z component of a camera's ground truth trajectory. In this simulation, the analysis defines out-of-plane distance as the median difference between the z component of the camera's ground truth trajectory and the height of the camera's elevated plane calibration model.

11.2.2 Camera-elevated plane calibration models

For each ground trajectory, the simulation constructed the camera-elevated plane calibration models – as described in Section 5.3.3 – using the control points and camera-rink plane calibration models documented in Chapter 8. The simulation projected each camera's control points at 45% and 59% of the skater's stature in the corner and straight respectively, to mitigate the effect of skating condition (Section 10.3.1) and skater stature (Section 10.3.2) on *out-of-plane error*.

The two scaling coefficients were determined using the six, real-world, fiducial marker trajectories described in Section 9.2. I calculated these coefficients as the mean height of the fiducial marker – normalised to the percentage of skater stature – during the corner and straight skating conditions defined in Section 8.3.3. Note that this calculation included the trial omitted from the synthetic fiducial marker dataset (Section 9.2.5).

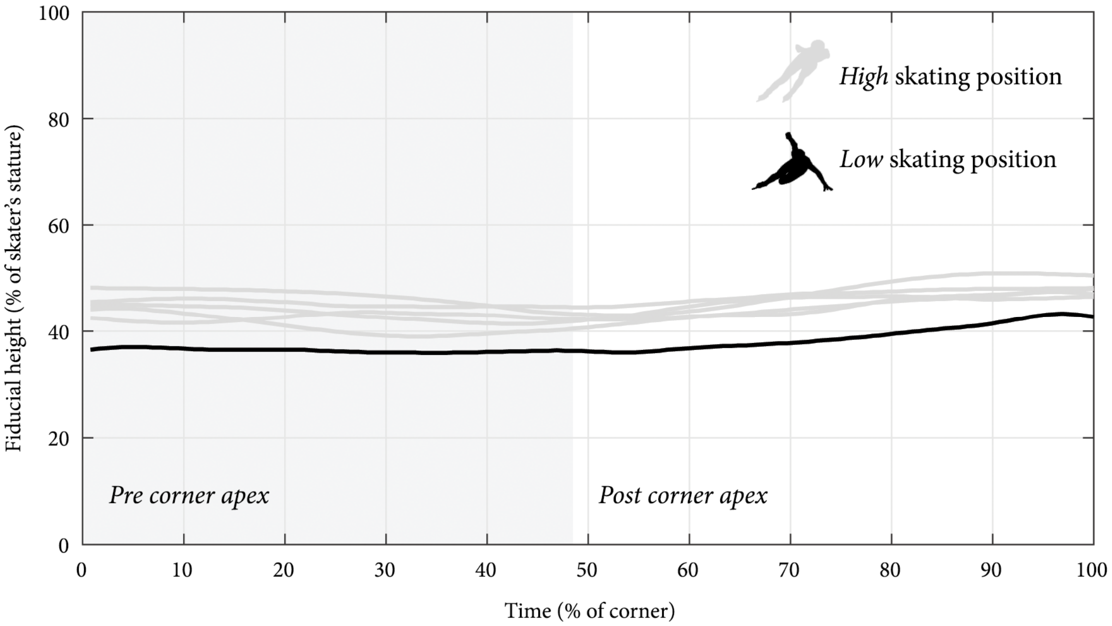

Figure 11-1. An example of the lower fiducial marker position during the corner skating condition when a skater supports their lean towards the centre of rotation by placing their left hand on the rink surface.

This trial characterised the height of the fiducial marker in the scenario where a skater supports their lean towards the corner's centre of rotation by placing their left hand on the rink surface. As illustrated in Figure 11-1, this scenario results in a lower fiducial marker height. The inclusion of this trial ensured that the scaling coefficients were more representative of short-track speed skating and less biased towards the ground truth dataset used in the simulation.

11.3 Results

A total of 6,846 ground truth and reconstructed position and velocity trajectories were compared (corner = 3,713, straight = 3,133). The descriptive statistics are reported in Table 11-1, with an example *out-of-plane error* for both corner and straight skating conditions shown in Figure 11-2. Overall, the multi-camera network's ± 95% confidence bounds in *out-of-plane error* were ± 0.25 m·s^{-1}, with 90% of the errors falling within the ± 0.19 m·s^{-1} target measurement error.

Table 11-1. *Out-of-plane error* descriptive statistics for the corner and straight skating conditions in the National Ice Centre (GBR) multi-camera network.

Statistic	Out-of-plane distance		X position error		Y position error		Resultant velocity error	
	Corner	Straight	Corner	Straight	Corner	Straight	Corner	Straight
Median	0.00	-0.01	0.01	0.01	0.01	0.01	0.07	0.09
Q_1, Q_3	-0.03, 0.04	-0.06, 0.02	0.01, 0.02	0.01, 0.02	0.01, 0.02	0.00, 0.02	0.05, 0.11	0.06, 0.12
Minimum	-0.13	-0.33	0.00	0.00	0.00	0.00	0.00	0.02
Maximum	0.26	-0.10	0.08	0.14	0.08	0.22	0.46	0.54
± 95% CB	0.16	0.06	0.05	0.05	0.05	0.09	0.25	0.26

Notes: Q_1 and Q_3 = first and third quartiles. CB = Confidence bounds. Out-of-plane distance, X position error, and Y position error measured in metres. Resultant velocity measured in m·s^{-1}.

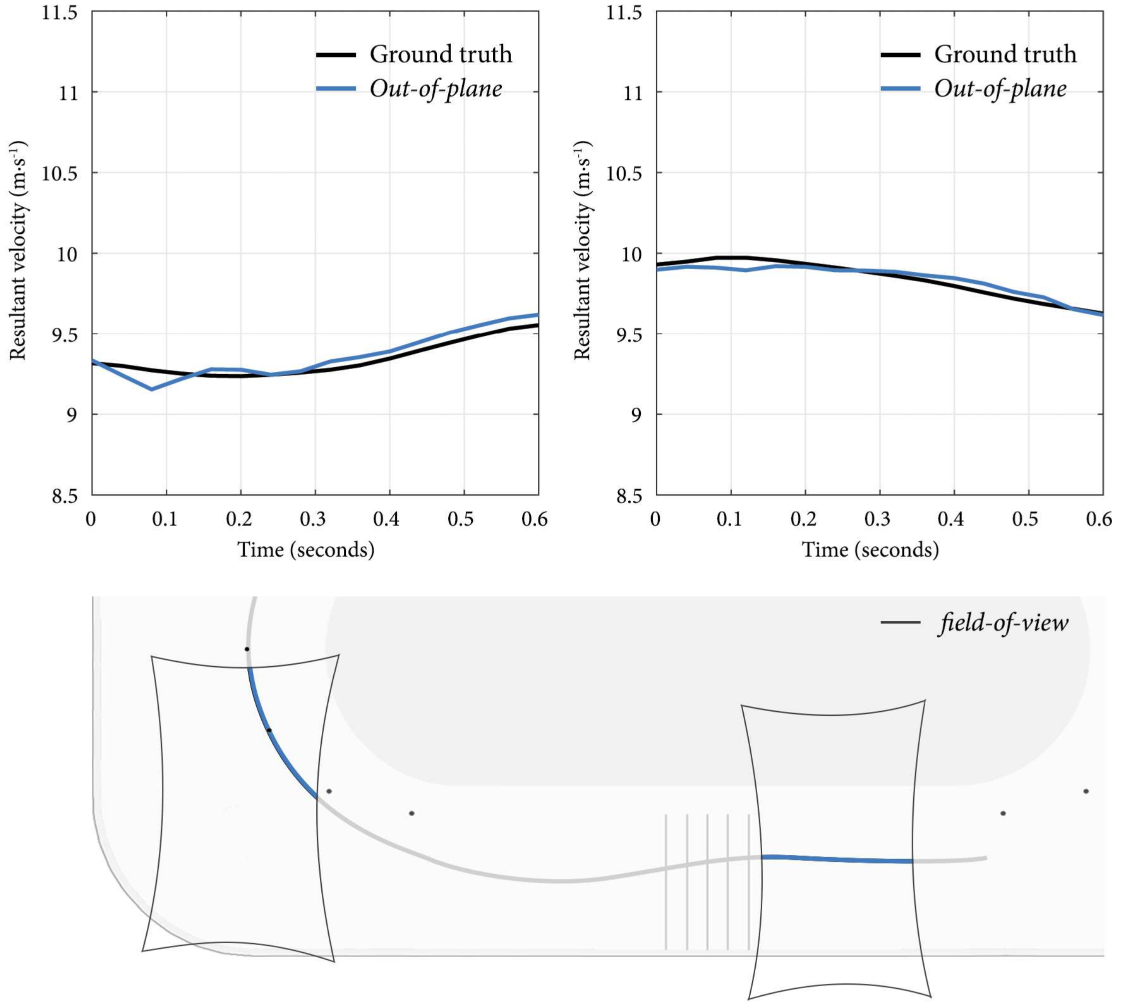

Figure 11-2. Example *out-of-plane errors* for a corner (left) and straight (right) skating condition camera in the National Ice Centre (GBR) multi-camera network when using camera-elevated plane calibration models.

11.3.1 Skating condition

There was a significant difference in *out-of-plane error* between the corner and straight skating conditions, U = 6.81 x 10^6, p = 0.000, r = 0.15 (a small effect). The RMS velocity error was smaller during the corner ($\widetilde{v_3}$ = 0.07 m·s^{-1}) than the straight ($\widetilde{v_3}$ = 0.09 m·s^{-1}).

11.3.2 Skater stature

There was a significant main effect for skater stature on *out-of-plane error* in both corner ($H(2)$ = 6.95 x 10^1, p = 0.000) and straight ($H(2)$ = 6.84 x 10^1, p = 0.000) skating conditions. The post hoc pairwise comparisons are summarised in Table 11-2. In both

Table 11-2. Effect of skater stature on *out-of-plane error*: post hoc pairwise comparisons.

Condition	Stature $_{(1-2)}$	$\tilde{z}$ Dist$_1$	$\tilde{z}$ Dist$_2$	$\widetilde{v_3}$ Error$_1$	$\widetilde{v_3}$ Error$_2$	U	p	r
Corner	Min - Mean	0.01	-0.02	0.06	0.07	$-1.86 \text{ x } 10^2$	0.000	-0.09
	Min - Max	0.01	0.01	0.06	0.08	$-3.59 \text{ x } 10^2$	0.000	-0.17
	Max - Mean	0.01	0.01	0.08	0.07	$-1.73 \text{ x } 10^2$	0.000	-0.08
Straight	Min - Mean	-0.01	0.00	0.08	0.09	$-1.92 \text{ x } 10^2$	0.000	-0.11
	Min - Max	-0.01	-0.01	0.08	0.10	$-3.26 \text{ x } 10^2$	0.000	-0.18
	Max - Mean	-0.01	0.00	0.10	0.09	$-1.33 \text{ x } 10^2$	0.000	-0.07

Notes: Skater statures (min, mean and max) represent values of 1.52, 1.69 and 1.86 m, respectively. $\tilde{z}$ Dist = Median out-of-plane distance measured in metres. $\widetilde{v_3}$ Error = Median *out-of-plane error* measured in m·s^{-1}. U = Mann-Whitney U-Test. Significance values adjusted using the Bonferroni correction to control for family-wise error. Magnitude of effect, r, measured using Pearson's correlation coefficient.

skating conditions, the magnitude of *out-of-plane error* was significantly smaller for the minimum stature compared to the mean stature (r_c = -0.09, r_s = -0.11), the mean stature compared to the maximum stature (r_c = -0.08, r_s = -0.07), and the minimum stature compared to the maximum stature (r_c = -0.17, r_s = -0.18).

11.3.3 Skating velocity

There was a significant main effect for skating velocity on *out-of-plane error* in both corner ($H(2) = 4.47 \text{ x } 10^2$, p = 0.000) and straight ($H(2) = 1.04 \text{ x } 10^2$, p = 0.000) skating conditions. Table 11-3 summarises the post hoc pairwise comparisons. In both skating conditions, the magnitude of *out-of-plane error* was significantly smaller for the slow velocity compared to the medium velocity (r_c = -0.02, r_s = -0.13), the medium velocity compared to the fast velocity (r_c = -0.4, r_s = -0.1), and the slow velocity compared to the fast velocity (r_c = -0.42, r_s = -0.22).

11.4 Discussion

This investigation aimed to minimise the National Ice Centre (GBR) multi-camera network's *out-of-plane error* by constructing camera-elevated plane calibration models.

Table 11-3. Effect of skating velocity on *out-of-plane error*: post hoc pairwise comparisons.

Condition	Velocity $_{(1-2)}$	$\tilde{z}$ Dist$_1$	$\tilde{z}$ Dist$_2$	$\widetilde{v_3}$ Error$_1$	$\widetilde{v_3}$ Error$_2$	U	p	r
Corner	Slow - Med	0.02	-0.02	0.06	0.06	-3.25×10^1	0.000	-0.02
	Slow - Fast	0.02	-0.04	0.06	0.10	-9.44×10^2	0.000	-0.42
	Fast - Med	-0.04	-0.02	0.10	0.06	-9.11×10^2	0.000	-0.40
Straight	Slow - Med	-0.03	0.01	0.08	0.09	-2.44×10^2	0.000	-0.13
	Slow - Fast	-0.03	0.00	0.08	0.10	-4.31×10^2	0.000	-0.22
	Fast - Med	0.00	0.01	0.10	0.09	-1.87×10^2	0.000	-0.10

Notes: Skating velocity (slow, med and fast) akin to approximately 12, 11, and 10 second lap times, respectively. $\tilde{z}$ Dist = Median out-of-plane distance measured in metres. $\widetilde{v_3}$ Error = Median *out-of-plane error* measured in m·s^{-1}. U = Mann-Whitney U-Test. Significance values adjusted using the Bonferroni correction to control for family-wise error. Magnitude of effect, r, measured using Pearson's correlation coefficient.

To provide a more detailed insight into the efficacy of these elevated calibration planes, the investigation also considered the effect of skating condition, skater stature, and skating velocity on *out-of-plane error*. The results showed that the multi-camera network's *out-of-plane error* (± 0.25 m·s^{-1}) still exceeded the ± 0.19 m·s^{-1} target measurement error when using these calibration models. Nevertheless, the camera-elevated plane calibration models significantly reduced the magnitude of *out-of-plane error* compared to the rink-plane calibration models (± 1.49 m·s^{-1}), with 90% of the errors now within the target measurement error. I attribute this reduction in *out-of-plane error* to the camera-elevated plane calibration models reducing the multi-camera network's out-of-plane distances. In Chapter 10, I reported that these distances ranged from 0.6 m to 1.2 m. In this investigation, the distances ranged from -0.33 m to 0.26 m.

The 10% of *out-of-plane errors* that exceeded the ± 0.19 m·s^{-1} target measurement error were the result of errors in the classification of the cameras' skating condition. In Chapter 8, I classified cameras as either corner or straight skating based on their rink surface field-of-view. However, as illustrated in Figure 10-3, depending on the current short-track and skater trajectory this classification can be incorrect. For example, in

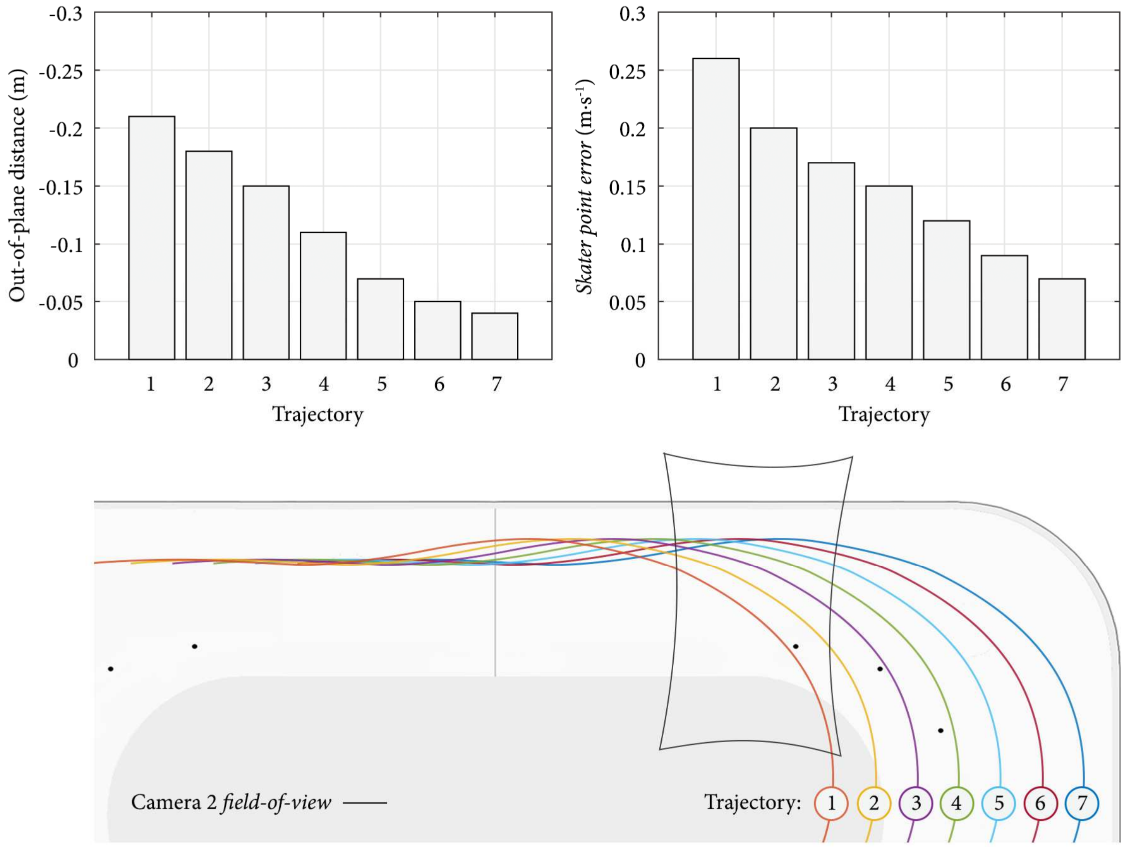

Figure 10-3. Example misclassification of skating condition cameras in the National Ice Centre (GBR) multi-camera network. The multi-camera network captures corner skating (Trajectory 1 and Trajectory 2) in a straight skating condition camera (Camera 2). As a result, the elevated calibration plane is less effective at minimising out-of-plane distances. This larger distance leads to *out-of-plane errors* that exceed the ± 0.19 m·s^{-1} target measurement error.

Figure 10-3, the multi-camera network captures corner skating – trajectory 1 and trajectory 2 – in a straight skating condition camera. As a result, the camera-elevated plane calibration model is less effective at reducing out-of-plane distances, leading to *out-of-plane errors* that exceed the ± 0.19 m·s^{-1} target measurement error. Accordingly, the multi-camera network can minimise these errors by dynamically classifying each camera's skating condition depending on the current short-track position.

Effect of skating condition on out-of-plane error

Consistent with the findings of Chapter 10, the results showed that *out-of-plane error* was significantly smaller in the corner skating condition than the straight. In Chapter 10, I reported that the difference in skating condition RMS velocity error was due to the skating technique. As skaters lean towards the centre of rotation to maintain the balance of forces between the skate and ice (Chun, 2001; Yule & Payton, 2000), the corner skating condition exhibited smaller out-of-plane distances as the fiducial marker was closer to the calibrated rink surface. This explanation was not the case in this investigation, as I minimised out-of-plane distances by constructing camera-elevated plane calibration models, at the expected height of the fiducial marker, in both skating conditions.

In this study, the difference in skating condition RMS velocity error was due to the corner's scaling coefficient being more effective at minimising out-of-plane distances. Table 11-1 shows that the corner had a smaller range of out-of-plane distances (0.39 m) compared to the straight (0.43 m). Interestingly, this result may be due to the misclassification of skating condition cameras rather than an incorrect straight scaling coefficient. As shown in Figure 11-3, straight skating condition cameras captured corner skating in the multi-camera network. Nevertheless, the size of this observed effect was small; the difference between the corner and straight median RMS velocity error (0.02 $m \cdot s^{-1}$) equivalent to only 8% of the ± 0.19 $m \cdot s^{-1}$ target measurement error. For this reason, the results suggest that when using camera-elevated plane calibration models, the multi-camera network's *out-of-plane error* is effectively invariant to the skating condition.

Effect of skater stature on out-of-plane error

In agreement with Chapter 10, in both corner and straight skating conditions, the multi-camera network's *out-of-plane error* significantly increased from the minimum, to mean, to maximum stature in Great Britain Short-Track Speed Skating's World Class Performance Programme. In Chapter 10, I reported that these differences were due to out-of-plane distances increasing with skater stature. However, this was not the case in this investigation, as I constructed camera-elevated plane calibration models to a set percentage of the skater's stature in both skating conditions.

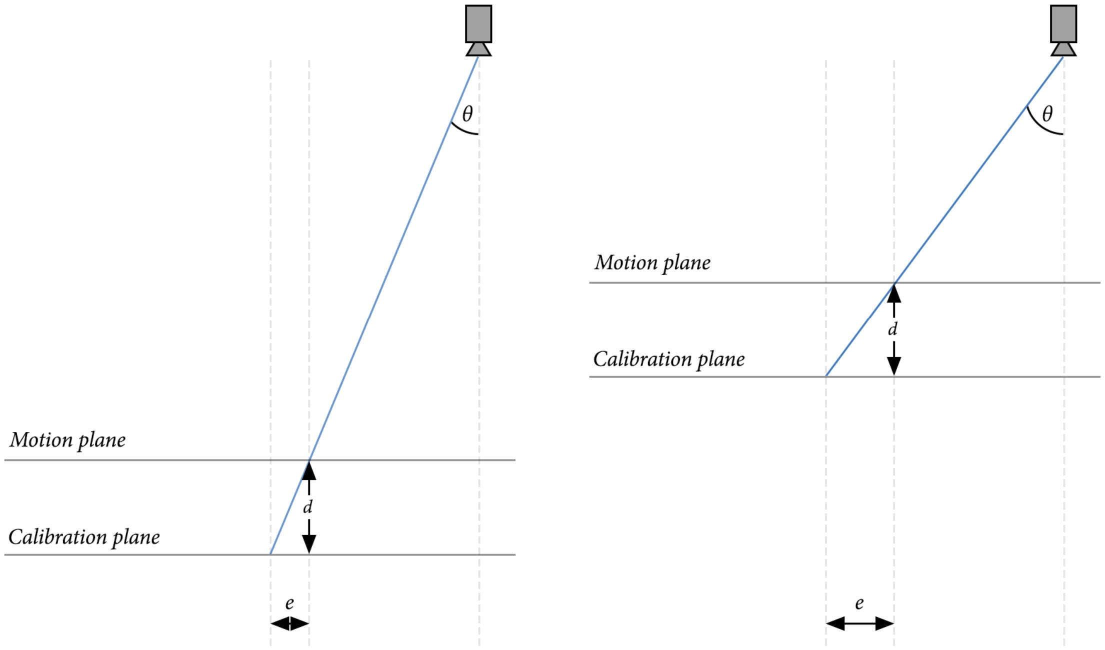

Figure 10-4. Effect of skater stature on *out-of-plane error*. For a given skater position and out-of-plane distance, *d*, the magnitude of *out-of-plane error*, *e*, is significantly larger for a taller skater stature (right), due to the angle of incidence, *θ*, increasing. The size of this effect – amplified in this figure for illustrative purposes – ranges from trivial to small.

In this investigation, *out-of-plane errors* significantly increased with skater stature due to the angle of incidence also increasing. Figure 10-4 demonstrates how constructing camera-elevated plane calibration models to a set percentage of a skater's stature, leads to a greater angle of incidence – and thus a larger *out-of-plane error* – for a taller stature skater. Importantly for the multi-camera network, when comparing the minimum and maximum skater stature condition, the difference between the median RMS velocity error in the corner (0.01 $m \cdot s^{-1}$) and straight (0.02 $m \cdot s^{-1}$) equated to only 7% and 10% of the ± 0.19 $m \cdot s^{-1}$ target measurement error. Accordingly, this findings suggest that when using camera-elevated plane calibration models, the multi-camera network's *out-of-plane error* is effectively invariant to the skater stature.

Effect of skating velocity on out-of-plane error

In both skating corner and straight skating conditions, the multi-camera network's *out-of-plane error* was significantly larger as the skating velocity increased from the slow, to medium, to fast velocity condition. As the magnitude of RMS velocity error did not increase with the associated out-of-plane distance (Table 11-3), as in Chapter 10, the larger *out-of-plane errors* were due to the effect of skating velocity being more sensitive to intra-camera *calibration model error* than out-of-plane distances. At faster skating velocities, a greater difference in two measured position's intrinsic model error – the result of non-uniform error's in each camera's intrinsic model – leading to larger *out-of-plane errors*.

Importantly for the multi-camera network, when comparing the slow and fast velocity condition, the difference between the median RMS velocity error in the corner (0.04 $m \cdot s^{-1}$) and straight (0.02 $m \cdot s^{-1}$) only equated to 21% and 9.8% of the ± 0.19 $m \cdot s^{-1}$ target measurement error. Interestingly, the corner skating condition was more sensitive to skating velocity than the straight due to a more substantial difference in out-of-plane distance (corner = 0.06 m, straight = 0.03 m). This greater distance suggests that while skating velocity is more sensitive to intra-camera *calibration model error*, the magnitude of out-of-plane distance still influences the overall velocity error. For this reason, future research could continue to explore minimising *out-of-plane error* in the National Ice Centre (GBR) multi-camera network by constructing camera-elevated plane calibration models specific to the skating velocity. Still, for this thesis, the findings suggest that when using camera-elevated plane calibration models, the multi-camera network's *out-of-plane error* is effectively invariant to the skating velocity.

11.5 Chapter summary

This chapter constructed camera-elevated plane calibration models – specific to the skating condition and skater stature – to minimise *out-of-plane error* in the National Ice Centre (GBR) multi-camera network. The chapter showed that the multi-camera network's *out-of-plane error* (± 0.25 $m \cdot s^{-1}$) still exceeded the ± 0.19 $m \cdot s^{-1}$ target measurement error when using these calibration models. However, the camera-elevated plane calibration models significantly reduced the magnitude of *out-of-plane error* compared to rink-plane calibration models (± 1.49 $m \cdot s^{-1}$), with 90% of the errors now within the target measurement error. Furthermore, the magnitude of *out-of-plane error* was now effectively invariant to the skating condition, skater stature, and skating velocity. The chapter concluded that this improvement in *out-of-plane error* was due to minimising the out-of-plane distances between the calibrated plane and fiducial marker. Furthermore, the remaining 10% of errors – attributed to the misclassification of each camera's skating condition – could be reduced by classifying each camera's skating condition dynamically.

Chapter 12

Digitisation uncertainty in the multi-camera network

12.1 Introduction

This chapter begins to address the sixth objective of the programme of research: to quantify *skater point error* in the multi-camera network. *Skater point error* describes how uncertainty in the automated digitisation of a skater propagates to errors in position and velocity. In the Olympic Oval (CAN) multi-camera network, this uncertainty (2.61 pixels) led to errors in velocity (± 1.04 $m{\cdot}s^{-1}$) that exceeded the ± 0.19 $m{\cdot}s^{-1}$ target measurement error. In Section 5.2, I identified that a fiducial marker-based automated digitisation algorithm could minimise this uncertainty by reducing the ambiguity in the digitised point. Moreover, to aid the digitisation algorithm, the fiducial marker should be coloured, and positioned on a dark skin suit, to enhance the contrast between the fiducial, skin suit, and rink surface.

In the following sections, I describe the developed fiducial marker-based automated digitisation algorithm and an investigation into the algorithm's digitisation uncertainty. First, the investigation quantifies the algorithm's automated digitisation uncertainty for six different candidate fiducial marker colours, as Great Britain Short-Track Speed Skating requires a minimum of four unique markers to distinguish between relay teams. Second, the investigation considers the effect of the skating condition on automated digitisation uncertainty, as the appearance of a skater – and thus the fiducial marker – differs between the corner and straight (Section 4.3.2). The results of this chapter are used in Chapter 13 to quantify the multi-camera network's *skater point error*.

12.2 Fiducial marker automated digitisation algorithm

The National Ice Centre (GBR) multi-camera network's fiducial marker-based automated digitisation algorithm was developed in MATLAB R2016a (MathWorks, 2016). The algorithm, described in Sections 12.2.1 to 12.2.7, consists of seven stages. The stages begin once the multi-camera network either manually initialises (Section 5.4.4) or automatically predicts (Section 5.4.2) the fiducial marker's position in the current image. In the multi-camera network, the predictions are made using the alpha-beta filter described in Section 5.4.2 ($\alpha = 0.5$ and $\beta = 2$). When applied to the ground truth dataset, a typical alpha-beta filter prediction error in the corner and straight skating condition, i.e. the resultant difference between the ground truth and predicted pixel coordinates, is 0.86 ± 0.44 pixels and 0.93 ± 0.61 pixels, respectively.

12.2.1 Search neighbourhood

The algorithm creates a 33 x 33-pixel search neighbourhood around the predicted fiducial marker position (measured to the nearest pixel). Figure 12-1b illustrates three typical examples of this search neighbourhood. In the first example, the search neighbourhood only contains the fiducial marker and skin suit. In the second and third example, ice is also present. In this scenario, the skin suit either completely or partially surrounds the fiducial marker. In the latter case, the fiducial marker meets the rink surface and highlights why a white coloured fiducial – which should provide the maximum contrast with a black skin suit – is not suitable in the multi-camera network.

12.2.2 Colour segmentation

The algorithm transforms the search neighbourhood from the RGB to HSV colour space, and then applies a threshold to the hue channel, to identify pixels similar to the colour of the fiducial marker. The result is a binary image where pixels similar to the colour of the fiducial marker are white (foreground), and all other pixels are black (background). Figure 12-1c demonstrates these binary images for each search neighbourhood example.

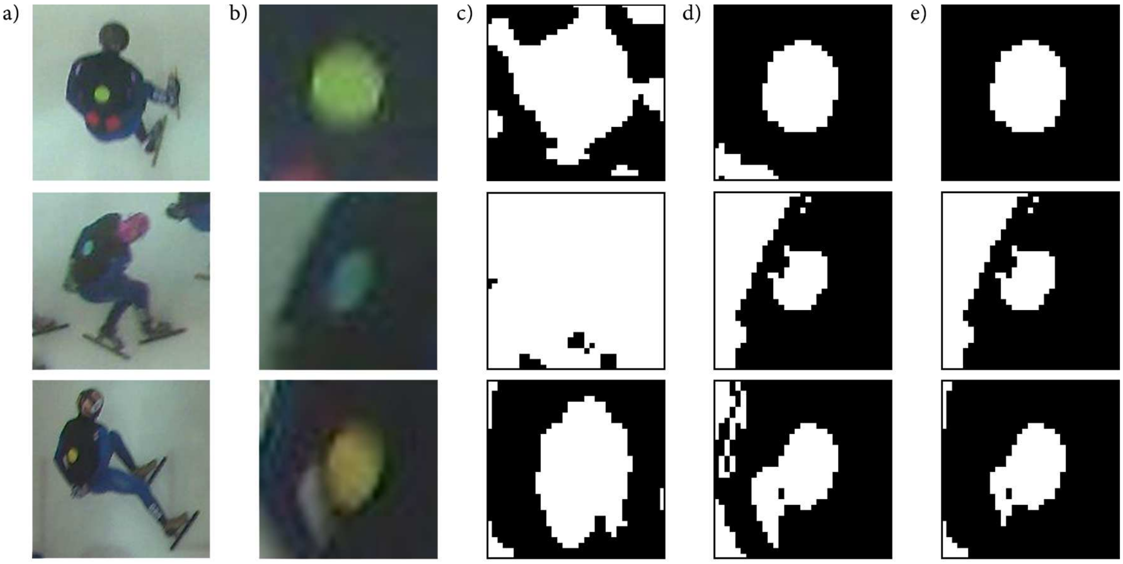

Figure 12-1. Three examples of the first three stages of the fiducial marker automated digitisation algorithm: (a) the fiducial marker as seen in the multi-camera network, (b) the search neighbourhood, (c) the colour segmentation binary image, (d) the skin suit segmentation binary image, and (e) the product of the colour segmentation and skin suit binary images.

The HSV colour space represents a colour by its hue (H), saturation (S) and value (V). Hue is a chromatic feature that describes a pure colour, saturation is a measure of how the white light dilutes the hue, and value is the intensity or brightness of the colour (Garcia-Lamont, Cervantes, López, & Rodriguez, 2018). The colour segmentation procedure uses the hue channel, as this channel is invariant to changes in illumination (Liu & Tang, 2009). The result of the hue data being decoupled from the value component (Garcia-Lamont et al., 2018). This decoupling is important in the multi-camera network as Section 4.3.1 demonstrated that the appearance of an image, i.e. it's intensity or brightness, varies due to changes in the ambient lighting and differences in the proximity of each camera to the available light sources.

12.2.3 Skin suit segmentation

At this stage, foreground pixels in the fiducial marker binary image include the skater's skin suit. The algorithm applies a threshold to the search neighbourhood's value channel to classify the skin suit as background. The result is a second binary image where the skin suit's pixels are black and all other pixels, including the fiducial marker, are white.

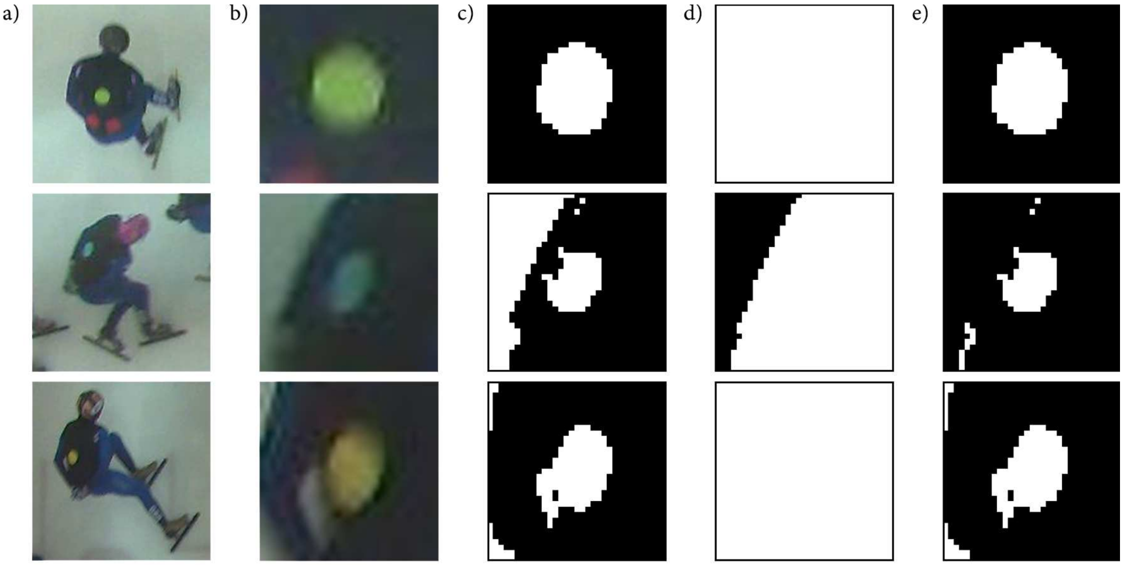

Figure 12-2. Three examples of the fiducial marker automated digitisation algorithm's ice segmentation: (a) the fiducial marker as seen in the multi-camera network, (b) the search neighbourhood, (c) the product of the colour segmentation and skin suit binary images, (d) the ice segmentation binary image, and (e) the product of the current fiducial marker and ice segmentation binary image.

Figure 12-1d demonstrates these binary images for each search neighbourhood example. As illustrated in Figure 12-1e, the product of these two binary images removes the skin suit from the fiducial marker binary image.

The algorithm selects the value channel's threshold using the search neighbourhood's median value and a set coefficient. The median value represents the intensity of the skin suit, and the addition of a set coefficient ensures that the threshold includes all skin suit pixel intensities.

12.2.4 Ice segmentation

As illustrated in Figure 12-2c, after the colour and skin suit segmentation the foreground pixels in the fiducial marker binary image may still include ice. The algorithm removes this ice by creating a third binary image where ice is black and all other pixels, including the fiducial marker and skin suit, are white. Figure 12-2d demonstrates these binary images for each search neighbourhood example. Note that if the search neighbourhood is all foreground, i.e. white, no ice was detected. As shown in

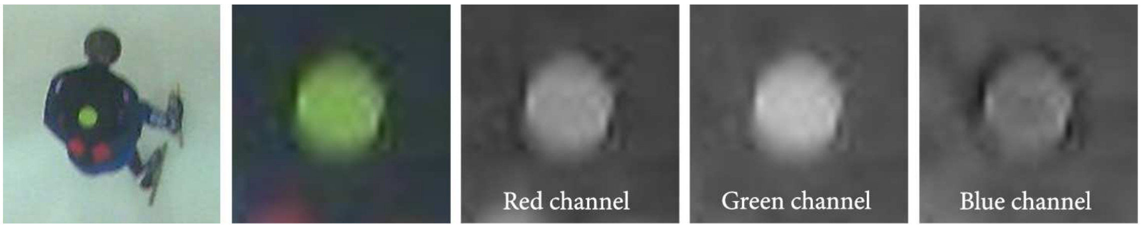

Figure 12-3. The green fiducial marker as seen in the Red, Green, and Blue colour channel in the National Ice Centre (GBR) multi-camera network. The blue channel is used to determine the ice segmentation threshold as the intensity of the fiducial marker and skin suit are most similar.

Figure 12-2e, the product of these two images removes ice from the fiducial marker binary image.

The algorithm creates the ice segmentation binary image by thresholding a single channel from the RGB search neighbourhood created in Section 12.2.1. The algorithm uses the colour channel where the intensity of the fiducial marker and skin suit are most similar. For example, and as illustrated in Figure 12-3, the blue channel when the fiducial marker is green. The intensity level of the threshold is selected using Otsu’s automated method (Otsu, 1979). The algorithm applies Otsu's method to the selected RGB channel on a 60 x 60-pixel search neighbourhood centred on the predicted position of the fiducial marker. The combination of the larger search neighbourhood and the selected RGB channel ensures that the distribution of intensities in the image is bimodal. One mode represents the ice, the other, the fiducial marker and skin suit.

12.2.5 Candidate selection

After colour, skin suit, and ice segmentation, all foreground objects in the binary image represent candidate fiducial markers. Figure 12-4c demonstrates these candidate fiducial markers for each search neighbourhood example. As illustrated in Figure 12-4d, to remove small foreground objects that don't represent the fiducial marker, the algorithm uses a morphological opening operation. The opening procedure – which uses a 1x1 disk-shaped structuring element – consists of morphological erosion followed by morphological dilation (Section 5.2.3). Then, in the case where more than one candidate

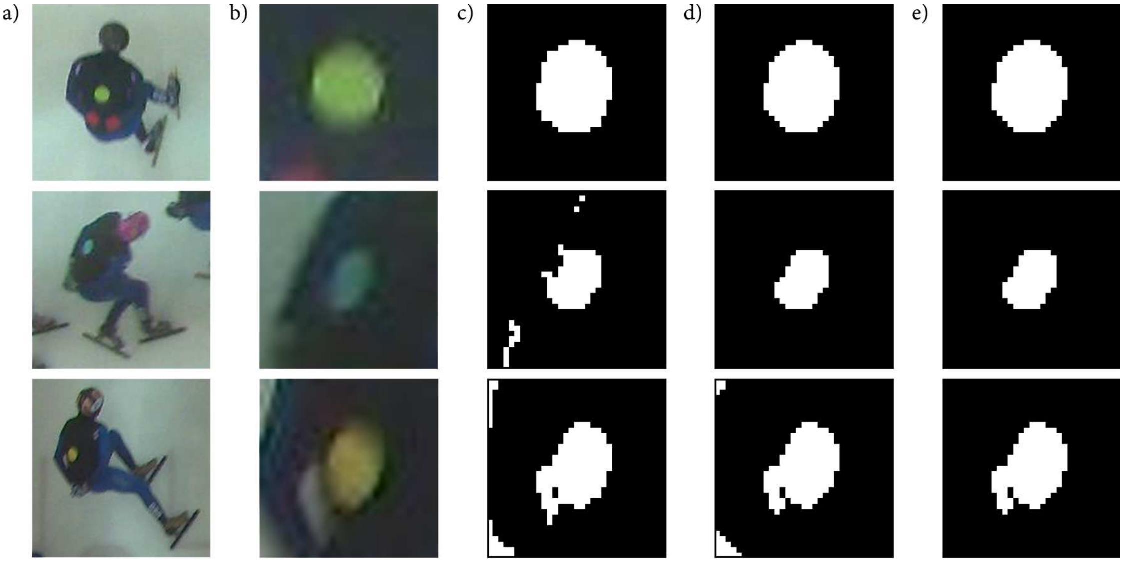

Figure 12-4. Three examples of the fiducial marker automated digitisation algorithm's candidate selection: (a) the fiducial marker as seen in the multi-camera network, (b) the search neighbourhood, (c) the product of the current fiducial marker and ice segmentation binary image, (d) the fiducial marker binary image after morphological opening, and (e) the fiducial marker binary image after candidate selection.

exists, the algorithm selects the best candidate. This procedure requires the geometric centroid of each object to be calculated (*Eq*. 5.1). As shown in Figure 12-4e, the algorithm selects the candidate with the smallest Euclidian distance from the geometric centroid to the centre of the search neighbourhood as the fiducial marker.

12.2.6 Fiducial marker processing

The selected fiducial marker's foreground object may include noise, i.e. the incorrect classification of pixels during the colour, skin suit, and ice segmentation methods. For example, Figure 12-5c shows a scenario where the algorithm does not remove the ice between a skater's torso and arm, as the intensity of the ice is similar to that of the skater. The algorithm removes this type of noise by filtering the product of the fiducial marker's foreground object and the search neighbourhood's value channel. This process removes any pixel from this image where the intensity is less than a selected threshold; set as the image's maximum pixel intensity minus the product of (1) the pixel intensity standard deviation, and (2) a set coefficient. The set coefficient, dependent on the fiducial marker

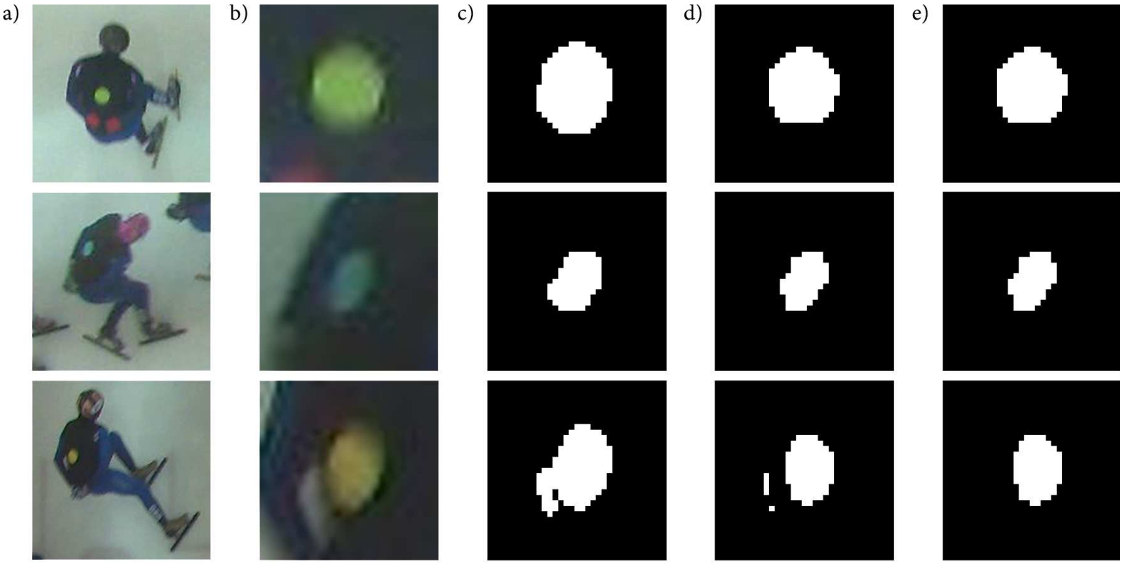

Figure 12-5. Three examples of the fiducial marker automated digitisation algorithm's fiducial marker processing: (a) the fiducial marker as seen in the multi-camera network, (b) the search neighbourhood, (c) the fiducial marker binary image after candidate selection, (d) the fiducial marker binary image after fiducial marker processing, and (e) the fiducial marker binary image after candidate selection.

colour, means that this process removes 0.1 to 5% of the minimum pixel intensities from the original foreground object.

In the example described above, this process separates the foreground object into two candidate markers (Figure 12-5d). As a result, the algorithm reperforms candidate selection (as described in Section 12.2.5) to select the correct candidate (Figure 12-5e). Note that in the scenario where no noise is present, the filtering procedure only removes pixels from the edge of the foreground object. This pixel removal does not notably change the geometric centroid of the fiducial marker.

12.2.7 Pixel coordinate transformation

At present, the algorithm has measured the fiducial marker's geometric centroid in the search neighbourhood coordinate system ($Search_u$, $Search_v$). The algorithm transforms these coordinates into the image's pixel coordinate system to allow the fiducial marker position to be reconstructed into the global coordinate system. Figure 12-6 illustrates this transformation.

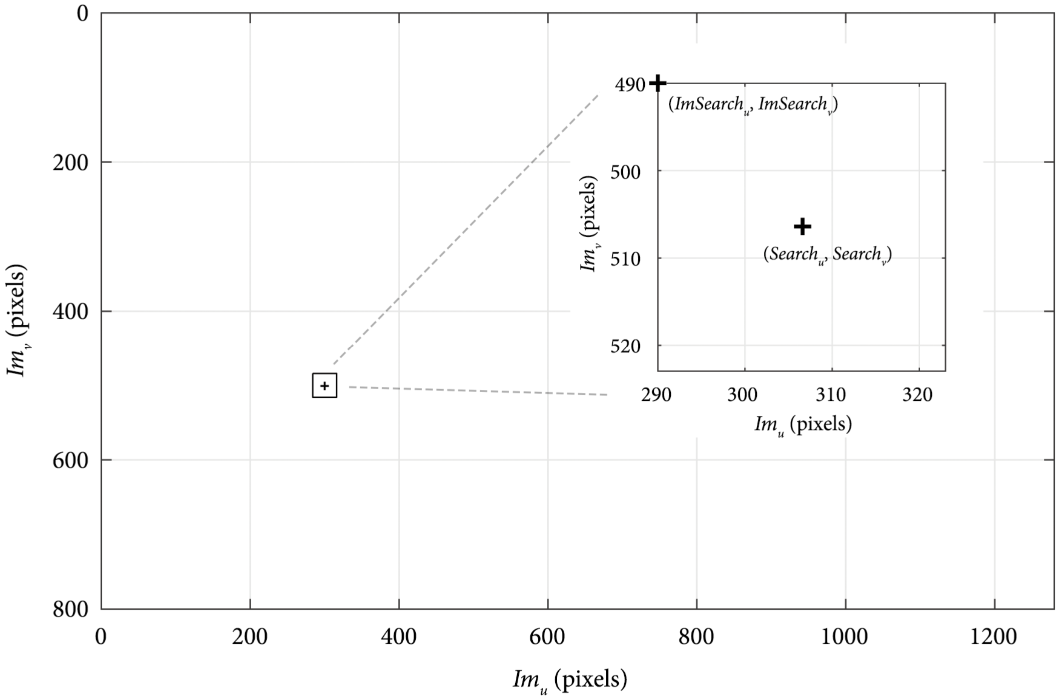

Figure 12-6. Pixel coordinate transformation. The automated digitisation algorithm transforms the fiducial marker position ($Search_u$, $Search_v$) from the search neighbourhood coordinate system to the image pixel coordinate system (Im_u, Im_v) using the pixel coordinates of the search neighbourhood's top left corner in the image pixel coordinate system ($ImSearch_u$, $ImSearch_v$).

First, the algorithm calculates the pixel coordinates of the search neighbourhood's top left corner in the image's pixel coordinate system ($ImSearch_u$, $ImSearch_v$),

$$ImSearch_u = nint(Predicted_u) - 16 \qquad (Eq. 12.1)$$

$$ImSearch_v = nint(Predicted_v) - 16 \qquad (Eq. 12.2)$$

where $Predicted_u$ and $Predicted_v$ is the predicted position of the fiducial marker used in Section 12.2.1. If either $ImSearch_u$ or $ImSearch_v$ is outside the image's pixel coordinate system, the algorithm sets the relevant coordinate to one. Second, the algorithm calculates the fiducial marker's position in the image's pixel coordinate system (Im_u, Im_v)

$$Im_u = ImSearch_u + Search_u \qquad (Eq. 12.3)$$

$$Im_v = ImSearch_v + Search_v \qquad (Eq. 12.4)$$

Figure 12-7. The six candidate fiducial marker colours as seen in the National Ice Centre (GBR) multi-camera network. From left to right (1) red, (2) yellow, (3) green, (4) cyan, (5) blue, and (6) magenta.

12.3 Method

This investigation quantified uncertainty in Section 12.2’s automated digitisation algorithm by comparing the algorithm's outputs to manually digitised ground truth data for six candidate fiducial marker colours.

12.3.1 Candidate fiducial marker colours

The six candidate fiducial marker colours – red, yellow, green, cyan, blue, and magenta – represented 60° intervals in the hue colour space. As described in Section 9.2.2, each fiducial marker (0.12 m in diameter) was positioned on a black vest 0.1 m above the skater’s two-dimensional centre-of-mass point estimate (i.e. the 1st lumbar vertebra). Figure 12-7 shows a typical image of each candidate fiducial marker colour in the National Ice Centre (GBR) multi-camera network.

12.3.2 Fiducial marker test set

Images of all candidate fiducial marker colours were collected using the National Ice Centre (GBR) multi-camera network during three Great Britain Short-Track Speed Skating training sessions over a two-week period. For each fiducial marker colour, the dataset consisted of three laps (one from each training session), on different short-track positions (one to five), akin to skating velocities of approximately 10, 11 and 12 second lap times. To evaluate the automated digitisation algorithm, a test set of 100 images were selected at random for each candidate fiducial marker colour (corner skating = 50 images, straight skating = 50 images). For both skating conditions, the investigation assumed that the random image selection from different training sessions, skating

Figure 12-8. The manual digitisation procedure. First, the image the image was zoomed to enlarge the view of the marker. Second, the cursor's diameter adjusted and aligned to match the marker's outline.

velocities, and short-track positions would account for the sources of variance in a skater's – and thus fiducial markers – appearance outlined in Section 4.3.

12.3.3 Data analysis

For each image in a fiducial marker colour's test set, the pixel coordinates of the marker centre were digitised both manually and automatically. In accordance with Landry et al. (2013), the investigation defined uncertainty in the automated digitisation as the resultant difference between these two methods.

Manual skater digitisation

Check2D (Centre for Sports Engineering Research, 2013) was used to digitise the centre of each fiducial marker manually. Figure 12-8 highlights this procedure. The image was zoomed to enlarge the view of the marker and the cursor's diameter adjusted and aligned to match the fiducial's outline. All manual digitisation was performed by a single operator to negate inter-operator digitisation error. As reported in Section 9.2.4, the procedures' intra-operator error was ± 0.52 pixels.

Automated skater digitisation

The algorithm described in Section 12.2 was used to digitise the centre of each fiducial marker automatically. Table 12-1 summarises the algorithm's parameters for the six

Table 12-1. Automated digitisation algorithm parameters for each candidate fiducial marker colour.

Candidate	Hue	Hue_1	Hue_2	Coefficient_1	Ice Channel	Coefficient_2
Red	0/360	270	60	0.04	Green	2.4
Yellow	60	0	150	0.08	Blue	2.2
Green	120	60	180	0.07	Blue	2.7
Cyan	180	90	240	0.07	Red	2.7
Blue	240	120	330	0.04	Red	3.3
Magenta	300	210	45	0.07	Green	2.2

Notes: All hue measurements are expressed in degrees. The hue thresholds include all angles from Hue_1 to Hue_2 when moving in a clockwise direction. Coefficent_1 is used in the skin suit segmentation with Coefficent_2 used in the fiducial marker processing.

candidate fiducial markers. The parameters include (1) the colour segmentation minimum and maximum hue thresholds, (2) the skin suit segmentation set coefficient, (3) the ice segmentation RGB channel, and (4) the fiducial marker processing set coefficient. For each image, the algorithm created the search neighbourhood (Section 12.2.1) by using the manually digitised fiducial marker position as the predicted fiducial marker position.

12.3.4 Statistical analysis

MATLAB R2016a (MathWorks, 2016) was used to compare the automated digitisation uncertainty in the National Ice Centre (GBR) and Olympic Oval (CAN) multi-camera networks. For each candidate fiducial marker, the analysis calculated the mean absolute digitisation uncertainty for the complete test set,

$$|Mean\ digitisation\ uncertainty| = \frac{\sum_{i=1}^{n}|R_i|}{n} \qquad (Eq. 12.5)$$

where n is the number of images in the candidate fiducial markers test (n = *100*), and R_i is the resultant uncertainty (measured in pixels) in the ith image. The analysis used the complete test set, as Landry et al. (2013) did not consider the effect of skating condition on digitisation uncertainty in the Olympic Oval (CAN) multi-camera network.

Table 12-2. Normality results for each candidate fiducial marker's automated digitisation uncertainty.

	Corner			Straight		
Colour	n	W	p	n	W	p
Red	50	0.977	0.455	50	0.983	0.696
Yellow	50	0.969	0.203	50	0.967	0.186
Green	50	0.961	0.095	50	0.983	0.714
Cyan	50	0.967	0.176	50	0.886	0.000*
Blue	50	0.914	0.002*	50	0.541	0.000*
Magenta	50	0.835	0.000*	50	0.910	0.001*

Notes: n = sample size. W = Shapiro-Wilk test statistic. * Distributions significantly deviate from normal.

For each candidate fiducial marker, a Mann Whitney U-test – performed in SPSS 24 (IBM, 2016) – was used to analyse differences in automated digitisation uncertainty between the corner and straight skating conditions. As shown in Table 12-2, the analysis treated the data as non-parametric as five of the twelve fiducial marker colour datasets violated the normality assumption of parametric statistical tests. In all statistical tests, the significance level, α, was set at $p < 0.05$, with effect sizes calculated using Pearson's correlation coefficient ($Eq.\ 8.1$). Effect size magnitudes were interpreted using Cohen's thresholds; where < 0.1, is trivial; 0.1–0.3, small; > 0.3–0.5, moderate; and > 0.5, large (Cohen, 1988).

12.4 Results

Of the 600 images analysed, the algorithm automatically digitised the fiducial marker 597 times. Figure 12-9 illustrates the candidate fiducial marker colours automated digitisation uncertainty. Compared to the Olympic Oval (CAN) multi-camera network, all fiducial marker colours exhibited a smaller mean absolute digitisation uncertainty. Table 12-3 reports the results of the Mann-Whitney U-tests. For all candidate fiducial marker colours, there was no significant difference in automated digitisation uncertainty between the corner and straight skating conditions.

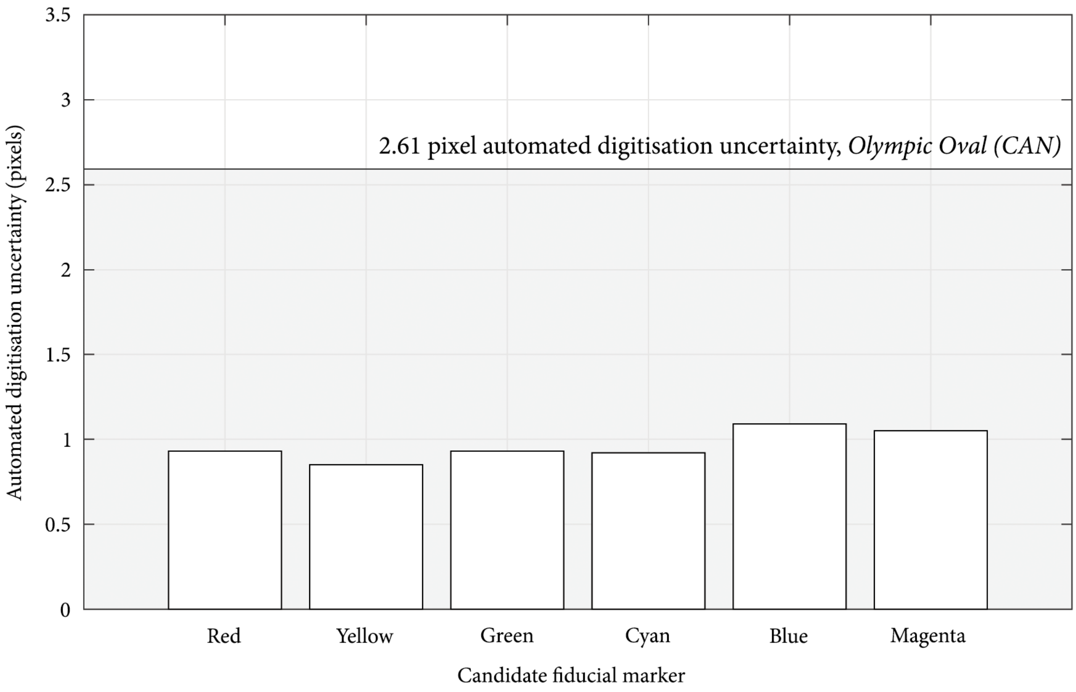

Figure 12-9. Automated digitisation uncertainty in the National Ice Centre (GBR)multi-camera network.

Table 12-3. Median automated digitisation uncertainty for the corner and straight skating conditions, Mann-Whitney *U*-test results, and effect sizes for each candidate fiducial marker colour.

Fiducial	Corner	Straight	U	p	r
Red	0.96	0.87	9.92×10^2	0.138	-0.15
Yellow	0.84	0.85	1.23×10^3	0.953	0.01
Green	0.88	0.88	1.23×10^3	0.961	0.00
Cyan	0.97	0.86	1.13×10^3	0.497	-0.07
Blue	1.05	0.97	1.08×10^3	0.236	-0.12
Magenta	0.98	1.01	1.18×10^3	0.763	-0.03

Notes: Automated digitisation uncertainty measured in pixels. Magnitude of effect, r, measured using Pearson's correlation coefficient.

12.5 Discussion

This investigation aimed to quantify automated digitisation uncertainty in the multi-camera network for six different candidate fiducial marker colours. Overall, the findings showed that for all candidate fiducial marker colours, the multi-camera network’s automated digitisation uncertainty was less than the Olympic Oval (CAN) multi-camera network. As Landry et al. (2013) reported that the Olympic Oval (CAN) multi-camera network uncertainty was due to ambiguity in the digitised point (Section 5.2.2), the observed reduction was attributed to the use of fiducial markers minimising this ambiguity. The use of fiducial markers is similar to other automated digitisation approaches, such as optical motion capture, where passive markers are used to identify anatomical landmarks of interest such as segment endpoints (Payton, 2008).

Of the 600 images analysed, the algorithm failed to digitise the fiducial marker on three occasions. Figure 12-10 illustrates each of these occasions. In the first two instances, the algorithm failed to digitise the red fiducial marker during the skin suit segmentation procedure, as the skin suit threshold was set too high (Section 12.2.3). As a result, the algorithm classified the fiducial marker's pixels as background in the skin suit binary image. This misclassification of pixels led to the loss of the fiducial marker during the multiplication of the fiducial marker and skin suit binary images. In the third instance, the algorithm failed to digitise the magenta fiducial marker during the colour segmentation procedure, as the predefined thresholds did not encapsulate the hue of the fiducial marker (Section 12.2.2). As a result, the algorithm classified the fiducial marker's pixels as background in the colour segmentation binary image. In this case, the misclassification of pixels was likely due to (1) the fiducial marker being partly occluded, and (2) noise in the image acquisition, rather than (3) incorrectly set hue thresholds. In this investigation, the magenta fiducial’s thresholds were set conservatively at ± 90° around the theoretical 300° hue (Table 12-1).

Interestingly, all three instances occurred in the periphery of Camera 1's field-of-view. As a result, the algorithm can make use of the multi-camera network's overlapping camera field-of-views to digitise these skater positions. Figure 12-10 shows that the multi-camera network sees aspects of Camera 1's field-of-view in Cameras 21, 22 and 25. These cameras provide a superior view of the fiducial marker in all three instances. In each of these new images, the algorithm successfully digitises the fiducial marker.

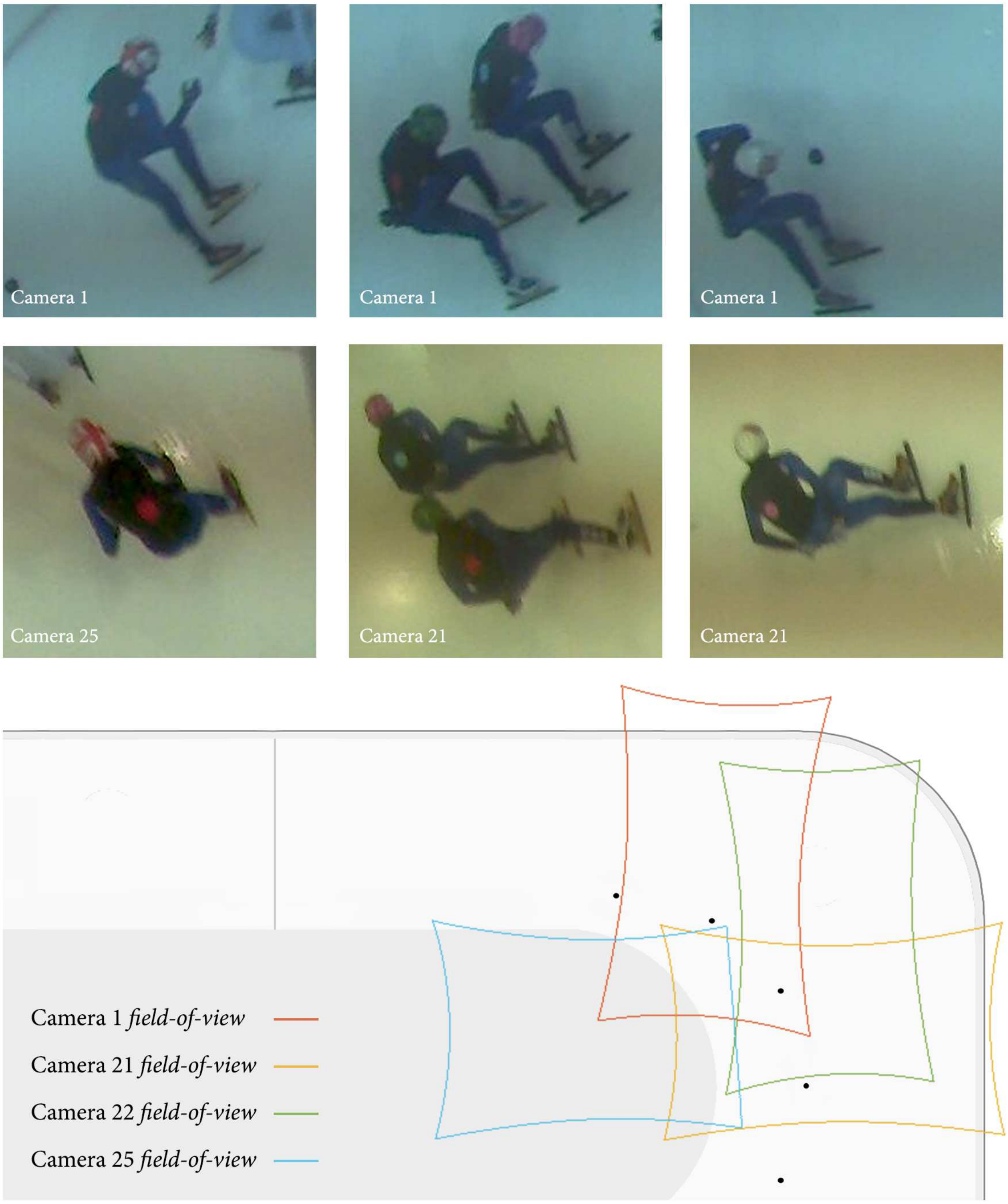

Figure 12-10. The three instances where the automated digitisation algorithm failed (top). Due to the National Ice Centre (GBR) multi-camera network's overlapping field-of-views, in each scenario an alternative camera provides a superior view of the fiducial marker for the automated digitisation algorithm. In each of these new images (bottom), the algorithm successfully digitises the fiducial marker.

Candidate fiducial marker performance

Great Britain Short-Track Speed Skating only require four unique fiducial marker colours to distinguish between relay teams. Section 12.4 showed that the automated digitisation uncertainty was less than one pixel for four fiducial marker colours (red, yellow, green, and cyan) and greater than one pixel for two fiducial markers (blue and magenta).

The blue fiducial marker’s larger uncertainty was due to the similarity in value channel pixel intensities for the fiducial marker and skin suit. This similarity led to the skin suit segmentation procedure classifying a proportion of the fiducial marker's pixels as background in the skin suit binary image (Section 12.2.3). This loss of fiducial marker pixels leads to increased digitisation uncertainty as the calculation of the geometric centroid is affected. This explanation, however, was not the case for the magenta fiducial marker as the differences in value channel pixel intensities for the fiducial marker and skin suit were akin to the other candidate fiducial marker colours. Accordingly, this suggests that other factors caused the larger automated digitisation uncertainty.

One explanation for the magenta’s larger uncertainty is that the randomly generated test sets used in the analysis were biased. For example, the magenta test set could have included more instances where a skater was in the periphery of the image, had a more pronounced lean towards the centre of rotation, and – as a result – had a partially occluded fiducial marker that was less conducive to accurate digitisation. While future work could explore whether the random selection of test set images introduced bias into the analysis, this is not necessary for this thesis as Great Britain Short-Track Speed Skating only requires four unique fiducial markers to distinguish between relay teams. As a result, the remainder of this thesis will use the four fiducial markers that exhibited sub-pixel automated digitisation uncertainty.

Effect of skating condition on automated digitisation uncertainty

The multi-camera network’s automated digitisation uncertainty was invariant to the skating condition. The results showed that there were no significant differences between the corner and straight skating condition for all six candidate markers (Table 12-3). This finding is important for the multi-camera network as the appearance of a skater in an image – and thus the fiducial marker – varies between the corner and straight due to differences in skating technique (Section 4.3.2). While both adopt a crouched skating position, skaters lean towards the centre of rotation to maintain the balance of forces between the skate and ice (Chun, 2001; Yule & Payton, 2000). As a result, the skin suit may not always surround the fiducial marker.

Limitations

This investigation has two limitations that require consideration. First, in accordance with Landry et al. (2013), the investigation assumed that the manually digitised fiducial markers represented the ground truth, i.e. the pixel coordinates contained no error. This assumption is not true as the manual digitisation procedure had a 0.52-pixel precision. Therefore, although this method allowed the National Ice Centre (GBR) multi-camera network to be compared to the Olympic Oval (CAN) multi-camera network, due to errors in the manual digitisation procedure it is possible that the investigation either over- or under-estimated the magnitude of automated digitisation uncertainty. Assuming that both the manual and automated digitisation procedures' uncertainty are stochastic and uncorrelated, the former is more likely as the overall automated digitisation uncertainty, δt, is equivalent to,

$$\delta t \;=\; \sqrt{\delta m^2 + \delta a^2} \qquad (Eq.\,12.6)$$

where δm is the uncertainty in the manual digitisation procedure, and δa is the uncertainty in the automated digitisation procedure.

Second, the investigation used the manually digitised fiducial marker pixel coordinates in the quantification of the automated digitisation algorithm's uncertainty on two occasions (1) to create the initial fiducial marker search neighbourhood (Section 12.2.1), and (2) to determine which candidate fiducial marker had the smallest Euclidean distance during the candidate selection procedure (Section 12.2.5). Therefore, despite the relatively low precision in the manual digitisation procedure, it is likely that the

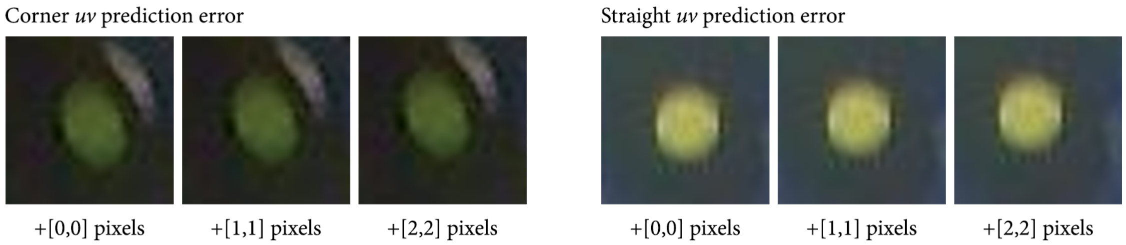

Corner *uv* prediction error

+[0,0] pixels +[1,1] pixels +[2,2] pixels

Straight *uv* prediction error

+[0,0] pixels +[1,1] pixels +[2,2] pixels

Figure 12-11. The corner and straight skating condition prediction error case studies. When I added one- and two-pixel errors to the fiducial markers' predicted position, there was no difference in the algorithm's digitised position.

investigation only evaluated the automated digitisation uncertainty in the scenario where the fiducial marker's predicted position error was less than one pixel.

Although Section 12.2 reported that the typical mean prediction error was less than one pixel in the multi-camera network (corner = 0.86 pixels, straight = 0.93 pixels), the low relative precision (corner = 0.44 pixels, straight = 0.61 pixels) means that a proportion of prediction errors will be greater than one pixel. Accordingly, the results may have underestimated the magnitude of automated digitisation uncertainty in the multi-camera network. However, in a randomly extracted corner and straight skating condition case study – illustrated in Figure 12-11 – there was no difference in automated digitisation uncertainty when I added one- and two-pixel errors to the fiducial markers' predicted position. Still, future work should provide a more detailed exploration of the effect of prediction error on automated digitisation uncertainty in the National Ice Centre (GBR) multi-camera network.

12.6 Chapter summary

This chapter began to address the sixth objective of the programme of research: to quantify *skater point error* in the multi-camera network. This error describes how uncertainty in the automated digitisation of a skater propagates to errors in position and velocity. First, the chapter described the seven stages of the National Ice Centre (GBR) multi-camera network's fiducial marker-based automated digitisation algorithm. Second, the chapter quantified the uncertainty in this developed algorithm. The results showed that the automated digitisation uncertainty was less than the Olympic Oval (CAN) multi-camera network, and invariant to the skating condition, for six candidate fiducial markers. The chapter concluded that this improvement was due to fiducial marker's, positioned at skaters' two-dimensional centre-of-mass point estimate, reducing ambiguity in the digitised point. In the next chapter, I explore how this automated digitisation uncertainty propagates to *skater point error* in the multi-camera network. As Great Britain Short-Track Speed Skating only requires four unique fiducial markers to distinguish between relay teams, the chapter uses the four fiducial markers that exhibited sub-pixel automated digitisation uncertainty.

Chapter 13

Skater point error in the multi-camera network

13.1 Introduction

Chapter 12 began to address the sixth objective of the programme of research – to quantify *skater point error* in the multi-camera network – by quantifying uncertainty in the automated digitisation of a skater. The chapter showed that the National Ice Centre (GBR) multi-camera network's automated digitisation uncertainty was less than the Olympic Oval (CAN) multi-camera network, and invariant to the skating condition, i.e. the corner and straight, for six different fiducial marker colours. The chapter attributed these results to the use of fiducial markers, positioned at skaters' two-dimensional centre-of-mass point estimate, reducing the ambiguity in the digitised point.

In this chapter, I explore how this smaller automated digitisation uncertainty propagates to *skater point error* in the multi-camera network, i.e. errors in position and velocity. As Great Britain Short-Track Speed Skating only requires four unique markers to distinguish between relay teams, I quantify the multi-camera network's *skater point error* for the four fiducial marker colours that exhibited sub-pixel automated digitisation uncertainty in Chapter 12. To provide a more detailed insight, I also consider the effect of skating condition, skater stature, and skating velocity on *skater point error*.

13.2 Method

For each fiducial marker colour, *skater point error* was quantified using Monte Carlo simulation methods in MATLAB R2016a (MathWorks, 2016).

13.2.1 Ground truth trajectories

All 315 synthetic ground truth trajectories created in Chapter 9 were used to simulate the effect of *skater point error* in the multi-camera network. These trajectories included three representative skating velocities (equivalent to ~ 10 s, 11 s, and 12 s lap times), three skater statures (1.52 m, 1.69 m, and 1.86 m), and 105 independent full-lap trajectories.

For each fiducial marker colour (red, yellow, green, and cyan), the simulation projected the 315 ground truth trajectories onto the multi-camera network's 26 image planes – as described in Section 5.3.2 – using the camera-rink plane calibration models constructed in Chapter 8. Before the projection procedure, the investigation partitioned each ground truth trajectory so that the simulation only projected the relevant ground truth coordinates into each camera's field-of-view. This process – detailed in Section 10.2.1 – negated false positives in the simulation, i.e. the incorrect projection of a global coordinate onto a camera's image plane.

13.2.2 Simulation

For each ground truth trajectory, the investigation performed 26 camera-specific Monte-Carlo simulations for each fiducial marker colour. A camera's simulation comprised of 100 independent iterations, with each iteration consisting of two scenarios. The first scenario, termed ground truth, added no automated digitisation uncertainty to the camera's ground truth projected pixel coordinates. The second scenario, termed simulated uncertainty, added the expected automated digitisation uncertainty to the camera's ground truth projected pixel coordinates.

The simulation added uncertainty to ground truth pixel coordinates by randomly sampling from a multivariate Gaussian distribution. The multivariate Gaussian distribution, an extension of the univariate Gaussian distribution to two or more correlated variables, has a mean vector, μ, and covariance matrix, $\sum$. The diagonal elements of $\sum$ contain the variances for each variable, while the off-diagonal elements of $\sum$ contain the covariance between variables. Modelling the automated digitisation uncertainty as a multivariate Gaussian distribution ensured that the simulation did not model u- and v-pixel coordinate uncertainty as independent variables.

For each fiducial marker colour, the investigation created corner and straight skating condition multivariate Gaussian distributions using the results of the study described in Chapter 12. As reported in Table 12-2, the National Ice Centre (GBR) multi-camera network's automated digitisation uncertainty was normally distributed for all fiducial marker colour datasets apart from the cyan fiducial marker's straight skating condition. The parameters of these multivariate Gaussian distributions are reported below, with an example raw and modelled distribution presented in Figure 13-1.

The red fiducial marker's corner and straight parameters (μ and $\sum$) were

$$\mu_{corner} = \begin{bmatrix} 0.6448 \\ 0.5288 \end{bmatrix} \qquad \sum_{corner} = \begin{bmatrix} 0.1549 & -0.0278 \\ -0.0278 & 0.2044 \end{bmatrix}$$

$$\mu_{straight} = \begin{bmatrix} 0.6254 \\ 0.4438 \end{bmatrix} \qquad \sum_{straight} = \begin{bmatrix} 0.1293 & 0.0179 \\ 0.0179 & 0.1969 \end{bmatrix}$$

The yellow fiducial marker's corner and straight parameters (μ and $\sum$) were

$$\mu_{corner} = \begin{bmatrix} 0.5730 \\ 0.4016 \end{bmatrix} \qquad \sum_{corner} = \begin{bmatrix} 0.1831 & -0.0212 \\ -0.0212 & 0.1988 \end{bmatrix}$$

$$\mu_{straight} = \begin{bmatrix} 0.5437 \\ 0.5414 \end{bmatrix} \qquad \sum_{straight} = \begin{bmatrix} 0.1282 & -0.0096 \\ -0.0096 & 0.1472 \end{bmatrix}$$

The green fiducial marker's corner and straight parameters (μ and $\sum$) were

$$\mu_{corner} = \begin{bmatrix} 0.4972 \\ 0.5342 \end{bmatrix} \qquad \sum_{corner} = \begin{bmatrix} 0.3250 & 0.0066 \\ -0.0066 & 0.2055 \end{bmatrix}$$

$$\mu_{straight} = \begin{bmatrix} 0.6143 \\ 0.5241 \end{bmatrix} \qquad \sum_{straight} = \begin{bmatrix} 0.1114 & 0.0016 \\ 0.0016 & 0.2126 \end{bmatrix}$$

The cyan fiducial marker's corner and straight parameters (μ and $\sum$) were

$$\mu_{corner} = \begin{bmatrix} 0.5996 \\ 0.6198 \end{bmatrix} \qquad \sum\nolimits_{corner} = \begin{bmatrix} 0.1634 & 0.0105 \\ 0.0105 & 0.1437 \end{bmatrix}$$

$$\mu_{straight} = \begin{bmatrix} 0.6412 \\ 0.3965 \end{bmatrix} \qquad \sum\nolimits_{straight} = \begin{bmatrix} 0.0718 & 0.0306 \\ 0.0306 & 0.3518 \end{bmatrix}$$

In each camera simulation iteration, the investigation reconstructed both scenarios' pixel coordinates into the global coordinate system – as described in Section 5.3.2 – using the relevant camera-elevated plane calibration model constructed in Chapter 10. This procedure, i.e. using the same calibration models for both scenarios, ensured that

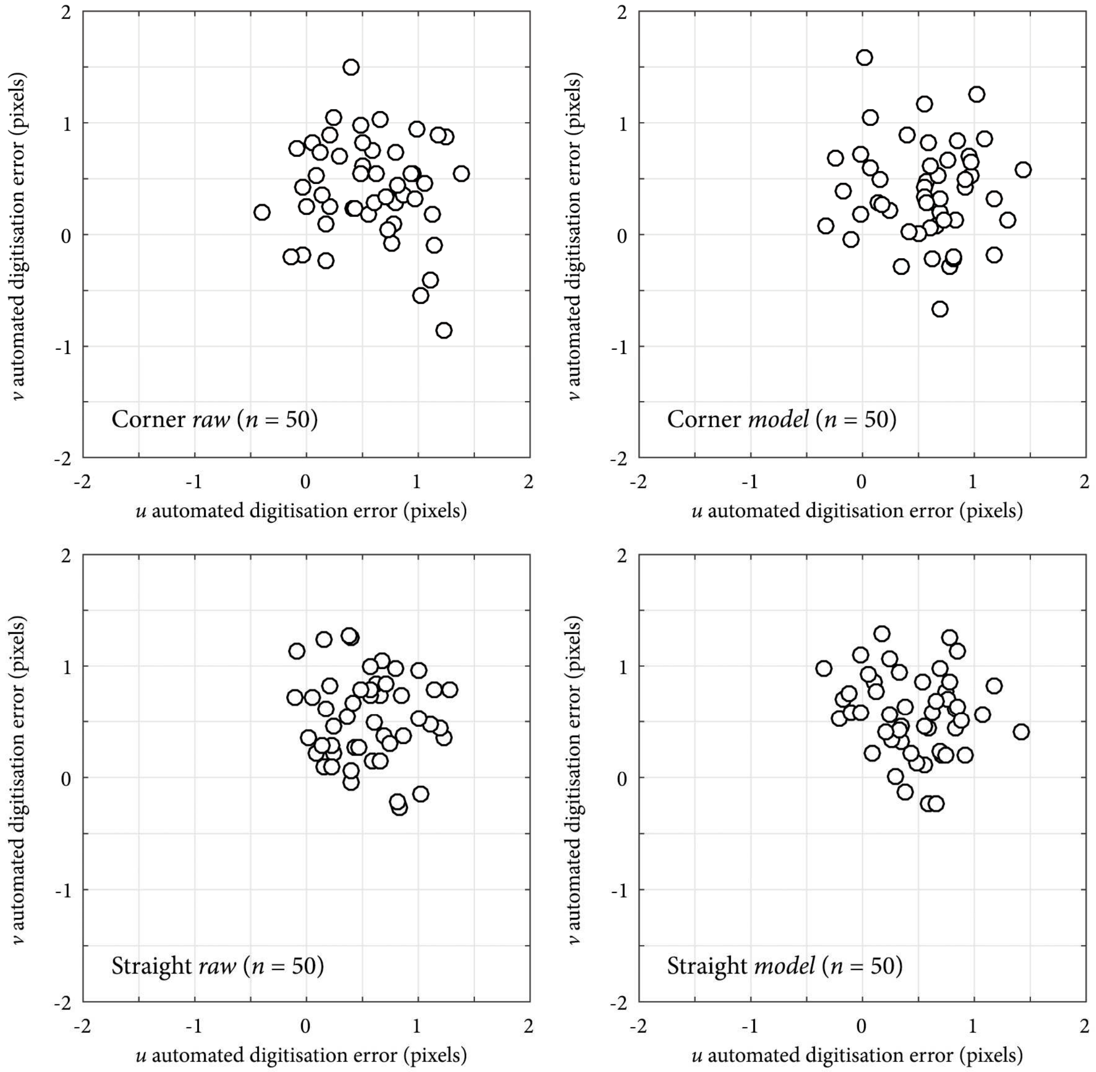

Figure 13-1. Example corner and straight skating condition raw and modelled automated digitisation uncertainty in the *skater point error* simulation.

out-of-plane error was not a confounding factor in the simulation's results. Resultant velocity was then calculated using $Eq. 5.24$, with finite difference techniques used to compute velocity in the x- and y-axis ($Eq. 5.25$ to $Eq. 5.27$). The simulation used a sampling interval of 0.04 seconds to compute velocity as the ground truth trajectories had a sampling frequency of 25 Hz (Section 9.2).

13.2.3 Data analysis

In each camera simulation iteration, the investigation calculated *skater point error* as the RMS error ($Eq. 5.34$) between the camera's ground truth and reconstructed position and velocity trajectories. This calculation assumed that the ground truth condition represented the actual value of position and velocity.

13.2.4 Statistical analysis

SPSS 24 (IBM, 2016) was used to calculate each fiducial marker's *skater point error* descriptive statistics (median, first quartile, third quartile, minimum, maximum, and ± 95% confidence bounds) for the corner and straight skating conditions (defined in Section 8.33). The analysis calculated the median and first and third quartiles, instead of the arithmetic mean and standard deviation reported in Section 5.7.1, as the statistics are more representative of systematic and random error in non-normally distributed datasets. As all *skater point errors* were positive due to the calculation of the RMS error, the ± 95% confidence bounds represented the 95th percentile, i.e. the value below which 95% of the *skater point errors* were found.

To investigate the effect of skating condition, skater stature, and skating velocity on *skater point error*, the analysis pooled the results of the four fiducial markers into a single dataset. This data was treated as non-parametric, as the underlying assumptions of parametric statistical tests, i.e. normality and homogeneity of variance, were violated. First, a Mann Whitney U-test was used to analyse differences in *skater point error* between the corner and straight skating condition. Second, for each skating condition, one-way Kruskal-Wallis ANOVAs were used to examine differences in *skater point error* between the three skater statures and the three skating velocities. Where main effects occurred, post hoc pairwise comparisons (Mann Whitney U-test) were used to identify the observed differences. Note that in all statistical tests, the analysis used the RMS velocity error as the sole metric of *skater point error*, as the numerical computation of velocity amplifies any uncertainty in position (Section 5.5.2).

In all statistical tests, the significance level, α, was set at $p < 0.05$. As described in Section 10.2.4, in post hoc comparisons the Bonferroni correction was used to correct each pairwise α so that the overall significance remained at $p < 0.05$ (Field, 2009). Effect sizes were also calculated using Pearson's correlation coefficient ($Eq. 8.1$), with the magnitudes interpreted using Cohen's thresholds; where < 0.1, is trivial; 0.1–0.3, small; > 0.3–0.5, moderate; and > 0.5, large (Cohen, 1988).

13.3 Results

For each fiducial marker, the investigation compared a total of 685,200 reconstructed ground truth and simulated uncertainty position and velocity trajectories (corner = 371,900, straight = 313,300). Table 13-1 reports each marker's descriptive statistics, with Figure 13-2 illustrating an example *skater point error* for both corner and straight skating conditions. Overall, the multi-camera network's ± 95% confidence bounds in *skater point error* were ± 0.14 $\text{m}\cdot\text{s}^{-1}$.

Table 13-1. *Skater point error* descriptive statistics for each fiducial marker colour in the National Ice Centre (GBR) multi-camera network.

Statistic	Colour	X position error		Y position error		Resultant velocity error	
		Corner	Straight	Corner	Straight	Corner	Straight
Median (Q_1, Q_3)	Red	0.007 (0.006, 0.008)	0.005 (0.005, 0.006)	0.007 (0.006, 0.008)	0.006 (0.005, 0.007)	0.082 (0.068, 0.100)	0.078 (0.062, 0.089)
	Yellow	0.006 (0.005, 0.007)	0.005 (0.005, 0.006)	0.006 (0.005, 0.007)	0.005 (0.005, 0.006)	0.083 (0.069, 0.102)	0.065 (0.054, 0.078)
	Green	0.007 (0.006, 0.008)	0.006 (0.005, 0.006)	0.007 (0.006, 0.008)	0.006 (0.005, 0.006)	0.094 (0.077, 0.118)	0.080 (0.064, 0.092)
	Cyan	0.007 (0.006, 0.008)	0.006 (0.005, 0.007)	0.007 (0.006, 0.008)	0.006 (0.005, 0.006)	0.074 (0.060, 0.091)	0.101 (0.081, 0.116)
Min – Max	Red	0.001 – 0.021	0.001 – 0.015	0.000 – 0.020	0.001 – 0.017	0.002 – 0.582	0.001 – 0.425
	Yellow	0.000 – 0.022	0.001 – 0.014	0.001 – 0.022	0.001 – 0.016	0.002 – 0.508	0.002 – 0.379
	Green	0.000 – 0.023	0.000 – 0.016	0.000 – 0.027	0.001 – 0.017	0.001 – 0.576	0.001 – 0.460
	Cyan	0.001 – 0.020	0.001 – 0.017	0.001 – 0.021	0.001 – 0.015	0.001 – 0.432	0.002 – 0.514
± 95% CB	Red	0.010	0.007	0.010	0.008	0.139	0.118
	Yellow	0.009	0.007	0.009	0.007	0.145	0.103
	Green	0.010	0.007	0.010	0.008	0.178	0.120
	Cyan	0.010	0.008	0.010	0.007	0.133	0.152

Notes: Q_1 and Q_3 = first and third quartiles. CB = Confidence bounds. X and Y position measured in metres. Resultant velocity measured in m·s^{-1}.

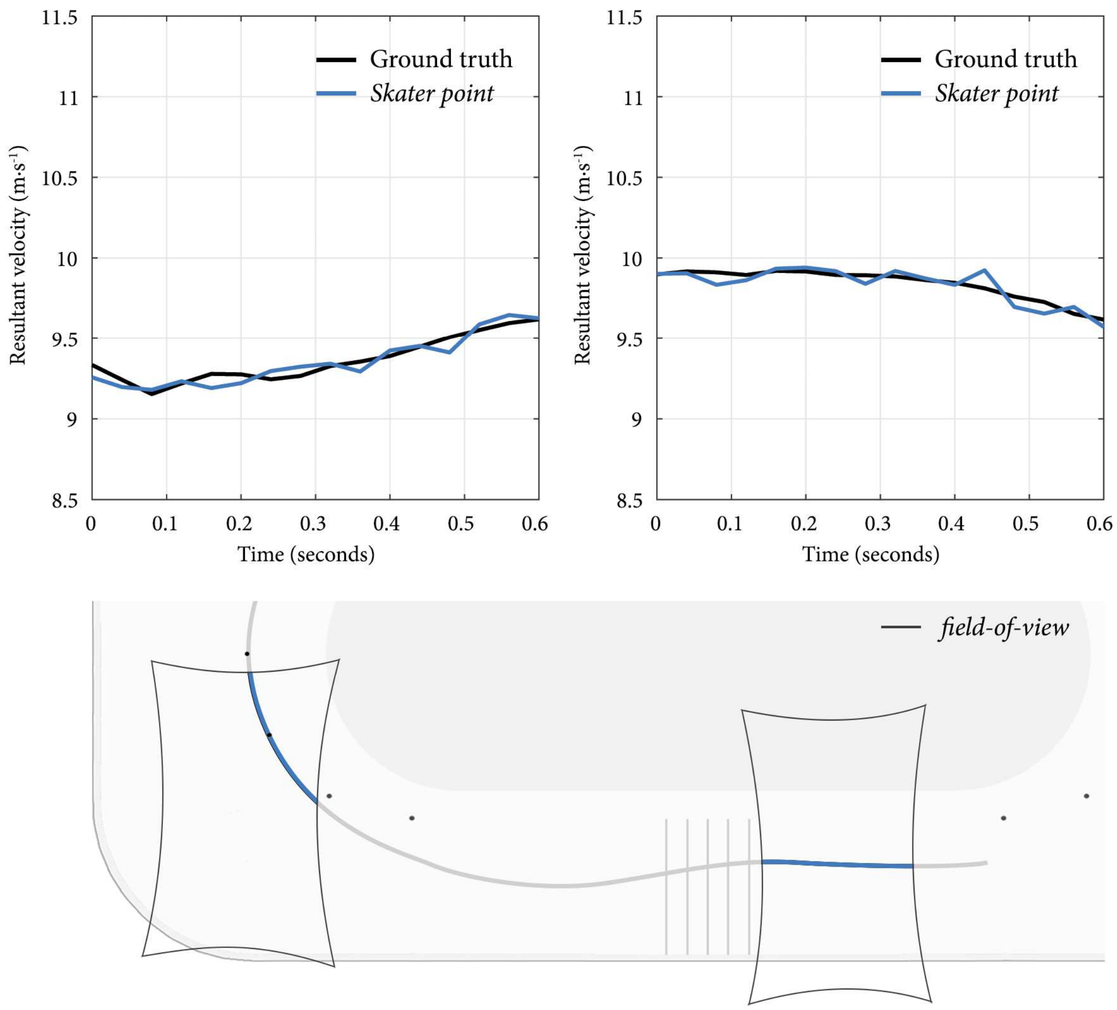

Figure 13-2. Example *skater point errors* for a corner (left) and straight (right) skating condition camera in the National Ice Centre (GBR) multi-camera network.

13.3.1 Skating condition

There was a significant difference in *skater point error* between the corner and straight skating conditions, U =8.07 x 10^{11}, p = 0.000, r = -0.11 (a small effect). The RMS velocity error was larger during the corner ($\widetilde{v_3}$ = 0.083 m·s^{-1}) than the straight ($\widetilde{v_3}$ = 0.077 m·s^{-1}).

13.3.2 Skater stature

There was a significant main effect for skater stature on *skater point error* in both corner (H (2) =6.71 x 10^{2}, p = 0.000) and straight (H (2) =1.11 x 10^{3}, p = 0.000) skating conditions. The post hoc pairwise comparisons are summarised in Table 13-2. In both

Table 13-2. Effect of skater stature on *skater point error*: post hoc pairwise comparisons.

Condition	Stature $_{(1-2)}$	N	$\widetilde{v_3}$ Error$_1$	$\widetilde{v_3}$ Error$_2$	U	p	r
Corner	Min - Mean	988,800	0.083	0.083	1.01×10^4	0.000	0.01
	Min - Max	989,600	0.083	0.082	2.23×10^4	0.000	0.03
	Max - Mean	988,800	0.082	0.083	1.22×10^4	0.000	0.01
Straight	Min - Mean	833,600	0.078	0.077	1.25×10^4	0.000	0.02
	Min - Max	835,600	0.078	0.076	2.63×10^4	0.000	0.04
	Max - Mean	833,600	0.076	0.077	1.39×10^4	0.000	0.02

Notes: Skater statures (min, mean and max) represent values of 1.52, 1.69 and 1.86 m, respectively. $\widetilde{v_3}$ Error = Median *skater point error* measured in m·s^{-1}. U = Mann-Whitney U-Test. Significance values adjusted using the Bonferroni correction to control for family-wise error. Magnitude of effect, r, measured using Pearson's correlation coefficient.

skating conditions, the magnitude of *skater point error* was significantly larger for the minimum stature compared to the mean stature (r_c = 0.01, r_s = 0.02), the mean stature compared to the maximum stature (r_c = 0.01, r_s = 0.02), and the minimum stature compared to the maximum stature (r_c = 0.03, r_s = 0.04).

13.3.3 Skating velocity

There was a significant main effect for skating velocity on *skater point error* in both corner (H (2) =3.81 x 10^2, p = 0.000) and straight (H (2) =3.69 x 10^2, p = 0.000) skating conditions. Table 13-3 summarises the post hoc pairwise comparisons. In both skating conditions, the magnitude of *skater point error* was significantly smaller for the slow velocity compared to the medium velocity (r_c = -0.01, r_s = -0.01), the medium velocity compared to the fast velocity (r_c = -0.01, r_s = -0.02), and the small velocity compared to the fast velocity (r_c = -0.02, r_s = -0.02).

13.4 Discussion

This investigation aimed to quantify *skater point error* in the multi-camera network for four fiducial marker colours, i.e. how uncertainty in the automated digitisation of a

Table 13-3. Effect of skating velocity on *skater point error*: post hoc pairwise comparisons.

Condition	Velocity $_{(1-2)}$	*N*	$\widetilde{v_3}$ Error$_1$	$\widetilde{v_3}$ Error$_2$	*U*	*p*	*r*
Corner	Slow - Med	1,186,800	0.082	0.083	-1.15 x 10^4	0.000	-0.01
	Slow - Fast	890,800	0.082	0.082	-1.71 x 10^4	0.000	-0.02
	Fast - Med	892,800	0.083	0.083	-5.59 x 10^3	0.000	-0.01
Straight	Slow - Med	1,001,200	0.077	0.077	-5.93 x 10^3	0.000	-0.01
	Slow - Fast	751,200	0.077	0.078	-1.70 x 10^4	0.000	-0.02
	Fast - Med	754,000	0.078	0.077	-1.10 x 10^4	0.000	-0.02

Notes: Skating velocity (slow, med and fast) akin to approximately 12, 11, and 10 second lap times, respectively. $\widetilde{v_3}$ Error = Median *skater point error* measured in m·s^{-1}. *U* = Mann-Whitney *U*-Test. Significance values adjusted using the Bonferroni correction to control for family-wise error. Magnitude of effect, r, measured using Pearson's correlation coefficient.

skater propagated to errors in position and velocity. The investigation also considered the effect of skating condition, skater stature, and skating velocity, to provide a more detailed insight into the multi-camera network's *skater point error*.

The results showed that the multi-camera network's *skater point error* was within the ± 0.19 m·s^{-1} target measurement error and significantly less than the Olympic Oval (CAN) multi-camera network's ± 1.04 m·s^{-1} *skater point error*, for all four fiducial marker colours. Overall, the multi-camera network had a *skater point error* of ± 0.14 m·s^{-1}. I attribute this improvement in *skater point error* to two factors. First, as reported in Chapter 12, the use of fiducial markers minimised uncertainty in the automated digitisation of a skater by reducing the ambiguity in the digitised point. As a result, I reduced *skater point error* at a pixel level before reconstructing the pixel coordinates into the global coordinate system. Second, as shown in Chapter 8, the National Ice Centre (GBR) multi-camera network has a superior spatial resolution of the rink surface; the result of using 26 cameras – all recording at a higher image resolution – to capture the short-track. This superior spatial resolution reduced *skater point error* in the global coordinate system after I reconstructed the pixel coordinates.

The multi-camera network's maximum *skater point error* did, however, exceed the ± 0.19 $m \cdot s^{-1}$ target measurement error for all four fiducial marker colours, in both skating conditions (Table 13-1). In Chapter 11, I reported that similar magnitudes of *out-of-plane error* were due to errors in the classification of skating condition cameras. This misclassification resulted in the camera-elevated calibration planes being less effective at minimising out-of-plane distances. This was not the case in this study, however, as both ground truth and simulated uncertainty scenarios were reconstructed into the global coordinate system using the same calibration model to negate *out-of-plane error*. In this study, the 2% of errors that exceeded the ± 0.19 $m \cdot s^{-1}$ target measurement error were due to uncertainty in the automated digitisation of a skater introducing high-frequency noise into the reconstructed fiducial marker positions. As described in Section 5.5.2, and demonstrated in Figure 13-2, the numerical computation of velocity amplifies these errors in position. For this reason, the results suggest smoothing raw reconstructed fiducial marker positions to attenuate high-frequency noise. As discussed in Section 5.5.2, a smoothing spline should be implemented instead of the commonly used Butterworth filter, as this technique does not require a constant sampling interval. As detailed in Section 5.5.1, in the National Ice Centre (GBR) multi-camera network the sampling interval is only constant between corresponding scanlines in consecutive images due to the image sensors' electronic rolling shutter.

Effect of skating condition on skater point error

The results showed that *skater point error* was significantly larger in the corner skating condition than the straight. This finding contradicts Chapter 12, where despite the pooled uncertainty for the four fiducial markers being larger in the corner (median = 0.93 pixels) than the straight (median = 0.89 pixels), automated digitisation uncertainty was found to be invariant to the skating condition. Instead, in this investigation, the corner's larger RMS velocity errors were due to differences in the spatial resolution of each skating condition's calibrated plane.

The spatial resolution of a calibration plane, i.e. the number of metres per pixel, increases as the camera-to-calibration plane distance decreases. As the multi-camera network constructs camera-elevated plane calibration models at 45% and 59% of the skater's stature, to mitigate *out-of-plane error* in the corner and straight, the corner skating condition has a greater camera-to-calibration plane distance and therefore a lower spatial resolution. For example, for a given pixel, a skater stature of 1.69 m has a spatial resolution of 0.0127 m per pixel in the corner and 0.0122 m per pixel in the straight. This lower spatial resolution, coupled with the larger automated digitisation uncertainty reported in Chapter 12, leads to *skater point error* being significantly larger in the corner skating condition than the straight.

Importantly for the multi-camera network, the size of this effect was small; the difference between the median RMS velocity error (0.006 $m \cdot s^{-1}$) equated to 3.2% of the ± 0.19 $m \cdot s^{-1}$ target measurement error. For this reason, the results suggest that the multi-camera network's *skater point error* is effectively invariant to the skating condition. As discussed in Section 12.5, this is important in the multi-camera network as the appearance of a skater – and thus the fiducial marker – varies between the corner and straight due to differences in the skating technique (Section 4.3.2).

Effect of skater stature on skater point error

In both corner and straight skating conditions, the results showed that *skater point error* was significantly larger as the skater stature decreased. These larger errors in RMS velocity (Table 13-2) were due to differences in the spatial resolution of each stature's calibrated planes. As discussed above, the spatial resolution of a calibration plane increases as the camera-to-calibration plane distance decreases. By constructing camera-elevated plane calibration models specific to each skater's stature, the spatial resolution of a calibration plane is lower for a shorter skater stature. For example, for a given pixel, the spatial resolutions of the minimum (1.52 m), mean (1.69 m), and maximum (1.86 m) skater stature were 0.0129 m, 0.0127 m and 0.0126 m in the corner skating condition, and 0.0124 m, 0.0122 m and 0.0121 m in the straight skating condition. As a result, the lower spatial resolution leads to a larger *skater point error* for a given pixel uncertainty.

Importantly for the multi-camera network, the size of these effects was trivial (Table 13-2). For example, when comparing the minimum and maximum skater stature, the difference between the median RMS velocity error in the corner (0.001 $m \cdot s^{-1}$) and straight (0.002 $m \cdot s^{-1}$) only equated to 0.8% and 0.9% of the ± 0.19 $m \cdot s^{-1}$ target measurement error. Consequently, these findings indicate that the multi-camera network's *skater point error* is effectively invariant to skater stature.

Effect of skating velocity on skater point error

In both corner and straight skating conditions, the results showed that *skater point error* was significantly larger as skating velocity increased. On the surface, this finding is unsurprising considering that the appearance of a skater – and thus fiducial marker – is dependent on the skating velocity (Section 4.3.2). At faster velocities, skaters travel further in a camera's 0.004-second exposure, leading to an increase in the image's motion blur and, as a result, automated digitisation uncertainty. However, this was not the case in this study as the multivariate Gaussian distributions only modelled automated digitisation uncertainty for the different skating conditions (Section 13.2.2). As a result, the simulated automated digitisation uncertainty was the same for each skating velocity condition.

In this study, consistent with the findings in Chapters 8, 10, and 11, *skater point error* significantly increased with skating velocity due to intra-camera *calibration model error*. As shown in Chapter 8, intra-camera *calibration model error* increases significantly with skating velocity due to greater differences in two measured positions' intrinsic calibration model errors. These results suggest that the effect of skating velocity in the multi-camera network is more sensitive to intra-camera *calibration model error* than *skater point error*.

Importantly for the multi-camera network, the effect of skating velocity on *skater point error* was trivial (Table 13-3). For example, when comparing the slow and fast skating velocity, the difference between the median RMS velocity error in the corner (0.001 $m\cdot s^{-1}$) and straight (0.001 $m\cdot s^{-1}$) equated to only 0.6% and 0.7% of the ± 0.19$m\cdot s^{-1}$ target measurement error. Accordingly, these findings suggest that the multi-camera network's *skater point error* is effectively invariant to the skating velocity. This outcome is important in the multi-camera network, as Chapter 2 showed that skating velocity varies during the short-track speed skating relay event.

Limitations

This study has two limitations that warrant consideration. First, as this study used the results of Chapter 12 to model uncertainty in the automated digitisation of a skater, the limitations discussed in Section 12.5 also apply to this study. Second, in Section 13.2.2, I reported that the distribution of uncertainty in the automated digitisation of a skater was non-normal in the cyan fiducial marker’s straight skating condition. Despite this, the investigation modelled this automated digitisation uncertainty as a multivariate Gaussian distribution due to the challenges surrounding the generation of multivariate non-Gaussian data. For example, while I could have applied non-linear transformations to the u- and v-pixel uncertainties to rectify the non-normality, this would have likely altered the dependence between the modelled variables (Ruscio & Kaczetow, 2008). Subsequently, the randomly sampled uncertainty added to the cyan fiducial marker’s raw pixel coordinates in the straight skating condition cameras may have manifested differently in the simulation using a multivariate non-Gaussian distribution. However, as the parameters of this distribution are similar to the other fiducial marker colour datasets, it is likely that the automated digitisation uncertainty would still have manifested as high-frequency noise in the multi-camera network.

13.5 Chapter summary

This chapter used Monte Carlo simulations to address the sixth objective of the programme of research: to quantify *skater point error* in the multi-camera network. More specifically, how uncertainty in the automated digitisation of a skater propagated to errors in position and velocity. The chapter showed that the multi-camera network's *skater point error* was within the ± 0.19 $m \cdot s^{-1}$ target measurement error, significantly less than the Olympic Oval (CAN) multi-camera network's ± 1.04 $m \cdot s^{-1}$ *skater point error*, and effectively invariant to the skating condition, skater stature, and skating velocity, for all four fiducial markers. Overall, the multi-camera network's *skater point error* was ± 0.14 $m \cdot s^{-1}$. The chapter concluded that the multi-camera network's improvement in *skater point error* was due to fiducial markers minimising the uncertainty in the automated digitisation of a skater and the National Ice Centre (GBR) multi-camera network having a superior spatial resolution of the rink surface. Furthermore, the 2% of errors that exceeded the target measurement error – attributed to automated digitisation uncertainty introducing high-frequency noise into reconstructed fiducial marker positions – could be attenuated by using smoothing splines.

Chapter 14

Total error in the multi-camera network

14.1 Introduction

The second part of this thesis has investigated developing the National Ice Centre (GBR) multi-camera network to measure accurate, two-dimensional, relay exchange kinematics. In Chapter 5, the literature review identified five sources of measurement error that would determine the multi-camera network's accuracy. Accordingly, Chapters 6 to 13 quantified how these sources of error propagated, independently, to errors in position and velocity. This programme of research ensured that multi-camera network's measurement workflow was empirically informed by identifying the sources of error that exceed the ± 0.19 $m \cdot s^{-1}$ target measurement error and need to be minimised, e.g. *out-of-plane error* in the multi-camera network.

In the final chapter of part two, I address the seventh objective of the programme of research: to quantify *total error* in the multi-camera network. *Total error* describes how the five sources of measurement error propagate, collectively, to errors in position and velocity. In doing so, this chapter answers the thesis's overarching research question *'Can multi-camera networks be used to measure accurate, two-dimensional, relay exchange kinematics in short-track speed skating'*. First, I quantify the multi-camera network's *total error* for the four selected fiducial marker colours used to identify the four teams in the short-track speed skating relay. Second, to provide a more comprehensive insight, I consider the effect of skating condition, skater stature, and skating velocity on the magnitude of *total error*.

14.2 Method

For each fiducial marker colour, the multi-camera network's *total error* was quantified using a revised version of the simulation described in Chapter 13.

14.2.1 Revisions

First, in Chapter 13, each camera simulation consisted of two scenarios: ground truth and simulated uncertainty. In this investigation, the simulation only used the simulated uncertainty scenario. This scenario adds the expected automated digitisation uncertainty to the camera's ground truth projected pixel coordinates by randomly sampling from the appropriate multivariate Gaussian distribution (Section 13.2.2). Second, based on the recommendations of Chapter 11, the simulation dynamically classified the skating condition camera depending on the short-track position. The dynamic classification ensured that corner skating was not reconstructed using camera-elevated plane calibration models created for straight skating and vice versa. Third, based on the recommendations of Chapter 13, the simulation smoothed raw reconstructed fiducial marker positions using a smoothing spline (Section 5.5.2). The smoothing parameter, λ, was set empirically at 0.3. The smoothing spline removed the high-frequency noise associated with the automated digitisation uncertainty from the calculated kinematic variables. Fourth, the simulation calculated *total error* as the RMS error ($Eq.\ 5.34$) between the camera's reconstructed simulated uncertainty scenario and the camera's ground truth trajectory position and velocity trajectories. This procedure ensured that the simulation included *out-of-plane error*.

14.3 Results

For each fiducial marker, the investigation compared a total of 684,600 ground truth and reconstructed simulated uncertainty position and velocity trajectories (corner = 369,600, straight = 315,000). Table 14-1 reports each marker's descriptive statistics, with Figure 14-1 illustrating an example *total error* for both corner and straight skating conditions. Overall, the multi-camera network's ± 95% confidence bounds in *total error* were ± 0.17 $m \cdot s^{-1}$.

Table 14-1. *Total error* descriptive statistics for each fiducial marker colour in the National Ice Centre (GBR) multi-camera network.

Statistic	Colour	X position error		Y position error		Resultant velocity error	
		Corner	Straight	Corner	Straight	Corner	Straight
Median (Q_1, Q_3)	Red	0.014 (0.009, 0.021)	0.012 (0.008, 0.018)	0.014 (0.009, 0.020)	0.009 (0.006, 0.016)	0.077 (0.056, 0.105)	0.082 (0.059, 0.113)
	Yellow	0.014 (0.009, 0.022)	0.012 (0.008, 0.018)	0.014 (0.009, 0.021)	0.010 (0.006, 0.016)	0.079 (0.057, 0.108)	0.083 (0.060, 0.114)
	Green	0.014 (0.009, 0.022)	0.012 (0.008, 0.018)	0.014 (0.009, 0.021)	0.010 (0.006, 0.016)	0.076 (0.055, 0.104)	0.086 (0.062, 0.117)
	Cyan	0.014 (0.009, 0.022)	0.012 (0.008, 0.018)	0.014 (0.009, 0.021)	0.010 (0.006, 0.016)	0.077 (0.056, 0.105)	0.083 (0.060, 0.114)
Min – Max	Red	0.000 – 0.091	0.000 – 0.045	0.000 – 0.091	0.000 – 0.061	0.000 – 0.730	0.002 – 0.281
	Yellow	0.000 – 0.096	0.000 – 0.045	0.000 – 0.093	0.001 – 0.061	0.000 – 0.763	0.001 – 0.296
	Green	0.000 – 0.092	0.001 – 0.045	0.000 – 0.092	0.001 – 0.061	0.000 – 0.698	0.003 – 0.291
	Cyan	0.000 – 0.093	0.001 – 0.045	0.000 – 0.095	0.001 – 0.061	0.000 – 0.745	0.002 – 0.283
± 95% CB	Red	0.038	0.028	0.039	0.032	0.173	0.166
	Yellow	0.038	0.028	0.039	0.032	0.177	0.167
	Green	0.038	0.028	0.039	0.032	0.172	0.168
	Cyan	0.038	0.028	0.039	0.032	0.172	0.166

Notes: Q_1 and Q_3 = first and third quartiles. CB = Confidence bounds. X and Y position measured in metres. Resultant velocity measured in $m \cdot s^{-1}$.

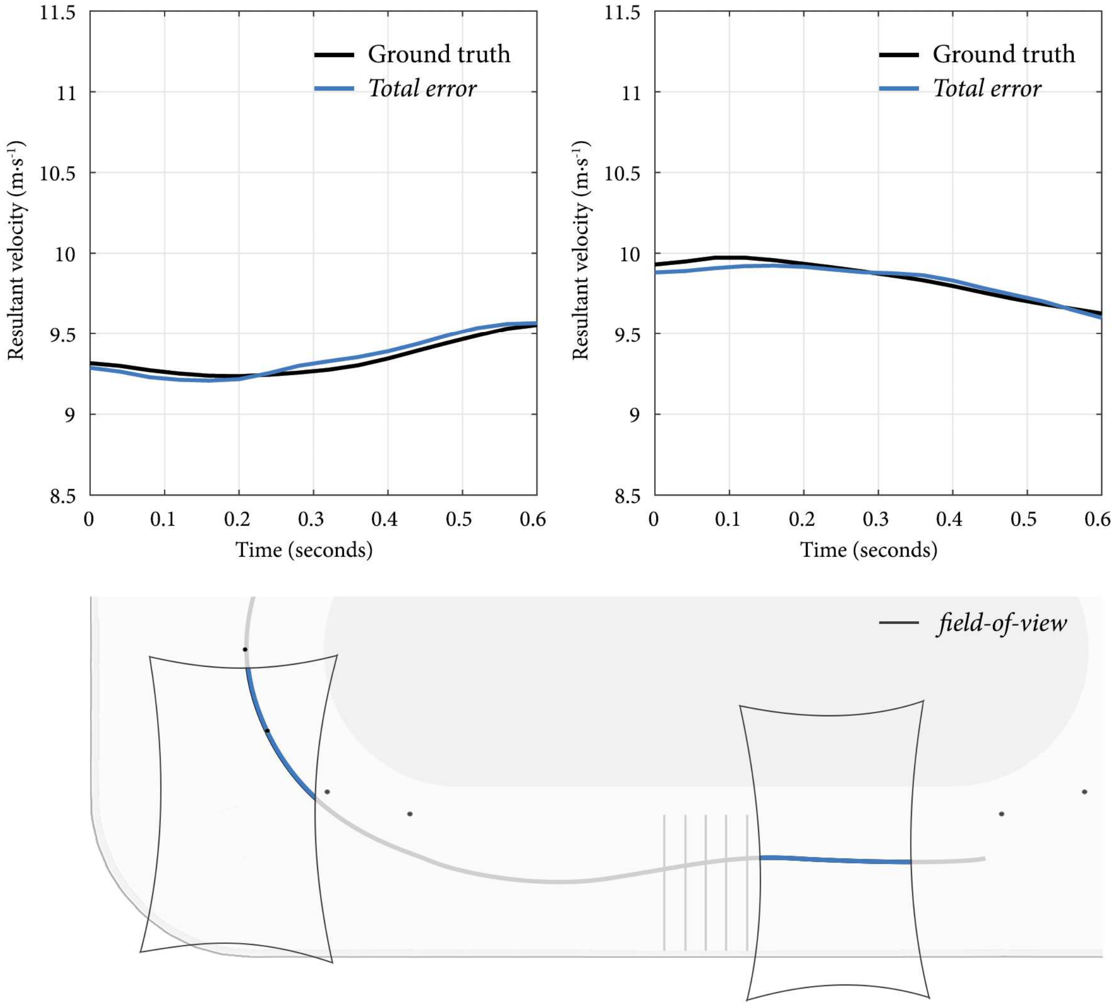

Figure 14-1. Example *skater point errors* for a corner (left) and straight (right) skating condition camera in the National Ice Centre (GBR) multi-camera network.

14.3.1 Skating condition

There was a significant difference in *total error* between the corner and straight skating conditions, U = 1.02 x 10^{9}, p = 0.000, r = 0.08 (a trivial effect). The RMS velocity error was smaller during the corner ($\widetilde{v}_3$ = 0.077 m·s^{-1}) than the straight ($\widetilde{v}_3$ = 0.084 m·s^{-1}).

14.3.2 Skater stature

There was a significant main effect for skater stature on *total error* in both corner (H (2) = 2.11 x 10^{4}, p = 0.000) and straight (H (2) = 2.95 x 10^{4}, p = 0.000) skating conditions. The post hoc pairwise comparisons are summarised in Table 14-2. In both skating

Table 14-2. Effect of skater stature on *total error*: post hoc pairwise comparisons.

Condition	Stature $_{(1-2)}$	N	$\widetilde{v_3}$ Error$_1$	$\widetilde{v_3}$ Error$_2$	U	p	r
Corner	Min - Mean	989,200	0.072	0.078	-64,833.20	0.000	-0.08
	Min - Max	985,200	0.072	0.083	-124,927.01	0.000	-0.15
	Max - Mean	982,400	0.078	0.083	-60,093.76	0.000	-0.07
Straight	Min - Mean	840,000	0.077	0.084	-71,238.16	0.000	-0.10
	Min - Max	840,000	0.077	0.091	-136,182.03	0.000	-0.19
	Max - Mean	840,000	0.084	0.091	-64,943.88	0.000	-0.09

Notes: Skater statures (min, mean and max) represent values of 1.52, 1.69 and 1.86 m, respectively. $\widetilde{v_3}$ Error = Median *skater point error* measured in $m \cdot s^{-1}$. U = Mann-Whitney U-Test. Significance values adjusted using the Bonferroni correction to control for family-wise error. Magnitude of effect, r, measured using Pearson's correlation coefficient.

conditions, the magnitude of *total error* was significantly smaller for the minimum stature compared to the mean stature (r_c = -0.08, r_s = -0.10), the mean stature compared to the maximum stature (r_c = -0.07, r_s = -0.09), and the minimum stature compared to the maximum stature (r_c = -0.15, r_s = -0.19).

14.3.3 Skating velocity

There was a significant main effect for skating velocity on *total error* in both corner (H (2) = 2 x 10^1, p = 0.000) and straight (H (2) = 3.3 x 10^1, p = 0.000) skating conditions. Table 14-3 summarises the post hoc pairwise comparisons. In both skating conditions, the magnitude of *total error* was significantly smaller for the slow velocity compared to the medium velocity (r_c = -0.08, r_s = -0.12), the medium velocity compared to the fast velocity (r_c = -0.39, r_s = -0.09), and the slow velocity compared to the fast velocity (r_c = -0.46, r_s = -0.20).

14.4 Discussion

This investigation aimed to quantify *total error* in the multi-camera network for four different fiducial marker colours, i.e. how the multi-camera network's five sources of

Table 14-3. Effect of skating velocity on *total error*: post hoc pairwise comparisons.

Condition	Velocity $_{(1-2)}$	N	$\widetilde{v_3}$ Error$_1$	$\widetilde{v_3}$ Error$_2$	U	p	r
Corner	Slow - Med	1,180,000	0.067	0.073	-67,337.02	0.000	-0.08
	Slow - Fast	886,000	0.067	0.106	-417,695.62	0.000	-0.46
	Fast - Med	890,800	0.073	0.106	-350,358.60	0.000	-0.39
Straight	Slow - Med	1,008,000	0.077	0.086	-86,078.16	0.000	-0.12
	Slow - Fast	756,000	0.077	0.091	-155,089.41	0.000	-0.20
	Fast - Med	756,000	0.086	0.091	-69,011.25	0.000	-0.09

Notes: Skating velocity (slow, med and fast) akin to approximately 12, 11, and 10 second lap times, respectively. $\widetilde{v_3}$ Error = Median *skater point error* measured in m·s^{-1}. U = Mann-Whitney U-Test. Significance values adjusted using the Bonferroni correction to control for family-wise error. Magnitude of effect, r, measured using Pearson's correlation coefficient.

measurement error propagated, collectively, to errors in position and velocity. The investigation also considered the effect of skating condition, skater stature, and skating velocity, to provide a more detailed insight into the multi-camera network's *total error*. The results showed that the multi-camera network's *total error* was within the ± 0.19 m·s^{-1} target measurement error and significantly less than the Olympic Oval (CAN) multi-camera network's ± 1.53 m·s^{-1} *total error*, for all four fiducial markers. Overall, the multi-camera network had a *total error* of ± 0.17 m·s^{-1}. I attribute this improvement in measuring relay exchange kinematics to reducing the multi-camera network's five sources of measurement error.

These findings have two clear implications for this thesis. First, the results answer the thesis's overarching research question '*Can multi-camera networks be used to measure accurate, two-dimensional, relay exchange kinematics*'. Yes, if the network's sources of measurement error are mitigated as outlined in Part II of this thesis. Second, the results confirm that the aim of the thesis – to develop a multi-camera network to measure accurate, two-dimensional, relay exchange kinematics – has been achieved. Importantly, this finding suggests that Great Britain Short-Track Speed Skating can use the National Ice Centre (GBR) multi-camera network as a tool to advance knowledge on '*how to* *execute the relay exchange effectively'*. In turn, supporting the team's targeted improvement of the relay exchange, and ultimately, their aim of delivering medal-winning performances at the Winter Olympic Games.

The multi-camera network's maximum *total error* did, however, exceed the ± 0.19 $m \cdot s^{-1}$ target measurement error for all four fiducial marker colours in both skating conditions (Table 14-1). In Chapter 13, I reported that similar maximum *skater point errors* were due to the amplification of automated digitisation uncertainty in the computation of velocity. However, as illustrated in Figure 14-1, this study reduced high-frequency noise by applying smoothing splines to each camera's raw reconstructed fiducial marker positions (Section 14.2.1). In this study, the maximum *total errors* were due to *out-of-plane errors*. In Chapter 11, I reported that 10% of *out-of-plane errors* exceeded the ± 0.19 $m \cdot s^{-1}$ target measurement error due to the misclassification of skating condition cameras, e.g. corner skating in a straight skating condition camera. This misclassification resulted in the camera-elevated plane calibration models being less effective at minimising out-of-plane distances and, as a result, larger *out-of-plane errors*. Although the potential for misclassification was minimised in this study by dynamically classifying the skating condition camera depending on the current short-track position, the wrong classification of skating condition camera still resulted in 3% of errors exceeding the target measurement error.

Effect of skating condition on total error

The results showed that *total error* was significantly smaller in the corner skating condition than the straight skating condition. This result contradicts our findings in Chapter 13 but is consistent with the outcomes of Chapter 11.

In Chapter 13, I reported that *skater point error* was significantly larger in the corner skating condition due to (1) the corner's camera-elevated calibration plane models having a smaller spatial resolution, and (2) the corner having a greater magnitude of automated digitisation uncertainty. The former was the result of a more substantial camera-to-calibrated plane distance, as I constructed corner calibration models at 45% of the skater's stature compared to 59% in the straight. The latter was due to differences in skating technique leading to less optimal views of the skater for the automated digitisation algorithm, e.g. the skin suit not surrounding the fiducial marker (Section 12.2.1). In contrast, in Chapter 11 I attributed significantly smaller *out-of-plane errors* in the corner skating condition to the scaling coefficient being more effective at minimising out-of-plane distances. It was noted, however, that this result may have been due to the misclassification of skating condition cameras, i.e. straight skating condition cameras capturing corner skating (Section 11.4).

Collectively, these findings suggest that the effect of skating condition in the multi-camera network is more sensitive to *out-of-plane error* than *skater point error*. Importantly for the multi-camera network, the effect of skating velocity on *total error* was trivial. The difference between the median RMS velocity error (0.007 $m \cdot s^{-1}$) equated to 3.7% of the ± 0.19 $m \cdot s^{-1}$ target measurement error. This finding suggests that the multi-camera network's *total error* is effectively invariant to the skating condition. As discussed in Section 12.5, this is important in the multi-camera network as the appearance of the fiducial marker differs between the two skating conditions.

Effect of skater stature on total error

In both corner and straight skating conditions, the results showed that the multi-camera network's *total error* significantly increased from the minimum, to mean, to maximum skater stature in Great Britain Short-Track Speed Skating's World Class Performance Programme. Again, these results contradict the findings from Chapter 13 but are consistent with the outcomes of Chapter 11.

In Chapter 13, I stated that *skater point error* significantly decreased as the skater stature increased due to the calibration planes having a higher spatial resolution, i.e. a greater number of pixels per metre. This higher spatial resolution was the product of taller stature skaters' elevated calibration planes having a smaller camera-to-elevated plane distance. In contrast, in Chapter 11 I reported that the multi-camera network's *out-of-plane error* significantly increased with skater stature due to the angle of incidence increasing. These findings further demonstrate that the multi-camera network is more sensitive to *out-of-plane error* than *skater point error.* The former accounted for 7% (corner) and 10% (straight) of the ± 0.19 $m{\cdot}s^{-1}$ target measurement error, the latter 0.8% (corner) and 0.9% (straight) of the ± 0.19 $m{\cdot}s^{-1}$ target measurement error.

Importantly for the multi-camera network, the effect of skater stature on *total erro*r was small. The difference between the minimum and maximum skater stature's median RMS velocity error in the corner (0.011 $m{\cdot}s^{-1}$) and straight (0.014 $m{\cdot}s^{-1}$) equated to only 5.8% and 7.4% of the ± 0.19 $m{\cdot}s^{-1}$ target measurement error. These values, approximately equivalent to the magnitude of *out-of-plane error* minus the magnitude of s*kater point error*, demonstrate that the multi-camera network's *total error* is effectively invariant to the skater stature.

Effect of skating velocity on total error

Consistent with our findings in Chapters 8, 10, 11, and 13, in both corner and straight skating conditions, *total error* significantly increased with skating velocity due to intra-camera *calibration model error*. In Chapter 8, I reported that intra-camera *calibration model error* increased with skating velocity due to velocity-dependent uncertainties in the sampling interval and reconstructed positions. While the former is irrelevant in this investigation, as the ground truth trajectories created in Chapter 9 had a constant 0.04-second sampling interval, the latter, caused by differences in two measured position's intrinsic *calibration model error*, was still present. In Chapters 10, 11 and 13, I showed that intra-camera *calibration model error* was more sensitive to skating velocity than both *out-of-plane* and *skater point error*.

Importantly, the difference between the slow and fast velocity condition’s median RMS velocity error in the corner (0.039 $m{\cdot}s^{-1}$) and straight (0.014 $m{\cdot}s^{-1}$) equated to only 20.5 % and 7.4% of the ± 0.19 $m{\cdot}s^{-1}$ target measurement error. In accordance with

Chapter 11, the corner skating condition's *total error* was larger than the straight due to a more substantial difference in out-of-plane distances (corner = 0.06 m, straight = 0.03 m). For this reason, future research could explore minimising *out-of-plane error* by constructing camera-elevated plane calibration models specific to the current skating velocity. Nevertheless, the results show that the multi-camera network's *total error* is effectively invariant to the skating velocity. As reported in Section 13.4, this is important in the multi-camera network as skating velocity varies during short-track speed skating relays.

Limitations

This investigation has two limitations that warrant consideration. First, as the investigation used a revised version of the simulation described in Chapter 13, the limitations discussed in Section 13.4 are also applicable here. Second, the simulation did not include the effect of the multi-camera network's *rolling shutter error*, as the ground truth trajectories created in Chapter 9 had a constant sampling interval. While this constant sampling interval is not representative of the multi-camera network, as the sampling interval is only constant between corresponding scanlines in consecutive images (Section 5.5.1), the simulation assumed that the multi-camera network would negate *rolling shutter error* by using the electronic rolling shutter model described in Chapter 6. However, as shown below, this would not always be the case due to uncertainty in the automated digitisation of a skater.

To recap, the electronic rolling shutter model allows the readout time $r_y^{(j)}$ for scanline y, in image j, to be calculated as,

$$r_y^{(j)} = t^{(j)} + \left(\frac{y}{S}\right) \Delta t \qquad (Eq. 5.28)$$

where Δt is the sampling interval, S is the total number of scanlines per image, and $t^{(j)}$ is the readout time of the first scanline in image j. Accordingly, the sampling interval $t_c^{(j)}$ between two consecutive frames is calculated as,

$$t_c^{(j)} = \left(r_y^{(j)} + \Delta t\right) - r_y^{(j-1)} \qquad (Eq. 5.29)$$

Uncertainty in the automated digitisation of a skater leads to errors in the model's calculated sampling interval, as the uncertainty represents an error in the measurement of scanline y in $Eq. 5.28$. The impact of this error in $Eq. 5.29$ can be explored using a simple simulation. The data from Chapter 12's investigation demonstrates that the median automated digitisation uncertainty in the v-axis, i.e. the y scanline, was ± 0.55 pixels. As each scanline in the multi-camera network is equivalent to 0.00005 seconds (sampling interval/ total number of scanlines), the median pixel automated digitisation uncertainty leads to sampling interval errors of ± 0.0000275 seconds. Consequently, in the two worst case scenarios the sampling interval error is ± 0.000055 seconds. Accordingly, for a skater travelling at 10 m·s^{-1}, the error in velocity would be ± 0.013 m·s^{-1}. As this value is considerably lower than the median RMS velocity errors reported in Table 14-1, this result demonstrates that the inclusion of *rolling shutter error* in the simulation would not have notably affected our findings.

14.5 Chapter summary

This chapter used Monte Carlo simulations to address the seventh and final objective of the programme of research: to quantify *total error* in the multi-camera network. This error described how the five sources of measurement error in the multi-camera network propagated, collectively, to errors in position and velocity. The chapter showed that the multi-camera network's *total error* was within the ± 0.19 m·s^{-1} target measurement error, significantly less than the Olympic Oval (CAN) multi-camera network's ± 1.53 m·s^{-1} *total error*, and effectively invariant to the skating condition, skater stature, and skating velocity, for all four fiducial markers. Overall, the multi-camera network had a *total error* of ± 0.17 m·s^{-1}. These findings had two clear implications for this thesis. First, the findings answered the thesis's overarching research question '*Can multi-camera networks be used to measure accurate, two-dimensional, relay exchange kinematics*'. Yes, if the network's sources of measurement error are mitigated as outlined in Part II of this thesis. Second, the findings confirmed that the aim of the thesis – to develop a multi-camera network to measure accurate, two-dimensional, relay exchange kinematics – had been achieved. Importantly, this finding suggested that Great Britain Short-Track Speed Skating can use the National Ice Centre (GBR) multi-camera network as a tool to advance knowledge on *'how to execute the relay exchange effectively'*.

Part III Multi-camera network demonstration

Chapter 15

Relay exchange execution in elite short-track speed skating

15.1 Introduction

To support their targeted improvement of the relay exchange, Great Britain Short-Track Speed Skating require a tool that can be used to advance knowledge on *'how to execute the relay exchange effectively'*; a tool that measures relay exchange kinematics in representative race scenarios, over its entirety, and with an acceptable level of measurement error (± 0.19 $m \cdot s^{-1}$). In Chapter 3, a review of existing measurement solutions found that the only tool that facilitated the measurement of the relay exchange in representative race scenarios, and over its entirety, was the Olympic Oval (CAN) multi-camera network. However, while this multi-camera network satisfied the metrics, scenarios, and scope of relay exchange measurement, its ± 1.53 $m \cdot s^{-1}$ error did not meet the target measurement error. For these reasons, this thesis aimed to develop a multi-camera network to measure accurate, two-dimensional, relay exchange kinematics.

In Chapter 14, Monte-Carlo simulations showed that the *total error* in the developed multi-camera network was ± 0.17 $m \cdot s^{-1}$. This error was within the ± 0.19 $m \cdot s^{-1}$ target measurement error, significantly less than the Olympic Oval (CAN) multi-camera network's ± 1.53 $m \cdot s^{-1}$ *total error*, and effectively invariant to the skating condition, skater stature, and skating velocity. These findings confirmed that the aim of the thesis had been achieved and suggested that Great Britain Short-Track Speed Skating could use the multi-camera network as a tool to advance knowledge on *'how to execute the relay exchange effectively'*.

In this chapter, I present two investigations that demonstrate how this reduction in error to within the target measurement error allows Great Britain Short-Track Speed Skating to advance knowledge on *'how to execute the relay exchange effectively'*. First, as I showed that the relay exchange's effect on race time is dependent on race speed (Section 2.4.1), I validate one of two theoretical mechanisms proposed for this phenomenon. This mechanism states that the relay exchange's effect on race time transitions from positive to negative, with increasing race speed, due to the relative velocity at first-contact increasing. Second, as I showed that the relay exchange scenario offers a superior opportunity for a team to overtake (Section 2.4.2), I explore *'how to execute the relay exchange to achieve a gain-in-race position'*. This work (1) examines whether the two factors reported critical for effective relay exchange execution – when a team is isolated from the pack race – are discriminative of successful overtakes, and (2) uses a single case study to explore the mechanisms that underlie the first critical factor: the time for $Skater_1$ to contact $Skater_2$ after exiting the corner.

In both investigations, I demonstrate how the developed multi-camera network allows greater insight into the execution of the relay exchange by considering how the National Ice Centre (GBR) and Olympic Oval (CAN) multi-camera networks' uncertainty in velocity affects the interpretation of the results. Collectively, the analyses show that only the National Ice Centre (GBR) multi-camera network enables Great Britain Short-Track Speed Skating to validate the proposed theoretical mechanisms and explore *'how to execute the relay exchange to achieve a gain-in-race position'*.

15.2 Method

The Faculty of Health & Wellbeing Research Ethics Committee, Sheffield Hallam University, UK, approved these investigations.

15.2.1 Performance data

Both investigations used data collected from two Great Britain Short-Track Speed

Skating training sessions during the 2017–2018 season. The dataset consisted of one 3,000 m and one 5,000 m, three-team, mixed-sex, relay race. Each race was captured using the multi-camera network developed in the second part of this thesis. In both races, skaters wore one of twelve fiducial markers. These markers consisted of the six circular fiducial marker colours tested in Chapter 12 (see Section 12.3.2) and an additional six triangular fiducial marker colours explored during the multi-camera network's development.

15.2.2 Race analysis procedure

For each race, I used the multi-camera network to automatically compute each teams' *Skater*$_1$ and *Skater*$_2$ position and velocity for every instance of a relay exchange where both skaters wore a circular fiducial marker that exhibited sub-pixel automated digitisation uncertainty (i.e. red, yellow, green, and cyan). As illustrated in Figure 15-1, I computed each skaters' kinematics from the moment when the centre of *Skater*$_1$'s fiducial marker first passed through the entry sector line ($t_{1ln.ent}$) until the centre of *Skater*$_2$'s fiducial marker first passed through the following entry sector line ($t_{2ln.ent}$). For each instance of a relay exchange, I also manually digitised the team's position in the pack race at the corner exit sector line, corner entry sector line, and the point in time of *Skater*$_1$ and *Skater*$_2$'s first- (t_{fir}) and final- (t_{fin}) contact (Figure 15-1). All manual digitisation was performed by a single operator to negate inter-operator digitisation error. In the scenario where a skater fell, no further measurements were computed for that team.

15.2.3 Data analysis

For each instance of a relay exchange, I calculated four metrics – depicted in Figure 15-2 – using the computed relay exchange kinematics: (1) *Skater*$_1$'s *corner exit time* (t_1): the time taken from when the centre of *Skater*$_1$'s fiducial marker first passed through the apex sector line to when the centre of *Skater*$_1$'s fiducial marker first passed through the exit sector line, (2) *Skater*$_1$'s *apex block distance* (x_1): the distance along the apex sector

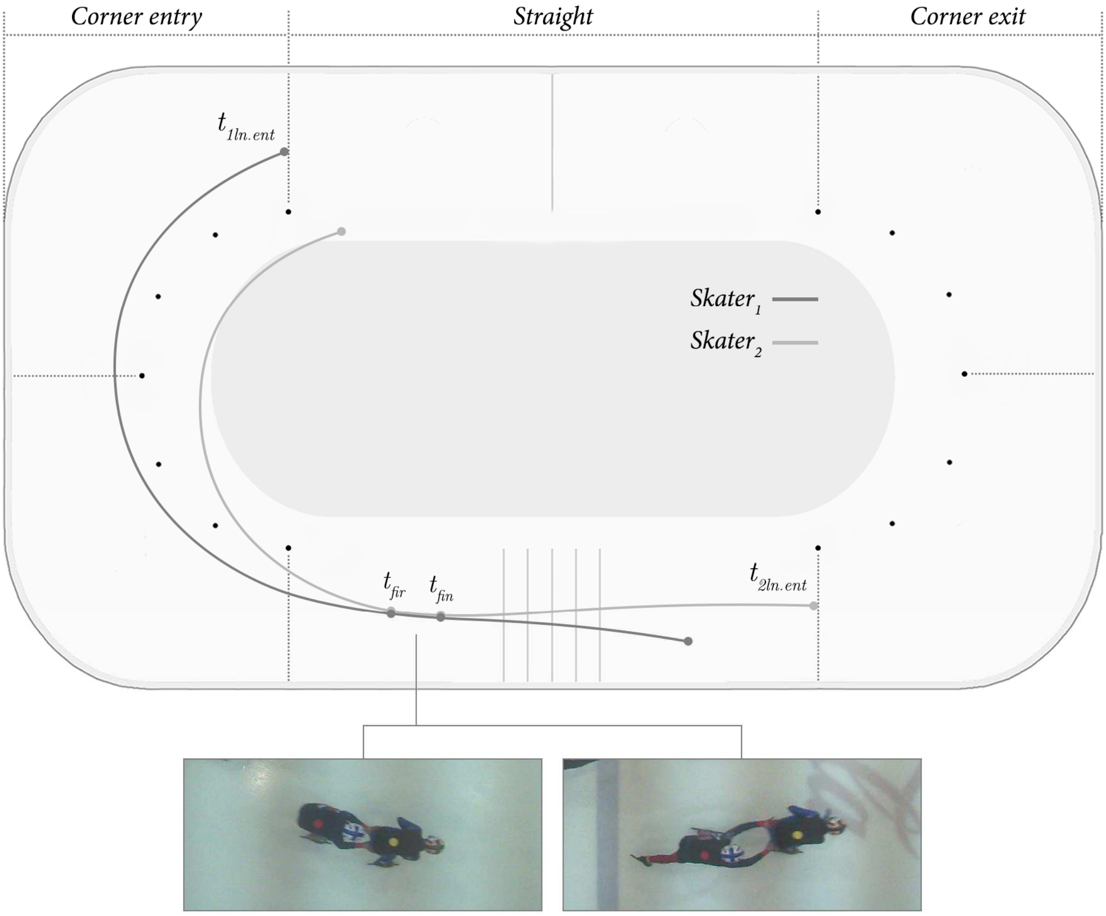

Figure 15-1. The race analysis procedure, highlighting (1) the period of computed kinematics, i.e. from when the centre of *Skater$_1$*'s fiducial marker first passes through the entry sector line ($t_{1ln.ent}$) until the centre of *Skater$_2$*'s fiducial marker first passes through the following entry sector line ($t_{2ln.ent}$), and (2) the manual digitisation of the first-(t_{fir}) and final-(t_{fin}) contact.

line from the track marking block to the centre of *Skater$_1$*'s fiducial marker, (3) *Skater$_1$'s exit block distance* (y_1): the distance along the exit sector line from the track marking block to the centre of *Skater$_1$*'s fiducial marker, and (4) the team's *gain-in-race position* count: the number of positive changes in race position from the corner exit sector line to the following corner entry sector line, e.g. if a team moved from 3rd to 1st position in the race, this would count as two gain-in-race positions.

To validate whether increasing race speeds led to larger relative velocities at first-contact, I calculated *Skater$_1$*'s corner exit speed, i.e. the team's current speed in the race, and the relative velocity at first-contact, as described in Section 3.2.1 (Equations 3.1 and 3.2). To examine whether the two factors reported critical for effective relay exchange execution

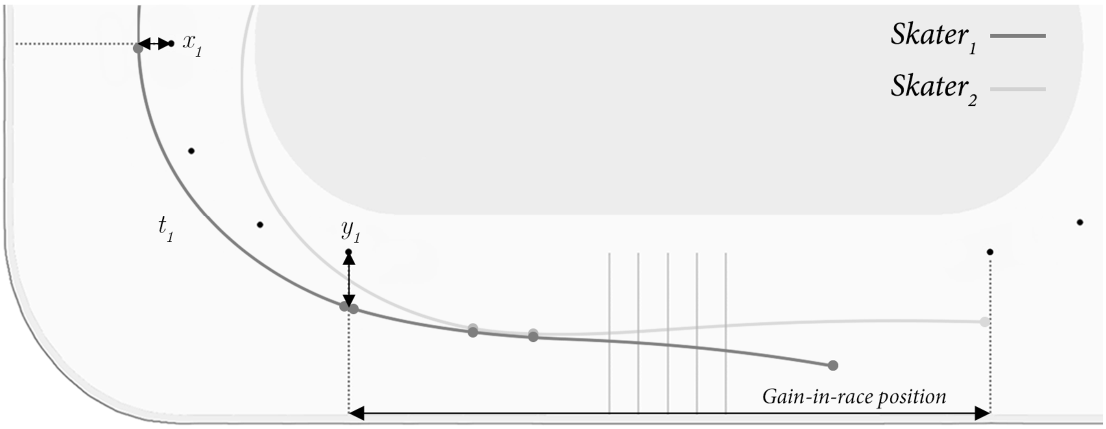

Figure 15-2. The four metrics calculated for each instance of a relay exchange: *Skater$_1$*'s corner exit time (t_1), *Skater$_1$*'s apex block distance (x_1), *Skater$_1$*'s exit block distance (y_1), and the *gain-in-race position* count.

– when a team is isolated from the pack race – are discriminative of successful overtakes, I calculated each factor for every gain-in-race position where both gain- and loss-in-race position teams' *Skater$_1$* and *Skater$_2$* wore a circular fiducial marker that exhibited sub-pixel automated digitisation uncertainty. Both factors, that is, the time for *Skater$_1$* to contact *Skater$_2$* after exiting the corner (t_{cont}) and the contact energy exchange efficiency (η_e), were computed as described in Section 3.2.1 (Equations 3.5 to 3.7). Finally, to examine the mechanisms that underlie the time for *Skater$_1$* to contact *Skater$_2$* after exiting the corner, I compared the gain- and loss-in-race position teams' position and velocity at the point in time when each team's *Skater$_1$* fiducial marker first passed through the corner entry, apex, and exit sector lines. To consider how the National Ice Centre (GBR) and Olympic Oval (CAN) multi-camera networks' uncertainty in velocity affected the interpretation of each sector line comparison, each comparison accounted for the multi-camera networks' reported uncertainty.

15.2.4 Statistical analysis

SPSS 24 (IBM, 2016) was used to analyse both race time and race position data. For the race time data, I examined the relationship between *Skater$_1$*'s corner exit speed and the relative velocity at first-contact using Pearson's correlation coefficient, r, for normally distributed datasets, or Spearman's Rho correlation coefficient, ρ, for non-normally distributed datasets. In both cases, the correlation coefficient ranges from -1 to $+1$, with a coefficient of $\pm\ 1$ indicating a perfect positive or negative relationship, and a coefficient of 0 indicating no relationship at all (Field, 2009). To test the correlation coefficient's statistical significance, I used a one-tailed hypothesis as the proposed theoretical mechanism is directional, i.e. the relative velocity at first-contact increases with *Skater₁*'s corner exit speed. To consider how the National Ice Centre (GBR) and Olympic Oval (CAN) multi-camera networks' uncertainty in velocity affected the interpretation of the calculated correlation coefficient, I estimated the coefficient's 95% confidence bounds using Monte-Carlo error analyses (Curran, 2014). For each multi-camera network, I added uncertainty to the measured relative velocities at first-contact – and recalculated the correlation coefficient – for 10,000 independent iterations. The analysis added uncertainty to the measured values by uniformly sampling from the multi-camera network's uncertainty in relative velocity at first-contact. In accordance with Taylor (1997), I calculated this uncertainty in relative velocity as

$$\delta v_{2fir|1fir} = \sqrt{\delta {v_1}^2 + \delta {v_2}^2} \qquad (Eq.\,15.1)$$

where $\delta {v_1}^2$ and $\delta {v_2}^2$ is the multi-camera network's uncertainty in *Skater*$_1$ and *Skater*$_2$'s velocity. This resulted in a ± 0.24 m·s^{-1} and ± 2.16 m·s^{-1} uncertainty in relative velocity in the National Ice Centre (GBR) and Olympic Oval (CAN) multi-camera networks, respectively. The 95% confidence bounds represented the values that 95% of the calculated correlation coefficients laid between.

For the race position data, I calculated each critical factor's $percent\ advantage$ (Graham & Mayberry, 2014). The $percent\ advantage$ represents the conditional percentage of relay exchange overtakes in which the gain-in-race position's critical factor i had a better value than the loss-in-race position's critical factor i. For example, if the gain-in-race position's time to first-contact was better in three out of five overtakes, and the same in one out of five overtakes, the time to first-contact would receive a

$percent\ advantage$ of 75%. Based on Riewald, Broker, Smith, & Otter (1997), better values for the time to first-contact and the contact energy exchange efficiency were smaller and greater values, respectively. For each critical factor the analysis also compared differences between the gain- and loss-in-race position teams using a dependent t-test. Again, I used a one-tailed hypothesis due to both critical factors being directional. Finally, to consider how the National Ice Centre (GBR) and Olympic Oval (CAN) multi-camera networks' uncertainty in velocity affected the interpretation of the contact energy exchange efficiency's $percent\ advantage$, I calculated each multi-camera network's uncertainty in contact energy exchange efficiency. In accordance with Taylor (1997), I calculated this uncertainty as

$$\frac{\delta\eta_e}{\eta_e} = \sqrt{\left(\frac{\delta E_{k2fin}}{E_{k2fin}}\right)^2 + \left(\frac{\delta E_{k1fir}}{E_{k1fir}}\right)^2 + \left(\frac{\delta E_{k2fir}}{E_{k2fir}}\right)^2} \qquad (Eq.\,15.2)$$

where δ represents the measurement uncertainty, E_{k2fin} is *Skater₂*'s kinetic energy at final-contact, E_{k1fir} is *Skater₁*'s kinetic energy at first-contact, and E_{k2fir} is *Skater₂*'s kinetic energy at first-contact. In this equation, the uncertainty in each skater's kinetic energy, δE_K, is calculated as

$$\frac{\delta E_K}{E_K} = 2\left(\frac{\delta v}{v}\right) \qquad (Eq.\,15.3)$$

where v is the skater's velocity at that point in time, and δv is the multi-camera network's uncertainty in velocity. The analysis did not consider how the National Ice Centre (GBR) and Olympic Oval (CAN) multi-camera networks' timing uncertainty affected the interpretation of the time to first-contact's $percent\ advantage$, as temporal uncertainty data was not available for the Olympic Oval (CAN) multi-camera network.

In all statistical tests, I used Kolmogorov–Smirnov tests to test for normality, set the significance level, $\propto$, at $p < 0.05$, and calculated effect sizes using Pearson's correlation coefficient, r (Field, 2009). Effect sizes were interpreted using Cohen's thresholds; where < 0.1, is trivial; 0.1–0.3, small; > 0.3–0.5, moderate, and > 0.5, large (Cohen, 1988).

15.3 Results

15.3.1 Race time

In total, $Skater_1$ and $Skater_2$ wore circular fiducial markers that exhibited sub-pixel automated digitisation uncertainty in 12 relay exchanges. These exchanges had a median $Skater_1$ corner exit speed of $11.08\ \text{m·s}^{-1}$ (IQR = $0.31\ \text{m·s}^{-1}$) and a median relative velocity at first-contact of $1.74\ \text{m·s}^{-1}$ (IQR = $0.29\ \text{m·s}^{-1}$). I used the Spearman's Rho correlation coefficient to examine the relationship between these two metrics as the Kolmogorov–Smirnov test showed that both the distribution of $Skater_1$'s corner exit speed ($D\ (12) = 1, p < 0.001$) and the relative velocity at first-contact ($D\ (12) = 0.925, p < 0.001$) significantly differed from normal. The coefficient showed that the relative velocity at first-contact was significantly related to $Skater_1$'s corner exit speed, $\rho = 0.74$, p (one-tailed) < 0.01. More specifically, as $Skater_1$'s corner exit speed increased, so did the relative velocity at first-contact. The correlation coefficient's 95% confidence bounds ranged from 0.44 to 0.82 in the National Ice Centre (GBR) multi-camera network and from -0.46 to 0.67 in the Olympic Oval (CAN) multi-camera network.

15.3.2 Race position

In total, the gain- and loss-in-race position teams' $Skater_1$ and $Skater_2$ wore circular fiducial markers that exhibited sub-pixel automated digitisation uncertainty in four relay exchanges. Table 15-1 presents each critical factor's descriptive statistics, significance test results, effect sizes, and *percent advantage*. The gain-in-race position teams' time for $Skater_1$ to contact $Skater_2$ after exiting the corner was significantly shorter than the loss-in-race position teams' ($p < 0.01$), with the magnitude of this effect large ($r = -0.95$). Moreover, the time for $Skater_1$ to contact $Skater_2$ after exiting the corner had a 100% *percent advantage*, i.e. in 100% of the relay exchange overtakes, the gain-in-race position team had a shorter time to first-contact.

Table 15-1. Descriptive statistics (mean ± standard deviation), significance test results, effect sizes, and $percent\ advantage$ for each critical factor.

Critical factor	Gain-in-race position	Loss-in-race position	t	p	r	$Percent\ advantage$
Time to first-contact	0.51 ± 0.16 s	0.81 ± 0.1 s	-5.415	0.006	-0.95	100%
Contact energy exchange efficiency	61.6 ± 4.7%	69.5 ± 5.2%	-1.600	0.896	0.68	25%

Note: Effect size measured using Pearson's correlation coefficient, r.

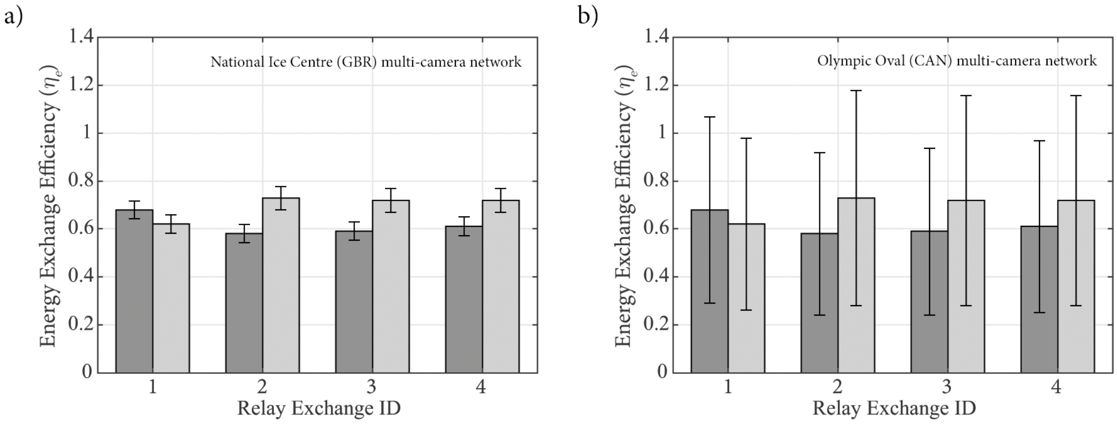

Figure 15-3. The gain- (dark grey) and loss- (light grey) -in-race position teams' contact energy exchange efficiency. The error bars represent the measurement uncertainty in the National Ice Centre (a) and Olympic Oval (b) multi-camera networks.

In contrast, the gain-in-race position teams' contact energy exchange efficiency was not significantly more efficient than the loss-in-race position teams' contact energy exchange efficiency (p = 0.90). In fact, the mean contact energy exchange efficiency was greater for the loss-in-race position team and the contact energy exchange efficiency only had a $percent\ advantage$ of 25%, i.e. the gain-in-race position team only had a more efficient energy exchange during skater contact in 25% of the relay exchange overtakes. When considering how each multi-camera network's uncertainty in velocity affected the interpretation of the contact energy exchange efficiency's $percent\ advantage$, Figure 15-3a shows that the developed multi-camera network could conclude that three of the four observed differences in contact energy exchange efficiency were real – and not due to measurement error – as the error bars did not overlap in exchanges two to four. These exchanges represented the three instances where the loss-in-race position team had a more efficient contact energy exchange efficiency. In contrast, Figure 15-3b shows that the Olympic Oval (CAN) multi-camera network could not conclude that any of the observed differences were real, as the error bars overlapped in all four relay exchanges.

Figure 15-4a illustrates the selected overtake case study used to examine the mechanisms that underlie the time for $Skater_1$ to contact $Skater_2$ after exiting the corner.

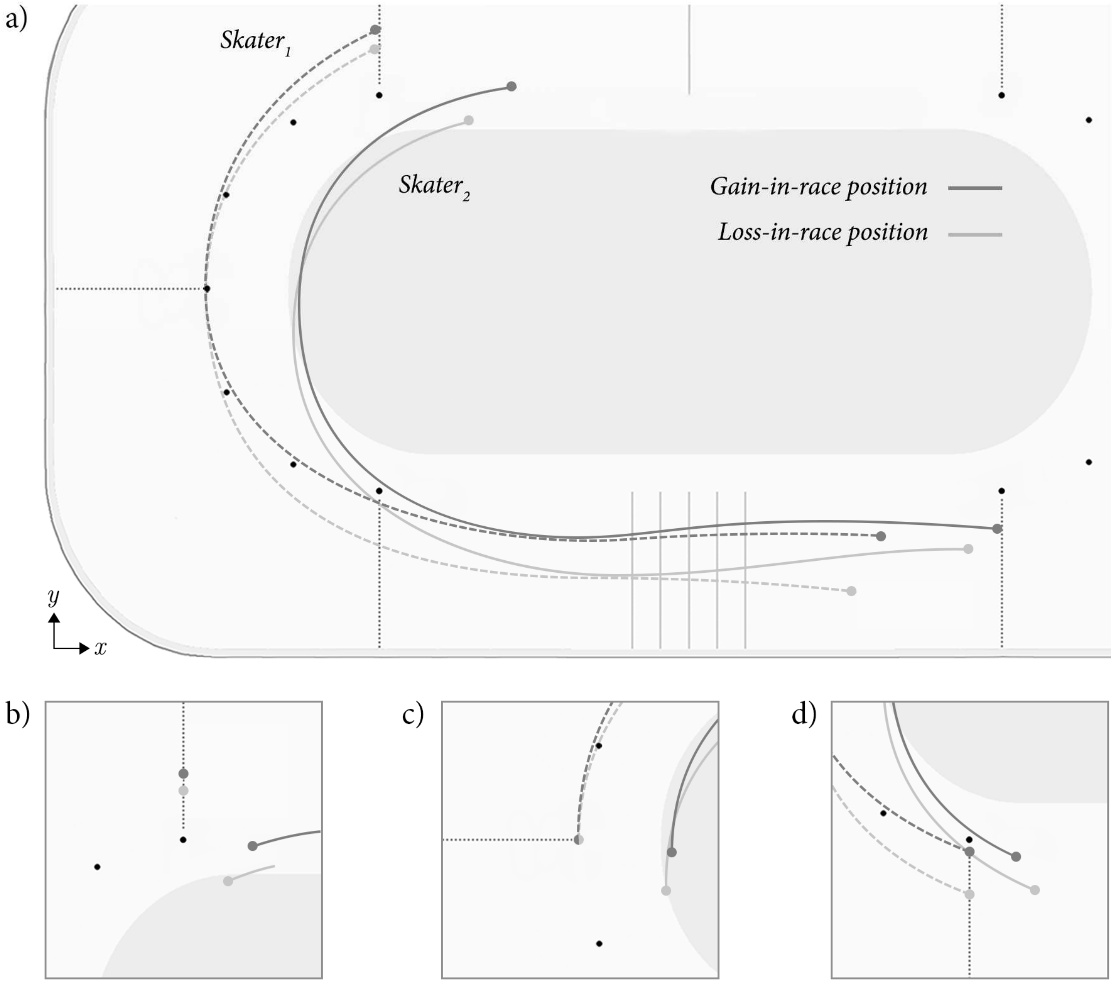

Figure 15-4. (a) The case study's gain- and loss-in-race position teams' *Skater*$_1$ and *Skater*$_2$ trajectories, and (b-d) the gain- and loss-in-race position teams' *Skater*$_1$ and *Skater*$_2$ track position when each teams' *Skater*$_1$ fiducial marker first passed through the corner entry, apex, and exit sector line.

The gain- and loss-in-race position teams' time were 0.52 seconds and 0.75 seconds, respectively. Figures 15-4b to 15-4d and Figure 15-5 show the position and velocity of each team's *Skater*$_1$ and *Skater*$_2$, when each teams' *Skater*$_1$ first passed through the corner entry, apex, and exit sector line.

Corner entry

At the corner entry sector line (Figure 15-4b), the teams' *Skater*$_1$ had comparable track positions in the y-axis (Δ = 0.45 m) and similar skating velocities (Δ = 0.05 m·s^{-1}). However, compared to the loss-in-race position team, the gain-in-race position team's *Skater*$_2$ was further behind *Skater*$_1$ in the x-axis (Δ = 1.03 m), closer to *Skater*$_1$ in the y-

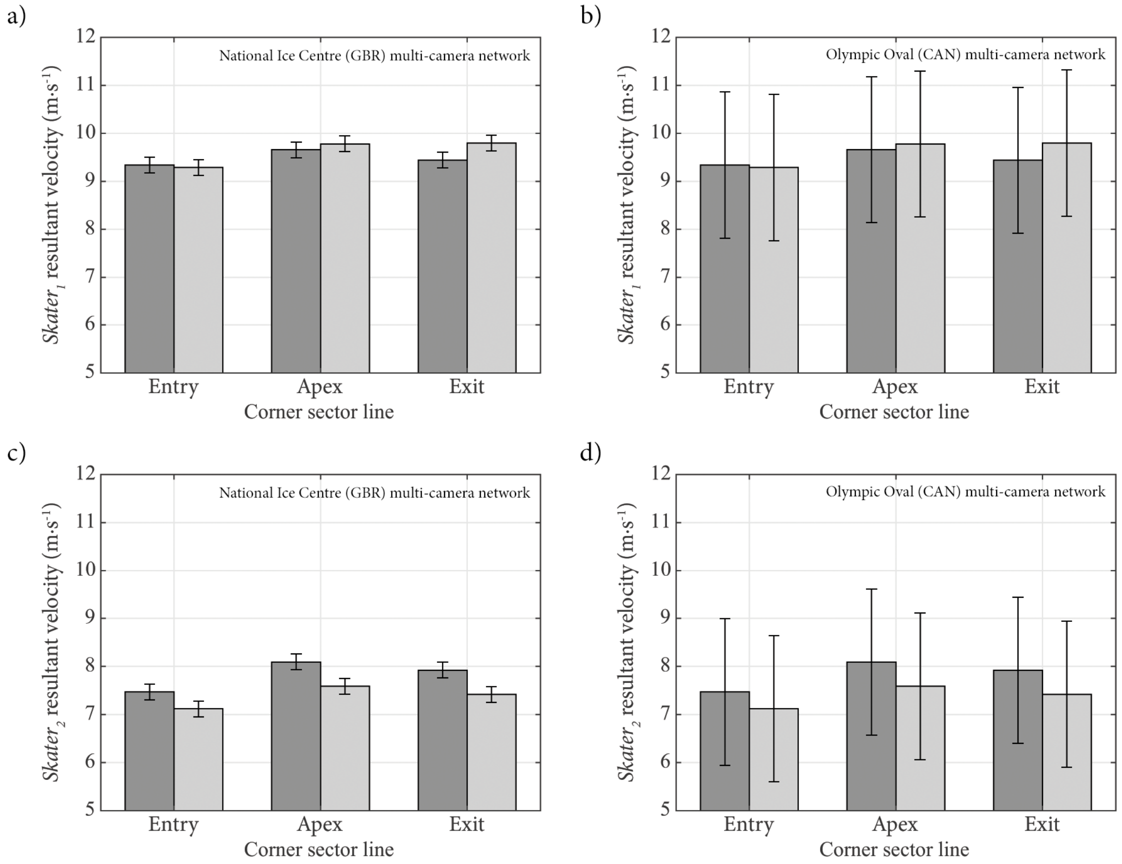

Figure 15-5. The gain- (dark grey) and loss- (light grey) -in-race position teams' $Skater_1$ and $Skater_2$ resultant velocity when each teams' $Skater_1$ fiducial marker first passed through the corner entry, apex, and exit sector line. The error bars represent the measurement uncertainty in the National Ice Centre (a & c) and Olympic Oval (b & d) multi-camera networks.

axis (Δ =1.44 m), and travelling faster (Δ = 0.35 m·s^{-1}). Figures 15-5c and 15-5d show that only the developed multi-camera network could conclude that this observed difference in velocity was real – and not due to measurement error – as the error bars did not overlap in the National Ice Centre (GBR) multi-camera network.

Corner apex

At the corner apex sector line (Figure 15-4c), the teams' $Skater_1$ and $Skater_2$ had similar track positions in the x-axis ($S_1\Delta$ = 0.06 m, $S_2\Delta$ = 0.25 m). Likewise, the teams' $Skater_1$ exhibited similar skating velocities (Δ = 0.13 m·s^{-1}). However, compared to the loss-in-race position team, the gain-in-race position team's $Skater_2$ was closer to $Skater_1$ in the y-axis (Δ =0.93 m) and had a faster skating velocity (Δ = 0.5 m·s^{-1}). Figures 15-5c and 15-5d show that only the developed multi-camera network could conclude that this observed difference in velocity was real – and not due to measurement error – as the error bars did not overlap in the National Ice Centre (GBR) multi-camera network.

Corner exit

At the corner exit sector line (Figure 15-4d), the gain-in-race position team's *Skater₁* was closer to the corner exit track marking block in the y-axis (Δ = 1.46 m), and had a slower skating velocity (Δ = 0.36 m·s^{-1}), compared to the loss-in-race position team's *Skater₁*. Similarly, the gain-in-race position team's *Skater₂* was closer to the corner exit track marking block in the y-axis (Δ = 1.41 m), closer to *Skater₁* in the x-axis (Δ = 0.73 m) and had a faster skating velocity (Δ = 0.5 m·s^{-1}). Figure 15-5 shows that only the developed multi-camera network could conclude that the observed differences in velocity were real – and not due to measurement error – as the error bars in the National Ice Centre (GBR) multi-camera network did not overlap.

15.4 Discussion

In the previous sections, I presented two investigations that demonstrate how the multi-camera network's reduction in error to within the target measurement error allows Great Britain Short-Track Speed Skating to advance knowledge on *'how to execute the relay exchange effectively'*. In this section, I discuss the findings of each investigation, the practical implications for the thesis and for Great Britain Short-Track Speed Skating, the limitations of the investigations, and how future work should continue to investigate the relay exchange's execution.

15.4.1 Race time

In the first investigation, I validated the first of two theoretical mechanisms proposed for why the relay exchange's effect on race time is dependent on race speed. This mechanism proposed that the relay exchange's effect on race time transitions from positive to negative, with increasing race speeds, due to the relative velocity at first-contact increasing. Overall, the results supported this mechanism, as the relative velocity at first-contact increased with *Skater$_1$*'s corner exit speed, i.e. the team's current race speed.

Importantly, the results also showed that due to its smaller uncertainty in velocity, only the developed multi-camera network could conclude that the observed relationship between the relative velocity at first-contact and race speed was real and not due to measurement error. In the National Ice Centre (GBR) multi-camera network, the correlation coefficient's 95% confidence bounds ranged from a medium ($\rho = 0.44$) to large ($\rho = 0.82$) positive relationship. In contrast, the correlation coefficient's 95% confidence bounds ranged from a medium negative ($\rho = -0.46$) to large positive ($\rho = 0.67$) relationship in the Olympic Oval (CAN) multi-camera network. This finding provides one example of how the multi-camera network's reduction in error to within the target measurement error allows Great Britain Short-Track Speed Skating to advance knowledge on *'how to execute the relay exchange effectively'*. The reduction enables Great Britain Short-Track Speed Skating to validate the theoretical mechanisms that underlie effective relay exchange execution. Mechanisms that the Olympic Oval (CAN) multi-camera network cannot validate due its large uncertainty in velocity.

15.4.2 Race position

In the second investigation, I explored *'how to execute the relay exchange to achieve a gain-in-race position'*, as the relay exchange scenario offers a superior opportunity for a team to overtake (Section 2.4.2). To do this, I (1) examined whether the two factors reported critical for effective relay exchange execution are discriminative of successful overtakes, and (2) used a single case study to explore the mechanisms that underlie the first critical factor: the time for *Skater$_1$* to contact *Skater$_2$* after exiting the corner.

First, the results showed that while the time for *Skater$_1$* to contact *Skater$_2$* after exiting the corner is discriminative of successful overtakes, the contact energy exchange efficiency is not. More specifically, the gain-in-race position team always had a shorter time to first-contact but only had a more efficient energy exchange in one of the four overtakes analysed. Second, the results showed that both the timing and velocity of *$Skater_2$* is an essential part of the mechanism that underlies the time for *$Skater_1$* to contact *$Skater_2$* after exiting the corner. When *$Skater_2$* was closer to *$Skater_1$* at the corner entry sector line, they were further ahead of *$Skater_1$* at both the corner apex and corner exit, which ultimately led to a greater time to first-contact. In order to be further behind *$Skater_1$* at the corner entry, *$Skater_2$* had to have a greater velocity to ensure that they arrived on the straight in-front of *$Skater_1$*.

Importantly, the results showed that due to its smaller uncertainty in velocity, only the developed multi-camera network could conclude that (1) the relay exchange's contact energy exchange efficiency was not discriminative of successful overtakes, and (2) that *$Skater_2$*'s velocity was an essential part of the mechanism that underlies the time to first-contact. The National Ice Centre (GBR) multi-camera network could identify that the observed differences between the gain- and loss-in-race position teams' contact energy exchange efficiency were real in three of the four relay exchanges analysed. Likewise, the multi-camera network could identify real differences in each team's *$Skater_2$* velocity at the corner entry, apex, and exit. In contrast, due to its large uncertainty in velocity, the Olympic Oval (CAN) multi-camera network could not conclude whether the observed differences in contact energy exchange efficiency and *$Skater_2$* velocity were real or due to measurement error. These findings provide two further examples of how the multi-camera network's reduction in error to within the target measurement error allows Great Britain Short-Track Speed Skating to advance knowledge on *'how to execute the relay exchange effectively'*. The reduction enables Great Britain Short-Track Speed Skating to explore *'how to execute the relay exchange to achieve a gain-in-race position'*.

15.4.3 Practical implications

This chapter has one clear implication for this thesis. In Chapter 14, I could only suggest that the developed multi-camera network could be used to advance knowledge on *'how to execute the relay exchange effectively'*, as its *total error* was within the target measurement error. In this chapter, however, I provide three examples that demonstrate how the developed multi-camera network's reduction in error enables greater insight into *'how to execute the relay exchange effectively'*. For this reason, Great Britain Short-Track Speed Skating can use the developed multi-camera network as a tool to support their targeted improvement of the relay exchange execution.

In addition, as the two studies presented in this chapter are the first to investigate their respective topics, Great Britain Short-Track Speed Skating can use the chapter's findings to advance their understanding of *'how to execute the relay exchange effectively'*. In the first investigation, I found that $Skater_1$ and $Skater_2$'s relative velocity at first-contact increased with race speed. One explanation for this phenomenon is that $Skater_2$ generates their speed on the inside of the short-track. As the inside of the short-track has a tighter corner radius, $Skater_2$ expends more energy compared to $Skater_1$ – at comparable race speeds – as they have to overcome higher cornering forces (Rundell, 1996). Therefore, as the race speed increases, it becomes more difficult for $Skater_2$ to match the speed of $Skater_1$. As demonstrated in Chapter 2, when the relative velocity at first-contact increases, $Skater_2$'s final-contact velocity relative to $Skater_1$'s first-contact velocity decreases. For this reason, to mitigate the relay exchange's effect on race time transitioning from positive to negative with increasing race speeds, $Skater_2$ should further attempt to match the speed of $Skater_1$ at faster race speeds.

In the second investigation, I first found that the time for $Skater_1$ to contact $Skater_2$ after exiting the corner is discriminative of successful overtakes. One explanation for this finding is that $Skater_1$ suffers pre-contact velocity losses after exiting the corner (Riewald et al., 1997). Subsequently, a greater time to first-contact may be associated with a greater loss in $Skater_1$'s pre-contact velocity. We can explore the effect of this velocity loss by modelling the relay exchange as a one-dimensional collision using the mean contact energy exchange efficiency reported by Riewald et al. (1997) and a constant $Skater_2$ first-contact velocity. Figure 15-6 shows that as $Skater_1$'s pre-contact velocity loss increases, the absolute magnitude of $Skater_2$'s final-contact velocity decreases. As a result,

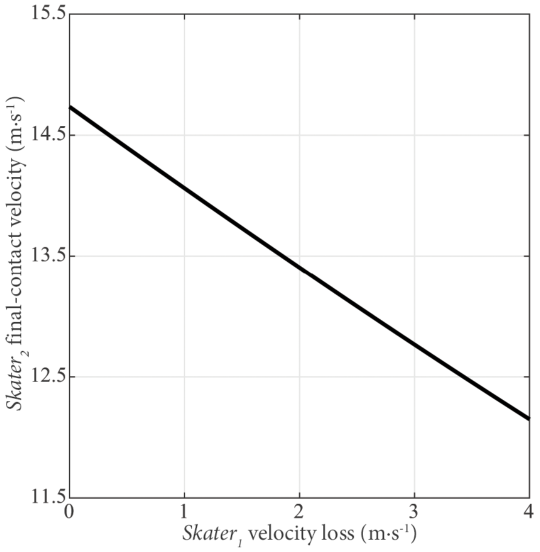

Figure 15-6. The effect of *Skater*$_1$ pre-contact velocity loss on *Skater*$_2$'s final-contact velocity.

it seems essential for the prospective gain-in-race position team to have a shorter time to first-contact compared to the prospective loss-in-race position team, as this is likely to lead to the team having a greater *Skater*$_2$ final-contact velocity.

Second, I found that the contact energy exchange efficiency is not discriminative of successful overtakes. As useful performance indicators should relate to successful performance outcomes (Hughes & Bartlett, 2002), this finding suggests that the contact energy exchange efficiency is not a suitable performance indicator of the relay exchange's execution in representative race scenarios. For example, consider two relay exchanges with the same *Skater*$_1$ first-contact velocity (12 m·s^{-1}), *Skater*$_2$ first-contact velocity (10 m·s^{-1}), and contact energy exchange efficiency (η_e = 65%). The only difference between these exchanges is that *Skater*$_1$ and *Skater*$_2$ have a mass of 65 kg in the first exchange and a mass of 70 kg and 65 kg in the second relay exchange. By rearranging Equation 3.6, we can calculate that in these relay exchanges, *Skater*$_2$'s final-contact velocity is 10.15 m·s^{-1} and 10.38 m·s^{-1}, respectively. These exchanges have different final-contact velocities due to differences in *Skater*$_1$'s mass. This difference in final-contact velocity is more important than the equal contact energy exchange efficiency when comparing the execution of relay exchanges in head-to-head scenarios.

Collectively, these findings suggest that the factors critical for effective relay exchange execution differ between the scenarios where a team is isolated from the pack race and when a team successfully achieves a gain-in-race position. Therefore, although the relay exchange always involves $Skater_1$ pushing $Skater_2$ at the start of the straight, its execution should be approached dynamically – based on the race scenario and the goal of the relay exchange – rather than a 'one-type-fits-all' approach.

Finally, I found that $Skater_2$'s timing and velocity is an essential part of the mechanism that underlies the time for $Skater_1$ to contact $Skater_2$ after exiting the corner; the factor critical to effective relay execution in all relay scenarios currently investigated. This finding is unsurprising considering that during the relay exchange, $Skater_1$ and $Skater_2$'s actions are interdependent and need to be coordinated to execute the relay exchange effectively. As reported by Steiner, Macquet, & Seiler (2017), when teams succeed in coordinating their aggregated resources effectively, for example by both individuals subtly adapting their movement displacement trajectories and velocity to create or minimise space and time (Duarte et al., 2012), they optimise the parameters relevant to their performance. Accordingly, it seems advisable that $Skater_2$ adapts their position and velocity to ensure that they are behind $Skater_1$ as this skater passes the corner entry sector line, and approximately level with $Skater_1$ at the apex sector line, to guarantee that they do not arrive at the start of the straight too early.

15.4.4 Limitations

As the chapter's findings can be used by Great Britain Short-Track Speed Skating to advance their understanding of *'how to execute the relay exchange effectively'*, the limitations of the investigations should be noted. First, the dataset used in both investigations consisted of two relay races collected during the multi-camera network's development period. At this point in the programme of research, twelve different fiducial markers were being evaluated for automated skater digitisation. Subsequently, the number of instances where both skaters or gain- and loss-in-race position teams wore circular fiducial markers that exhibited sub-pixel automated digitisation was small (n = 12 and n = 4, respectively). Still, the samples are similar to the twelve (Riewald et al., 1997) and six (Osborough & Henderson, 2009) relay exchanges analysed in existing investigations.

Second, the teams in both relay races were mixed-sex. For this reason, the analysis included male-to-male, female-to-female, and female-to-male, relay exchanges. Although the mixed-sex relay event is being introduced at the 2022 Winter Olympic Games (ISU, 2018), this thesis is focused on the men's 5,000 m relay event (Section 2.4.4). Accordingly, due to sexual dimorphisms in skeletal muscle mass, strength, anaerobic power, anaerobic capacity, and maximal aerobic capacity (Seiler, de Koning, & Foster, 2007), it is unclear whether male-to-male relay exchanges would produce the same findings found in this chapter given the already small sample size.

Finally, both relay races comprised of three teams. Although this race format does occur in elite short-track speed skating, the relay event typically involves four teams racing head-to-head (ISU, 2016). As there is no current understanding of how different spatial constraints – afforded by the team's race position and the number of teams in the pack race – affect the factors discriminative of successful overtakes, the findings at present should only be deemed relevant for the scenario where three-teams are involved in the relay exchange scenario.

15.4.5 Future work

The chapter's findings also provide a rationale for how Great Britain Short-Track Speed Skating should continue to investigate the relay exchange execution. First, to address the limitations reported in Section 15.4.4, future work should repeat both investigations using a larger sample of same- and mixed-sex relay exchanges, from three- and four-team relays. Second, as the relay exchange's effect on race time transitions from positive to negative with increasing race speeds due to larger relative velocities at first-contact, future work should investigate *'how to execute the relay exchange to minimise the relative* *velocity at first-contact'*. This work should begin by determining the upper-limit of *Skater*$_2$'s velocity during the corner, to understand whether skaters can match the velocity of *Skater*$_1$ at first-contact but choose not to. Third, as Section 15.4.2 showed that not all relay exchange metrics are suitable performance indicators in representative race scenarios, future work should explore new metrics for quantifying the relay exchange's execution. Finally, as the timing and velocity of *Skater*$_2$ is an essential part of the mechanism that underlies the time to first-contact, future work should continue to investigate *Skater*$_1$ and *Skater*$_2$'s interpersonal coordination tendencies. To provide a more detailed insight, this work should use additional measures – such as *Skater*$_1$ and *Skater*$_2$'s relative distance and relative velocity – over a continuous time scale, as this investigation only considered the skaters' position and velocity at three key locations: the corner entry, apex, and exit.

15.5 Chapter summary

This chapter presented two investigations that demonstrated how the multi-camera network's reduction in error to within the target measurement error allows Great Britain Short-Track Speed Skating to advance knowledge on *'how to execute the relay exchange effectively'*. The first investigation validated one of two theoretical mechanisms proposed for why the relay exchange's effect on race time transitions from positive to negative as the race speed increases. The results showed that due to its smaller uncertainty in velocity, only the developed multi-camera network could conclude that this phenomenon, in part, is due to *Skater*$_1$ and *Skater*$_2$'s relative velocity at first-contact increasing with race speed. The second investigation explored *'how to execute the relay exchange to achieve a gain-in-race position'*. This work examined whether the factors currently reported critical for effective relay exchange execution are discriminative of successful overtakes and used a single case study to explore the mechanisms that underlie the first critical factor. Again, the results illustrated that due to its smaller uncertainty in velocity, only the developed multi-camera network could conclude that (1) the relay exchange's contact energy exchange efficiency was not discriminative of successful overtakes, and (2) that *Skater*$_2$'s velocity was an essential part of the mechanism that underlies the time to first-contact.

Part IV Summary and conclusion

Chapter 16

Summary and conclusion

16.1 Introduction

This thesis investigated developing a tool to measure accurate, two-dimensional, relay exchange kinematics in short-track speed skating. More specifically, based on a review of existing measurement solutions, this thesis aimed to develop a multi-camera network to measure accurate, two-dimensional, relay exchange kinematics. Accordingly, the overarching aim of this thesis was to answer the research question *'Can multi-camera networks be used to measure accurate, two-dimensional, relay exchange kinematics'*. This investigation was formed of three parts. Part I contextualised the need for this programme of work, Part II investigated developing the National Ice Centre (GBR) multi-camera network, and Part III demonstrated how this tool allows Great Britain Short-Track Speed Skating to advance knowledge on *'how to execute the relay exchange effectively'*. In this chapter, for each part of the thesis, I summarise the key findings, discuss their practical implications for Great Britain Short-Track Speed Skating, acknowledge the limitations of the research, and provide a rationale for future work, before presenting an overall thesis conclusion.

16.2 Part I – Multi-camera network contextualisation

The first part of the thesis contextualised the need for developing a multi-camera network to measure accurate, two-dimensional, relay exchange kinematics. First, Chapter 2 evidenced the strategic opportunity of the relay exchange and provided a rationale for how future work should advance knowledge on *'how to execute the relay* *exchange effectively'*. Second, based on this rationale, Chapter 3 formulated a relay exchange measurement needs analysis and reviewed existing short-track speed skating measurement solutions.

16.2.1 Summary of findings

Chapter 2 used spatiotemporal data extracted from three ISU Short Track World Cups to examine the efficacy of the relay exchange in elite short-track speed skating. By quantifying the relay exchange's effect on race time and race position during the 5,000 m relay, the chapter evidenced the strategic opportunity of the relay exchange. For the former, the chapter showed that the relay exchange's effect on race time was dependent on race speed; having a positive effect at slower speeds and a negative effect at faster speeds. For the latter, the chapter showed that – compared to free skating – the relay exchange scenario presented a superior opportunity for a team to overtake. Collectively, these results were used to rationalise how scholars and practitioners should advance knowledge on *'how to execute the relay exchange effectively'*. This work included (1) validating the proposed theoretical mechanisms for why the relay exchange's effect on race time is dependent on race speed, and (2) investigating *'how to execute the relay exchange to achieve a gain-in-race position'*. For the latter, the chapter suggested that this work should begin by investigating whether the factors critical for effective relay exchange execution – when a team is isolated from the pack race – are discriminative of achieving a gain-in-race position, and the mechanisms that underlie these factors.

Chapter 3 used this rationale to formulate a relay exchange measurement needs analysis. The needs analysis showed that to advance knowledge on *'how to execute the relay exchange effectively'*, Great Britain Short-Track Speed Skating need to be able to measure relay exchange kinematics in (1) representative race scenarios, i.e. for up to four teams simultaneously, (2) over its entirety, i.e. the straight and proceeding corner, and (3) with an acceptable level of measurement error; operationally defined as 'the ability to measure skating velocity to within ± 0.19 $m{\cdot}s^{-1}$'. This absolute error, which reflected both the trueness (i.e. the systematic error) and precision (i.e. the random error) of the measurement, was selected to ensure that Great Britain Short-Track Speed Skating could (1) validate the proposed theoretical mechanisms for why the relay exchange's effect on race time is dependent on race speed, and (2) detect the smallest enhancement in skating velocity required to achieve a gain-in-race position.

Chapter 3 used the needs analysis as a criterion to review existing, vision-based, short-track speed skating measurement solutions. The review showed that only one existing method facilitated the measurement of the relay exchange in (1) representative race scenarios, and (2) over its entirety: the multi-camera network installed at the Olympic Oval in Calgary (CAN). However, while this multi-camera network satisfied the metrics, scenarios, and scope of relay exchange measurement, its ± 1.53 $m \cdot s^{-1}$ error in skating velocity did not meet the ± 0.19 $m \cdot s^{-1}$ target measurement error. Accordingly, the remainder of the thesis investigated developing a multi-camera network to measure accurate, two-dimensional, relay exchange kinematics.

16.2.2 Practical implications

The first part of the thesis had several practical implications for Great Britain Short-Track Speed Skating. To the author's knowledge, the study presented in Chapter 2 is the first to investigate the efficacy of the relay exchange in elite short-track speed skating. Therefore, in addition to providing empirical data to support the team's targeted improvement of the relay exchange, coaches and athletes can use the chapter's findings to further improve their tactical preparation and decision-making before and during relay races. First, the chapter showed that the relay exchange's effect on race time is dependent on race speed. This finding suggests that the current norm of executing the relay exchange every 1½ laps may not be optimal. Instead, varying the frequency of the relay exchange execution could allow time to be gained relative to other teams in the race. For example, at faster race speeds (typical of the race end), a team could decrease the frequency of the relay exchange as it has a negative effect on race time. Second, the chapter showed that the relay exchange offers a superior opportunity for a team to overtake. Therefore, if a team knows '*how to execute the relay exchange to achieve a gain-in-race position*', the relay exchange could be used to facilitate other race strategies which are underutilised due to the difficulties in overtaking, e.g. drafting (Hoffman et al., 1998).

16.2.3 Limitations

The first part of the thesis had one notable limitation that warrants consideration. In Chapter 2, the investigation into the relay exchange's efficacy only considered the men's 5,000 m relay event. Consequently, the chapter's evidence regarding (1) the strategic opportunity of the relay exchange, (2) the rationale for how future work should advance knowledge on '*how to execute the relay exchange effectively*', and (3) the relay exchange measurement needs analysis formulated in Chapter 3, were only based on the 5,000 m relay event and not the women's 3,000 m relay event. Although other strategic aspects of short-track speed skating races, such as the relationship between start and finishing position (Maw et al., 2006; Muehlbauer & Schindler, 2011), have shown to exhibit similar relationships when comparing sex, these analyses compared events with the same race distances. As a result, it is currently unclear whether an analysis of the 3,000 m relay event would have led to the same findings as reported in part one. Still, this approach was sufficient for this thesis, as Great Britain Short-Track Speed Skating's targeted relay exchange improvement was primarily focussed on the 5,000 m relay event, as this was the distance funded for the Winter Olympic Games by UK Sport.

16.3 Part II – Multi-camera network development

The second part of the thesis investigated developing the National Ice Centre multi-camera network to measure accurate, two-dimensional, relay exchange kinematics. In Chapter 5, the literature review identified five sources of measurement error that would determine the multi-camera network's accuracy. The quantification of these errors, alongside the creation of a ground truth dataset of kinematics, formed the thesis's first six objectives. Compared to previous investigations, the ground truth dataset facilitated a more detailed quantification of error by allowing all sources of measurement error, in addition to the multi-camera network's intended use-cases, i.e. the effect of skating condition, skater stature, and skating velocity, to be considered. The seventh and final objective of the thesis determined whether the multi-camera network could measure accurate, two-dimensional, relay exchange kinematics. In Section 16.3.1, I summarise the thesis's findings in relation to each of these objectives.

16.3.1 Summary of findings

Rolling shutter error

Chapter 6 used a computer simulation to address the first objective of the programme of research: to quantify *rolling shutter error* in the multi-camera network. *Rolling shutter error* described how within-camera sampling interval error – caused by temporal shear from the image sensor's electronic rolling shutter – propagated to errors in velocity. The chapter showed that the multi-camera network's *rolling shutter error* exceeded the ± 0.19 $m{\cdot}s^{-1}$ target measurement error. Moreover, the magnitude of this error, which ranged from 0.48 $m{\cdot}s^{-1}$ to 1.05 $m{\cdot}s^{-1}$, was dependent on the current skating velocity. The chapter concluded that *rolling shutter error* should be minimised in the multi-camera network by using an electronic rolling shutter model to correct within-camera sampling interval errors.

Out-of-phase error

Chapter 7 used a computer simulation to address the second objective of the programme of research: to quantify *out-of-phase error* in the multi-camera network. *Out-of-phase error* described how between-camera sampling interval uncertainty – caused by two camera shutters being out-of-phase by up-to ± 0.02 seconds – propagated to errors in velocity. The chapter showed that the multi-camera network's *out-of-phase error* exceeded the ± 0.19 $m{\cdot}s^{-1}$ target measurement error. Moreover, the absolute magnitude of this error, which ranged from -7.5 $m{\cdot}s^{-1}$ to 7.5 $m{\cdot}s^{-1}$, was dependent on the magnitude of the between-camera sampling interval uncertainty and the skater's current velocity. As the multi-camera network cannot minimise between-camera sampling interval uncertainties, the chapter concluded that *out-of-phase error* should be negated in the multi-camera network by only calculating two-dimensional relay exchange kinematics within each camera's field-of-view.

Calibration model error

Chapter 8 addressed the third objective of the programme of research: to quantify *calibration model error* in the multi-camera network. *Calibration model error* described how incorrect relationships between the pixel and global coordinate systems propagated to (1) errors in position and velocity within (intra-) cameras' field-of-view, and (2) errors in position between (inter-) cameras' field-of-view. For the former, the chapter showed that the multi-camera network's intra-camera *calibration model error* was within the ± 0.19 $m \cdot s^{-1}$ target measurement error, significantly less than the Olympic Oval (CAN) multi-camera network's ± 0.48 $m \cdot s^{-1}$ intra-camera *calibration model error*, and effectively invariant to the skating condition and skating velocity. The multi-camera network, overall, had a RMS intra-camera *calibration model error* of 0.06 $m \cdot s^{-1}$. As both multi-camera networks had similar reprojection errors, the chapter attributed this significant reduction in intra-camera *calibration model error* to the National Ice Centre (GBR) multi-camera network having a superior spatial resolution of the rink surface. For the latter, the chapter showed that the multi-camera network's inter-camera *calibration model error* was undetectable from one camera to the next when visualising a trajectory over the 60 x 30 m rink surface. The multi-camera network had an overall RMS inter-camera *calibration model error* of 0.01 m and 0.02 m, in the x-and y-axis respectively.

Ground truth kinematics

Chapter 9 described the two-stage process used to address the fourth objective of the programme of research: to create a representative dataset of ground truth short-track speed skating kinematics. Ground truth short-track speed skating kinematics represent the criterion values used in the quantification of the multi-camera network's measurement error. The first stage used four high-speed video cameras, and the multi-camera network, to measure five, real-world, three-dimensional trajectories of a fiducial marker positioned at a skater's two-dimensional centre-of-mass point estimate. The five trajectories, collected over a corner and proceeding straight, covered a range of skating velocities equivalent to 10.12 second to 11.88 second lap times. The second stage applied a suite of geometric transformations to each real-world trajectory to create 21 different full-lap skating trajectories for the minimum, mean, and maximum skater statures in Great Britain Short-Track Speed Skating's World Class Performance Programme. By including various skater statures and skating trajectories, the chapter concluded that the synthetic ground truth dataset (n = 315) was suitable for assessing the multi-camera network's sources of measurement error over this range of skating velocities.

Out-of-plane error

Chapter 10 used a computer simulation to address the fifth objective of the programme of research: to quantify *out-of-plane error* in the multi-camera network. *Out-of-plane error* described how measured points (i.e. the fiducial marker) not on the calibrated plane (i.e. the rink surface) propagated to errors in position and velocity. The chapter showed that the multi-camera network's *out-of-plane error* (± 1.49 $m \cdot s^{-1}$) exceeded the ± 0.19 $m \cdot s^{-1}$ target measurement error and was dependent on the skating condition and skater stature. Fiducial marker out-of-plane distances, ranging from 0.6 m to 1.2 m, led to substantial errors in position (0.01 m to 0.68 m) and velocity (0.66 $m \cdot s^{-1}$ to 1.85 $m \cdot s^{-1}$). The chapter concluded that the multi-camera network's *out-of-plane error* must be minimised in order to measure accurate, two-dimensional, relay exchange kinematics.

To minimise the multi-camera network's *out-of-plane error*, Chapter 11 constructed camera-elevated plane calibration models specific to the skating condition and skater stature. The chapter showed that the multi-camera network's *out-of-plane error* (± 0.25

m·s^{-1}) still exceeded the ± 0.19 m·s^{-1} target measurement error when using these calibration models. Nevertheless, the camera-elevated plane calibration models significantly reduced the magnitude of *out-of-plane error* compared to the rink-plane calibration models (± 1.49 m·s^{-1}), with 90% of the errors now within the target measurement error. In addition, the magnitude of *out-of-plane error* was now effectively invariant to the skating condition, skater stature, and skating velocity. The chapter concluded that this improvement in *out-of-plane error* was due to minimising the out-of-plane distances between the calibrated plane and fiducial marker. Furthermore, the remaining 10% of errors – attributed to the misclassification of each camera's skating condition – could be reduced by classifying each camera's skating condition dynamically.

Skater point error

Chapter 12 began to address the sixth of the programme of research: to quantify *skater point error* in the multi-camera network. *Skater point error* described how uncertainty in the automated digitisation of a skater propagated to errors in position and velocity. By comparing the developed automated digitisation algorithm to manually digitised ground truth data (n = 600 images), the chapter showed that the multi-camera network's automated digitisation uncertainty was less than the Olympic Oval (CAN) multi-camera network, and invariant to the skating condition, for six candidate fiducial marker colours. The four fiducials that exhibited sub-pixel digitisation uncertainty were selected for use as Great Britain Short-Track Speed Skating only required four unique markers to distinguish between relay teams. The chapter concluded that the multi-camera network's improvement in automated digitisation uncertainty was due to fiducial markers, positioned at skaters' two-dimensional centre-of-mass point estimate, reducing ambiguity in the digitised point.

Chapter 13 used Monte Carlo simulations to investigate how this uncertainty propagated to *skater point error*. The chapter showed that the multi-camera network's *skater point error* was within the ± 0.19 $m \cdot s^{-1}$ target measurement error, significantly less than the Olympic Oval (CAN) multi-camera network's ± 1.04 $m \cdot s^{-1}$ *skater point error*, and effectively invariant to the skating condition, skater stature, and skating velocity, for all four fiducial markers. Overall, the multi-camera network's *skater point error* was ± 0.14 $m \cdot s^{-1}$. The chapter concluded that the multi-camera network's improvement in *skater point error* was due to (1) fiducial markers minimising the uncertainty in the automated digitisation of a skater, and (2) the National Ice Centre (GBR) multi-camera network having a superior spatial resolution of the rink surface. Furthermore, the 2% of errors that exceeded the target measurement error – attributed to automated digitisation uncertainty introducing high-frequency noise into reconstructed fiducial marker positions – could be attenuated by using smoothing splines.

Total error

Chapter 14 used Monte Carlo simulations to address the seventh objective of the programme of research: to quantify *total error* in the multi-camera network. *Total error* described how the multi-camera network's five sources of measurement error propagated, collectively, to errors in position and velocity. The chapter showed that the multi-camera network's *total error* was within the ± 0.19 $m \cdot s^{-1}$ target measurement error, significantly less than the Olympic Oval (CAN) multi-camera network's ± 1.53 $m \cdot s^{-1}$ *total error*, and effectively invariant to the skating condition, skater stature, and skating velocity, for all four fiducial markers. Overall, the multi-camera network had a *total error* of ± 0.17 $m \cdot s^{-1}$. These findings had two clear implications for the thesis. First, the findings answered the thesis's overarching research question '*Can multi-camera networks be used to measure accurate, two-dimensional, relay exchange kinematics*'. Yes, if the network's sources of measurement error are mitigated as outlined in this thesis. Second, the findings confirmed that the aim of the thesis – to develop a multi-camera network to measure accurate, two-dimensional, relay exchange kinematics – had been achieved.

16.3.2 Practical implications

The second part of the thesis had one significant practical implication for Great Britain Short-Track Speed Skating. As Chapter 14 showed that the multi-camera network's *total error* was within the ± 0.19 $m{\cdot}s^{-1}$ target measurement error, the results suggested that Great Britain Short-Track Speed Skating could use the National Ice Centre (GBR) multi-camera network as a tool to advance knowledge on *'how to execute the relay exchange effectively'*. In turn, supporting the team's targeted improvement of the relay exchange, and ultimately, their aim of delivering medal-winning performances at the Winter Olympic Games.

16.3.3 Limitations

Although the findings presented in part two of the thesis confirmed that the aim of the thesis had been achieved, Chapters 6 to 14 identified several limitations that may have influenced this result. Of these limitations, two warrant the most consideration. First, Chapter 14 did not quantify the multi-camera network's *total error* for the full range of expected velocities, as the ground truth dataset only included velocities equivalent to 10.12 second to 11.88 second lap times. In short-track speed skating, the fastest lap times can reach 8 seconds. However, by comparing the different velocities in the ground truth dataset, Chapter 14 did show that the multi-camera network's *total error* was effectively invariant to skating velocity. Second, Chapter 13 only quantified the multi-camera network's *skater point error* in the scenario where the fiducial marker's prediction error was less than one pixel. Although, on average, this is the case in the multi-camera network, the prediction errors relatively low precision means that a proportion of prediction errors would be greater than one pixel. While Chapter 12 showed that there was no difference in a skater's digitised position with an additional one- and two-pixel prediction error, and Chapter 14 showed that high-frequency noise associated with digitisation error was attenuated using a smoothing spline, a more detailed understanding of the effect of prediction error on *total error* is required.

16.3.4 Future work

The results presented in the second part of the thesis provide a rationale for how future work should continue to investigate developing the National Ice Centre multi-camera network to measure accurate, two-dimensional, relay exchange kinematics. First, future investigations should address the limitations reported in Section 16.3.3 by quantifying the multi-camera network's *total error* at the fastest expected skating velocities and in the scenario where a fiducial marker has a prediction error greater than one pixel. Second, future work should investigate minimising the multi-camera network's *out-of-plane error* by (1) improving the dynamic classification of skating condition camera, and (2) constructing camera elevated-plane calibration models specific to the current skating velocity, as Chapter 14 showed that the multi-camera network's *total error* was most sensitive to this source of measurement error.

16.4 Part III – Multi-camera network demonstration

The third part of the thesis demonstrated how the multi-camera network's reduction in error to within the target measurement error allowed Great Britain Short-Track Speed Skating to advance knowledge on *'how to execute the relay exchange effectively'*. Chapter 15 presented two investigations on the relay exchange's execution that considered how the developed National Ice Centre (GBR) and benchmark Olympic Oval (CAN) multi-camera networks' uncertainty in velocity affected the interpretation of the results.

16.4.1 Summary of findings

In the first investigation, Chapter 15 used the developed multi-camera network to validate one of two theoretical mechanisms proposed for why the relay exchange's effect on race time transitions from positive to negative with increasing race speeds (Section 2.4.1). This mechanism stated that the relay exchange's effect on race time transitions from positive to negative due to the relative velocity at first-contact increasing. By examining the relationship between the team's current race speed and the relative velocity at first-contact in 12 relay exchanges, the chapter provided empirical data that supported this mechanism. Furthermore, the chapter showed that due to its smaller uncertainty in velocity, only the developed multi-camera network could conclude that the observed relationship was real and not due to measurement error.

In the second investigation, Chapter 15 used the developed multi-camera network to explore *'how to execute the relay exchange to achieve a gain-in-race position'*. This work examined whether the factors reported critical for effective relay exchange execution were discriminative of successful overtakes and investigated the mechanisms that underlie the first critical factor: the time for $Skater_1$ to contact $Skater_2$ after exiting the corner. Again, the chapter showed that due to its smaller uncertainty in velocity, only the developed multi-camera network could conclude that (1) the relay exchange's contact energy exchange efficiency was not discriminative of successful overtakes, and (2) that $Skater_2$'s velocity was an essential part of the mechanism that underlies the time to first-contact.

16.4.2 Practical implications

The third part of the thesis had several practical implications for Great Britain Short-Track Speed Skating. First and foremost, the investigations presented in Chapter 15 demonstrated how the developed multi-camera network's reduction in error enables Great Britain Short-Track Speed Skating to advance knowledge on *'how to execute the relay exchange effectively'*. Accordingly, Great Britain Short-Track Speed Skating can use the developed multi-camera network as a tool to support their targeted improvement of the relay exchange, and ultimately, their aim of delivering medal-winning performances at the Winter Olympic Games.

In addition, as the studies presented in Chapter 15 were the first to investigate their respective topics, Great Britain Short-Track Speed Skating can use the findings to advance their understanding of *'how to execute the relay effectively'*. First, Chapter 15 found that the relative velocity at first-contact increased with race speed. Therefore, to mitigate the negative effect of the relay exchange at faster race speeds, $Skater_2$ should further attempt to match the speed of *Skater*$_1$; even though this requires the skater to expend more energy. Second, Chapter 15 found that the factors critical for effective relay exchange execution differed between the scenarios where a team is isolated from the pack race and achieving a gain-in-race position. Therefore, although the relay exchange always involves *Skater*$_1$ pushing *Skater*$_2$ at the start of the straight, its execution should be approached dynamically – based on the race scenario and the goal of the relay exchange – rather than a 'one-type-fits-all' approach. Finally, the chapter demonstrated that the timing and velocity of *Skater*$_2$ was an essential part of the mechanism that underlies the time to first-contact; the factor that appears critical for effective relay execution in all race scenarios. In this respect, it seemed advisable that *Skater*$_2$ adapts their position and velocity to ensure that they are behind *Skater*$_1$ when this skater passes the corner entry sector line, and approximately level with *Skater*$_1$ at the apex sector line, to guarantee that they do not arrive at the start of the straight too early.

16.4.3 Limitations

The third part of the thesis had three limitations that warrant consideration. First, the number of relay exchanges (n = 12) and relay exchange overtakes (n = 4) analysed in Chapter 15 was small. Although these samples were similar to existing relay exchange investigations (Osborough & Henderson, 2009; Riewald et al., 1997), readers should exercise caution when drawing conclusions from this chapter. Second, the two datasets used in Chapter 15 included male-to-male, female-to-female, and female-to-male, relay exchanges. Although all of these relay exchange scenarios exist in elite short-track speed skating, this thesis was focused on the men's 5,000 m relay event (Section 2.4.4). Accordingly, due to sexual dimorphisms, it is unclear whether male-to-male relay exchanges would produce the same findings given the already small sample size. Finally, the two datasets used in Chapter 15 consisted of relay exchanges from three-team relay races. Although this race format occurs in elite short-track speed skating, the relay event typically involves four-teams racing head-to-head (ISU, 2016). As there is no current understanding of how different spatial constraints – afforded by the team's race position and the number of teams in the pack race – affect the factors discriminative of successful overtakes, the associated findings should only be deemed relevant for three-team race scenarios at present.

16.4.4 Future work

The results presented in the third part of the thesis provide a rationale for how Great Britain Short-Track Speed Skating should continue to investigate the relay exchange execution. First, future work should address the limitations reported in Section 16.4.3, by repeating both investigations using a larger sample of same- and mixed-sex relay exchanges, from three- and four-team relays. Second, future work should investigate *'how to execute the relay exchange to minimise relative velocity at first-contact'*, as this explains, in part, why the relay exchange's effect on race time transitions from positive to negative with increasing race speeds. Third, future work should explore new metrics for quantifying the relay exchange's execution in competitive race scenarios, as only one of the factors currently reported critical for effective relay exchange execution was discriminative of successful relay exchange overtakes. Finally, future work should continue to investigate $Skater_1$ and $Skater_2$'s interpersonal coordination tendencies, as $Skater_2$'s timing and velocity were shown to be an essential part of the mechanism that underlies the time to first-contact. This work should use additional measures – such as $Skater_1$ and $Skater_2$'s relative distance and velocity – over a continuous time scale, as Chapter 15 only considered the skaters' position and velocity at the corner entry, apex, and exit.

16.5 Conclusion

This thesis developed a multi-camera network to measure accurate, two-dimensional, relay exchange kinematics in short-track speed skating. Compared to existing measurement solutions, the multi-camera network can measure relay exchange kinematics in representative race scenarios, over the entirety of the exchange, and with an acceptable level of error. Monte Carlo simulations showed that the multi-camera network's *total error* was ± 0.17 $\text{m}\cdot\text{s}^{-1}$. This error was within the target measurement error (± 0.19 $\text{m}\cdot\text{s}^{-1}$) and significantly less than the benchmark Olympic Oval (CAN) multi-camera network (± 1.53 $\text{m}\cdot\text{s}^{-1}$). Investigations into the execution of the relay exchange demonstrated how this reduction in error allows Great Britain Short-Track Speed Skating to advance knowledge on *'how to execute the relay exchange effectively'*. In turn, supporting the team's targeted improvement of the relay exchange, and ultimately, their aim of delivering medal-winning performances at the Winter Olympic Games.

Chapter 17

References

Atkinson, G., & Nevill, A. M. (1998). Statistical methods for assessing measurement error (reliability) in variables relevant to sports medicine. *Sports Medicine*, *26*(4), 217–238.

Barris, S., & Button, C. (2008). A review of vision-based motion analysis in sport. *Sports Medicine*, *38*(12), 1025–1043.

Bartlett, R. (2014). Quantitative analysis of movement. In *Introduction to sports biomechanics: Analysing human movement patterns* (Third ed., pp. 115–162). Oxford, United Kingdom: Routledge.

Bernards, J., Sato, K., Haff, G., & Bazyler, C. (2017). Current research and statistical practices in sport science and a need for change. *Sports*, *5*(4), 87.

Bouguet, J.-Y. (2015). Camera calibration toolbox for MATLAB. Retrieved from http://www.vision.caltech.edu/bouguetj/calib_doc/

Bradley, D., Atcheson, B., Ihrke, I., & Heidrich, W. (2009). Synchronization and rolling shutter compensation for consumer video camera arrays. In *Proceedings of the IEEE Computer Science Conference on Computer Vision and Pattern Recognition Workshops* (pp. 1–8). Miami, FL, United States of America: IEEE Computer Society.

Bradski, G., & Kaehler, A. (2008). *Learning OpenCV*. (M. Loukides, Ed.). Sebastopol, CA, United States of America: O’Reilly.

Bullock, N., Martin, D. T., & Zhang, A. (2008). Performance analysis of world class short track speed skating: What does it take to win? *International Journal of Performance Analysis in Sport*, *8*(1), 9–18.

Ceccon, S., Ceseracciu, E., Sawacha, Z., Gatta, G., Cortesi, M., Cobelli, C., & Fantozzi, S. (2013). Motion analysis of front crawl swimming applying CAST technique by means of automatic tracking. *Journal of Sports Sciences*, *31*(3), 276–287.

Challis, J. H. (2018). Data processing and error estimation. In C. J. Payton & A. Burden (Eds.), *Biomechanical evaluation of movement in sport and exercise* (Second, pp. 168–194). Oxford, United Kingdom: Routledge.

Chiari, L., Croce, U. D., Leardini, A., & Cappozzo, A. (2005). Human movement analysis using stereophotogrammetry. Part 2: Instrumental errors. *Gait and Posture*, *21*(2), 197–211.

Chun, M.-K. (2001). The kinematic analysis of the cornering movements in short track speed skating. *The International Journal of Applied Sports Science*, *13*(2), 63–80.

Cohen, J. (1988). *Statistical power analysis for the behavioural sciences* (Second ed.). Hillsdale, NJ, United States of America: Lawrence Erlbaum Associates.

Comer, M. L., & Delp, E. J. (1999). Morphological Operations For Color Image Processing. *Journal of Electronic Imaging*, *8*(3), 279–289.

CSER. (2013). Check2D. Retrieved from http://www.check2d.co.uk/

Curran, P. A. (2014). Monte Carlo error analyses of Spearman's rank test. *ArXiv*.

Currell, K., & Jeukendrup, A. E. (2008). Validity, reliability and sensitivity of measures of sporting performance. *Sports Medicine*, *38*(4), 297–316.

de Koning, J. J., de Groot, G., & van Ingen Schenau, G. J. (1992). Ice friction during speed skating. *Journal of Biomechanics*, *25*(6), 565–571.

de Koning, J. J., & van Ingen Schenau, G. J. (2000). Performance-determining factors in speed skating. In V. M. Zatsiorsky (Ed.), *Biomechanics in sport: Performance enhancement and injury prevention* (pp. 232–246). Oxford, United Kingdom: Blackwell Science.

de Queiroz, D. P., Gomide, J. V. B., & de Albuquerque Araújo, A. (2012). Evaluation of real time tracking methods for an open source motion capture system. In *Proceedings of the 25th Conference on Graphics, Patterns and Images*. Ouro Preto, Brazil.

Derrick, T. R., & Gordon, D. G. E. (2014). Signal processing. In D. G. E. Robertson, G. E. Caldwell, J. Hamill, G. Kamen, & S. N. Whittlesey (Eds.), *Research Methods in Biomechanics* (Second ed., pp. 270–290). Champaign, IL, United States of America: Human Kinetics.

Duarte, R., Araújo, D., Davids, K., Travassos, B., Gazimba, V., & Sampaio, J. (2012). Interpersonal coordination tendencies shape 1- vs-1 sub-phase performance outcomes in youth soccer. *Journal of Sports Sciences*, *30*(9), 871–877.

Dunn, M. D., Wheat, J., Miller, S., Haake, S., & Goodwill, S. R. (2012). Reconstructing 2D planar coordinates using linear and non-linear techniques. In E. J. Bradshaw, A. Burnett, & P. A. Hume (Eds.), *ISBS Conference Proceedings* (pp. 380–383). Melbourne, Australia.

Emgu. (2015). Emgu CV-3.0.0. Retrieved from http://www.emgu.com/wiki/index.php/Main_Page

Field, A. (2009). *Discovering statistics using SPSS* (Third ed.). London, United Kingdom: SAGE.

Fitzgibbon, A., Pilu, M., & Fisher, R. B. (1999). Direct least square fitting of ellipses. *IEEE Transactions on Pattern Analysis and Machine Intelligence*, *21*(5), 476–480.

Flam, D. L., de Souza Ramos, T. L. A., de Queiroz, D. P., de Albuquerque Araújo, A., & Gomide, J. V. B. (2009). OpenMoCap: An open source software for optical motion capture. In S. Ceballos (Ed.), *Proceedings of the Brazilian Symposium on Games and Digital Entertainment* (pp. 151–161). Rio de Janeiro, Brazil: IEEE Computer Society.

Garcia-Lamont, F., Cervantes, J., López, A., & Rodriguez, L. (2018). Segmentation of images by color features: A survey. *Neurocomputing*, *292*, 1–27.

Gilbert, A. L., Giles, M. K., Flachs, G. M., Rogers, R. B., & Hsun U, Y. (1980). A real-time video tracking system. *IEEE Transactions on Pattern Analysis and Machine Intelligence*, *PAMI-2*(1), 47–56.

Gordon, D. G. E., & Caldwell, G. E. (2014). Planar kinematics. In D. G. E. Robertson, G. E. Caldwell, J. Hamill, G. Kamen, & S. N. Whittlesey (Eds.), *Research Methods in Biomechanics* (Second ed., pp. 9–34). Champaign, IL, United States of America: Human Kinetics.

Graham, J., & Mayberry, J. (2014). Measures of tactical efficiency in water polo. *Journal of Quantitative Analysis in Sports*, *10*(1), 67–79.

Haug, W. B., Drinkwater, E. J., Mitchell, L. J., & Chapman, D. W. (2015). The relationship between start performance and race outcome in elite 500-m short-track speed skating. *International Journal of Sports Physiology and Performance*, *10*(7), 902–906.

Heikkilä, J., & Silvén, O. (1997). A four-step camera calibration procedure with implicit image correction. In *Proceedings of the IEEE Computer Society Conference on Computer Vision and Pattern Recognition* (pp. 1106–1112). San Juan, Puerto Rico: IEEE Computer Society.

Herda, L., Fua, P., Plänkers, R., Boulic, R., & Thalmann, D. (2001). Using skeleton-based tracking to increase the reliability of optical motion capture. *Human Movement Science*, *20*(3), 313–341.

Hesford, C. M., Laing, S. J., Cardinale, M., & Cooper, C. E. (2012). Asymmetry of quadriceps muscle oxygenation during elite short-track speed skating. *Medicine and Science in Sports and Exercise*, *44*(3), 501–508.

Hettinga, F. J., Konings, M. J., & Cooper, C. E. (2016). Differences in muscle oxygenation, perceived fatigue and recovery between long-track and short-track speed skating. *Frontiers in Physiology*, *7*(619), 1–14.

Hext, A., Heller, B., Kelley, J. W., & Goodwill, S. R. (2016). Measuring straight time in elite short track speed skating relays. *Procedia Engineering*, *147*, 622–626.

Hoffman, E., Listemann, E., McManaman, C., & Rundell, K. W. (1998). Short track speed skating: Analysis of drafting during world championship competition. *Medicine and Science in Sports and Exercise*, *30*(Suppplement 5), 310.

Hopkins, W. G., Hawley, J. A., & Burke, L. M. (1999). Design and analysis of research on sport performance enhancement. *Medicine and Science in Sports and Exercise*, *31*(3), 472–485.

Hopkins, W. G., Marshall, S. W., Batterham, A. M., & Hanin, J. (2009). Progressive statistics for studies in sports medicine and exercise science. *Medicine and Science in Sports and Exercise*, *41*(1), 3–13.

Hoshikawa, H., Yoshino, T., Tamaki, K., Tomita, H., Kato, K., Ishihara, K., … Kawakami, T. (2005). The effects of drafting on blood lactate accumulation during short track speed skating. *Proceedings of the 13th Annual Meeting of the Canadian Soceity for Exercise Physiology*, *30*(Supplement 1).

Hudson, C. R. (2015). *Automated tracking of swimmers in the clean swimming phase of a race*. Sheffield Hallam University.

Hughes, M. D., & Bartlett, R. M. (2002). The use of performance indicators in performance analysis. *Journal of Sports Sciences*, *20*(10), 739–754.

IBM. (2016). IBM SPSS statistics for Windows, Version 24.0. Armonk, NY, United States of America: IBM Corp.

ISO. (1994). 5725-1 Accuracy (trueness and precision) of measurement methods and results — Part 1: General principles and definitions.

ISU. (2016). Special regulations and technical rules. Speed skating and short track speed skating. Dubrovnik, Croatia: International Skating Union.

ISU. (2018). Short-track speed skating mixed gender relay event included in the 2022 Olympic Program. Retrieved January 3, 2018, from https://www.isu.org/news/145-news/12131-short-track-speed-skating-mixed-gender-relay-approved-by-the-ioc-for-beijing-2022?templateParam=15

ITU. (2011). Recommendation ITU-R BT.601-7, Studio encoding parameters of digital television for standard 4:3 and wide-screen 16:9 aspect ratios. *BT Series, Broadcasting Service (Television)*. International Telecommunication Union.

JCGM. (2012). International vocabulary of metrology – Basic and general concepts and associated terms. *Technical Report*.

Kelley, J. W. (2011). *Measuring ball spin rates in match play tennis*. Sheffield Hallam University.

Kim, T.-H., Jun, M.-K., Yoo, S.-H., & Park, S.-K. (2013). Kinematic analysis of cornering with different radius of curve course in short track speed skating. *Korean Journal of Sport Biomechanics*, *23*(2), 109–116.

Kjendlie, P.-L., & Bjørn, H. O. (2012). Automatic 3D motion capture of swimming: Marker resistance. In W. Kohrt & S. Blair (Eds.), *Proceedings of the 59th Annual*

Meeting of the American College of Sports Medicine. San Francisco, CA, United States of America.

Konings, M. J., Elferink-Gemser, M. T., Stoter, I. K., van der Meer, D., Otten, E., & Hettinga, F. J. (2015). Performance characteristics of long-track speed skaters: A literature review. *Sports Medicine*, *45*(4), 505–516.

Konings, M. J., & Hettinga, F. J. (2018). Objectifying tactics: Athlete and race variability in elite short-track speed skating. *International Journal of Sports Physiology and Performance*, *13*(2), 170–175.

Konings, M. J., Noorbergen, O. S., Parry, D., & Hettinga, F. J. (2016). Pacing behaviour and tactical positioning in 1500 m short-track speed skating. *International Journal of Sports Physiology and Performance*, *11*(1), 122–129.

Krig, S. (2014). Ground truth data, content, metrics, and analysis. In *Computer Vision Metrics. Survey, Taxonomy, and Analysis* (pp. 283–312). Berkeley, CA, United States of America: Apress.

Landry, T., Gagnon, L., & Laurendeau, D. (2013). A GIS-centric optical tracking system and lap simulator for short track speed skating. In *Proceedings of the International Conference on Computer and Robot Vision* (pp. 288–294). Regina, SK, Canada: IEEE Computer Society.

Liu, C. (2014). *A computer-aided training (CAT) system for short track speed skating*. Utah State Uinversity.

Liu, G., & Tang, X. (2009). Tracking high speed skater by using multiple model. *Computer and Information Science*, *2*(1), 126–131.

Liu, G., Tang, X. L., Cheng, H. D., Huang, J. H., & Liu, J. F. (2009). A novel approach for tracking high speed skaters in sports using a panning camera. *Pattern Recognition*, *42*(11), 2922–2935.

Liu, G., Tang, X. L., Huang, J. H., Liu, J. F., & Sun, D. (2007). Hierarchical model-based human motion tracking via unscented Kalman filter. In *Proceedings of the 11th IEEE Conference on Computer Vision* (pp. 1–8). Rio de Janeiro, Brazil: IEEE Computer Society.

Magalhães, F. A., Sawacha, Z., Di Michele, R., Cortesi, M., Gatta, G., & Fantozzi, S. (2013). Effectiveness of an automatic tracking software in underwater motion analysis. *Journal of Sports Science & Medicine*, *12*(4), 660–667.

Malcata, R. M., & Hopkins, W. G. (2014). Variability of competitive performance of elite athletes: A systematic review. *Sports Medicine*, *44*(12), 1763–1774.

Malik, N. A., Dracos, T., & Papantoniou, D. A. (1993). Particle tracking velocimetry in three-dimensional flows. *Experiments in Fluids*, *15*(4–5), 279–294.

MathWorks. (2016). MATLAB R2016a. Natick, MA, United States of America: MathWorks.Inc.

Maw, S., Proctor, L., Vredenburg, J., & Ehlers, P. (2006). Influence of starting position on finishing position in World Cup 500 m short track speed skating. *Journal of Sports Sciences*, *24*(12), 1239–1246.

McGarry, T., Anderson, D. I., Wallace, S. A., Hughes, M. D., & Franks, I. M. (2002). Sport competition as a dynamical self-organizing system. *Journal of Sports Sciences*, *20*(10), 771–781.

McGarry, T., Khan, M. A., & Franks, I. M. (1999). On the presence and absence of behavioural traits in sport: An example from championship squash match-play. *Journal of Sports Sciences*, *17*(4), 297–311.

Moeslund, T. B., & Granum, E. (2001). A survey of computer vision-based human motion capture. *Computer Vision and Image Understanding*, *81*(3), 231–268.

Moeslund, T. B., Hilton, A., & Krüger, V. (2006). A survey of advances in vision-based human motion capture and analysis. *Computer Vision and Image Understanding*, *104*(2–3), 90–126.

Muehlbauer, T., & Schindler, C. (2011). Relationship between starting and finishing position in short track speed skating races. *European Journal of Sport Science*, *11*(4), 225–230.

Noorbergen, O. S., Konings, M. J., Micklewright, D., Elferink-Gemser, M. T., & Hettinga, F. J. (2016). Pacing and tactical positioning in 500- and 1000-m short-track speed skating. *International Journal of Sports Physiology and Performance*, *11*(6), 742–748.

Osborough, C., & Henderson, S. (2009). Effect of relay changeover position on skating speed for elite short track speed skaters. In A. J. Harrison, R. Anderson, & I. Kenny (Eds.), *ISBS Conference Proceedings* (Vol. 1). Limerick, Ireland.

Otsu, N. (1979). A threshold selection method from gray-level histograms. *IEEE Transactions on Systems, Man, and Cybernetics*, *9*(1), 62–66.

Park, S.-H., Yun, N.-S., Lee, K.-O., & Baik, J.-H. (1998). The kinematic analysis of short track speed skating in straight. *Journal of Korean Physical Education Association for Girls and Women*, *12*, 103–117.

Payton, C. J. (2008). Motion analysis using video. In C. J. Payton & R. Bartlett (Eds.), *Biomechanical evaluation of movement in sport and exercise* (pp. 8–32). Oxford, United Kingdom: Routledge.

Peikon, I. D., Fitzsimmons, N. A., Lebedev, M. A., & Nicolelis, M. A. L. (2009). Three-dimensional, automated, real-time video system for tracking limb motion in brain-machine interface studies. *Journal of Neuroscience Methods*, *180*(2), 224–233.

Pintaric, T., & Kaufmann, H. (2007). Affordable infrared-optical pose-tracking for virtual and augmented reality. In *Proceedings of Trends and Issues in Tracking for*

Virtual Environments Workshop, IEEE VR (pp. 44–51). Charlotte, NC, United States of America: IEEE Computer Society.

Reed, D., & Hughes, M. (2006). An Exploration of Team Sport as a Dynamical System. *International Journal of Performance Analysis in Sport*, *6*(2), 114–125.

Riewald, S. A., Broker, J. P., Smith, S. L., & Otter, J. (1997). Energetics and timing of relay exahnges in short-track speed skating. *Medicine and Science in Sports and Exercise*, *29*(Supplement 5), 8.

Rundell, K. W. (1996). Effects of drafting during short-track speed skating. *Medicine and Science in Sports and Exercise*, *28*(6), 765–771.

Ruscio, J., & Kaczetow, W. (2008). Simulating multivariate nonnormal data using an iterative algorithm. *Multivariate Behavioral Research*, *43*(3), 355–381.

Russ, J. C., & Brent, N. F. (2011). *The image processing handbook* (Sixth ed.). Boca Raton, FL, United States of America: CRC Press.

Sampe, I. E., Vijai, N. A., Latifah, R. M. T., & Aprintono, T. (2009). A study on the effects of lightning and marker color variation to marker detection and tracking accuracy in gait analysis system. In *Proceedings of the International Conference on Instrumentation, Communication, Information Technology, and Biomedical Engineering* (pp. 1–5). Bandung, Indonesia: IEEE Computer Society.

Seiler, S., de Koning, J. J., & Foster, C. (2007). The fall and rise of the gender difference in elite anaerobic performance. *Medicine and Science in Sports and Exercise*, *39*(3), 534–540.

Shafiq, M. S., Tümer, S. T., & Güler, H. C. (2001). Marker detection and trajectory generation algorithms for a multicamera based gait analysis system. *Mechatronics*, *11*(4), 409–437.

Shapiro, S. S., & Wilk, M. B. (1965). An analysis of variance test for normality (complete samples). *Biometrika*, *52*((3-4)), 591–611.

Sih, B. L., Hubbard, M., & Williams, K. R. (2001). Correcting out-of-plane errors in two-dimensional imaging using nonimage-related information. *Journal of Biomechanics*, *34*(2), 257–260.

Sinclair, J., Taylor, P. J., & Hobbs, S. J. (2013). Digital filtering of three-dimensional lower extremity kinematics: An assessment. *Journal of Human Kinetics*, *39*(1), 25–36.

Skorski, S., Etxebarria, N., & Thompson, K. G. (2016). Breaking the myth that relay swimming is faster than individual swimming. *International Journal of Sports Physiology and Performance*, *11*(3), 410–413.

Sobral, A., & Vacavant, A. (2014). A comprehensive review of background subtraction algorithms evaluated with synthetic and real videos. *Computer Vision and Image Understanding*, *122*(May), 4–21.

Song, M.-H., & Godøy, R. I. (2016). How fast is your body motion? Determining a sufficient frame rate for an optical motion tracking system using passive markers. *PLoS ONE*, *11*(3), 1–14.

Steiner, S., Macquet, A.-C., & Seiler, R. (2017). An integrative perspective on interpersonal coordination in interactive team sports. *Frontiers in Physiology*, *8*(1440).

Stelzer, A., Pourvoyeur, K., & Fischer, A. (2004). Concept and application of LPM - A novel 3D local position measurement system. *IEEE Transactions on Microwave Theory and Techniques*, *52*(12), 2664–2669.

Taylor, J. (1997). *Introduction to error analysis: The study of uncertainties in physical measurements* (Second edition). California, USA: University Science Books.

Theobalt, C., Albrecht, I., Haber, J., Magnor, M., & Seidel, H.-P. (2004). Pitching a baseball - Tracking high-speed motion with multi-exposure images. *ACM Transactions on Graphics*, *23*(3), 540–547.

van der Kruk, E., Schwab, A. L., van der Helm, F. C. T., & Veeger, H. E. J. (2016). Getting the angles straight in speed skating: A validation study on an IMU filter design to measure the lean angle of the skate on the straights. *Procedia Engineering*, *147*, 590–595.

van der Kruk, E., Veeger, H. E. J., van der Helm, F. C. T., & Schwab, A. L. (2017). Design and verification of a simple 3D dynamic model of speed skating which mimics observed forces and motions. *Journal of Biomechanics*, *64*, 93–102.

van Ingen Schenau, G. J. (1982). The influence of air friction in speed skating. *Journal of Biomechanics*, *15*(6), 449–458.

Walton, J. S. (1981). *Close-range cine-photogrammetry: A generalized technique for quantifying gross human motion*. Pennsylvania State University, USA.

Wang, X. (2013). Intelligent multi-camera video surveillance: A review. *Pattern Recognition Letters*, *34*(1), 3–19.

Wang, Y. (2012). *A Novel and Effective Short Track Speed Skating Tracking System*. Utah State University.

Wang, Y., Cheng, H. D., & Shan, J. (2014). Multiplayer tracking system for short track speed skating. *IET Computer Vision*, *8*(6), 629–641.

Wang, Y., Liu, J. F., Liu, G., Tang, X. L., & Liu, P. (2009). Observation and analysis of high-speed human motion with frequent occlusion in a large area. *Measurement Science and Technology*, *20*(12).

Ward-Smith, A. J., & Radford, P. F. (2002). A mathematical analysis of the 4 × 100 m relay. *Journal of Sports Sciences*, *20*, 369–381.

Wilburn, B., Joshi, N., Vaish, V., Levoy, M., & Horowitz, M. (2004). High-speed videography using a dense camera array. In *Proceedings of the IEEE Computer Society Conference on Computer Vision and Pattern Recognition* (Vol. 2, pp. 294–301). Washington, DC, United States of America: IEEE Computer Society.

Yeasin, M., & Chaudhuri, S. (2000). Development of an automated image processing system for kinematic analysis of human gait. *Real-Time Imaging*, *6*(1), 55–67.

Yoo, J.-C., & Kim, Y.-S. (2003). Alpha-beta-tracking index (α-β-Λ) tracking filter. *Signal Processing*, *83*(1), 169–180.

Yoo, Y., Im, J., & Paik, J. (2014). Flicker removal for CMOS wide dynamic range imaging based on alternating current component analysis. *IEEE Transactions on Consumer Electronics*, *60*(3), 294–301.

Yu, B., Gabriel, D., Noble, L., & An, K.-N. (1999). Estimate of the optimum cutoff frequency for the butterworth low-pass digital filter. *Journal of Applied Biomechanics*, *15*(3), 318–329.

Yule, T., & Payton, C. J. (2000). Angle of body lean and speed around the curve in short-track speed skating. *Journal of Sports Sciences*, *18*(1), 11–12.

Zhang, Z. (1999). Flexible camera calibration by viewing a plane from unknown orientations. In *Proceedings of the IEEE International Conference on Computer Vision* (Vol. 1, pp. 666–673). Kerkyra, Greece: IEEE Computer Society.